

THE METALLOGRAPHY OF FATIGUE IN HIGH STRENGTH  
ALUMINIUM ALLOYS.

By  
Kevin John Nix

A Thesis submitted for the Degree of Doctor of  
Philosophy of the University of London and for  
the Diploma of Imperial College.

December 1980

Department of Metallurgy  
and Materials Science  
Imperial College  
London SW7.

ABSTRACT

A study has been made of some aspects of the initiation and growth of fatigue cracks in high strength commercial aluminium alloys, principally the recently developed Al-Zn-Mg-Cu alloy 7010 T76. The microstructure of this alloy has been investigated in some detail: Using electron optical techniques, the composition, morphology and crystallography of second phase particles have been determined and the alloy grain structure and texture have also been investigated.

The crack initiation studies have involved an investigation of fatigue crack initiation from bored holes. Fatigue specimens have been produced containing holes prepared by various combinations of drilling, reaming and deburring processes. Fatigue tests have been executed under constant amplitude loading at a frequency of 100 Hz until specimen failure. Significant differences in fatigue life have been observed, dependent on the hole manufacturing process: The deburring operation has been found to give the largest improvement with deburred specimens, containing both drilled and reamed holes, showing only small differences in life and fatigue limit. Metallographic studies have been made of hole surface topography and microstructure and these observations have been related to crack initiation behaviour and fatigue performance. The growth of short cracks (<Imm in length) has also been studied, using high resolution scanning electron microscopy to measure fatigue striation spacing. Crack growth rates obtained via this method have been related using linear elastic fracture mechanics (L.E.F.M.) to growth rates for long cracks. Results have indicated that L.E.F.M. cannot accurately predict growth rates in this regime; observed rates being lower than those predicted.

An investigation has been made of the micromechanisms of fatigue crack growth using principally electron optical techniques. Transmission electron microscopy has been used in combination with high resolution scanning electron microscopy to study the fracture surface topography and deformation structure associated with crack growth. Such studies have

been made on specimens of 7010 T76 tested in environments of laboratory air (50% relative humidity), dry oxygen and dry argon (<10 ppm H<sub>2</sub>O ). Test frequencies of 0.2, 10 and 100 Hz have been employed at stress ratios (ratio of minimum to maximum stress) of 0.1, -0.3 and 0.5 at a stress intensity range ( $\Delta K$ ) between 6 and 30 MNm<sup>-3/2</sup>. Tests have also been carried out under a simple programme load sequence of varying load amplitude. A similar, less rigorous, study has been made for comparison of crack growth in the Al-Cu-Mg alloy 2024 T3.

Crack growth in laboratory air has been shown to be crystallographically related with segments of fracture on {011} planes. A regular structure of deformation bands, separated by regions of low dislocation density, has been observed below the fracture surface. The structure has been investigated under various conditions of loading and test frequency and it is proposed that it results from brittle/ductile transition occurring during each load cycle, the cleavage component being on {011} planes. The band structure and crystallographic crack plane have been found absent in dry environments and a hydrogen embrittlement mechanism, due to reaction of water vapour at the crack tip, is invoked. This involves the transport of hydrogen ahead of the crack leading to the formation of an embrittled zone in that region, through which the crack propagates.

The formation of fatigue striations has also been investigated in great detail: Two types of striation have been observed, one of sawtooth profile and one consisting of essentially parallel regions of fracture separated by deep slots. The two types of striation have been shown to occur in adjacent areas and can be produced simultaneously on opposing fracture surfaces. Using combined transmission and scanning electron microscopy the striations have been related to underlying deformation structure and show a constant relationship to deformation bands. Under dry test conditions no striations of profiles similar to those above were observed and in fact very few striation-like features were found. A mechanism is proposed to describe the formation of striations which takes into account the basic mechanism of environmentally influenced

crack growth. The formation of striations and their significance in terms of local crack growth rate has also been investigated by relating their spacing to macroscopic crack growth rates.

CONTENTS.

	<u>Page.</u>
<u>PART I. INTRODUCTION.</u>	I
<u>PART 2. EXPERIMENTAL PROCEDURE.</u>	7
I Fatigue Test Piece Manufacture.	7
I.I Initiation Studies.	II
I.2 Crack Propagation Studies.	II
2 Fatigue Testing Details.	II
2.I Crack Initiation Studies.	II
2.2 Crack Propagation Studies.	I6
3 Optical Metallography.	I8
3.I General.	I8
3.2 Microhardness Testing.	20
4 Electron Metallography.	20
4.I General.	20
4.2 Special Techniques.	22
4.2.I High Resolution Fractography.	22
4.2.2 Thin Foil Techniques.	24
4.2.3 Micro-Etch Pitting Studies.	29
<u>PART 3. ALLOY MICROSTRUCTURES.</u>	32
I. THE MICROSTRUCTURE OF HIGH STRENGTH ALUMINIUM ALLOYS CONTAINING ZINC, MAGNESIUM AND COPPER:-LITERATURE REVIEW.	
I.I Introduction.	32
I.I.I Intermetallic Particles Produced During Casting.	32
I.I.2 Particles Produced During Heat Treatments Prior to Ageing.	33
I.2 Precipitation During Ageing.	34
I.2.I Sequence of Precipitation.	34
I.2.2 Structure and Morphology of Precipitate Particles.	38
2. RESULTS AND DISCUSSION.	4I
2.I Grain Structure.	4I
2.2 Intermetallic Particles.	4I
2.2.I Large Inclusions.	4I

2.2.2	Small Intermetallics Present Prior to Ageing.	46
2.2.3	Precipitate Distribution in the T76 Heat Treated Condition.	46
2.3	The Alloy 2024 T3.	49
2.4	Texture Determination.	55

PART 4. CRACK INITIATION STUDIES.

I.	FATIGUE CRACK INITIATION FROM BORED HOLES:-LITERATURE REVIEW.	6I
I.I	Introduction.	6I
I.2	The Metallurgical Effects of Hole Boring.	6I
I.2.I	Subsurface Deformation Produced by Machining.	6I
I.2.2	Residual Stresses	65
I.3	Fatigue Crack Initiation from Bored Holes.	68
I.3.I	Crack Initiation in High Strength Aluminium Alloys.	70
I.3.2	The Effect of Surface Deformation on Crack Initiation.	72
I.4	Microcrack Growth.	77
2.	EXPERIMENTAL RESULTS.	
2.I	Hole Surface Topography and Subsurface Deformation Structure.	88
2.2	Fatigue Test Results.	100
2.3	Fractographic Observations.	114
2.4	Microcrack Growth.	126
3.	DISCUSSION.	
3.I	The Role of Hole Surface Topography in Fatigue Crack Initiation.	129
3.2	The Role of Subsurface Microstructural Damage in Fatigue Crack Initiation.	133
3.2.I	Deformation Structure.	133
3.2.2	The Relationship Between Surface Deformation and Crack Initiation.	136
3.3	The Growth of Short Cracks.	140
3.4	Technological Significance.	144

PART 5. CRACK PROPAGATION STUDIES.

I.	THE MICROSCOPIC MECHANISMS OF FATIGUE CRACK PROPAGATION IN HIGH STRENGTH ALUMINIUM ALLOYS:-LITERATURE REVIEW.	
I.1	Introduction.	I46
I.2	Ductile Crack Propagation.	I47
I.2.1	The Influence of Test Environment.	I47
I.3	The Influence of Water Vapour on Crack Propagation.	I52
I.3.1	Combined Fracture Mechanics-Surface Chemistry Studies.	I52
I.3.2	Surface Reactions.	I58
I.4	Brittle Crack Propagation.	I61
I.4.1	Experimental Evidence.	I61
I.4.2	Theoretical Considerations.	I62
I.4.3	Embrittlement Due to Environmental Interaction.	I64
I.4.4	Embrittlement Via Dislocation/Corrosion Product interaction.	I65
I.4.5	Hydrogen Embrittlement Mechanisms.	I65
I.4.6	Hydrogen Transport and Distribution.	I72
I.5	Fractographic Features.	I75
I.5.1	Mechanisms of Fatigue Striation Formation.	I77
I.5.2	General Features.	I86
I.6	The Influence of Metallurgical Variables.	I86
I.6.1	Precipitate Distribution.	I86
I.6.2	Large Inclusions and Grain Structure.	I90
2.	EXPERIMENTAL RESULTS.	
2.1	Introduction.	I92
2.2	General Fracture Appearance.	I92
2.3	High Resolution Fractography.	I96
2.4	TEM Observations.	201
2.5	Combined HRSEM and TEM Observations.	216
2.5.1	Crack Growth at High and Low Stress Intensity Range.	221
2.6	The Effect of Stress Ratio.	234
2.7	Programme Load Tests.	234
2.8	Crack Growth in the Alloy 2024 T3.	239
2.9	Etch Pitting Studies.	244

2.IO Measurement of Crack Growth Rate from Striation Spacing.	250
2.II Crack Growth in Dry Environments.	250
3. DISCUSSION OF RESULTS.	
3.I Introduction.	258
3.2 The Mechanism of Crack Growth.	258
3.2.I The Crystallographic Fracture Plane.	258
3.2.2 Crack Tip Deformation.	262
3.2.3 Environmental Considerations.	271
3.3 Fractographic Features.	280
3.3.I General Features.	280
3.3.2 Fatigue Striations.	282
3.3.3 The Relationship Between Crack Tip Deformation Structure and Fatigue Striations.	293
3.4 The Influence of Loading Conditions on Crack Growth.	295
3.4.I The Effect of Mean Stress.	297
3.4.2 Programme Loading.	299
3.5 The Relationship Between Cyclic Crack Growth Mechanism and Crack Growth Rate.	302
3.6 The Influence of Metallurgical Variables on Crack Growth.	309
<u>PART 6. PROPOSALS FOR FUTURE RESEARCH.</u>	313
<u>CONCLUSIONS.</u>	317
<u>ACKNOWLEDGEMENTS.</u>	320
<u>REFERENCES.</u>	321
<u>APPENDICES.</u>	

List of Commonly Used Symbols and Abbreviations.

All percentages referred to in alloy composition are weight percent unless otherwise stated.

LEFM	= Linear elastic fracture mechanics
CT	= Compact tension
TEM	= Transmission electron microscope (microscopy)
SADP	= Selected area diffraction pattern
SEM	= Scanning electron microscope (microscopy)
HRSEM	= High resolution scanning electron microscope (microscopy)
EPMA	= Electron probe microanalyser (microanalysis)
HVEM	= High voltage electron microscope (microscopy)
$K_t$	= Elastic stress concentration factor
$K$	= Crack tip stress intensity
$\Delta K$	= Stress intensity range
$K_{max}$	= Maximum stress intensity
$\Delta K_{th}$	= Threshold stress intensity range
$K_C$	= Fracture toughness
$K_{IC}$	= Plane strain fracture toughness
LT	= Long transverse grain axis
$\sigma$	= Stress (in crack initiation studies stresses are quoted as net mean section)
$\sigma_{lim}$	= Fatigue limit
$\Delta\sigma_{lim}$	= Stress range at fatigue limit
$\sigma_y$	= Yield stress
$\phi$	= Crack front shape correction factor
$a$	= Crack length
$a_e$	= Preexisting flaw size
$da/dn$	= Cyclic crack growth rate
$P_{H_2O}$	= Partial pressure of water vapour
$P_c$	= Critical water vapour pressure for full environmental enhancement of growth rate
$f$	= Cyclic frequency
$\sigma_{cr}$	= Theoretical tensile strength (tensile stress required for cleavage at crack tip)
$\tau_{cr}$	= Theoretical shear strength (shear stress required for shear at crack tip via dislocation motion)
$\gamma$	= Surface energy
$b$	= Burgers vector

- $D_H$  = Diffusivity of hydrogen in aluminium
- $V_C$  = Critical velocity for dislocation transport of hydrogen
- $r_p$  = Plastic zone size

PART I. INTRODUCTION.

## INTRODUCTION.

High strength aluminium alloys, containing as alloying additions various combinations of zinc, magnesium and copper, are widely used in the construction of modern high performance aircraft. These alloys have advantages over other materials in terms of their strength and stiffness in relation to density. With fuel economy becoming increasingly important, particularly in transport aircraft, there is a requirement to make full use of these properties in order to save weight. Aluminium alloys also offer great advantage over, for example, titanium alloys in their cost. Aluminium alloys are much cheaper to produce and also are much more easily fabricated, via forging, rolling and extrusion routes into aircraft components.

The alloys most commonly used are those containing copper as the major alloying addition and those based on zinc additions but usually containing a smaller percentage of magnesium. The former are designated 2000 series alloys by the Aluminium Association of America and the latter 7000. (The Aluminium Association of America classification is used throughout this thesis in reference to commercial aluminium alloys. Tables of alloy compositions and tempers are given in Appendix II). The 7000 series alloys can be heat treated to give an ultimate tensile strength (U.T.S.) in excess of 600 MPa, the highest of all aluminium alloys.

Advances in aircraft design and in aluminium alloy strength have both allowed improvements in aircraft performance to be made. However, the reliability of an aircraft in service is also of vital importance and here problems such as fatigue and stress corrosion cracking (S.C.C.) are encountered. Unfortunately high strength aluminium alloys are particularly susceptible to both problems: While great increases in strength can be produced by precipitation hardening both 2000 and 7000 series alloys, improvements in fatigue properties are slight. Often in the peak strength condition susceptibility to stress corrosion cracking is a maximum and fatigue crack growth resistance a minimum. These problems are particularly marked in the 7000 series alloys containing relatively large amounts of magnesium and in most cases these alloys cannot be used in the

peak strength condition. Fracture toughness is also a property of great importance in alloy design, since fatigue and stress corrosion cracks are often difficult to detect and their presence can lead to catastrophic failure, in alloys of low toughness, before they achieve a detectable size.

Recently, great advances have been made, both in the fracture mechanics analysis of fatigue crack growth in aircraft components and also in crack inspection technology. These advances have meant that the safe life of a component can be predicted with some accuracy, cracked components can be detected and repairs effected, before catastrophic failure. There is, nevertheless, a great deal of work required with the aim of improving the properties of aluminium alloys from a fatigue viewpoint and in recognising potential sites for fatigue cracking in order that they may be eliminated. Two types of study are necessary for these goals to be achieved: Firstly, fatigue properties must be related to engineering parameters such as fatigue life, load amplitude and crack tip stress intensity factor. Secondly, a fundamental understanding of the actual micromechanisms of the fatigue phenomenon must be developed. Quite clearly both types of study are equally important and must be integrated in order to make fullest use of them.

In the alloy development field, improvements in stress corrosion resistance in 7000 series alloys have been achieved via the addition of copper and by improved thermomechanical treatments. Thus, improved properties have been obtained in alloys such as, the now commonly used, 7075. Alloys such as this are still found to offer relatively poor fracture toughness and hence further developments have recently been carried out leading to two 'new generation' 7000 series alloys 7010 and 7050. Both alloys have been developed from the viewpoint of optimising fracture toughness and stress corrosion resistance. The alloy 7010, developed by Alcan, is now being used in aircraft construction and the present work has centred around the study of some aspects of the fatigue properties of this alloy. The general properties of the alloy are presented in Reference I. A table of mechanical properties is given in Appendix II.

Some of the problems of fatigue cracking which relate specifically to aircraft have been reviewed by Forsyth (2). Fatigue crack origins are in most cases found to be associated with sites of elastic stress concentration. Despite careful design many such sites are unavoidable and a commonly observed crack origin is at a bored hole or machined cut-out in a component. Bored holes are often filled with fasteners of some kind, for example rivets or bolts, but in many cases are open to allow the passage of cables, fuel pipes etc. Since these holes cannot be avoided completely it is essential to investigate fatigue crack initiation from bored holes of various types in order to optimise fatigue properties. Analyses based on linear elastic fracture mechanics (L.E.F.M.) principles have been carried out in order to predict crack growth rates from bored holes and hence predictions of component life can be made from the time of detection of a fatigue crack.

Recently, interest has been shown in investigating the various methods of hole manufacture and assessing their effect on fatigue properties. The Advisory Group on Aerospace Research and Development (A.G.A.R.D.), an international research co-ordination body, recently set into motion a world-wide research programme with this aim (3): The programme is basically one of fatigue testing of components containing bored holes produced by various machining processes. Most fatigue tests are carried out under complex loading conditions in order to simulate in-service loads.

Part of the present study is also concerned with crack initiation from bored holes: The intention has been to investigate the metallurgical effects of hole boring processes in the alloy 7010 and to study the initiation of cracks from these holes. By this route it may be possible to develop a fundamental understanding of the initiation processes involved and thereby explain some of the differences in fatigue properties attributed to hole preparation. The studies have been made, under the S.R.C. C.A.S.E. award scheme, in conjunction with the Royal Aircraft Establishment who are themselves participating in the A.G.A.R.D. programme. Hole production techniques as specified in the A.G.A.R.D. programme have been used and it is hoped that the present results can be integrated into this

larger study.

Despite possible methods of inhibiting crack initiation in aircraft components via, for example, carefully controlled machining processes as studied here, fatigue cracks are unavoidable. It is therefore vitally important to develop alloys of high fatigue crack growth resistance. However, as noted earlier, while improvements in toughness and particularly strength have been achieved, the fatigue crack growth resistance, particularly in 7000 series alloys, remains poor.

The problems of crack propagation, like those of initiation, have been subject to the two principal types of study: Many workers have related crack growth rates to engineering variables, such as load amplitude and stress ratio (ratio of minimum to maximum stress) and, with the development of linear elastic fracture mechanics, to maximum crack tip stress intensity ( $K_{max}$ ) and stress intensity range ( $\Delta K$ ). Data collected from these studies have allowed comparison to be made between different alloys and also many models for fatigue crack growth have been developed based purely on this continuum approach.

The second group of workers have attempted to explain the fatigue crack growth mechanisms from a microstructural viewpoint. These studies have generally been based on metallographic observations, the earliest employing light microscopy. The scope of this type of study has however been greatly extended by the development of electron optical techniques: In high strength materials at realistic crack growth rates most of the significant features are on a fine scale, resolvable using only scanning and transmission electron microscopy.

The scanning electron microscope (SEM) is now routinely used as an *investigative* tool in fatigue observations, to identify initiation sites, for example, but its use in the observation of fine scale features has been greatly extended by the development of high resolution scanning electron microscopes (HRSEM). Prior to this development the transmission electron microscope (TEM) was used for surface observation on a fine scale, via the use of shadowed surface replicas. However, with HRSEM resolution of around  $30 \text{ \AA}$  such techniques are no longer neces-

sary. The TEM has not been used extensively to study fatigue crack propagation by direct microstructural observation, owing to the difficulties of specimen preparation, it has however, found wide use in the study of pre-crack deformation structures.

The recent development of the combined scanning and transmission 'TEMSCAN' type of microscope has further extended this type of study with its provision of both HRSEM and TEM. Hence, in suitable specimens, both surface and microstructural observations are possible.

As reported later, specimen preparation problems are severe in this type of study, particularly in the examination of microstructures adjacent to crack tips. The use of high voltage electron microscopy (HVEM) with its provision of extra specimen penetrating power is therefore also of great value.

While such metallographic studies cannot provide information of immediate use in the assessment of fatigue performance in terms of engineering parameters, they are essential if the actual processes occurring during crack growth are to be understood. It may then be possible to carry out controlled alloy developments based on these observations. In the present study, metallographic techniques, principally electron optical have been used in order to further develop the earlier studies and gain a better understanding of the mechanisms of fatigue crack growth in high strength commercial aluminium alloys. The study concentrates on the microstructural and environmental aspects of the crack growth mechanism; moist environments having been found to be particularly effective in increasing crack growth rates. Most of the work involves the alloy 7010 but the commonly used alloy 2024 is also investigated. A table of the mechanical properties of this alloy is also given in Appendix II. In order to integrate the metallographic results with engineering parameters observations of crack growth under controlled conditions are vitally important: Such observations have been facilitated in this study by cooperation with a research programme in progress in the Mechanical Engineering Department at Imperial College. The aims of this programme have been to develop crack growth rate laws under

various loading conditions, particularly in the field of the interaction of fatigue and stable crack growth (for details see References 4 and 5). In this study crack growth rates under carefully monitored loading conditions have been measured and hence correlation with metallographic observations of material tested in this programme have been most informative.

The thesis is divided into three major parts: Firstly, the microstructures of the alloys used, particularly 7010, are investigated in some detail. Such a study is particularly important in the case of 7010 since, being recently developed, little information of this kind exists in the literature. The second part concerns the studies of hole boring and crack initiation and the third part deals with crack propagation. The experimental procedures used are in many cases similar in the three parts and hence, in order to minimise repetition, these are detailed together.

PART 2. EXPERIMENTAL PROCEDURE.

## EXPERIMENTAL PROCEDURE.

### I. Fatigue Test Piece Manufacture.

I.I. Initiation Studies. The basic test piece design used in the initiation studies is shown in Fig.2.I. Machined blanks, without the centre drilled hole, were manufactured at the Royal Aircraft Establishment, from rolled 7010 T76 plate, which was supplied by Alcan Ltd. Test pieces were manufactured in three batches over the period of the study.

The first batch (A) of 30 specimens were bored according to the two A.G.A.R.D., hole qualities (3). The boring processes were carried out by British Aerospace, Aircraft Group, Filton Division. The precise details of machine tools used etc. are laid out in a British Aerospace report (6). The general conditions under which the drilling, reaming and deburring operations were carried out for the two hole qualities are shown in Table 2.I. The surface roughness of each hole was measured at this stage using a 'Talisurf' stylus type machine. 15 specimens were prepared to each hole quality.

The second batch of 20 specimens (B) were prepared to the A.G.A.R.D., high quality specification except that the deburring operation was not carried out. 5 of the specimens were then deburred according to the standard route used earlier in order to test the effect of this operation on fatigue properties. The third batch of 21 specimens (C), were manufactured to the low quality, drilled, standard but then the deburring operation as used in the high quality route was carried out.

In order to simplify later identification, specimen types were coded according to the hole manufacture operations carried out upon them; drilled specimens were coded 'D', reamed 'R', reamed and deburred 'RD', etc, Table 2.II shows the specimen codes. These codes are used to distinguish specimen types in all later sections. A summary of the number of specimens of each type in accordance to batch is given in Table 2.III.

In order to allow extensive metallographic investigation of the hole boring processes, holes were also bored in equal thickness plate to the various standards. Some further holes were also

Fig. 2.1

Crack initiation test piece design

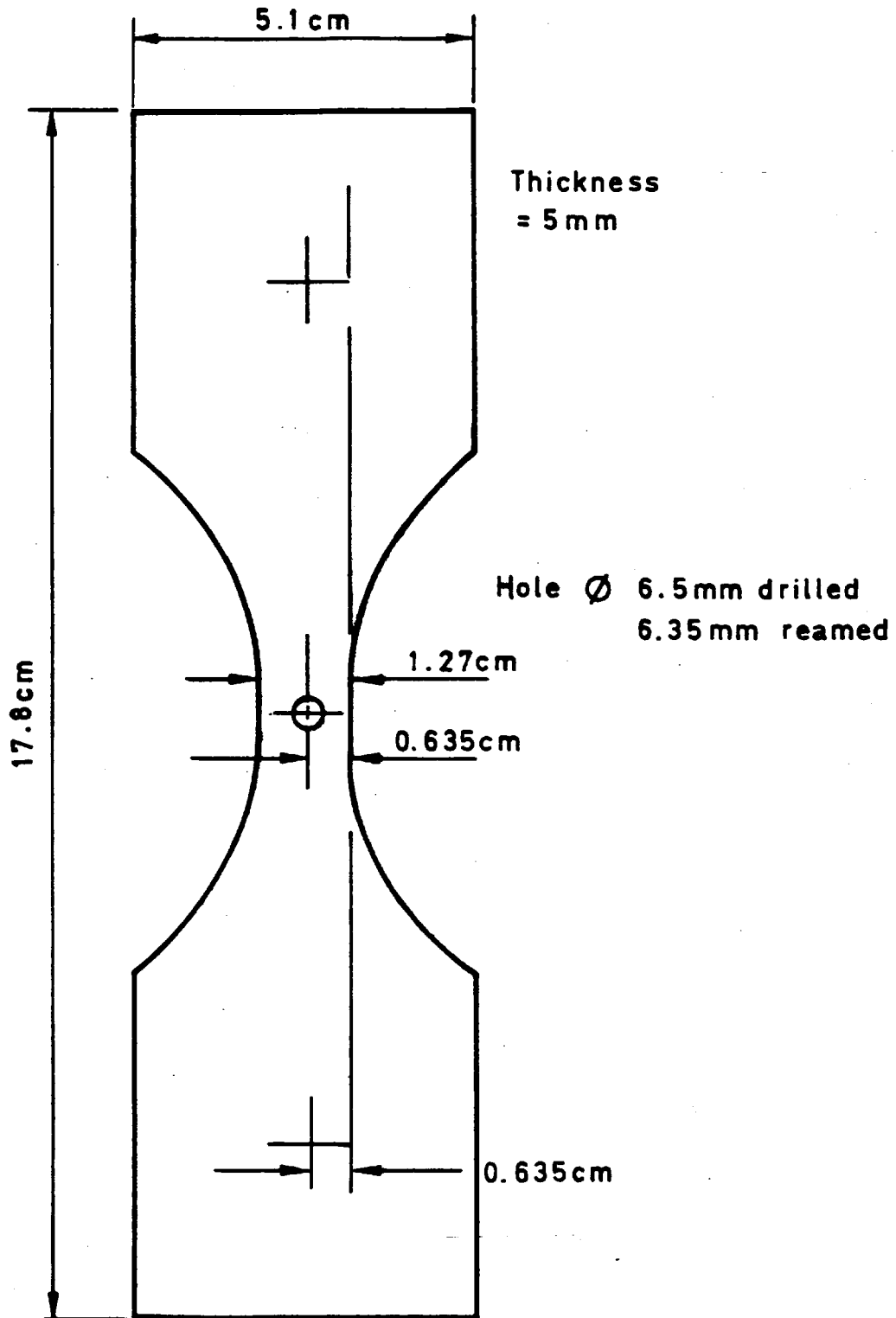


Table 2.I Hole Machining Conditions for A.G.A.R.D. Standards.

(a). High Quality Hole

- (I) Open up 3.2mm pilot hole with a 6.0mm drill at 2000 r.p.m. with an approximate feed rate of 0.08mm/rev.
- (II) Finish hole with a 6.35mm (0.25") reamer at 1100 r.p.m. with an approximate feed rate of 0.2mm/rev.
- (III) Deburr hole edges with a radiused deburring cutter  $\approx 0.25$ mm radius.

(b). Low Quality Hole

- (I) Open up 3.2mm pilot hole with a 6.5mm drill at 2000 r.p.m. with an approximate feed rate of 0.08mm/rev.

Table 2.II

	CODE	MANUFACTURING OPERATION
A.G.A.R.D. Low Quality	D	Drilled
	R	Drilled and Reamed
	DD	Drilled and Deburred
A.G.A.R.D. High Quality	RD	Drilled, Reamed and Deburred

Table 2.III

Specimen Batch	Number of Specimens			
	D	R	DD	RD
A	15	-	-	15
B	-	16	-	4
C	-	-	21	-

drilled without lubricant in order to observe the effect of lubricant on surface metallography.

I.2 Crack Propagation Studies. A major part of the study of crack propagation was made using the initiation type of test piece detailed above and approximate stress intensity-crack length calibration was carried out as detailed in Appendix I. One other type of centre notched test piece was also manufactured as shown in Fig.2.2 primarily for use in the controlled environment tests. All manufacturing operations were carried out at the R.A.E. These specimens were again produced from 2.5 cm 7010 T76 plate.

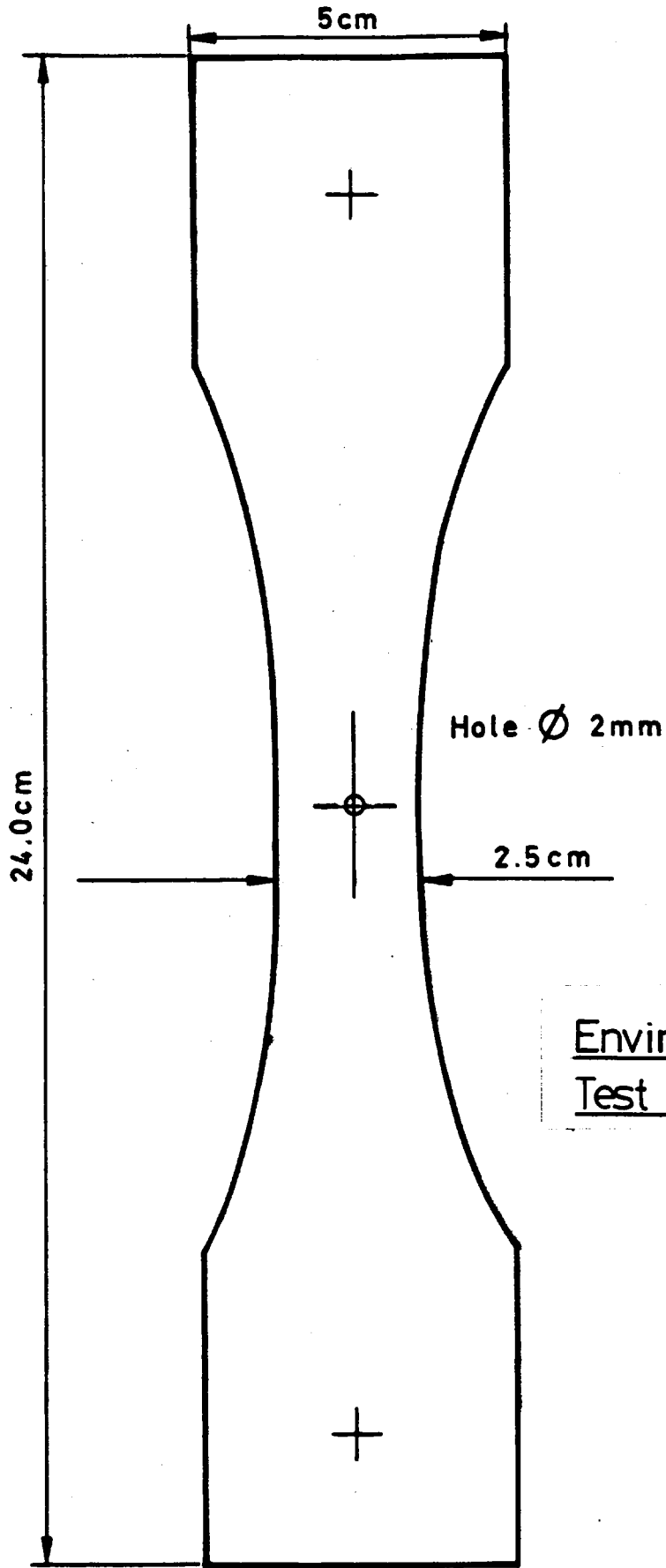
Further metallographic studies were made on specimens of a compact tension (C.T) design (Fig.2.3). These specimens were manufactured and tested in the Mechanical Engineering Department at Imperial College as part of a research programme in that department, discussed earlier, and were supplied in a tested (i.e. cracked) condition. These specimens were manufactured from 7010 T76 plate in a 7.5 cm (3") form. Specimens of this design were similarly supplied of the alloy 2024 T3.

The orientation of the three test piece types with respect to rolling axis are shown in Fig.2.4. The load axis in all three cases was in fact in the long transverse grain direction.

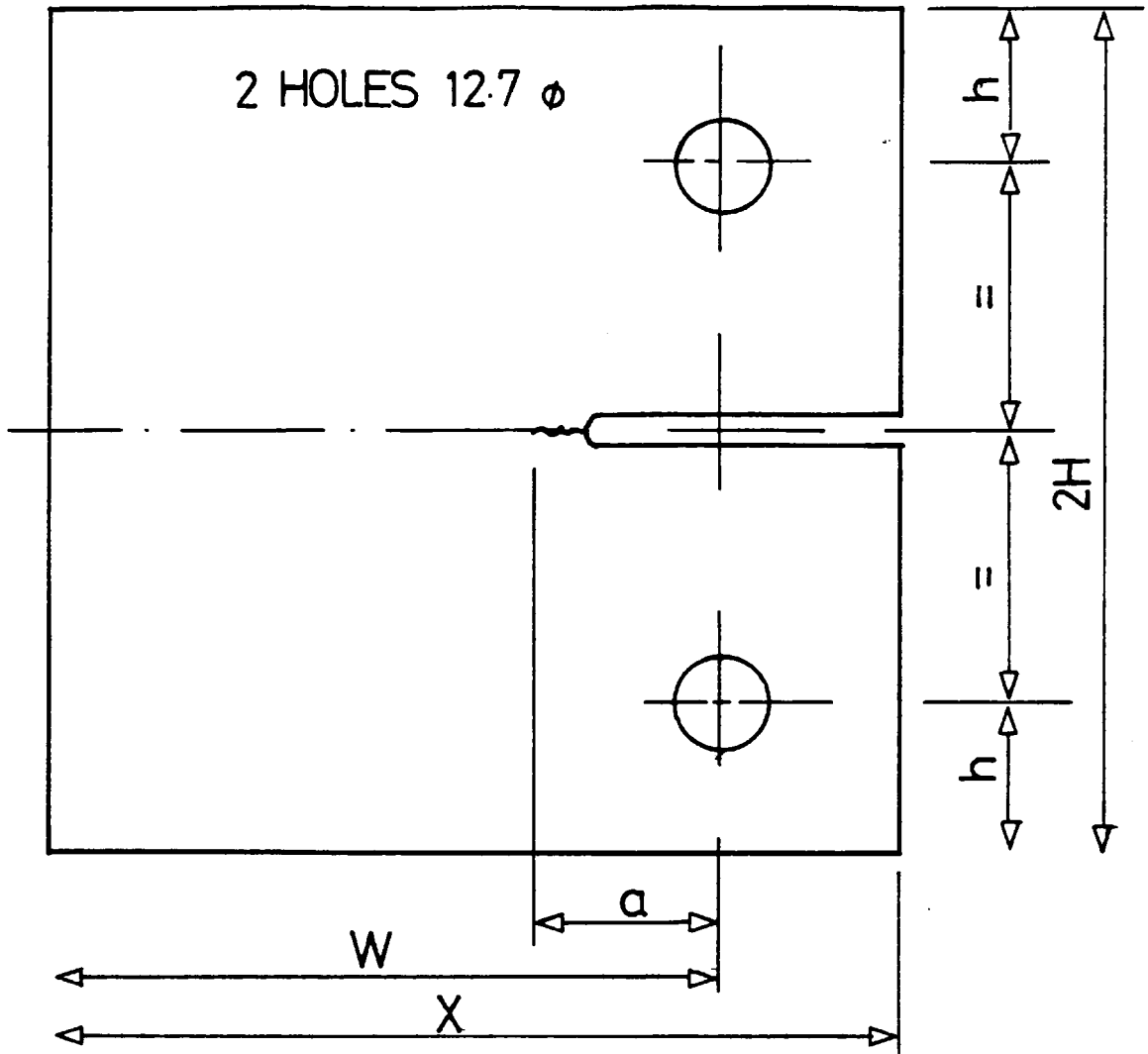
## 2. Fatigue Testing Details.

2.I Crack Initiation Studies. All fatigue tests in the crack initiation studies were made using an Amsler 'Vibrophore' resonance type of fatigue machine operating at a frequency of approximately 100 Hz and at a constant load. A ratio of minimum to maximum stress or stress ratio (R) of 0.1 was used for all tests. Peak stress levels were chosen to give fatigue lives for the various specimen types in the range  $10^5$  cycles to infinity. The stress levels chosen together with the number of specimens of each type tested at each are shown in Table 2.IV. The fatigue tests were automatically terminated by a strain limiting cut-out. This device halted the test at the point of total failure of one side of the centre notched portion of the specimen. In order to determine the fatigue limit (stress level for infinite life) tests were allowed to continue

Fig.2.2

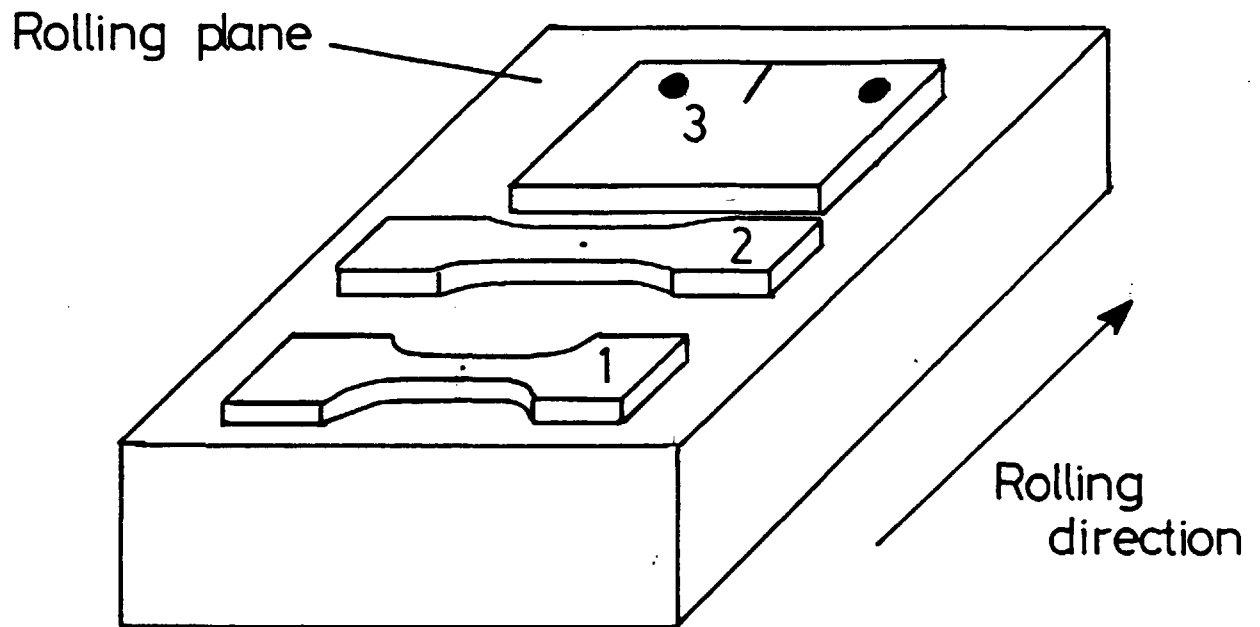


Environmental Cell  
Test Piece



W	X	2H	h
91	174	110	20
107	133	128	25
152	190	183	25

Compact Tension Test Piece Geometry



1. Initiation type specimen
- 2 Specimen type used for dry tests
- 3 Compact tension specimen

### Orientations of Fatigue Specimens

Table 2.IV. Fatigue Test Stress Levels According to Specimen Type.

Peak Stress MPa	Specimen Code			
	D	R	RD	DD
I30	3	-	--	-
I50	5	5	2	-
I75	7	6	II	4
I90	-	-	--	6
200	-	6	6	6
225	-	-	--	5

All stresses shown are net mean section at hole.

to greater than  $3 \times 10^7$  cycles.

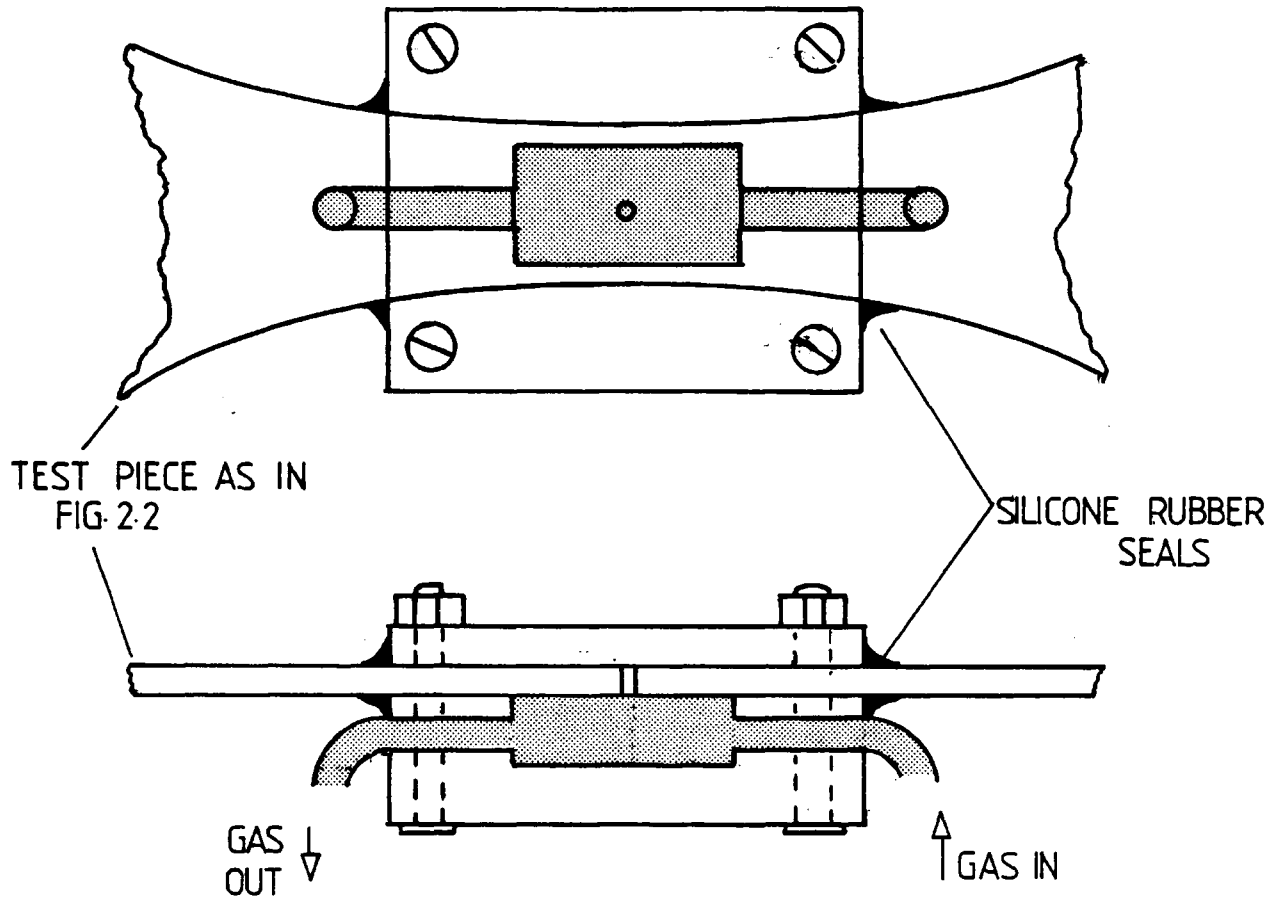
2.2 Crack Propagation Studies. Metallographic studies of crack propagation were carried out on the fractures produced in the initiation studies detailed above. Here, no attempt was made to measure crack growth rates. C.T. test pieces of both 7010 T76 and 2024 T3, as detailed earlier, were provided in a tested condition. Here test frequencies of 0.2 and 10 Hz had been used at stress ratios of 0.1, 0.5 and -0.3. These specimens were found to be particularly useful since they afforded a large area of fracture surface. Also as part of the initial test programme for which they had been used, crack growth rates, as measured optically, had been determined. Some specimens were also provided cracked, but not broken open.

In order to carry out fatigue tests under controlled environments an environmental cell was manufactured to take the second type of centre notched test piece shown in Fig.2.2. The design of the cell is shown in Fig. 2.5. The cell was manufactured to fit closely around the test piece and hence compressive minimum loads could not be used in these tests. The cell was assembled around the test piece with an acetic acid free silicone rubber sealant applied over all areas except the central chamber region. The compound was allowed to cure for several days before testing.

The gas supplies used in these tests were high purity argon and oxygen. The gas was passed over magnesium perchlorate before entry into the cell. The gas outlet from the cell was connected to a dewpoint type of humidity meter, registering from 0 to 1000 ppm  $H_2O$ . The gas was flushed through the system for at least 24 hours prior to testing.

Fatigue tests were again carried out using the Amsler Vibraphore resonance fatigue machine, operating at 100 Hz and  $R=0.1$ . Tests were carried out with gas flowing through the cell with the humidity continuously monitored to detect any breaks in the silicone rubber sealant. A level of water vapour in the atmosphere of less than 10 ppm was maintained at all times. Stress levels were chosen in order to give a fatigue life, in a laboratory air environment, of approximately  $10^5$  cycles.

Fig. 2.5



Environmental Cell Design

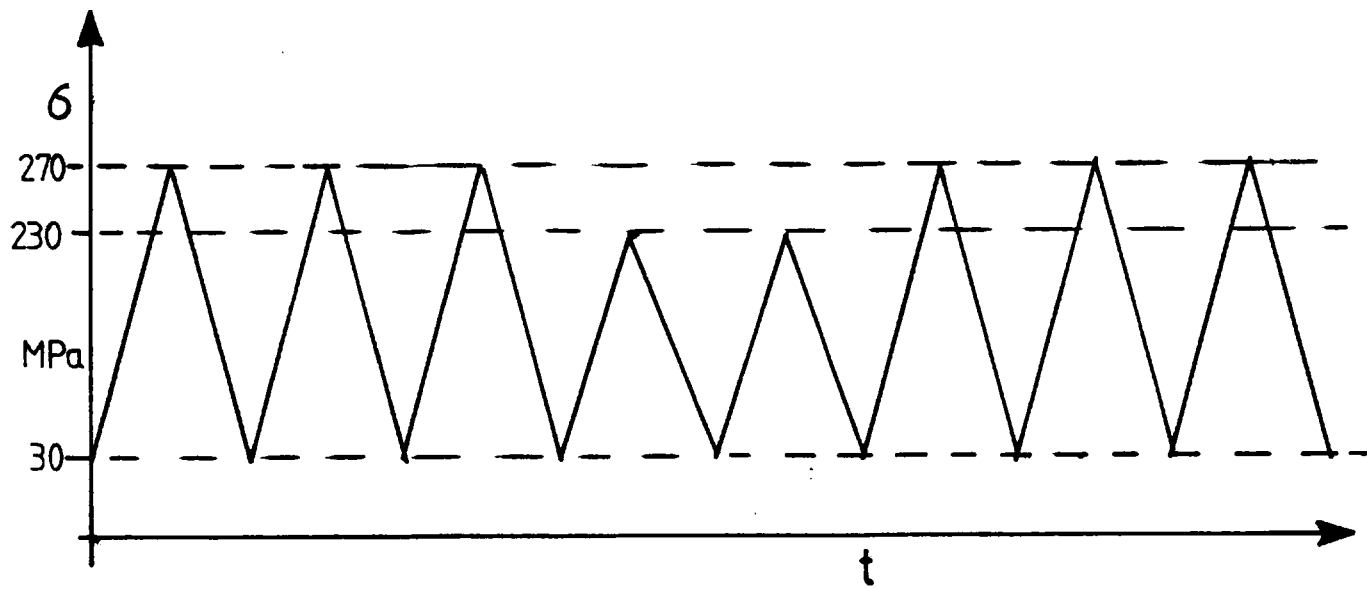
The nature of the cell did not allow the crack growth rate to be monitored and tests were continued to specimen failure.

In order to observe the effect of varying load amplitude on the fractographic features of crack growth some fatigue tests were carried out using a simple programme load. In order to avoid the large crack growth retardation effects caused by large reductions in stress, the peak stress levels chosen differed by only ~20%. The initiation type centre notched specimens were used and two peak stress levels were chosen as 270 and 230 Mpa (net mean section stress) with a constant minimum of 30 Mpa. The most successful programme from the stand point of metallographic observation was found to be one as shown in Fig. 2.6, with groups of three high peak stress cycles, separated by two low peak stress cycles. A constant minimum load was employed. The use of different numbers of each cycle group was found to be most informative from the point of view of fractographic observation. Similar programmes using equal numbers of each cycle type were found to give less easily interpreted results. Tests were carried out using a Dowty servo-hydraulic fatigue machine at a frequency of 10 Hz. The output from the load cell was monitored with an oscilloscope to ensure responses in applied load level were according to the programme.

### 3. Optical Metallography.

3.1. General. The optical microscope was employed to examine the general microstructure of the as-supplied alloy plate and also to investigate the formation of deformation zones around bored holes as part of the initiation study.

All specimens were mechanically polished down to 1µm diamond paste, followed by etching in a solution of 1.5% HCl 2.5% HNO<sub>3</sub> 0.5% HF by volume in water. In order to observe the depth of deformed layers around bored holes, it was found necessary to mount the bored plate in resin prior to mechanical polishing. This allowed the region of interest around the intersection of the hole with the plate surface to be more readily preserved. In all cases a Vickers 'photoplan' microscope was used.



Variable Amplitude Load Programme

3.2. Microhardness Testing. In order to investigate the changes in hardness produced by hole boring operations adjacent to the hole bore, use was made of the microhardness testing facility available on a Reichert optical microscope. This allowed a load as low as 5g to be used producing a standard pyramidal hardness indent. The machine was calibrated before use, allowing the indent size to be converted to the standard Vickers pyramidal hardness number (V.P.N.). In order to resolve the changes in hardness with distance from the hole bore, taper section specimens were manufactured as shown in Fig. 2.7. The drilled plate was cut to produce a semi-cylindrical hole-bore region and this was then ground at a very shallow angle ( $\theta < 1^\circ$ ) producing, along the line x-y, a great magnification of the depth hardness profile. Position along the line x-y was then converted to depth below the hole by the simple calculation shown. Preparation of the specimens was carried out by mechanical polishing to 0.5 $\mu$ m diamond paste. In order to test the possible hardening effect of mechanical polishing, control specimens were electropolished lightly in a solution of 30 vol% HNO<sub>3</sub> in CH<sub>3</sub>OH at 20V and -30°C. However, no detectable differences were observed in hardness between the surfaces prepared by the two techniques. Electropolishing had the disadvantage of producing a slightly irregular surface.

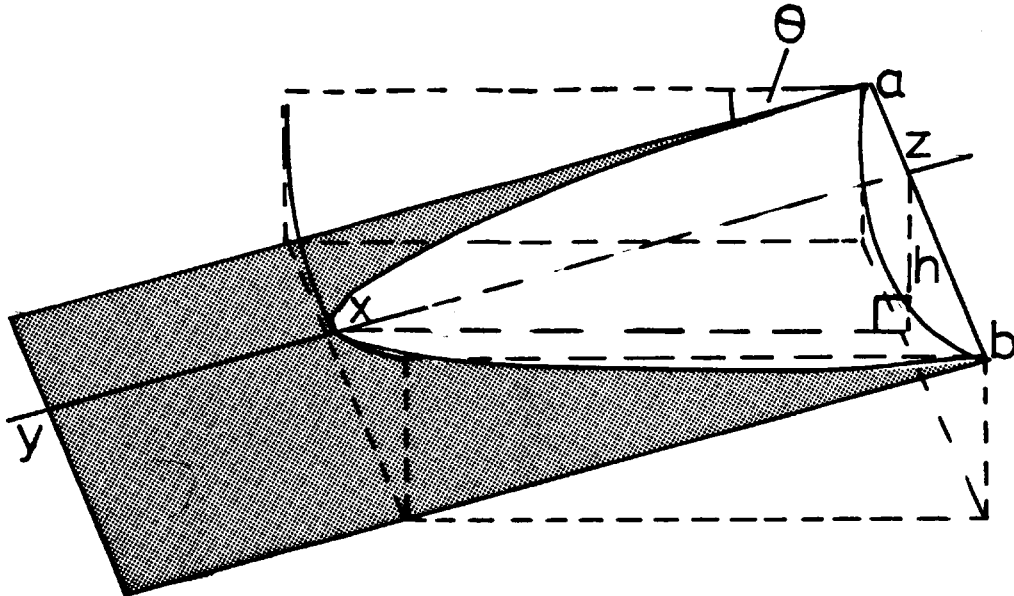
#### 4. Electron Metallography.

##### 4.1. General.

(a) Scanning Electron Microscopy. The scanning electron microscope (SEM) was employed to carry out routine fractographic analysis of all failed crack initiation specimens in order to determine the position and nature of the crack initiation site. Similarly the hole surface topography of each type of specimen was carefully investigated. A JEOL JSM 35 SEM operating at 25 KV was employed for most of these observations. Some use was made also of a JEOL I20CX TEMSCAN microscope operating in scanning mode at 40 KV. This machine had provision for energy dispersive X-ray microanalysis and hence it was possible to carry out qualitative elemental analysis of surface features.

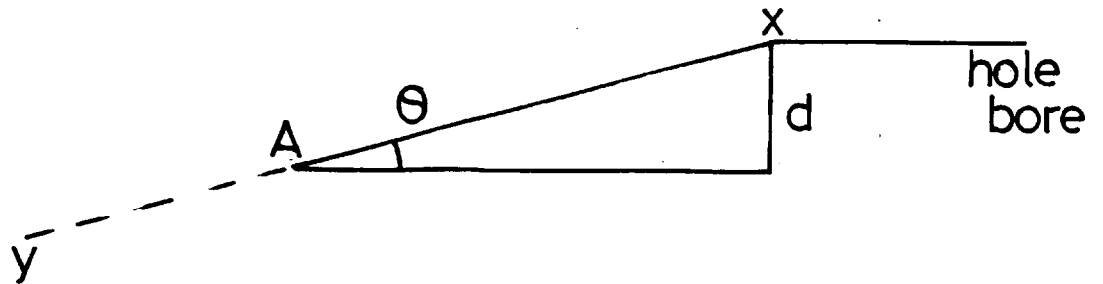
(b) Transmission Electron Microscopy. A rigorous analysis of the microstructure of the alloy 7010 was carried out using the transmission electron microscope (TEM). Both bright field and dark field microscopy were employed, together

Taper Section for Microhardness Profile



$$\theta = \sin^{-1} h/xz$$

h calculated via  
measurement of ab



$$AX \times \sin \theta = d$$

A=position of indent  
d=depth below hole

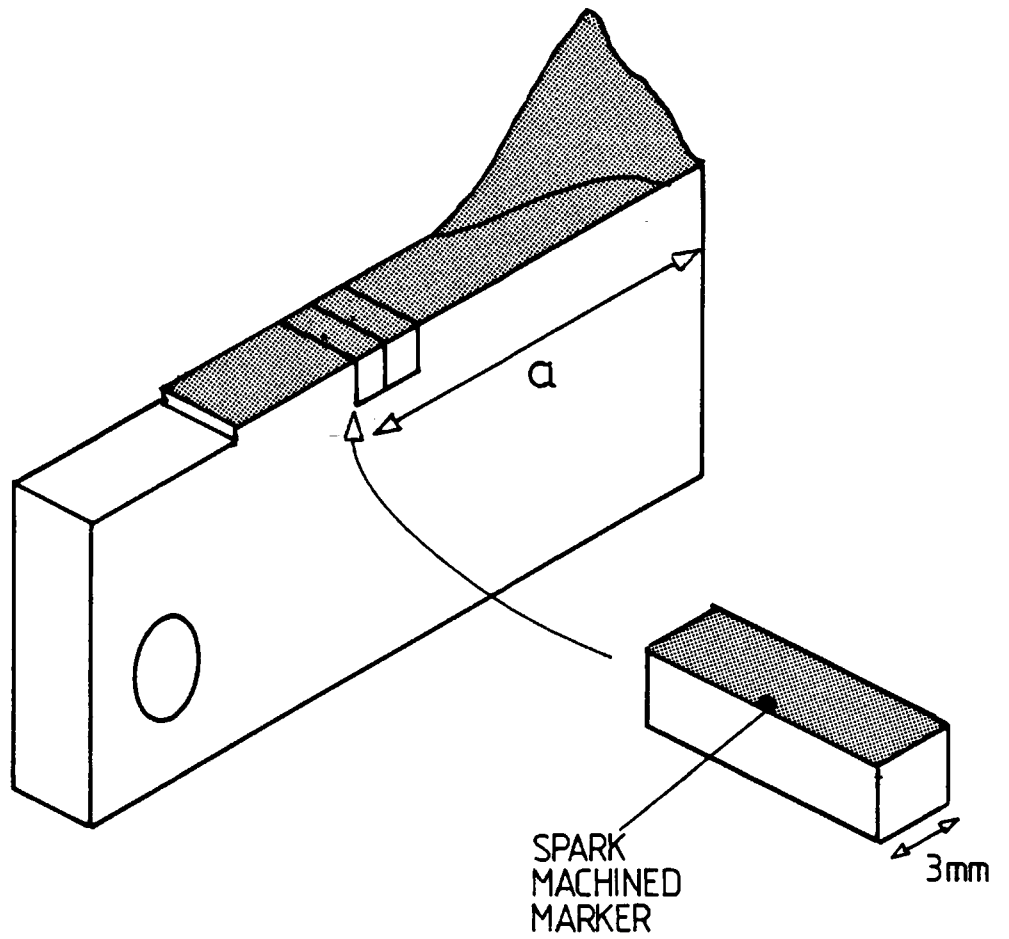
with selected area diffraction in order to investigate precipitate type and morphology. Since little information of this type exists for 7010, observations were made both of the as-supplied, commercially aged, condition and of re-resolution treated material. Imm strip material was prepared and solution treatment was carried out at 465°C for 1 hour, followed by a cold water quench. Thin foils were prepared by electropolishing using a Struers 'Tenupol' jet polisher. A solution of 30 vol% HNO<sub>3</sub> in CH<sub>3</sub>OH was used at a temperature of -20°C and a voltage of 15 to 20V. Observations were conducted in a Philips EM301 TEM operating at 100 KV.

(c) Electron Probe Microanalysis. Mechanically polished specimens of 7010 plate were prepared for observation in the electron probe microanalyser (EPMA). The purpose of the study was to conduct elemental analysis of the large inclusions present in the alloy. The observations were made in a Cambridge Microscan 9 instrument equipped with wavelength dispersive X-ray spectrometers. X-ray intensity maps were obtained for various different areas of the plate and hence the compositions of all the possible particles were qualitatively determined.

#### 4.2. Special Techniques.

4.2.1. High Resolution Fractography. In order to investigate in great detail the features found on the fatigue fracture surfaces use was made of the high resolution scanning electron microscope (HRSEM) facility available on the JEOL I20CX TEM-SCAN. The optimum resolution obtainable using secondary electrons was specified as 30 Å. Stereo microscopy was found to be particularly informative eliminating many possible ambiguities in observation .

It was found to be most important to avoid any possible confusion over the direction of crack growth. In the case of centre notched specimen types no particular problems were apparent since it was possible to observe the entire fracture surface. The large C.T. design specimens were, however, sectioned by spark machining, as shown in Fig. 2.8. Vertical slices were cut initially and the distance,  $a$ , relating the position of each slice to the overall crack length was measured for each slice. A circular marker, around 0.5mm



Position of Sections for Fractographic Observation

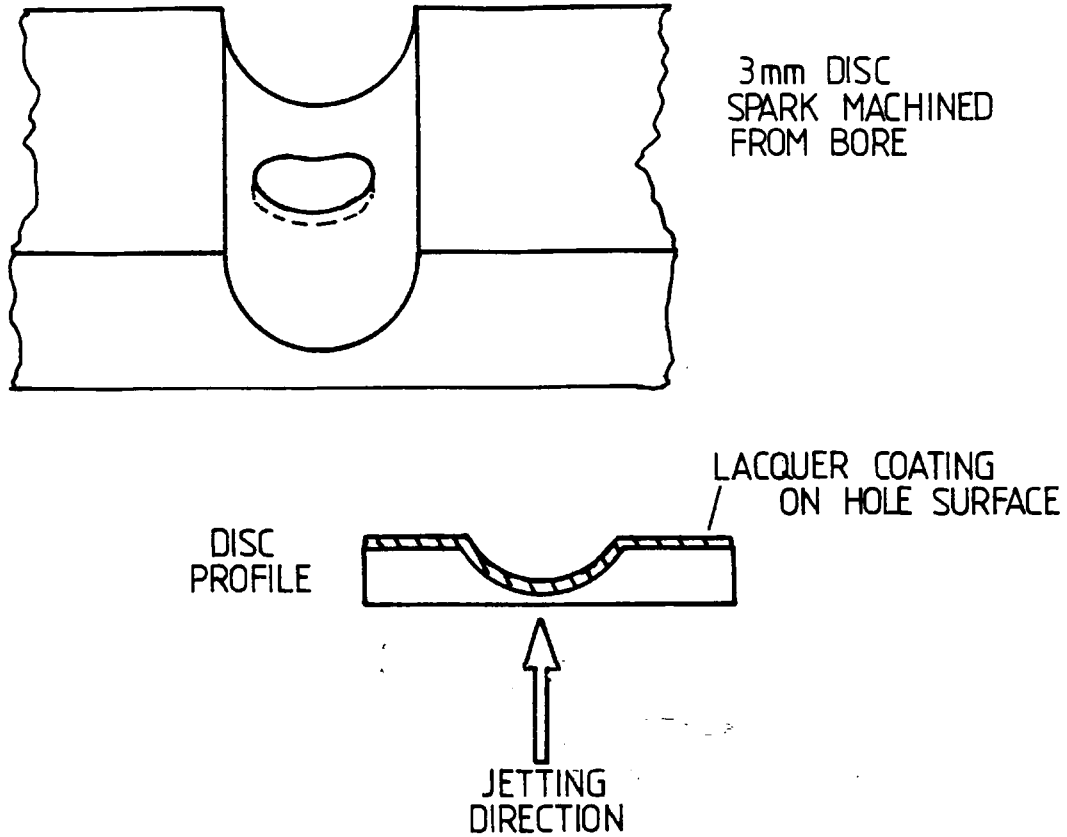
in diameter, was then spark machined in to the fracture surface at the edge of the slice nearest the origin. The slices were then removed by a horizontal spark machined cut. By this method it was possible to relate any features observed to the local overall crack growth rate and stress intensity range previously determined. Also, possible rotations of crack growth direction were avoided.

Great care was taken to avoid contact of water with the fracture surface at any stage during preparation. Specimens were observed, without conductive coating, at an accelerating voltage of 40 KV.

In order to further investigate the formation of fractographic features it was attempted to match opposing faces of the same specimen at magnifications in excess of 10,000x. Various methods were attempted but the most successful was found to involve mounting the matching fracture faces together on the same specimen holder. The two halves were then observed consecutively until some clear point of reference was found, visible at low magnification of the order of 100x. Features were then observed in the environs of the reference point at high magnification. The fitting of a screen delineated with a 1cm square grid to the SEM display was found to be most useful.

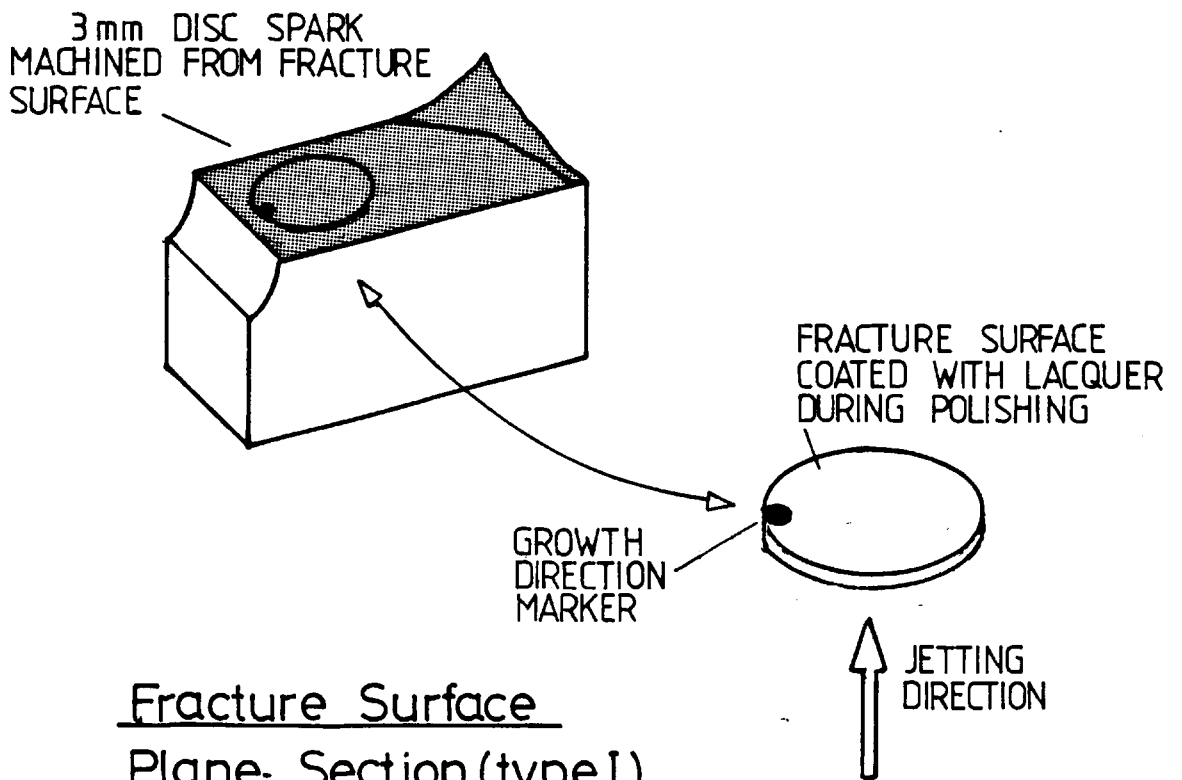
4.2.2. Thin Foil Techniques. In order to observe the deformation structure adjacent to the surface of a bored hole thin foil specimens were prepared by the technique outlined in Fig. 2.9. 3mm discs were first spark machined from the bore of the hole as shown, one face of the disc being the hole surface itself. The hole surface was then coated with a protective lacquer. A dilute solution of 'Lacomit' in acetone was used. This afforded protection for the hole surface during subsequent grinding operations and during electropolishing. Electropolishing was carried out using the TENU-POL jet polisher under identical conditions to those detailed earlier. In this case however, polishing was conducted from the reverse side only, final perforation of the foil occurring adjacent to the hole bore. The lacquer was then carefully removed by dissolution in acetone.

Fig. 2.9



Hole Surface Foil : Specimen Preparation

Fig. 2.10



Fracture Surface  
Plane- Section (type I)  
Foil : Specimen Preparation

Thin foils of this type were observed both in the Philips EM30I and JEOL I20CX operating at 100 KV. In order to investigate the complex structures found in these specimens it was found informative to employ the micro-beam diffraction facility available on the TEMSCAN. Here an electron probe, diameter of 20 Å can be produced, allowing electron diffraction information to be obtained from areas of less than 500 Å in diameter (taking into account beam spreading through the foil).

Two thin foil techniques were developed in order to investigate the microstructural features associated with fatigue crack growth. The first, and most successful, allowed electron transparent areas to be obtained directly adjacent to the fracture surface. The technique illustrated in Fig. 2.10 involved initially the spark machining of 3mm disc type specimens from the fracture surface. Once again, prior to their removal from the surface, circular markers were machined into the edge of the disc to delineate crack growth direction. In the case of C.T. design specimens the disc positions were also measured to ensure accurate stress intensity calibration. In fact, since few C.T. design specimens were available it was found necessary to prepare thin foil specimens from slices manufactured for HRSEM, after their observation in the microscope.

After removal, the fracture surface was coated with a thin lacquer and preparation then proceeded in a manner similar to that used for hole surface specimens. The lacquer was found to adhere extremely strongly to the fracture surface during polishing but could be removed almost completely by acetone dissolution. Hence it was possible to obtain thin foil specimens of areas directly adjacent to the original fracture surface with fractographic features retained on the surface.

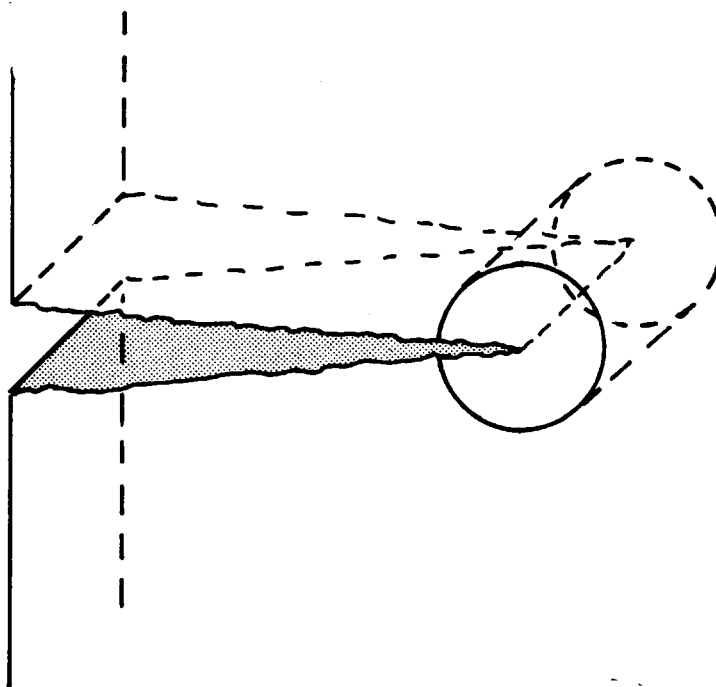
The specimens thus obtained were observed generally in the JEOL I20CX operating at 100 KV. Some specimens were however not electron transparent at 100 KV and were observed in a 200CX operating at 200 KV or in an AEI EM7 high voltage electron microscope operating at 500 KV. Using the I20CX

TEMSCAN in both TEM and HRSEM modes it was possible using this specimen type to directly relate surface fractographic features to underlying microstructural and electron diffraction information. This technique was found to be most valuable.

The second type of thin foil specimen was prepared as shown in Fig. 2.II. Here it was attempted to obtain electron transparent areas including the fatigue crack tip. Test pieces of the C.T. design were supplied pre-cracked, the crack tip stress intensity at which the test ceased being accurately known. The crack tip region was first spark machined from the test piece of a Icm cylinder. The Icm cylinders were then cut, again by spark machining, into discs approximately 1mm thick. These discs were then mounted on flat plate using an acetone soluble, electrically conductive, adhesive. Great care was taken not to subject the crack tip, approximately central within each disc, to any stress.. The discs were then ground to 0.2-0.3mm thickness and were mechanically polished to produce a smooth finish. The position of the crack tip was determined within each disc by observation under the optical microscope and its position marked. 3mm discs were then spark machined from each Icm disc, the crack tip being as nearly central as possible within each 3mm disc.

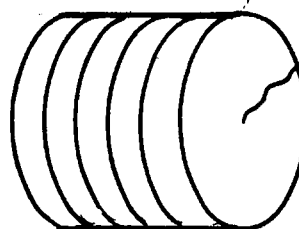
Three different routes were attempted to thin the 3mm disc type specimens. Some specimens were simply jet polished in the normal way in the TENUOL polisher. This technique did not prove successful since no control was possible over the point of perforation. In most cases perforation occurred behind the crack tip and very little thin area was produced. In other cases perforation occurred ahead of the crack, the crack tip region being electron opaque.

It was found that specimens prethinned in the TENUOL could be further electropolished using a purpose built jet-polisher. The design is shown in Fig. 2.I2 and pumping of solution was effected by the rotation of a magnetic stirrer. A solution of 30 vol% HNO<sub>3</sub> in CH<sub>3</sub>OH was again used at a temperature of -20°C and 15 V. The specimens were thinned from one side only, the opposite face being coated with protective lacquer.

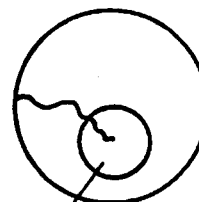


1cm CYLINDER  
SPARK MACHINED  
FROM TEST PIECE,  
CONTAINING CRACK  
TIP

CYLINDER CUT  
INTO DISCS  
= 1mm THICK



EACH DISC MOUNTED  
AND POLISHED IN ORDER  
TO LOCATE CRACK TIP



3mm DISC SPARK MACHINED  
WITH CRACK TIP CENTRAL

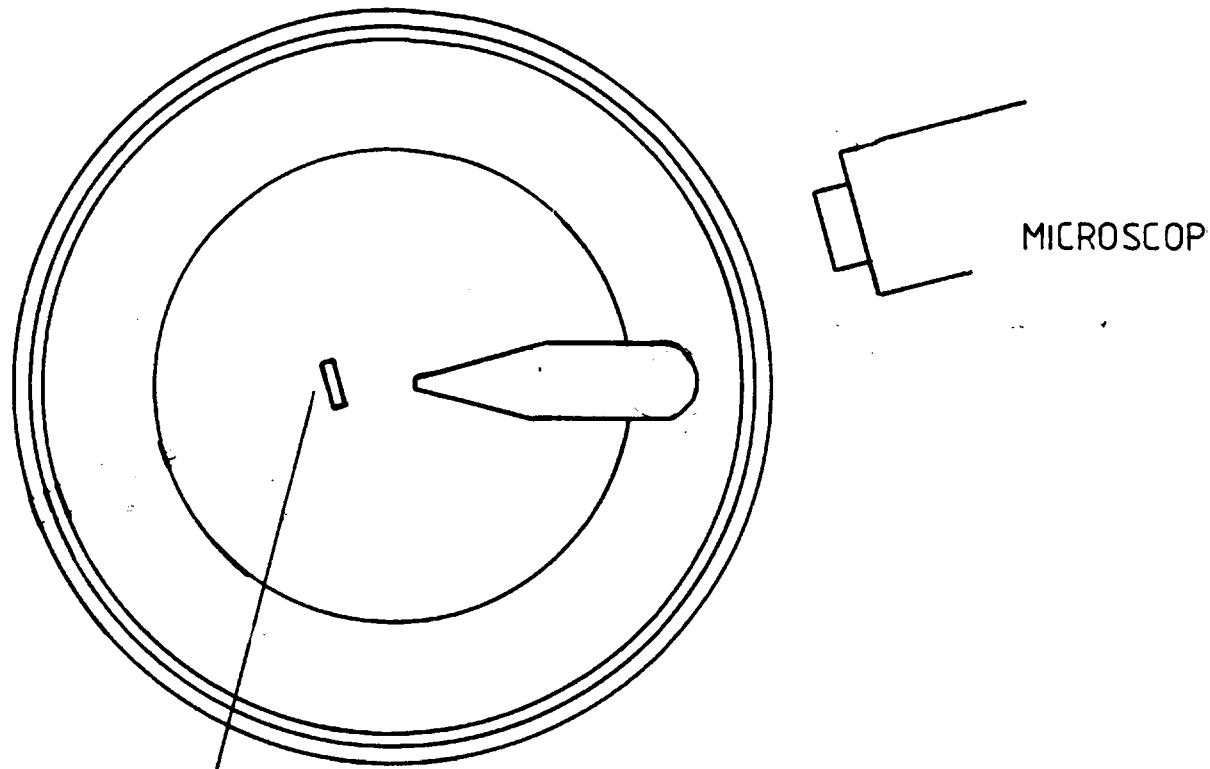
Crack Tip Cross Section (type II)  
Thin Foil: Specimen Preparation

The jet was angled to the specimen surface at around  $45^{\circ}$ . Such an angled jet was employed by Unwin and Wilkins (7) to successfully prepare similar foils in aluminium alloys. The specimens were observed in a long focal length optical microscope during polishing and as soon as the perforation approached the crack tip polishing was stopped and the specimen removed.

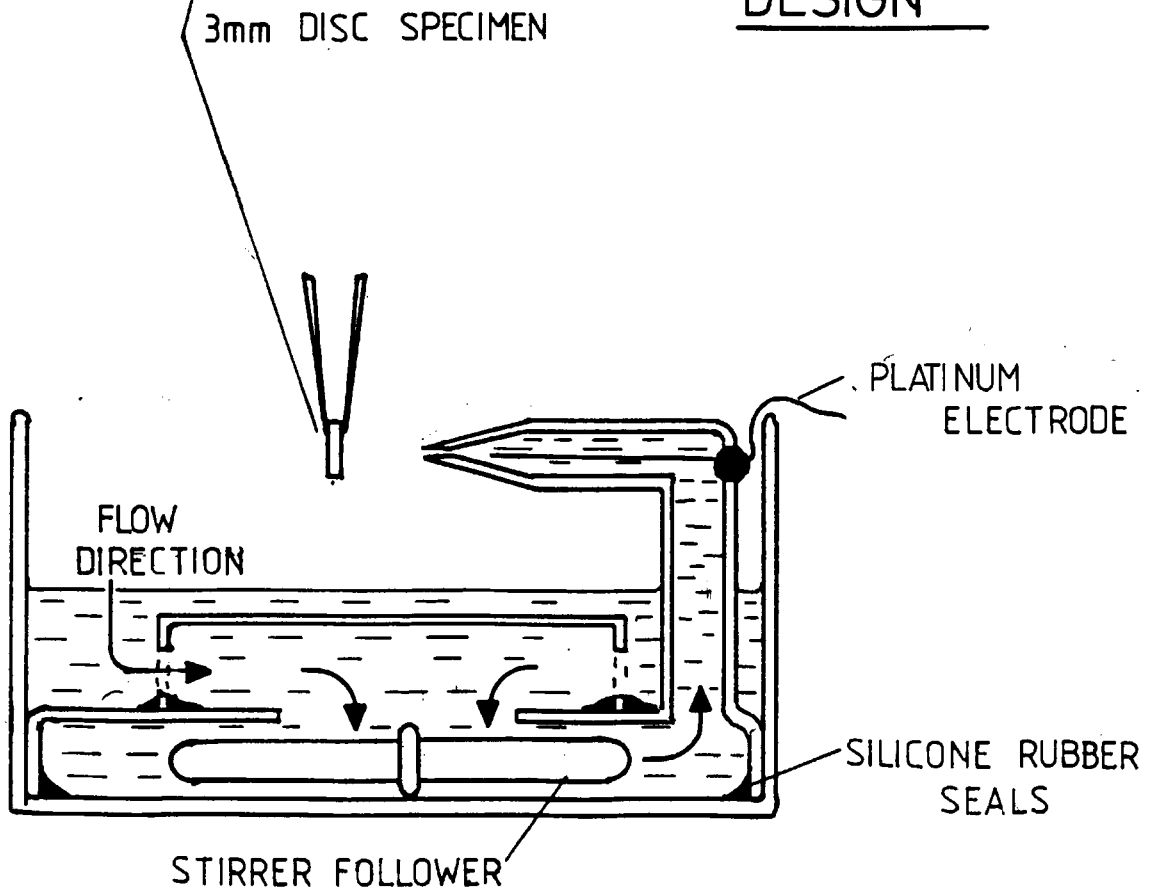
The third method of preparation involved ion-beam thinning. Specimens were thinned in an Ion-tech 'Super Microlap' thinner with an accelerating voltage of 5 KV. Thinning proceeded very slowly and the crack was not preferentially polished to any extent. It was therefore possible to obtain electron transparent regions adjacent to and ahead of the crack tip.

All specimens of this type were observed in the AEI EM7 high voltage electron microscope operating at 500 KV. However, even with the extra penetrating power afforded by the high accelerating voltage it was not possible to observe areas in the region of the crack tip in any electropolished specimens and observations were limited to a very narrow region  $\sim 2-3\mu\text{m}$  maximum to the side of the crack, some distance from the crack tip. Thin area was produced in the crack tip region by ion-beam thinning but, as detailed later, the ion-beam thinning process was found to give rise to a great modification of the alloy microstructure, resulting in many artifacts.

4.2.3. Micro-Etch Pitting Studies. In order to investigate the crystallographic nature of regions of the fracture surface a micro-etch pitting technique was used. The process involved the etching of the fracture surface in order to produce geometrically shaped etch pits which were then related to surface crystallography. The etchant used consisted of 14%HF 43% $\text{HNO}_3$  43%HCl by volume. Etching times were extremely short, less than one second. Similar etchants have been used previously and, as discussed later, are believed to produce pits whose faces are segments of {100} planes. In order to verify this thin foil specimens were etched in a similar manner and pit shapes were compared with selected area diffraction data obtained with the foil untilted. Use was again made of the



JET POLISHER  
DESIGN



combined TEM/HRSEM facilities available on the JEOL I20CX TEMSCAN in order to do this. Bulk, fracture surface, specimens were similarly etched and were also observed in the HRSEM mode. Pit shapes were determined very carefully using stereo pair techniques, since in two dimensions the pit shapes, and hence fracture surface orientation, could not be unambiguously determined.

PART 3. ALLOY MICROSTRUCTURES.

## I. THE MICROSTRUCTURE OF HIGH STRENGTH COMMERCIAL ALUMINIUM ALLOYS CONTAINING ZINC, MAGNESIUM AND COPPER:-LITERATURE REVIEW.

### I.I Introduction.

As already mentioned, the alloy 7010 has only recently been developed and hence little microstructural information is available. A moderately detailed study was therefore made in the present work and it is useful at this stage to discuss relevant areas in the literature. Many workers have studied the structure and properties of alloys within the Al-Zn-Mg-Cu system and a review of this work is provided by Mondolfo (8,9).

All high strength commercial aluminium alloys of this type are produced by casting followed by thermomechanical treatments, which can in many cases be extremely complex (10), and finally solution treatment and ageing. At all stages during processing second phase particles can be precipitated and these can all have a profound effect on final properties. These particles fall basically into three groups:

- (a) Large 1.0→10 $\mu$ m diameter particles produced during casting
- (b) Intermediate 0.05→0.5 $\mu$ m diameter particles precipitated during homogenisation and solution treatments, and during hot working at temperatures between 400 and 500<sup>o</sup>C.
- (c) Precipitates 0.01→0.5 $\mu$ m produced during ageing.

I.I.I Intermetallic Particles Produced During Casting. The particles produced at this stage are generally rich in iron, copper and silicon in commercial alloys (11). They are produced by reactions occurring in the melt or in the final stages of solidification. In alloys containing significant quantities of copper, particles rich in this element have been found to be particularly prevalent (12). Di Russo and Buratti (13) found that in the alloy 7175 second phase particles consisted of an Al-Fe-Si intermetallic compound together with Al<sub>7</sub>Cu<sub>2</sub>Fe with smaller amounts of Mg<sub>2</sub>Si. In the alloy 7050, an alloy very similar in composition to 7010, another phase containing copper and possibly magnesium and zinc was also observed. All these particle types were found to be essentially unaffected by subsequent heat treatment and were found therefore in the final wrought product. The particles were found by Peel and Forsyth (12) to decorate the as cast grain boundaries in many cases and to be

drawn out into long stringers after hot working.

These particles have attracted a good deal of attention in the literature since they are well known to have a great effect on fracture toughness (II) as they fracture and decohere ahead of a propagating stable crack giving rise to failure by microvoid coalescence. Peel and Forsyth found that fracture toughness was particularly low in the case where long stringers of particles were produced; failure was then found to occur along these planes of weakness. In order to improve toughness high purity aluminium is used as a starting material in the production of 7010 thereby reducing iron and silicon levels. Also zirconium is added to the alloy as a grain refiner rather than the previously used chromium. It is possible however that a reaction may occur during casting to give  $ZrAl_3$  in a body centred tetragonal form (8). This reaction takes place at  $661^{\circ}C$  in a binary Al-Zr alloy, and would give rise to undesirable, large particles.

I.I.2. Particles Produced During Heat Treatments Prior to Ageing. After casting it is possible that coring has led to eutectic formation and various thermomechanical treatments are used (10) to break up these colonies and also impart an elongated grain structure to the alloy. Homogenisation treatments are generally carried out at around  $500^{\circ}C$  and at this stage, and during subsequent solution treatment at  $450^{\circ}C$ , various precipitation reactions can occur. In the case of 7010 the most important reaction is that which produces  $ZrAl_3$  in a metastable cubic form. This phase was found by Ryum (14) to be simple cubic  $a=4.08\text{\AA}$  and to have a cube/cube relationship with the aluminium matrix. The phase was found to form by precipitation from solid solution at  $450^{\circ}C$  as small spherical particles less than  $0.1\mu\text{m}$  in diameter. These particles are of great importance since they are believed to pin the grain boundaries preventing grain growth during the recrystallisation processes which are apparent during thermomechanical treatments (II). Smaller particles of this type, less than  $0.5\mu\text{m}$  diameter, were found by Hahn and Rosenfield (II) to be more resistant to cracking and therefore to be less important in limiting toughness than the much larger iron, copper and silicon rich particles.

The solubility of copper in the alloy at solution treatment and homogenisation temperatures is considerable (Fig. 3.I) but is somewhat lower than in pure aluminium at this temperature and such heat treatments often occur close to the  $\alpha+S$  ( $CuMgAl_2$ ) phase field boundary. It is possible therefore that S phase can be stable at these temperatures and therefore be retained. Peel (I5) and Singh and Fleming (I6) studied S phase formation and believed that it might form by diffusion of zinc from the quaternary eutectic colonies. Singh and Fleming in fact stated that S phase might in turn transform to  $\theta$  ( $CuAl_2$ ) via magnesium diffusion but Peel could find no evidence of this. It seems likely therefore that fully heat treated material contains large,  $\sim 0.1-10\mu m$ , particles of S phase produced by transformation of the eutectic colonies.

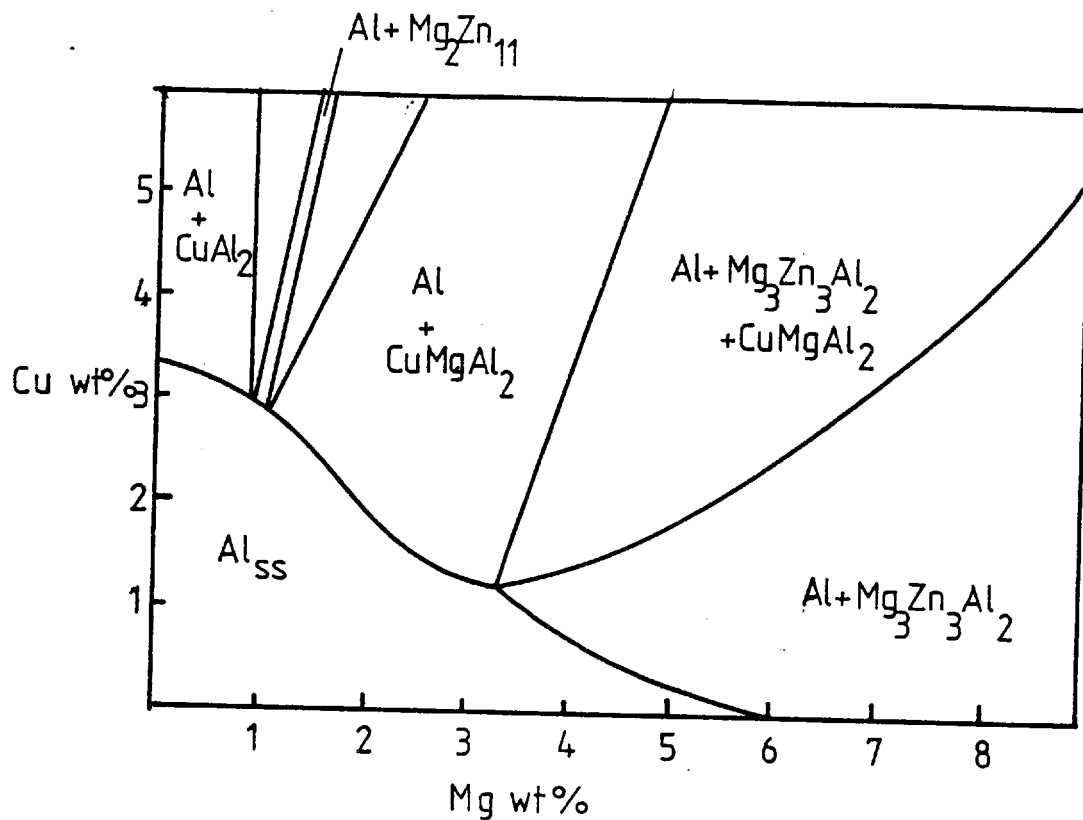
## I.2. Precipitation During Ageing.

I.2.I. Sequence of Precipitation. A great deal of literature has been published concerning age-hardening reactions in high strength aluminium alloys, the general principles being outlined by Kelly and Nicholson (I7):

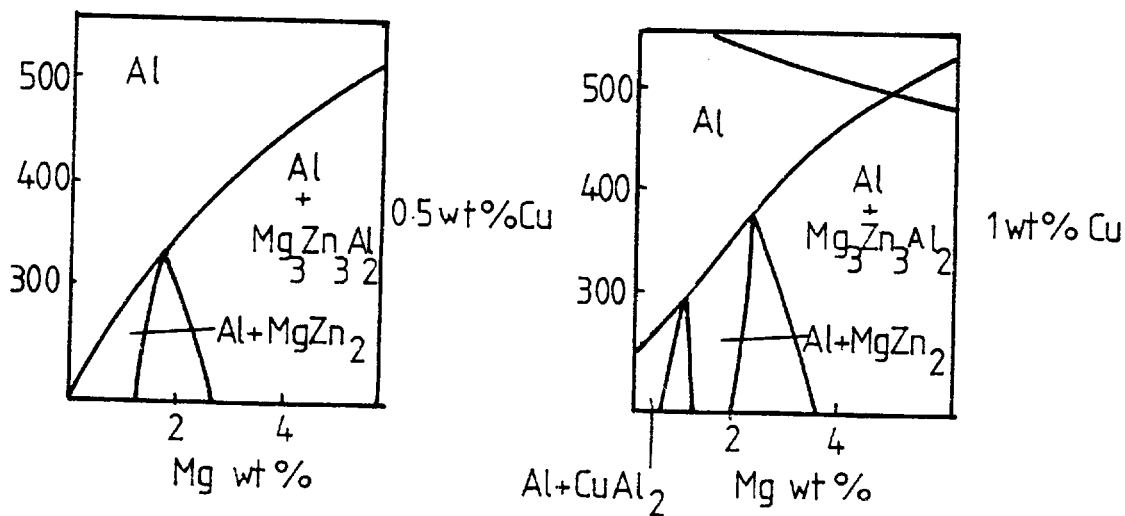
Supersaturated  $\rightarrow$  G.P Zones  $\rightarrow$  Intermediate  $\rightarrow$  Final  
Solid Solution ppt. ppt.

The first stage of precipitation involves the formation of G.P zones which nucleate homogeneously. A temperature above which zones are unstable has however been found by Lorimer and Nicholson (I8). They quoted a temperature of  $150^{\circ}C$  for a ternary alloy of 5.9%Zn and 2.9%Mg. The existence of this critical temperature is of great importance in the case of commercial heat treatment since most alloys are initially aged at a low temperature to produce a fine G.P zone distribution. These zones then act as nuclei for the intermediate precipitate, prior to their dissolution, at the final ageing temperature which is generally above the G.P zone solvus. For example, the heat treatment applied to the 7010 used in the present work, T76, involves heating to the final temperature,  $170^{\circ}C$  at a rate not exceeding  $10^{\circ}C/hour$ , during which time G.P zone formation can occur.

Large amounts of information have been obtained concerning the

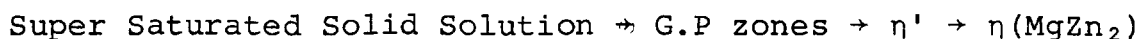


(a) Isothermal section at 460°C through the Al-Zn-Mg-Cu system containing 6% Zn



(b) Vertical sections through the Al-Mg-Zn-Cu system, 6% Zn, at 0.5 and 1% Cu

intermediate and final precipitates produced during the ageing of Al-Zn-Mg and Al-Zn-Mg-Cu alloys although much of this evidence is confused: Thomas and Nutting (19) proposed the sequence



This presumably can only apply to alloys whose compositions lie within the  $\alpha+\eta$  phase field at the ageing temperature. All the final phases which can be produced in Al-Zn-Mg alloys have been summarised by Mondolfo (8) (Fig.3.2).

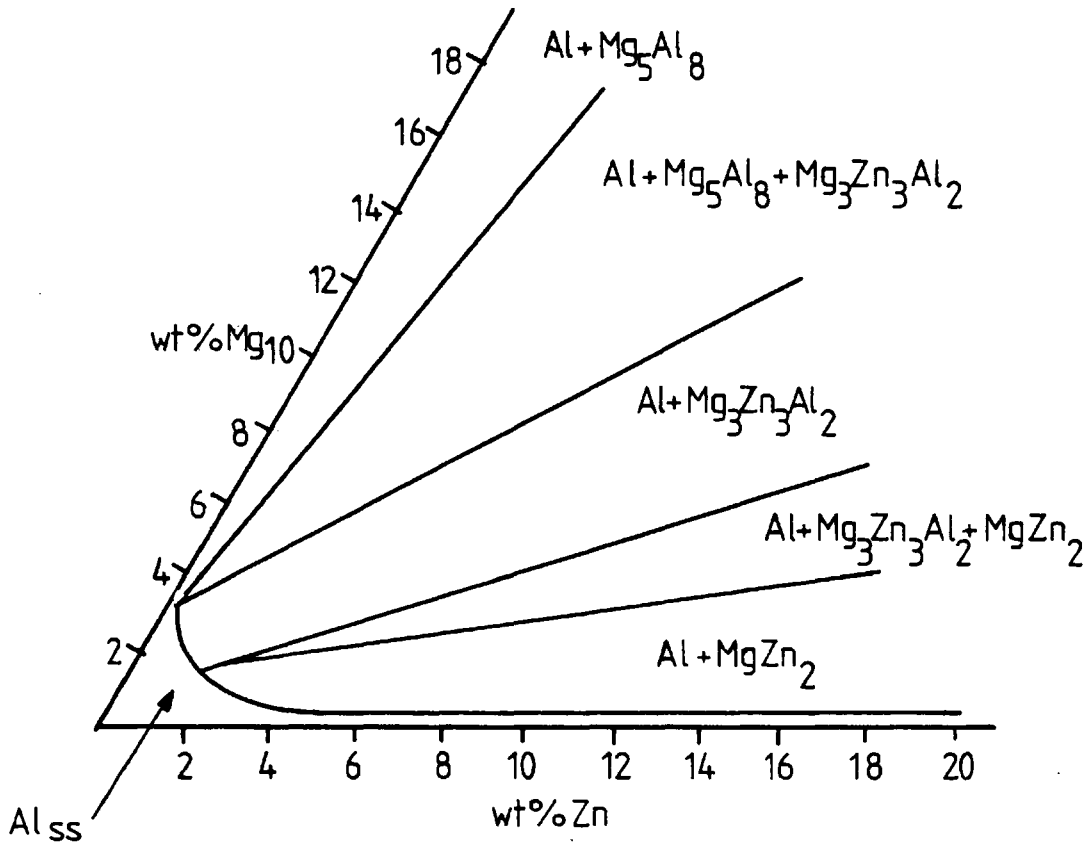
- (a) Mg:Zn > 6:1  $\text{Mg}_5\text{Al}_8$  predominates
- (b) Mg:Zn 6:1  $\rightarrow$  3:7  $\text{Mg}_3\text{Zn}_3\text{Al}_2$  (T) predominates at least at high temperatures
- (c) Mg:Zn 2:5  $\rightarrow$  1:7  $\text{MgZn}_2$  ( $\eta$ ) predominates
- (d) Mg:Zn < 1:10  $\text{Mg}_2\text{Zn}_{11}$  predominates

Since many commercial alloys, for example, 7010, lie at the transition between regions (b) and (c) the possibility of the formation of T phase must be considered.

The generally accepted sequence of formation of T is via an intermediate phase T'. This phase was first discovered by Thackery (20) in a ternary Al-Zn-Mg alloy who termed the phase 'X'. T phase itself has been found to predominate at temperatures greater than 200°C (8) and is therefore not likely to form in most commercial ageing treatments.

The most commonly observed transformation during ageing is that to  $\eta(\text{MgZn}_2)$  via an intermediate  $\eta'$ . The circumstances under which  $\eta'$  is found have been in some dispute. Graf (21) and Auld and Cousland (22) stated that  $\eta'$  was not found in alloys lying within the  $\alpha+\eta$  phase field at the ageing temperature: Prior to their work there had been some confusion on this point. Gjønnes and Simensen (23) observed the transformation from G.P zones to  $\eta'$  to  $\eta$  via electron diffraction and observed the fading of  $\eta'$  reflections with the progression of the transformation to  $\eta$ .  $\eta'$  has been found to form extremely rapidly (21) even at 75°C and often masks the presence of G.P zones.

The formation of S phase,  $\text{CuMgAl}_2$ , during ageing has been suggested in alloys containing less than 2% Cu (24) but studies by Peel



Isothermal section - 200°C  
of Al-Zn-Mg phase diagram

after Mondolfo (8)

(15) and Weatherly (25) revealed that this phase was only found in alloys containing greater than 2.5%Cu. The phase was found to form via G.P zones, termed G.P.B. zones (25) and the ageing reaction was found to occur very rapidly at room temperature in an Al 3%Cu 1.5%Mg 0.5%Ag alloy by Sen and West (26). While it appears that this ageing sequence would not be expected in 7010 the reaction is of some importance in the present work since it is likely to occur during the natural ageing (T3) process in the alloy 2024, which was utilised in part of the crack propagation study.

The grain boundary precipitation reactions have been reviewed by Mondolfo (8): Precipitate nucleation occurs rapidly and only equilibrium precipitates are found with an orientation relationship to the grain on one side of the boundary only. The inhibition of precipitate nucleation along the grain boundaries leads to the characteristic precipitate free zone or P.F.Z. Workers have explained this effect by a combination of solute depletion in the region, due to grain boundary precipitation, and reduced vacancy concentration, due to vacancy migration to the boundary. The critical vacancy concentration for precipitate nucleation has been found to be reduced by lowering the ageing temperature (18) and therefore P.F.Z. width can be minimised by low initial temperatures.

#### I.2.2. Structure and Morphology of Precipitate Particles.

The term G.P zone is strictly only applicable to small particles discovered by Guinier and Preston (27), formed during the initial stages of ageing in Al-Cu alloys. However the term is used generally to describe similar particles formed in all aluminium alloys. In Al-Zn-Mg alloys, zones are thought to be predominantly clusters of Mg and Zn atoms and have been found to be approximately spherical in shape (28). In many alloys zones, have been found to be replaced by  $\eta'$  very rapidly and in fact Lyman and Van der Sande (28) proposed an intermediate hexagonal zone as a precursor to  $\eta'$ .

Auld and Cousland (29) determined a structure for  $\eta'$  as hexagonal  $a=4.96 \text{ \AA}$ ,  $c=14.02 \text{ \AA}$ . Other workers have however proposed  $a=4.96 \text{ \AA}$ ,  $c=8.6 \text{ \AA}$ . Mondolfo (9) suggested that this discrepancy might be due to differences in the interpretation of the many weak electron and X-ray diffraction reflections which occur. Auld

and Cousland proposed a composition  $Mg_4Zn_{11}Al$  and an orientation relationship:

$$\eta' (a). (00\cdot I)\eta' // \{I\bar{I}I\}Al, (IO\cdot O)\eta' // \{IIO\}Al$$

More recently however Chou (30) proposed a second variant:

$$\eta' (b). (IO\cdot O)\eta' // \{IOO\}Al, (OOI)\eta' // \{OI\bar{I}\}Al$$

Gjønnnes and Simensen (23) found the particles to be of plate morphology with the long axis coherent. Auld and Cousland (29) confirmed this and quoted a maximum size  $30 \text{ \AA}$  by  $100 \rightarrow 200 \text{ \AA}$  coherent on  $\{III\}$  planes as expected.

The structure for  $\eta$ , the final phase, was found by Auld and Cousland (29) to be hexagonal  $a=5.16 \text{ \AA}$ ,  $c=8.5 \text{ \AA}$ . Nine different orientation relationships have been observed (8,23) and two morphologies noted:

(a)	$(I\bar{2}\cdot O)\eta // \{I\bar{I}I\}Al, (OO\cdot I)\eta // \{IIO\}Al$	Rods
(b)	$(I\bar{2}\cdot O)\eta // \{I\bar{I}I\}Al, (3O\cdot 2)\eta // \{IIO\}Al$	Rods
(c)	$(I\bar{2}\cdot O)\eta // \{I\bar{I}I\}Al, (2O\cdot I)\eta // \{I2I\}Al$	Rods
(d)	$(I\bar{2}\cdot O)\eta // \{I\bar{I}I\}Al, (IO\cdot 4)\eta // \{IIO\}Al$	Rods
(e)	$(OO\cdot I)\eta // \{I\bar{I}I\}Al, (I\cdot OO)\eta // \{IIO\}Al$	Plates
(f)	$(OO\cdot I)\eta // \{I\bar{I}I\}Al, (II\cdot O)\eta // \{IIO\}Al$	Plates
(g)	$(IO\cdot O)\eta // \{IOO\}Al, (OO\cdot I)\eta // \{OI\bar{I}\}Al$	Plates
(h)	$(I2\cdot O)\eta // \{I\bar{I}2\}Al, (OO\cdot I)\eta // \{3I\bar{I}\}Al$	Rods
(i)	$(I2\cdot O)\eta // \{OOI\}Al, (OO\cdot I)\eta // \{IIO\}Al$	Plates

Note that the only  $\eta$  variants of orientation relationship equivalent to  $\eta'$  are  $\eta(e)$  and  $\eta(g)$ , an interesting point since the ageing reaction is generally considered to occur via  $\eta'$ .

In a quaternary alloy similar in composition to 7010 Peel (15) noted after an overageing treatment akin to T76 the presence of mostly  $\eta(a)$  and  $\eta(f)$  variants plus possibly  $\eta(e)$ .

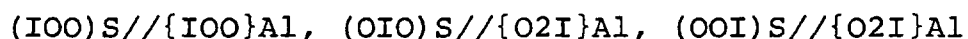
Thackery (20) initially discovered the phase 'X' which was later found by Auld and Cousland (22) to be an intermediate to T, and was therefore termed T'. They proposed a hexagonal structure  $a=19.11 \text{ \AA}$ ,  $c=28.04 \text{ \AA}$ . The orientation relationship was found

to be:



T' was found to form as either triangular or polygonal shaped equiaxed particles. The final phase T, has been found to be cubic  $a=14.02 \text{ \AA}$ . It is not proposed to go into any detail here however since its occurrence is not to be expected in 7010, see reference (8) for details.

S phase ( $CuMgAl_2$ ) which is found in the alloy 2024 (9) and may form in Al-Zn-Mg-Cu alloys such as 7010 is orthorhombic  $a=4.01 \text{ \AA}$ ,  $b=9.25 \text{ \AA}$ ,  $c=7.15 \text{ \AA}$  (25). An orientation relationship has been suggested for low temperature transformation:



(25). G.P.B. zones, the precursor to S, have been found to be of spherical morphology which then transform to lath shaped S particles (15,25).

The addition of copper to Al-Zn-Mg ternary alloys also leads to copper substitution in the phases found in the ternary system: Most phases in the Al-Cu-Mg system are completely miscible with those in the Al-Zn-Mg system (8). These are  $CuMg_4Al_2$  with  $Mg_3Zn_3Al_2$  (T),  $CuMgAl$  with  $MgZn_2$  ( $\eta$ ), and  $Cu_6Mg_2Al_5$  with  $MgZn_{11}$ . Copper is also thought to effect the precipitation sequence, reducing the activation energy for nucleation of G.P zones and raising that for  $\eta'$ . Improvements in resistance to stress corrosion cracking S.C.C, have been attributed to this effect (31).

## 2. RESULTS AND DISCUSSION.

### 2.1. Grain Structure.

Observation of the grain structure in the rolling plane using the light microscope (Fig.3.3) revealed a structure of large grains, 400→800 $\mu$ m in diameter, elongated slightly in the rolling direction. Perpendicular to the rolling plane the structure was found to be highly elongated, the grains being around 50 $\mu$ m x 800 $\mu$ m, both in the rolling direction and perpendicular to it. The optically resolvable grain structure could be considered therefore to be one of pancake like grains. At low magnification in the TEM a much finer substructure was revealed (Fig.3.4). This consisted of grains and subgrains, 2→10 $\mu$ m in diameter and approximately equiaxed. Since these regions were separated by both high and low angle boundaries this structure should perhaps be considered as the true alloy grain structure, with packets of these grains making up the optically resolvable superstructure. It is felt that the optically resolvable structure is a remnant of the original as cast microstructure with the smaller grains being produced by recovery and recrystallisation during heat treatment.

### 2.2 Intermetallic Particles.

2.2.1. Large Inclusions. Large intermetallic particles, 10→100 $\mu$ m in size were observed optically, (Fig.3.3) in some cases in long stringers along the rolling direction. These particles were analysed by wavelength dispersive X-ray methods and the results are shown in the form of X-ray maps in Fig.3.5. Particles were found to be rich in magnesium, silicon, copper, iron and titanium. Magnesium and silicon were found in combination, as were copper and iron. The two most likely intermetallic compounds observed were therefore Mg<sub>2</sub>Si and Al<sub>7</sub>CuFe, as observed by Di Russo and Buratti (13) in 7I75. No Al-Fe-Si or Cu-Mg-Zn intermetallics of the types observed by these authors in 7I75 and 7050 were found. Also there did not appear to be evidence of CuMgAl<sub>2</sub>(S) or CuAl<sub>2</sub>( $\theta$ ), as suggested in similar alloys by Peel (15) and Singh and Fleming (16). Zirconium was found to be uniformly distributed throughout the alloy and was not segregated into large particles, the possibility of such segregation was postulated by Mondolfo (8) due to the formation of ZrAl<sub>3</sub> during casting.

Fig. 3.3 Light micrographs showing alloy grain structure. Upper surface equals rolling plane. Rolling direction arrowed. x80.

Fig. 3.4 Low magnification TEM bright field. Finer structure of grains and subgrains.

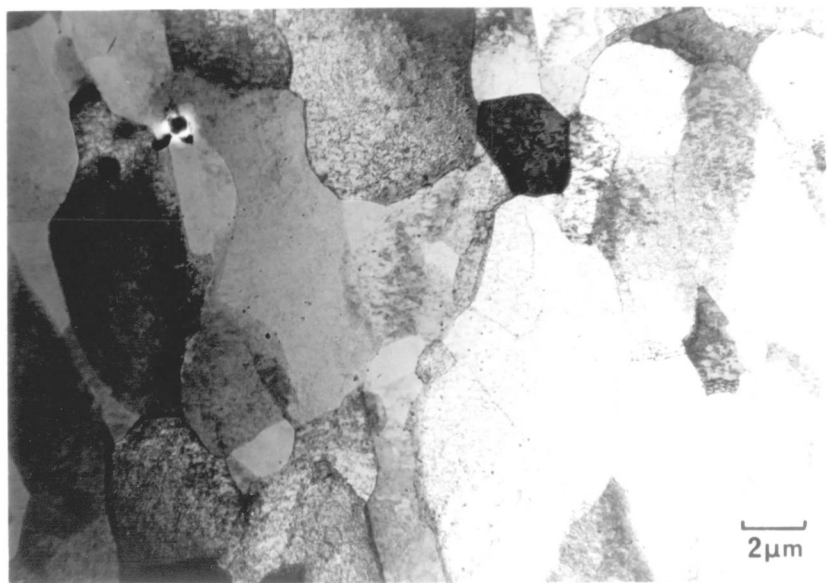
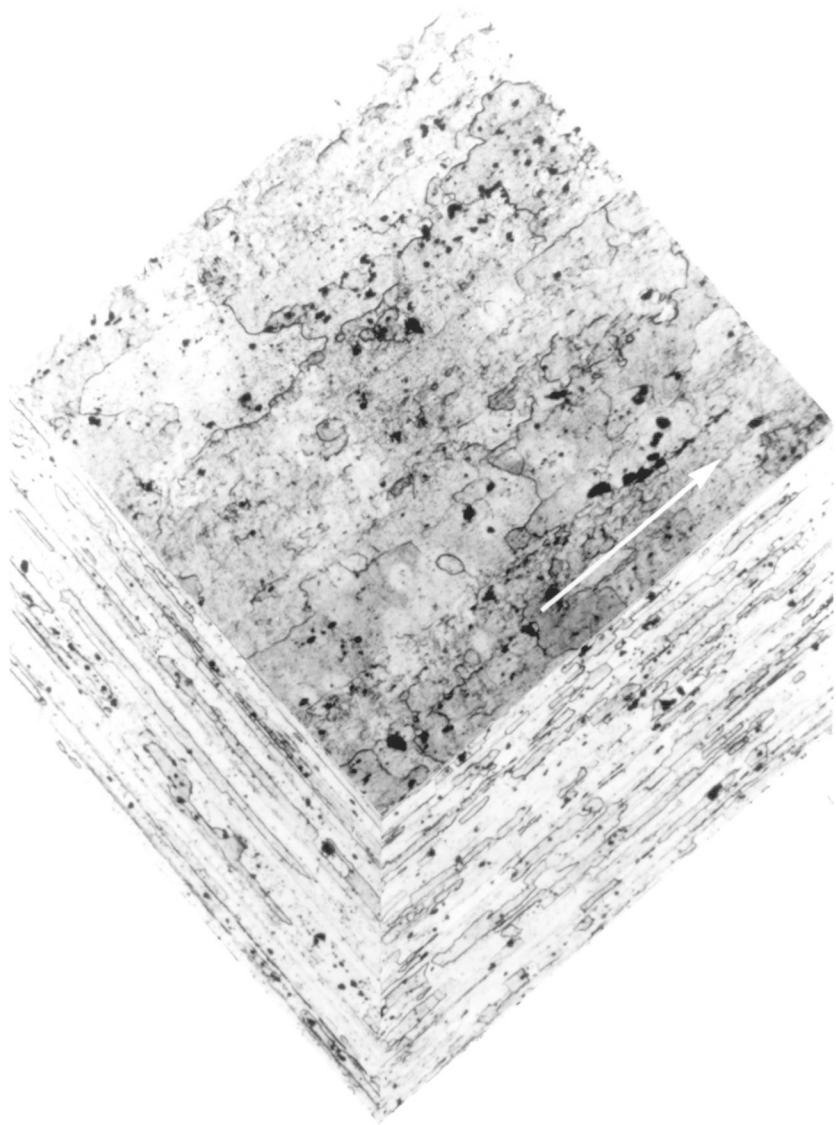
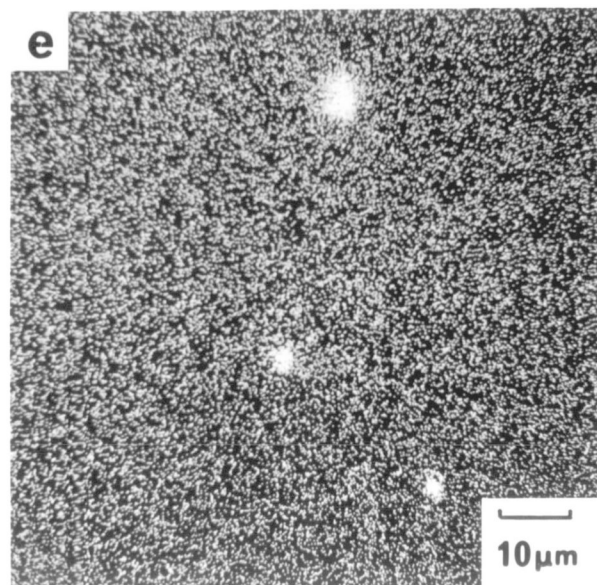
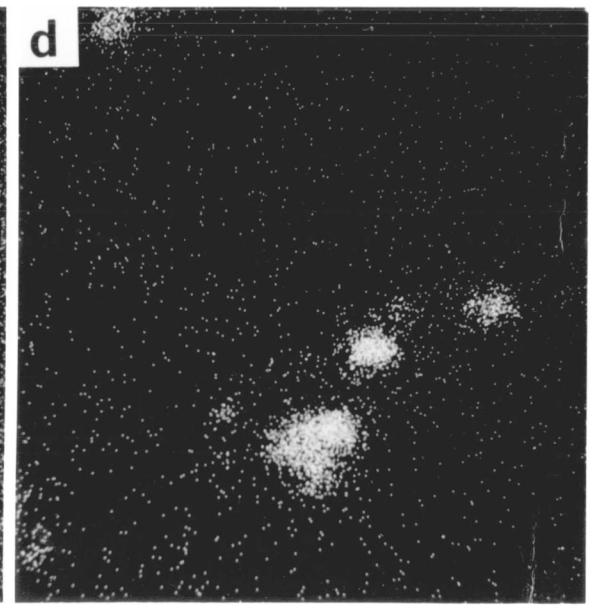
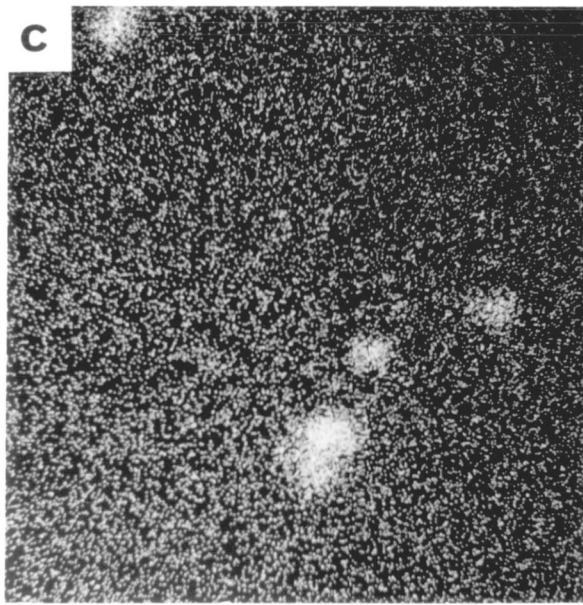
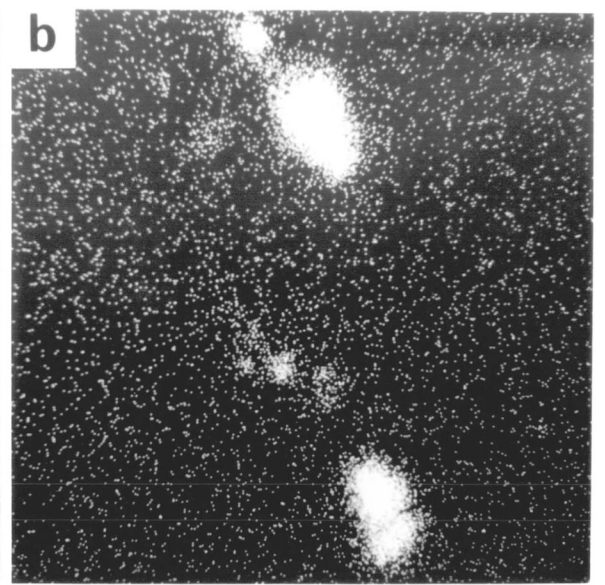
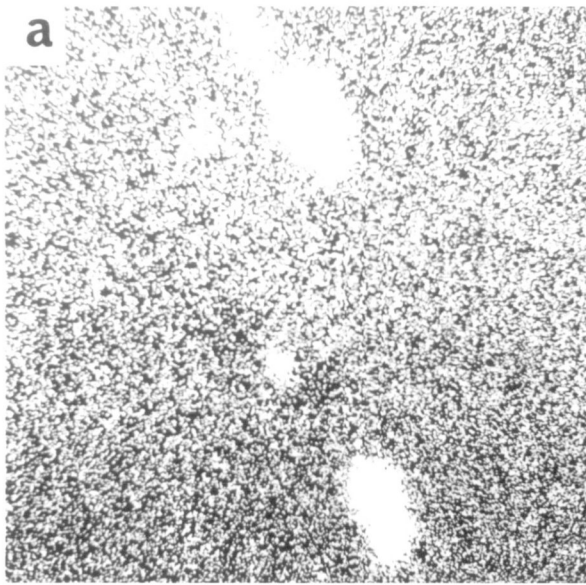


Fig. 3.5 Wavelength dispersive X-Ray analysis of large intermetallic particles in the form of X-Ray maps. Single area of polished plate.

- (a) magnesium concentration.
- (b) silicon concentration.
- (c) copper concentration.
- (d) iron concentration.
- (e) titanium concentration.



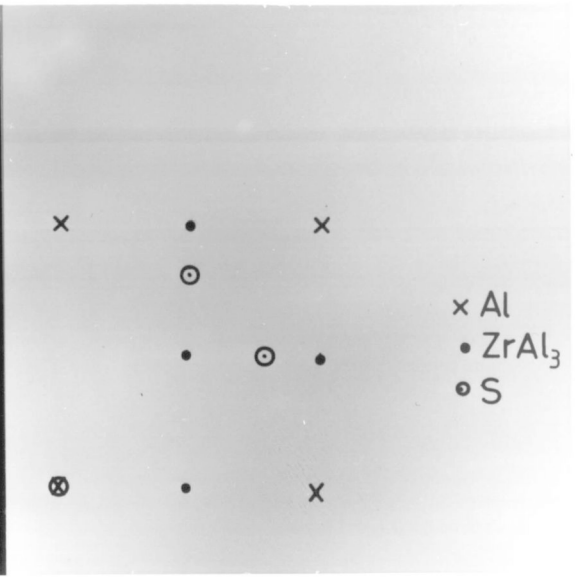
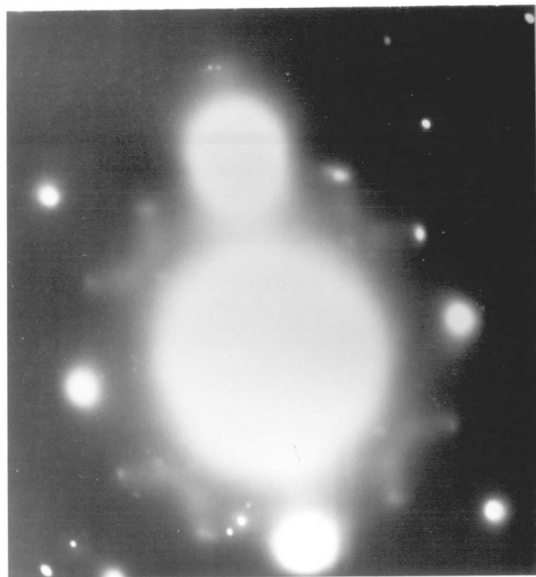
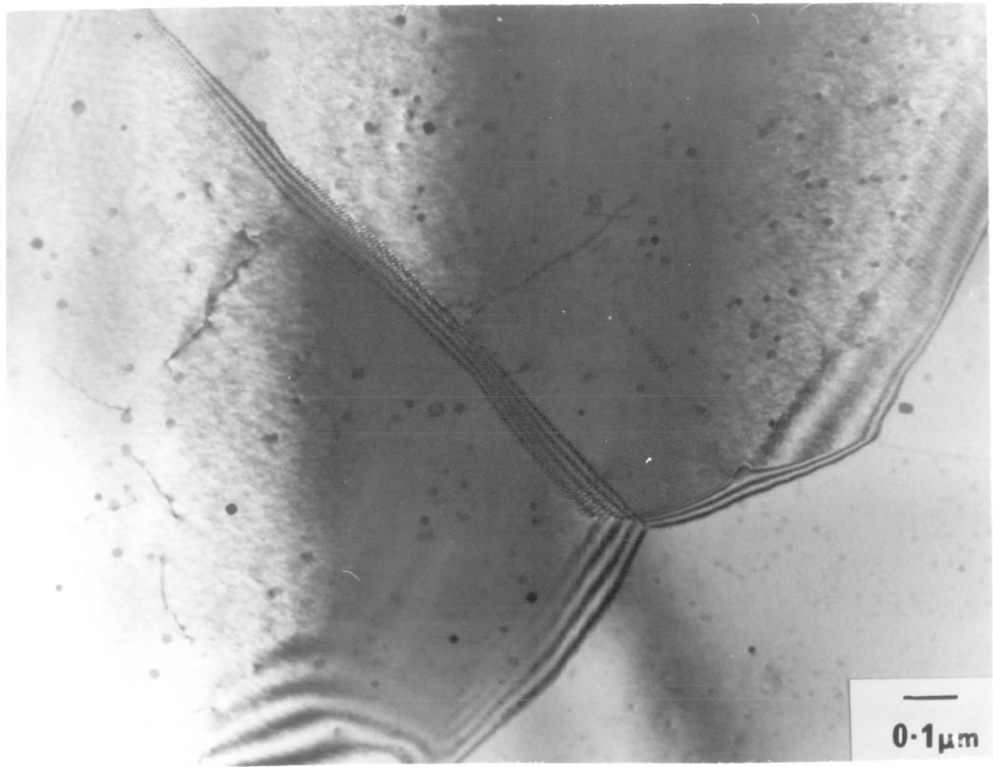
2.2.2. Small Intermetallics Present Prior to Ageing. In order to observe the intermetallic particles present prior to ageing, 7010 plate, supplied in aged form, was re-solution treated. Thin foil specimens were then observed in the TEM. Spherical particles, around 300 Å in diameter, were observed in large clusters (Fig.3.6). The density of particles was around 200/μm<sup>3</sup>, clusters being of the order of 2μm across. Analysis of selected area diffraction data obtained from within clusters revealed reflections consistent with the cubic, coherent, form of ZrAl<sub>3</sub> (I4). The particles were in fact morphologically similar to those observed by Ryum (I4). The fine distribution of cubic ZrAl<sub>3</sub> particles is consistent with the ageing reaction at 450→500°C. The Zr additions in 7010 would therefore appear to have the desired effect of forming small coherent particles to restrict grain growth during recrystallisation without forming large incoherent particles which would reduce fracture toughness (II).

Other reflections were also found in the SADP's which could not be analysed as ZrAl<sub>3</sub> but were consistent with S phase (CuMgAl<sub>2</sub>). In fact the diffuse reflections were consistent with those observed due to S during the natural ageing of Al-Cu-Mg-Ag alloy by Sen and West (26). The particles observed may have formed by this route although TEM studies by Peel (I5) and Weatherly (25) revealed no such reaction in Al-Zn-Mg-Cu alloys containing less than 2.5%Cu. As discussed in I., the formation of S during solution treatment at 465°C is probable but in this case small coherent particles, as implied by the electron diffraction data, would not be expected. A third route involves their formation during quenching, although steps were taken to ensure a rapid quench. Any reaction at this stage would therefore be of necessity extremely rapid.

The occurrence of S phase cannot therefore be readily explained and the possibility exists that the reflections may be due to some, crystallographically similar, unidentified phase. Certainly in the aged condition, as discussed later, a number of unidentifiable reflections were found in SADP's.

2.2.3. Precipitate Distribution in the T76 Heat Treated Condition. The precipitate distribution within the alloy in the as supplied, T76, heat treated condition was investigated using the TEM.

Fig. 3.6 Typical clusters of small intermetallics  
found in re-solution treated material.  
(a) TEM bright field.  
(b) SADP from left hand grain zone axis  
= $\langle 001 \rangle$ .



Bright field micrographs together with corresponding SADP's are shown in Fig.3.7. Matrix particles were found to be disc or rod shaped. With the foil in  $\langle III \rangle$  zone axis orientation many particles appeared approximately circular,  $100 \rightarrow 400 \text{ \AA}$  in diameter, while others were elongated in the  $\langle I\bar{1}0 \rangle$  directions. Particles were found to be  $30 \rightarrow 100 \text{ \AA}$  in thickness. Grain boundary precipitates were considerably larger ranging in length from  $500 \rightarrow 1500 \text{ \AA}$ . Precipitate free zones were found to range in width from  $500 \text{ \AA}$  for a sub-boundary to  $1500 \text{ \AA}$  for a high angle grain boundary.

The precipitate types were identified by rigorous analysis of  $\langle 001 \rangle$  and  $\langle III \rangle$  zone axis SADP's. Model diffraction patterns were constructed as shown in Fig.3.8. By comparison to the SADP's shown in Fig.3.7  $\eta'$  in variant (a) was identified together with  $\eta$  in variants (e) and (f). A few much weaker reflections were attributed to  $\eta(a)$ . Reflections corresponding to  $ZrAl_3$  were also obtained. A number of other reflections were however observed which could not be readily identified and must therefore correspond to other particle types or variants.

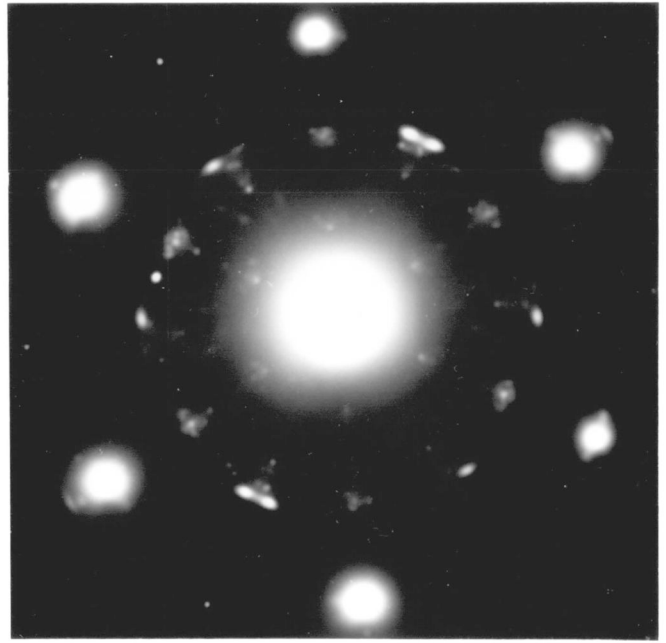
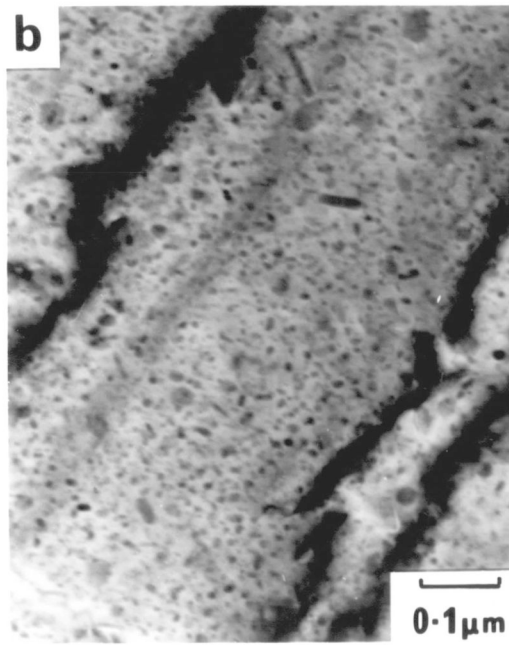
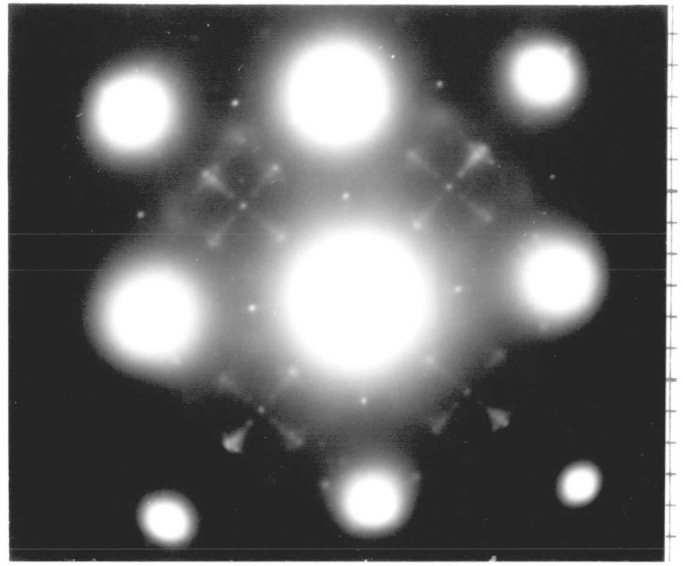
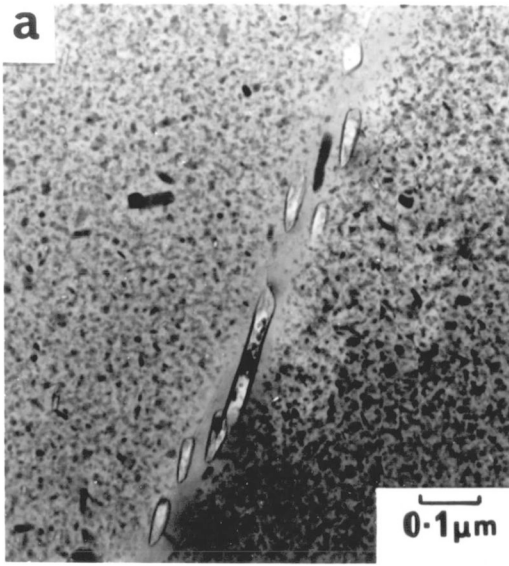
With reference to the studies of Gjønnes and Simensen (23) the strong  $\eta$  reflections would be expected in this somewhat overaged condition. The observations of  $\eta$  variants (a), (e) and (f) are consistent with those of Peel (15) in a high purity Al-Zn-Mg-Cu quaternary alloy of similar composition and heat treatment to 7010 T76. The  $\eta$  particle morphologies also appear to correspond to the observations of Gjønnes and Simensen. They found that  $\eta(e)$  and  $\eta(f)$  particles were disc shaped, lying on  $\{III\}$  planes, while  $\eta(a)$  particles were found to be rod shaped. The observation of equiaxed disc shaped particles and a smaller number of rod shaped particles with the foil in a  $\langle III \rangle$  zone axis orientation (Fig.3.7(a)) is consistent with this analysis.

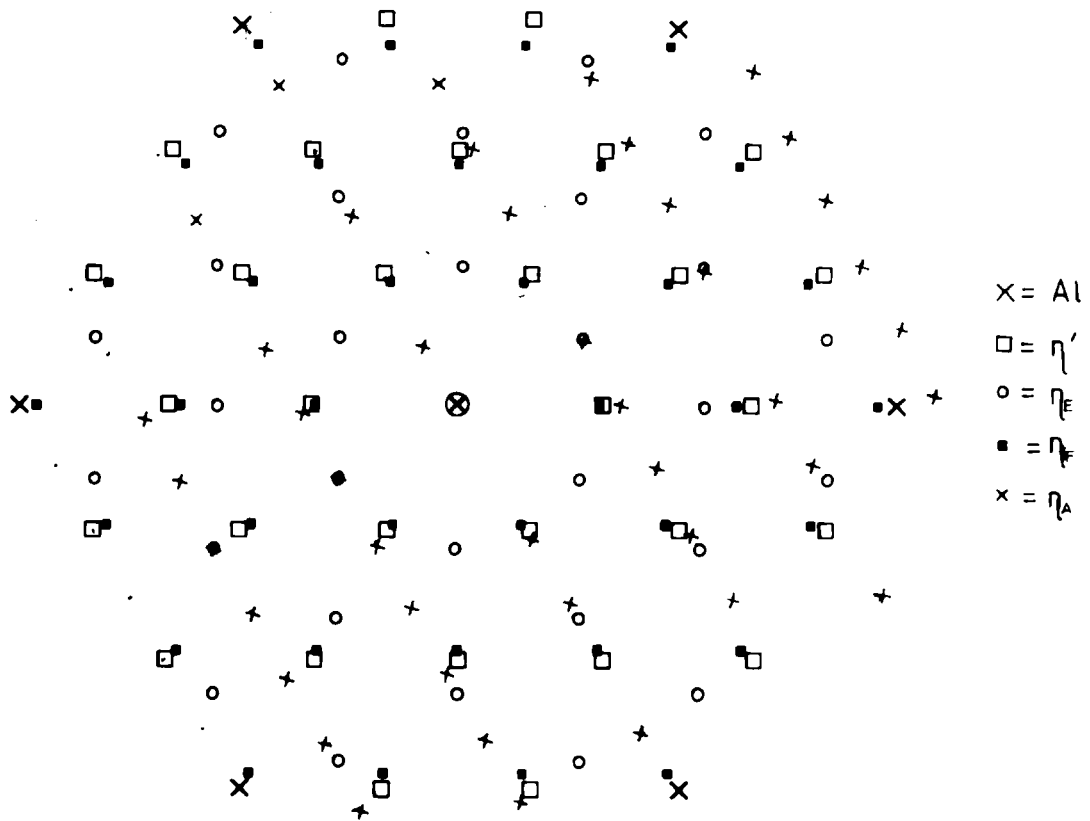
### 2.3. The Alloy 2024 T3.

The microstructure of this alloy is well documented (9) and a detailed study was not therefore carried out. A TEM study (Fig.3.9) revealed a structure on a fine scale of intermediate sized,  $\sim 0.5 \mu\text{m}$ , intermetallic particles, irregular in shape, in a matrix of moderately high dislocation density, presumably due to 'stretching' processes carried out on the alloy plate.

Fig. 3.7 Precipitate distribution in 7010 T76. TEM bright fields with corresponding SADP's.

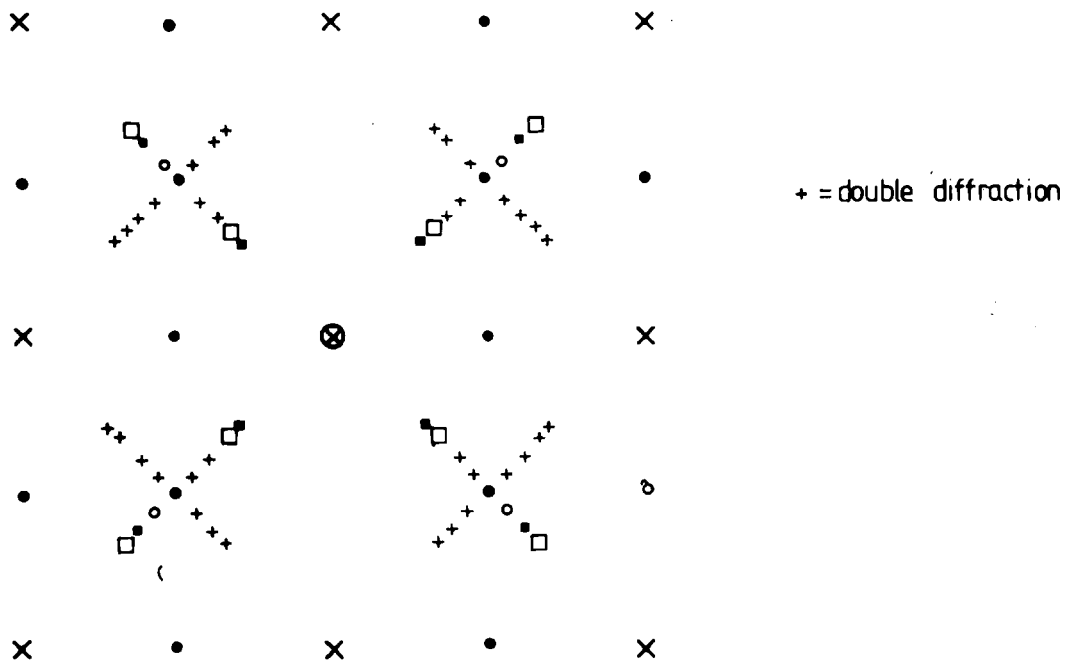
- (a) Area showing grain boundary with SADP from right hand grain zone axis =  $\langle 001 \rangle$ .
- (b) Area in  $\langle 111 \rangle$  zone axis orientation with SADP.





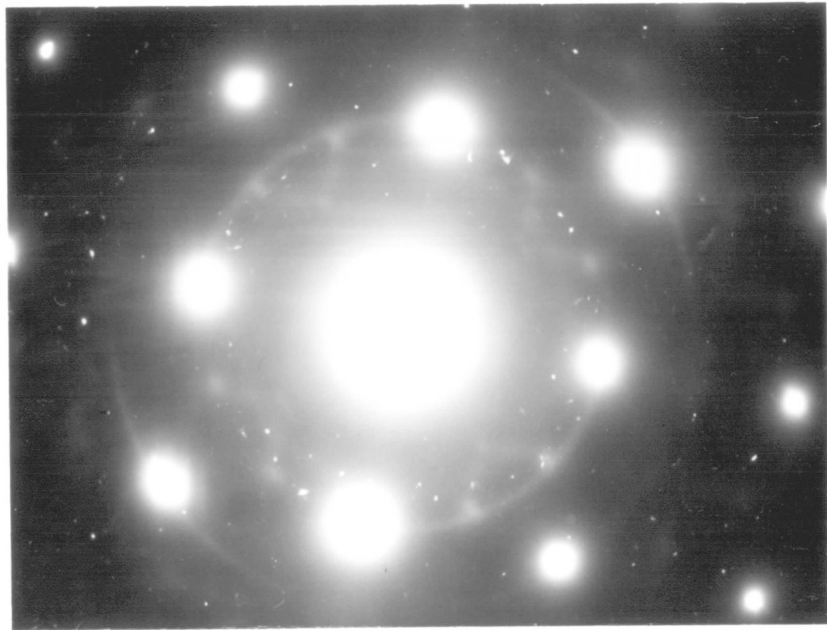
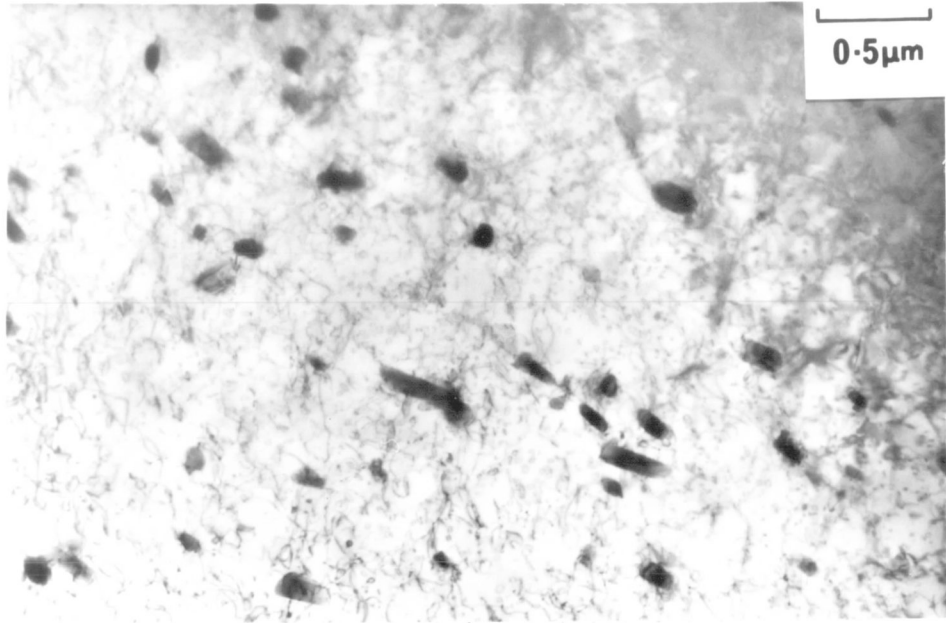
[111] Zone axis pattern including  $\eta'$ ,  $\eta_E$ ,  $\eta_F$  and  $\eta_A$  variants

(only one of six  $\eta_A$  orientations shown)



[001] Zone axis pattern including  $\eta'$ ,  $\eta_E$  and  $\eta_F$  variants

Fig. 3.9 TEM bright field + SADP,  $\langle 001 \rangle$  zone axis.  
Alloy 2024 T3, typical area.



The T3 heat treatment involves natural ageing at room temperature and hence a very fine precipitate distribution would be expected. This was in fact found, the SADP showing diffuse reflections and streaks which were analysed as S phase. Heterogeneous precipitation upon dislocations was apparent. It is interesting to note the similarity between the electron diffraction data obtained here and from solution treated and naturally aged 7010.

No attempt was made to identify the medium sized ( $0.1 \rightarrow 0.5 \mu\text{m}$ ) intermetallics which were found to be incoherent. It is very likely that they are a complex intermetallic of Al-Fe-Mn-Cu-Mg-Si. Possibly  $\text{Cu}_2\text{FeAl}_7$ ,  $\text{Cu}_2\text{Mn}_3\text{Al}_{20}$ ,  $(\text{Fe},\text{Mn})_3\text{SiAl}_{12}$  or  $\text{Mg}_2\text{Si}$  (9).

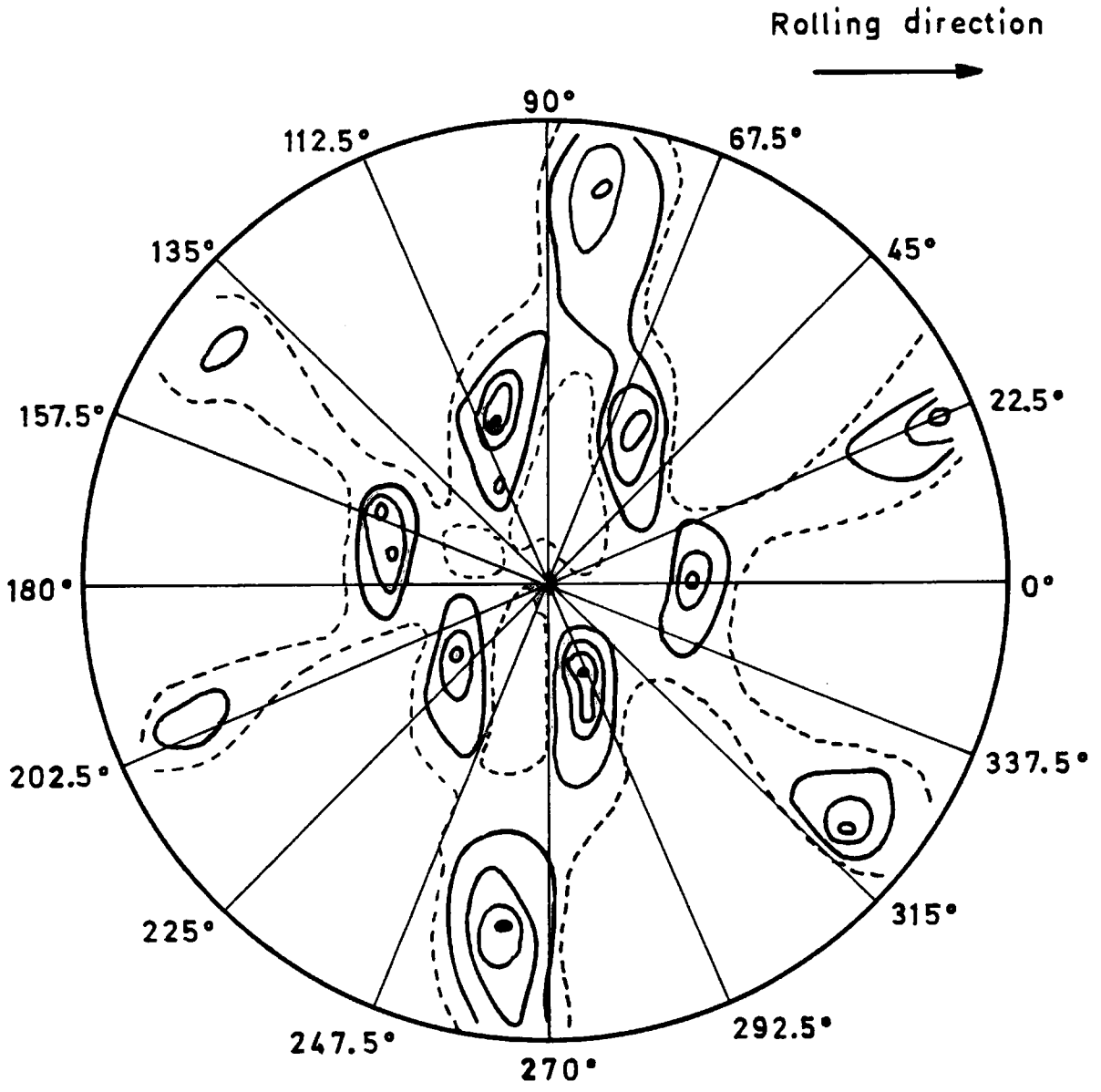
#### 2.4. Texture Determination.

The X-ray pole figures obtained for 2.5 cm 7010 plate both in the rolling plane and perpendicular to it parallel to the rolling direction are reproduced in Fig.3.10. The plane investigated perpendicular to the rolling plane was in fact the overall plane of fatigue fracture in all centre notched test pieces. Both  $\langle 111 \rangle$  and  $\langle 220 \rangle$  pole figures were obtained.

The plate was found to be heavily textured with  $\{111\}$  planes lying in the plane perpendicular to the rolling plane and  $\{110\}$  planes in the rolling plane itself. Considering the plate to be a single crystal it is possible to construct an orientation diagram, (Fig.3.11). The rolling direction appears to be perpendicular to both  $(110)$  and  $(\bar{1}\bar{1}\bar{1})$  directions. A likely texture is therefore a  $(110)(112)$ . This has been found to be a texture exhibited by hot rolled materials (9) and hence it would appear that heat treatments after hot rolling have little effect on texture, recrystallisation being inhibited by intermetallic particles.

The texture in the 7.5cm plate from which the C.T. design test pieces were manufactured, was not determined. It is expected however that since such plate does not undergo such severe rolling operations during manufacture a less marked texture would be found.

Fig.3.10

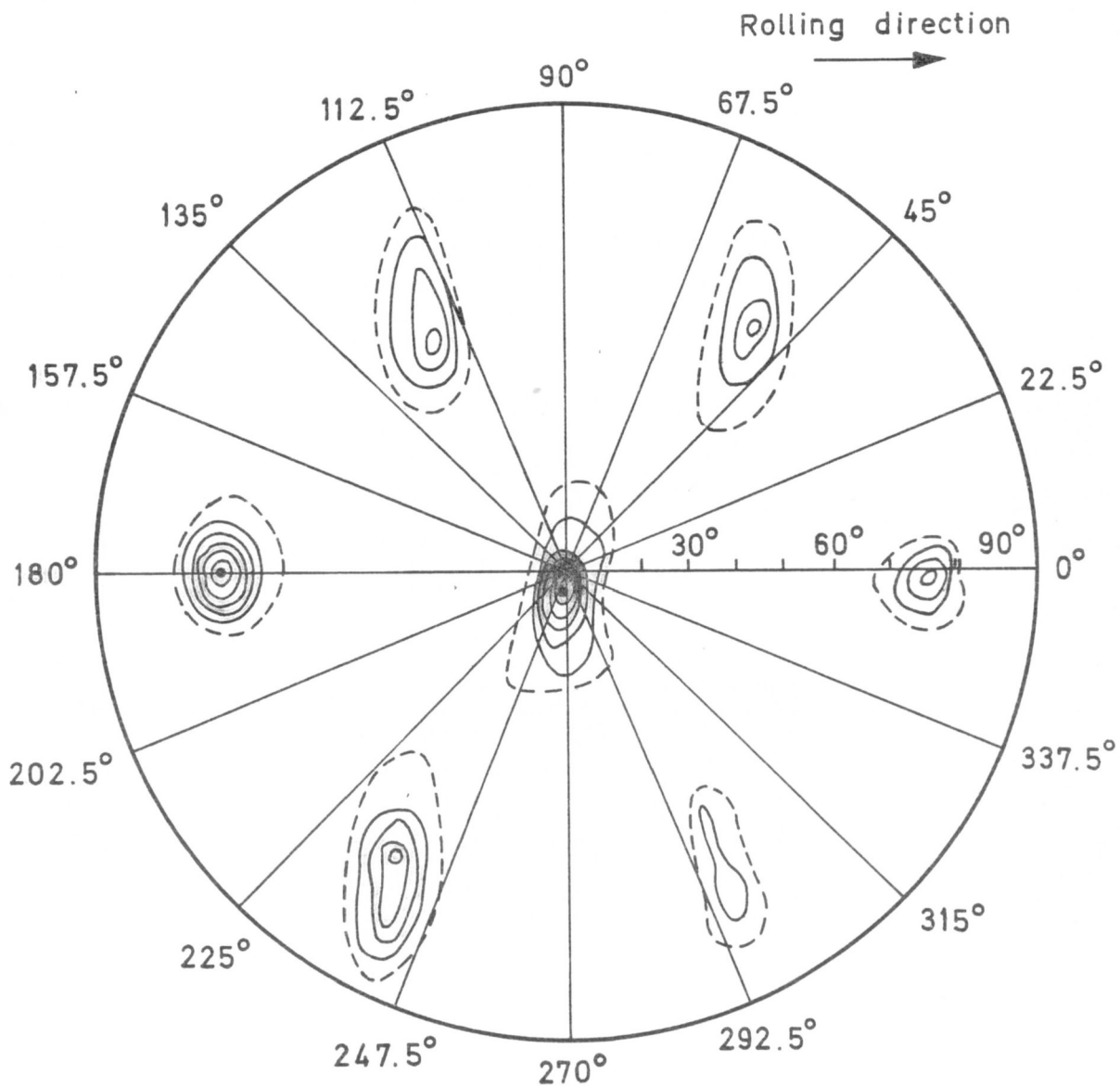


(220) Pole figure

In plane of fatigue fracture

- 200 c/s
- 400 c/s
- 800 c/s
- 1200 c/s
- 1600 c/s

Fig. 3.10(cont)

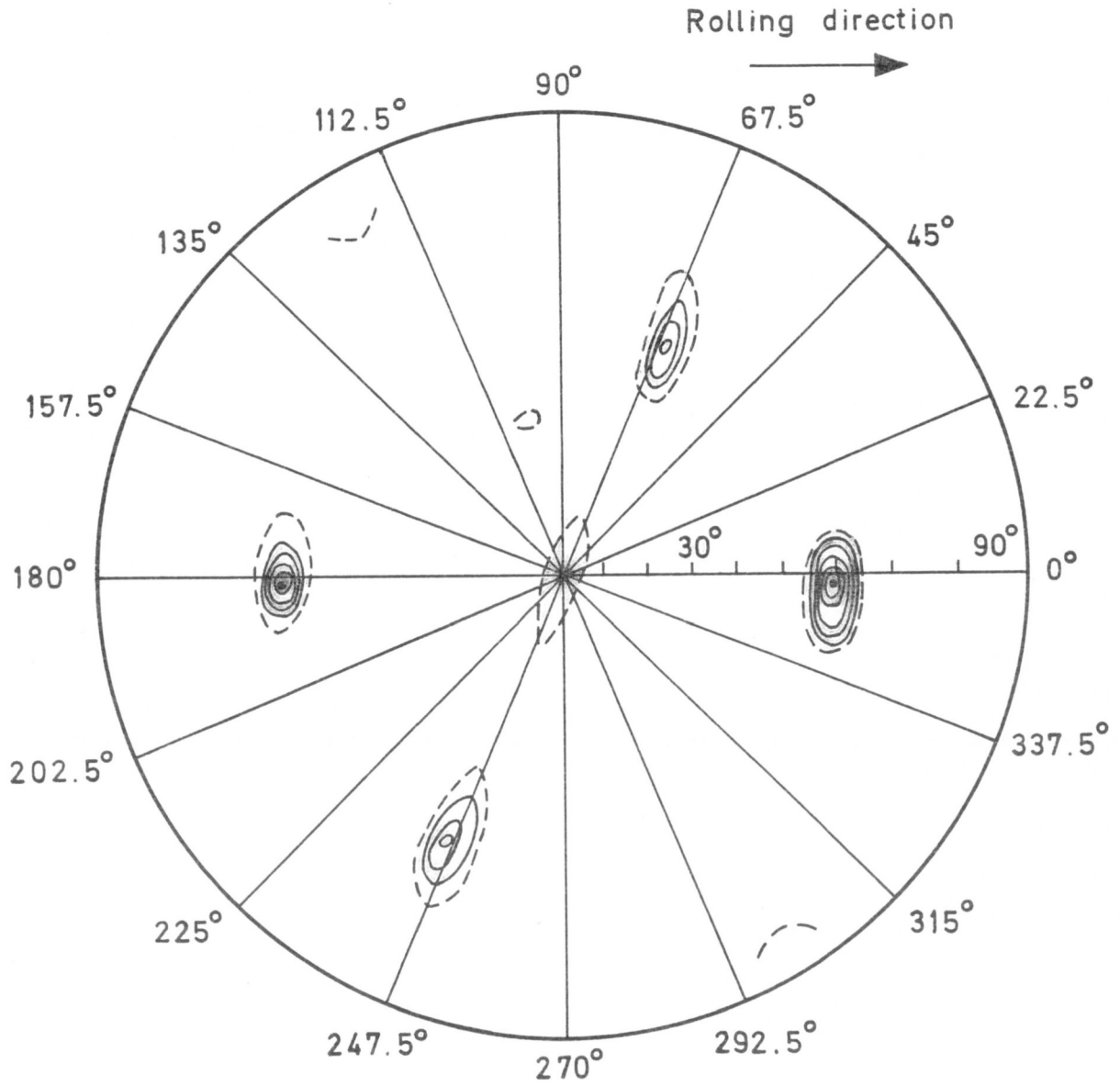


(fff) Pole figure

In plane of fatigue fracture

- 1000 c/s
- 1000 c/s intervals
- 7000 c/s

Fig. 3.10 (cont)

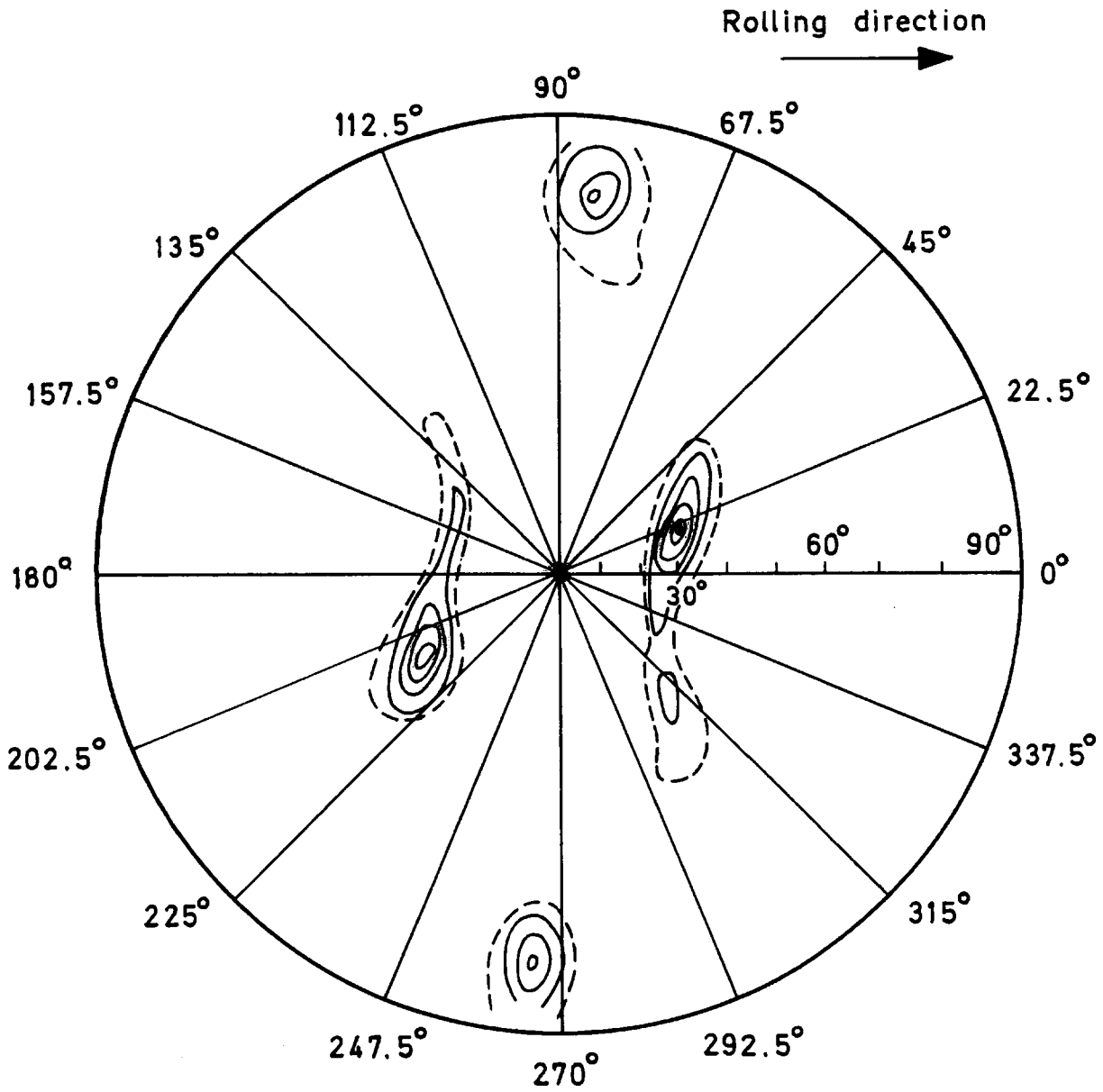


(220) Pole figure

In rolling plane

- 1000 c/s
- 8000 c/s
- 1000 c/s intervals

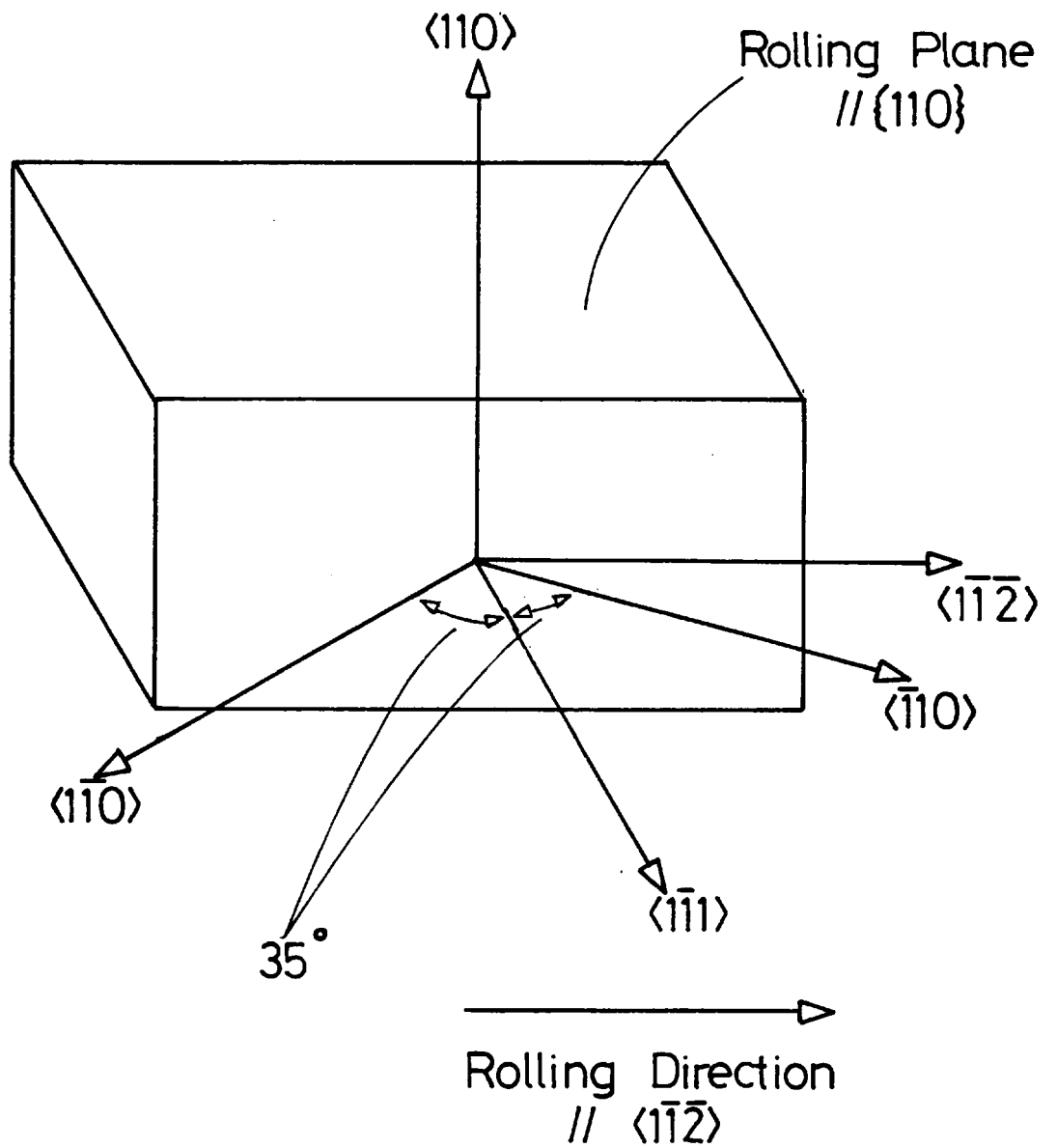
Fig.3.10(cont)



(111) Pole figure

In rolling plane

- 1000 c/s
- 2000 c/s
- 4000 c/s
- 6000 c/s
- 8000 c/s
- 10 000 c/s



Alloy Plate Texture

PART 4. CRACK INITIATION STUDIES.

## I. FATIGUE CRACK INITIATION FROM BORED HOLES--:LITERATURE REVIEW.

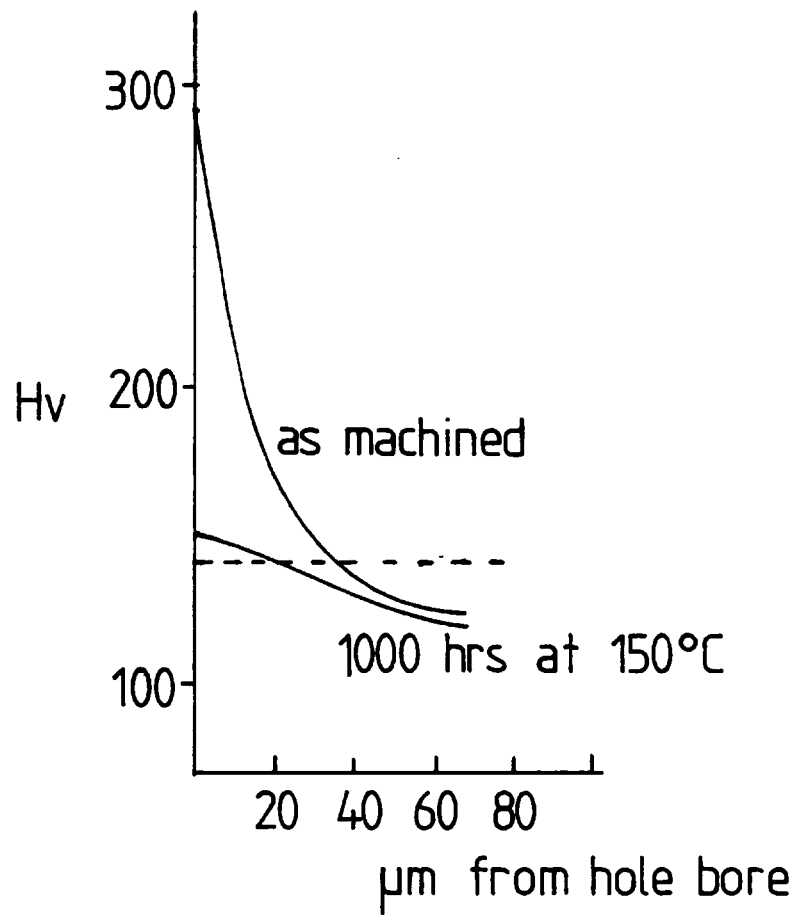
### I.I. Introduction.

The common hole boring processes, drilling, reaming and deburring are all likely to have an effect on both the surface finish and extent of microstructural damage in the finished product. These processes may all have an influence, therefore, on fatigue crack initiation at the hole. In this section a review is made of the available literature concerning the metallurgical effects of machining and their relationship to crack initiation. A brief appraisal is also made of the commonly observed modes of initiation in high strength commercial aluminium alloys.

### I.2. The Metallurgical Effects of Hole Boring.

Very little information exists to describe the effects of hole boring processes on surface finish and underlying microstructure but a number of workers have studied machining (most commonly turning) and grinding, and their results provide some useful information which may be applicable to boring processes. There are two areas of interest here, the microstructural damage produced and also the resulting residual stress distribution.

I.2.I. Subsurface Deformation Produced by Machining. Forsyth (32) was one of the few workers to study the microstructural modifications produced by drilling. He used light microscopy and microhardness testing to investigate the deformation produced adjacent to drilled holes in the commercial aluminium alloy RR58. The microhardness results demonstrated that a marked hardening of the surface layer occurred during drilling to a depth of around 40 $\mu$ m (Fig. 4.I). The microstructural studies showed that large intermetallic particles, present in a high volume fraction in this alloy, were concentrated in the surface layer and that a fine ( $\sim$ 2 $\mu$ m diameter) subgrain structure was produced. Heat treatment after drilling was found to remove the hardness profile but had no effect on the particle distribution. Forsyth concluded therefore that the subgrain structure, which was modified by heat treatment, gave rise to the initially hard surface layer. He applied a Hall-Petch type of equation, as suggested by Abson and Jonas (33) for a subgrain structure to explain the great



Microhardness profile adjacent to  
a drilled hole in RR58

from Forsyth [32]

increase in hardness from a bulk value of around 150 V.P.N. to a surface value of 300 V.P.N. His conclusion was that the sub-grain size was consistent with a hardness increase of this order.

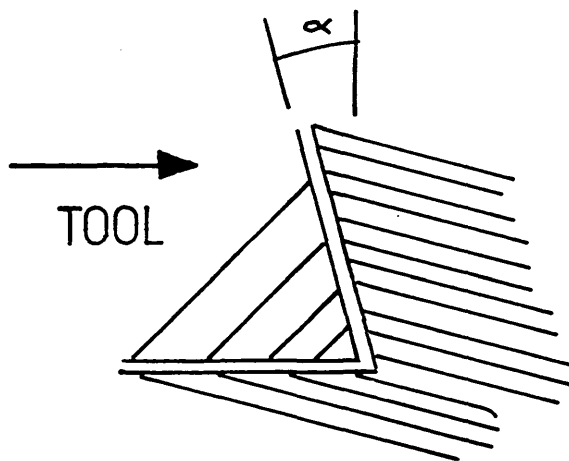
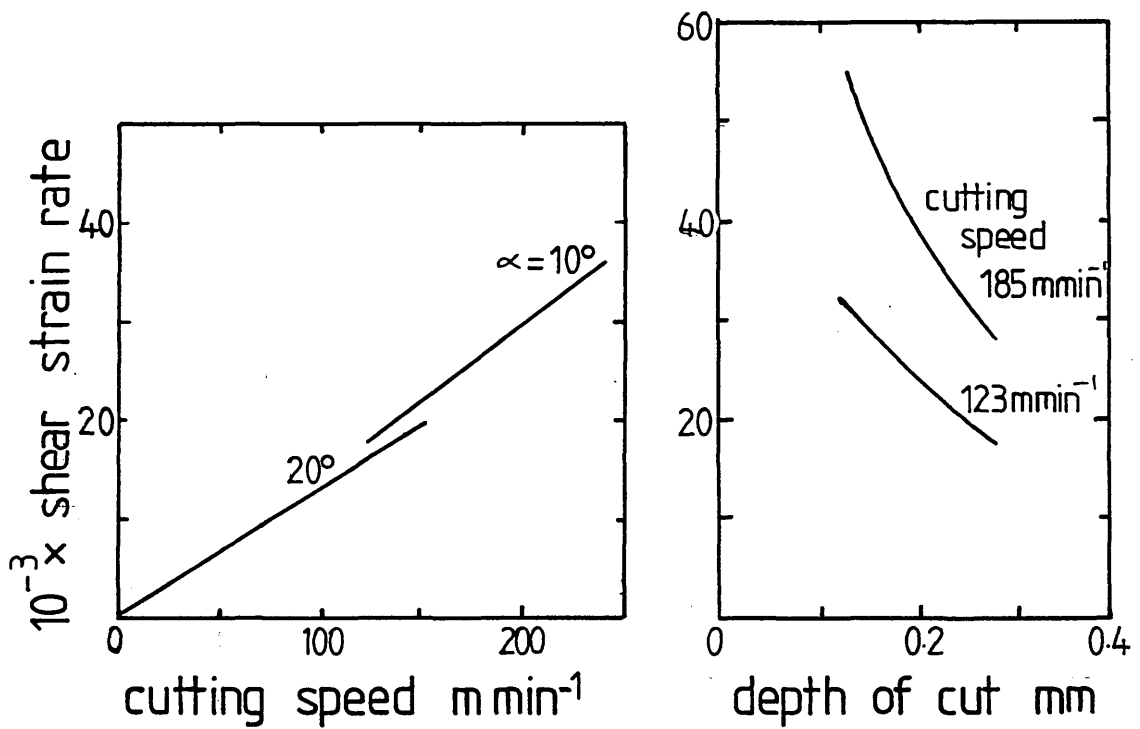
The production of this severely deformed layer is predicted if reference is made to one of the treatises on the strain rate involved in machining processes. No such information exists for drilling but several workers have studied turning, for example Oxley and Hastings (34). They developed a theoretical model for strain rate and were able to relate this to some experimental results (Fig. 4.2). During machining at cutting speeds of around  $100 \text{ m min}^{-1}$ , strain rates of the order of  $10^4 \text{ sec}^{-1}$  were produced in the surface layer of the work piece. Their results referred to a 0.13% C steel but it is likely that the results would be appropriate to a high strength aluminium alloy, at least to an order of magnitude. Oxley and Hastings noted that strain rate depended on cut angle ( $\alpha$  in Fig. 4.2) and depth of cut.

Little information exists to suggest the surface temperatures which might be achieved during machining, most work of this nature has been concerned with tool wear and hence tool temperatures only have been measured. Work piece temperatures might be expected to be slightly lower, depending on conductivity and thermal mass. However the surface temperatures would not be expected to differ greatly. Wright and Trent (35), for example, measured tool temperatures as high as  $850^\circ\text{C}$  during cutting of low carbon iron at  $183 \text{ m min}^{-1}$  cutting speeds.

The strain rates achieved during metal cutting are, according to available information, generally much higher than those found during hot torsion or extrusion tests, for example (36). Hence it would be very difficult to predict the deformation processes occurring during machining and the resultant micro-structure. For example, dynamic recrystallisation has not normally been considered possible during the hot deformation of aluminium alloys: Since the rate of recovery is high, aluminium alloys having a high stacking fault energy, it has generally been considered that the dislocation density achieved is insufficient for dynamic recrystallisation during deformation

### Strain Rate Associated with Machining

From Oxley and Hastings[34]



(36). However under the severe conditions of machining such processes would be impossible to eliminate from consideration alongside recovery and static recrystallisation. The evidence of Wright and Trent (35) would also suggest that temperatures as high as the melting point may even be possible, giving rise to local melting in the surface layer.

I.2.2. Residual Stresses. Residual stress considerations are of importance in any process involving surface deformation and have a particular significance in terms of fatigue crack initiation as discussed later.

Surface residual stresses produced by machining have generally been considered to be compressive due to the tensile nature of the plastic deformation occurring during machining, (Fig.4.3.). In a recent study however, Dölle and Cohen (37) were of the opinion that this was only the case in well lubricated machining processes with a low cutting speed and that the general situation was more complex. Tsuchida et al (38) investigated in detail the residual stresses attained during machining under various conditions of cutting speed, depth of cut, feed rate and lubrication. An X-ray technique was used to measure residual stress. They surmised that the stresses at the test piece surface during machining could be divided into three parts, (Fig. 4.4): (a) tensile behind the cutting edge, (b) compressive ahead of the tool and (c) tensile due to friction between tool and work piece. The frictional force was also considered to give rise to considerable surface heating, leading to a substantial thermal gradient and compressive plastic deformation in the surface caused by stresses due to differential expansion. All these separate components were believed to contribute to the final residual stress distribution. Their investigations centred around a 0.45%C steel, ( $UTS \sim 700 \text{ MNm}^{-2}$ ) machined by turning, and some typical results are reproduced in Fig. 4. 5. The diagrams clearly only show part of the total residual stress distribution since in order to obtain a total balance a region of opposite sign residual stress must exist further into the bulk. (a) and (b) show the effect of cutting speed and clearly a reduction in speed was found to have a great effect, particularly on the hoop stress which could be transformed from tensile to com-

Fig.4.3

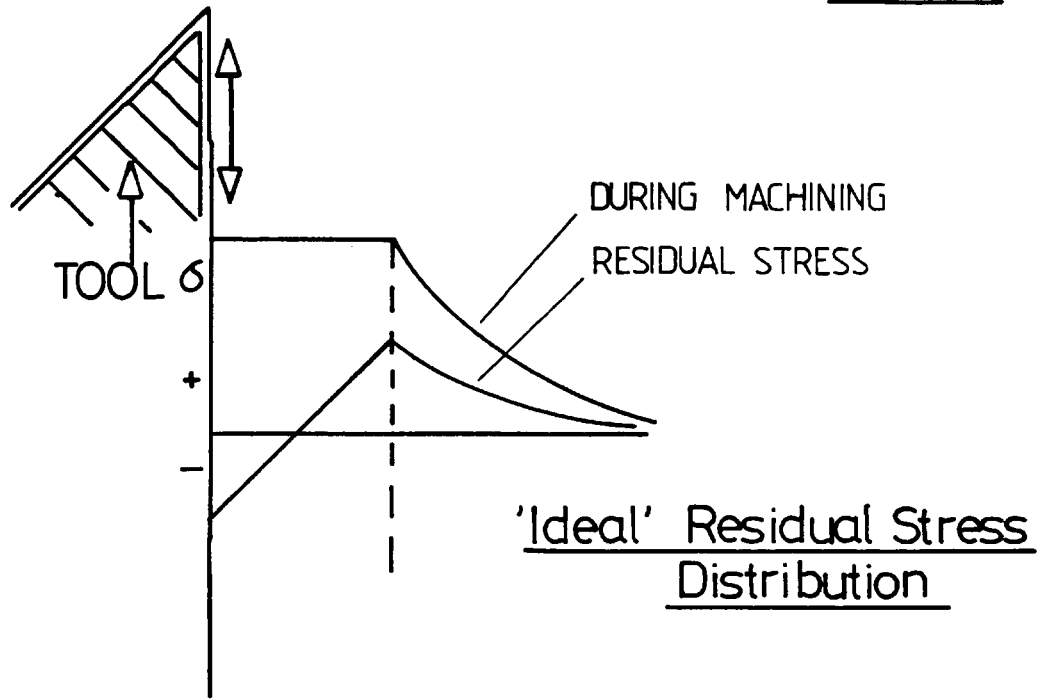
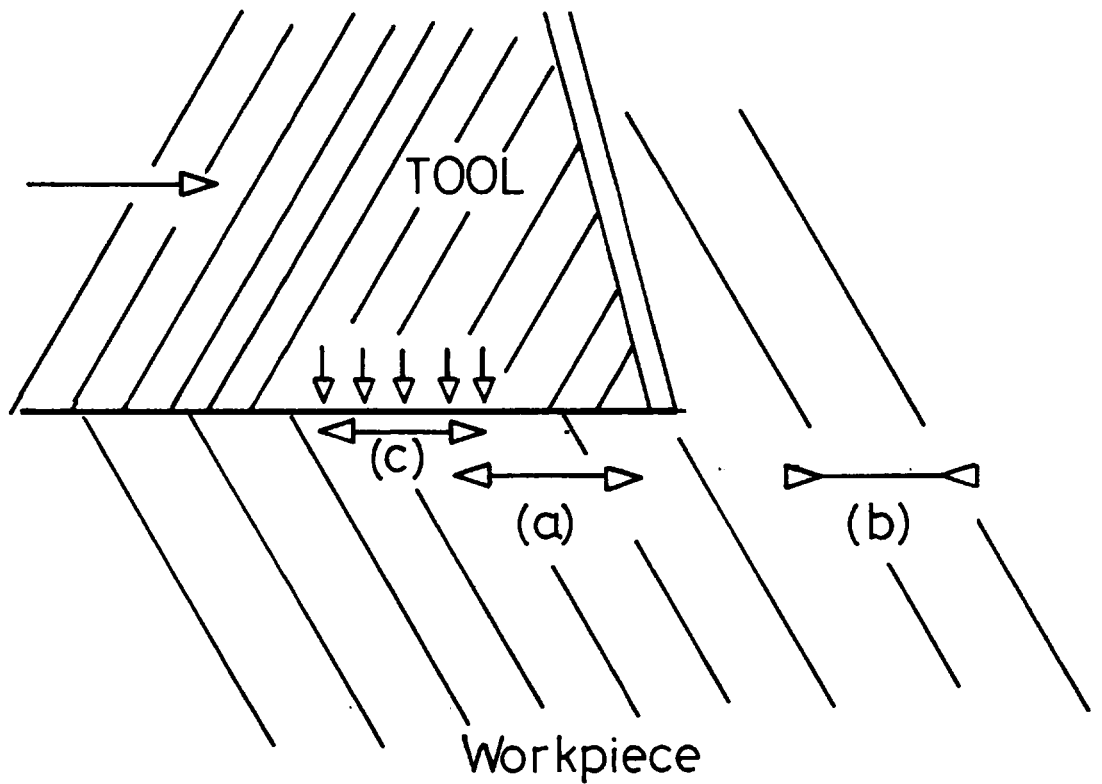


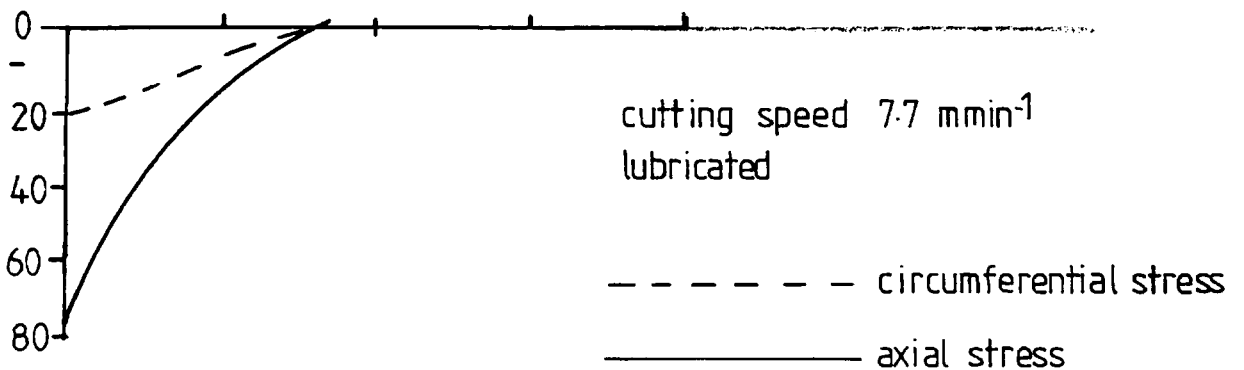
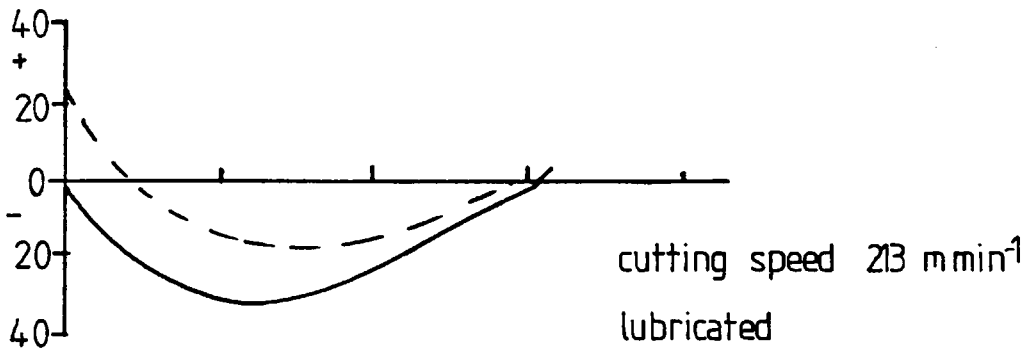
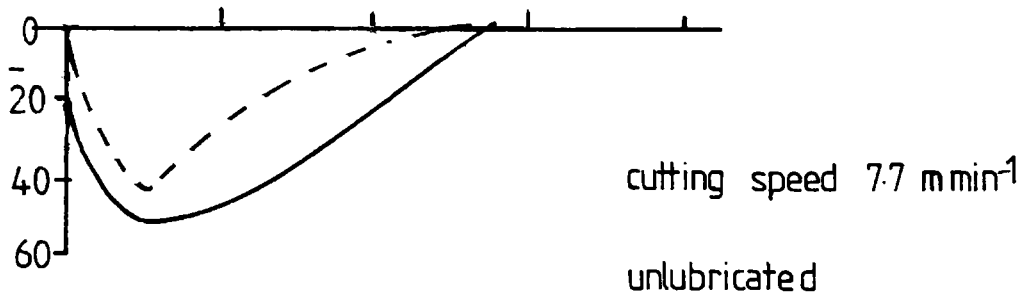
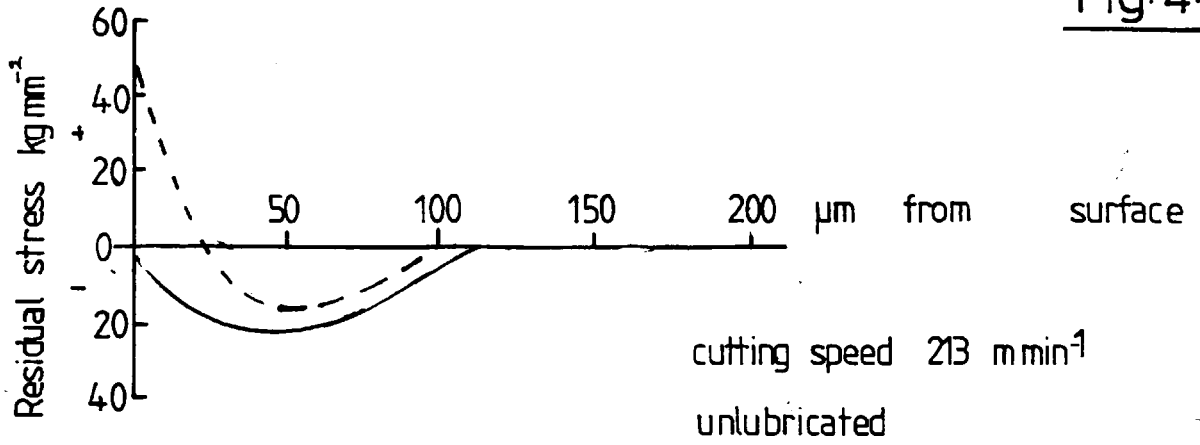
Fig.4.4



Stresses in Workpiece during Machining

from Tsuchida et al [38]

Fig.4.5



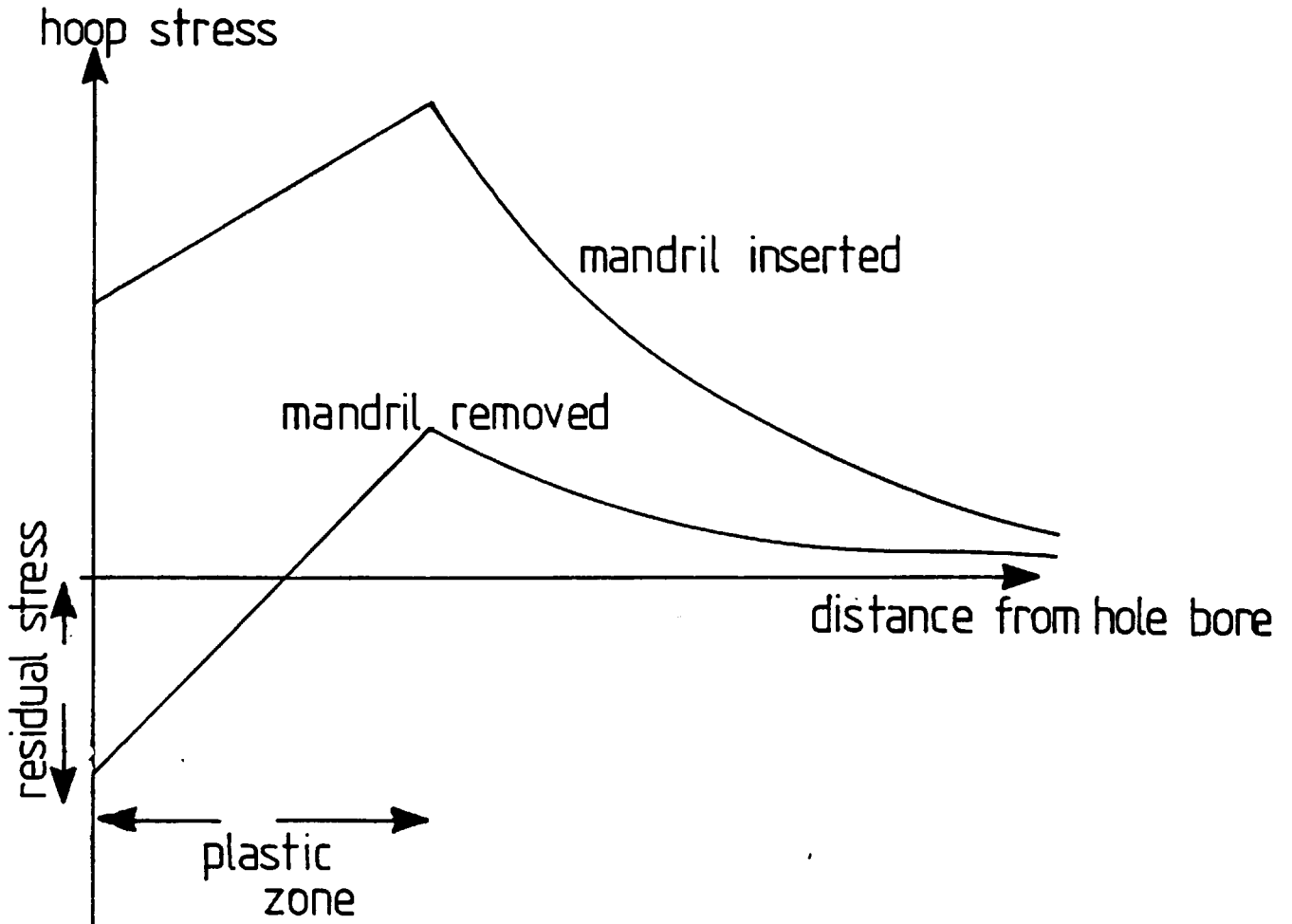
The influence of cutting speed and lubricating oil  
on residual stress distribution at machined surface  
from Tsuchida et al [38]

pressive at the surface. Tsuchida et al used the explanation that at low cutting speeds the mechanical cutting action, giving a tensile component of surface plastic deformation in the circumferential axis, overcame the heating effect, leading to compressive residual stress. At higher cutting speeds the attainment of higher surface temperatures was thought to promote compressive deformation due to expansion, giving a tensile residual. Cutting lubricant was found to have a similar significance to speed: The explanation was that by reducing friction, lubricant inhibited thermal expansion and compressive plastic deformation, compressive residuals were therefore obtained at all but the highest cutting speeds. Increasing feed rate and depth of cut were also found to be similar in effect to increased cutting speed, leading to a greater likelihood of tensile surface residual stresses.

The general considerations involved above can be applied to drilling or reaming operations but unfortunately no quantitative information exists to describe the actual stress distribution built up during boring. The only quantitative information available to describe residual stress distributions around holes in commercial aluminium alloy components refers to 'coining' operations, in which an oversize mandril is inserted, deforming the surface layer in tension in the hoop direction. Rich and Impellizzeri (39) developed a theoretical expression for the stress distribution in this situation, which is reproduced graphically in Fig. 4.6. They calculated that by inserting a 0.22 mm oversize mandril into a 6.35 mm hole, a surface residual hoop stress of  $-558 \text{ MNm}^{-2}$  would be produced in the case of 7075 T6, yield stress  $\approx 483 \text{ MNm}^{-2}$ . It is possible that after drilling similar stresses could be developed, but in the case of coining no heating is involved and hence recovery and recrystallisation are inhibited, the stresses calculated here are probably therefore an overestimate of the situation at the surface of a bored hole.

### 1.3. Fatigue Crack Initiation from Bored Holes.

It is now proposed to discuss fatigue crack initiation processes with reference to the microstructural and residual stress factors detailed above. It is useful however to first make a brief appraisal of the commonly observed modes of fatigue



Schematic residual stress distribution  
produced by surface deformation

from Rich and Impellizzeri [39]

crack initiation in high strength commercial aluminium alloys.

### I.3.I. Crack Initiation in High Strength Aluminium Alloys.

The early stages of failure by fatigue can involve three phases; cyclic slip, crack nucleation and microcrack growth. These processes need not all be apparent but together can consume the greater proportion of the fatigue life of a component. Schijve (40) found, for example, that in unnotched pure aluminium samples the major proportion of fatigue life was taken up by the development of cracks less than 0.1 mm in length.

The subject of cyclic slip and pre-crack plastic deformation has attracted a great deal of attention and a recent review of the voluminous literature has been provided by Mughrabi (41). The importance of cyclic slip in the case of high strength aluminium alloys was proven by Forsyth and Stubbington (42,43) who demonstrated that dislocation motion during cycling could lead to the formation of extrusions and intrusions on the specimen surface which subsequently acted as sites for crack nucleation. This process was then followed by stage I fatigue crack growth on planes of high shear stress.

While extrusions/intrusions have been found to be of importance in crack nucleation in high purity ternary alloys, such as those studied by Forsyth and Stubbington, crack nucleation in commercial alloys has often been found to be associated with large inclusions, normally intermetallic particles, (see Part 3 for details) situated close to the specimen surface. Grosskreutz and Shaw (44), for example, studied initiation in 2024 T3 and found that cracks nucleated exclusively at inclusions. Larger particles, greater than 1µm in diameter, were found to be most damaging, particularly if these particles were grouped in clusters. The actual crack nuclei were thought to form by debonding of the particles from the matrix, the particles being incoherent. No cracked particles were observed.

Various researchers have found that these intermetallics may become cracked during prior mechanical treatment (45,46). Forsyth and Smale (45) were in fact able to show that strains as low as 4 to 5% were sufficient. Bowles and Schijve (46) believed that this process led to the formation of the inclu-

sion clusters observed by Grosskreutz and Shaw and also gave rise to voids adjacent to particles, which were found to be particularly effective as sites for crack nucleation. Cracking of inclusions during cycling has been observed in some cases, for example by Morris (47) in the alloy 2219 T851. In this alloy some particles were found to be laminated, laminations running along the rolling direction. This led to inhomogeneity in fatigue properties since delamination of particles was found to occur readily.

More recent work has shed further light on the actual process of crack nucleation. Debonding and cracking of particles appear to be the prevalent processes, but as demonstrated by Kung and Fine (48) the formation of a crack nucleus must involve plastic deformation in the vicinity of the particle. To slightly qualify this statement, the debonding or cracking step must presumably be unnecessary in the case of prior particle damage due to mechanical treatments. Kung and Fine found that in 2024 T3, at low cyclic strains, crack nucleation occurred on many occasions at the point of intersection of a cyclic slip band and a particle. At high cyclic strains, a situation in which surface extrusion/intrusions formation was marked, crack initiation switched from particles to surface irregularities.

The inclusion crack initiation process has been quantified by Chang et al (49) who developed a model for initiation based around the earlier observations of particle cracking by Morris (47). Their theory was based upon the concentration of stress at the inclusion/matrix interface due to dislocation pile-up. Fracture of the brittle particle was considered to occur when a critical elastic strain energy was achieved within the particle due to the pile-up. The second stage of initiation was then considered to be the extension of the crack into the matrix. The expression developed for the number of cycles at which cracking extended into the matrix (N) was of the form:

$$N = \frac{C_1}{DW^m (\tau_{\text{eff}} - \tau_0)^2} + \frac{C_2}{DW^{\frac{1}{2}} (\tau_{\text{eff}} - \tau_0)^2}$$

Where:  $C_1$ ,  $C_2$  and  $\tau_0$  are material parameters

$W$  = particle width

$D$  = maximum slip distance - related to grain size, see Fig. 4.7  
 $m$  is a constant related to the mode of particle fracture and ranges from  $m=1$  for simultaneous fracture of the whole particle to  $m=3$  for initial fracture at a localised site.

$\tau_{eff}$  = the effective shear stress on a particle taking such factors as misfit into account.

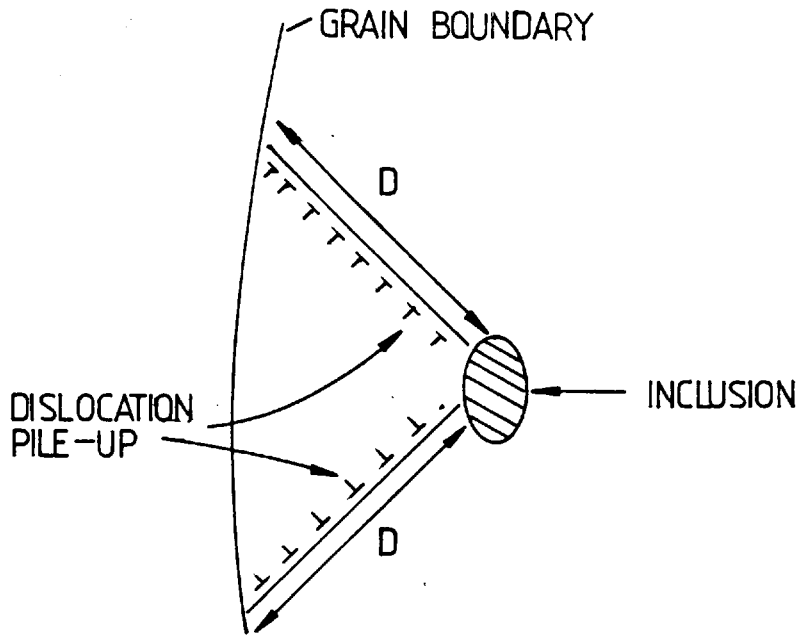
The theory was tested by Morris and James (50) in the alloy 2219 T851. Probability functions were produced for initiation versus  $D\sqrt{W}$  and are reproduced in Fig.4.8. together with experimental data for comparison.

A certain ratio of particle size to grain size was found to give the highest probability of initiation depending on stress level. Their predictions showed the general trend that at lower stress levels, with correspondingly longer life, crack initiation would be expected to occur at smaller particles within smaller grains. This is presumably related to the amount of dislocation activity at lower stresses and hence the size of dislocation pile-ups, Morris and James did not discuss the effect in any detail however.

### I.3.2. The Effect of Surface Deformation on Crack Initiation.

As discussed earlier, surface deformation, such as that occurring during hole boring, can lead to the formation of a deformation substructure in the surface layer with considerable hardening. Also produced are residual stress distributions which may be either compressive or tensile in the hoop direction at the surface, depending on boring conditions. Also different boring processes may lead to differences in surface roughness which may also be of some significance. A number of workers have studied these effects, mostly in combination, and for a variety of different materials.

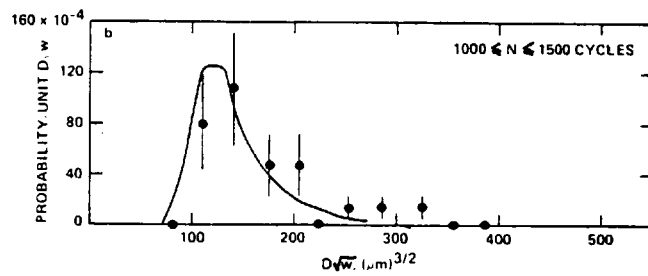
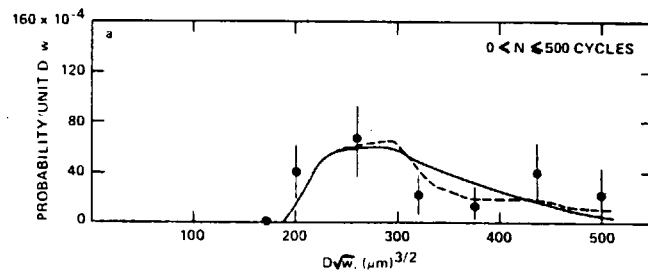
Benson (51) conducted a literature review and concluded that dislocation tangles in the surface layer would inhibit slip processes preventing crack nucleation. Residual compressive stresses, in this case produced by shot peening were thought to be of great importance, particularly in the high cycle regime  $NF > 10^4$  where cyclic plasticity was insufficient to



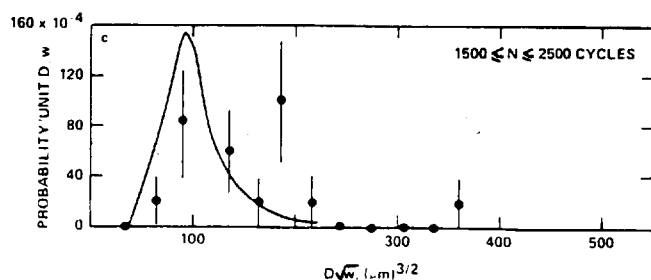
Dislocation Pile-up Model of Initiation

FROM CHANG ET AL [49]

Fig. 4.8



FROM MORRIS AND JAMES [50]

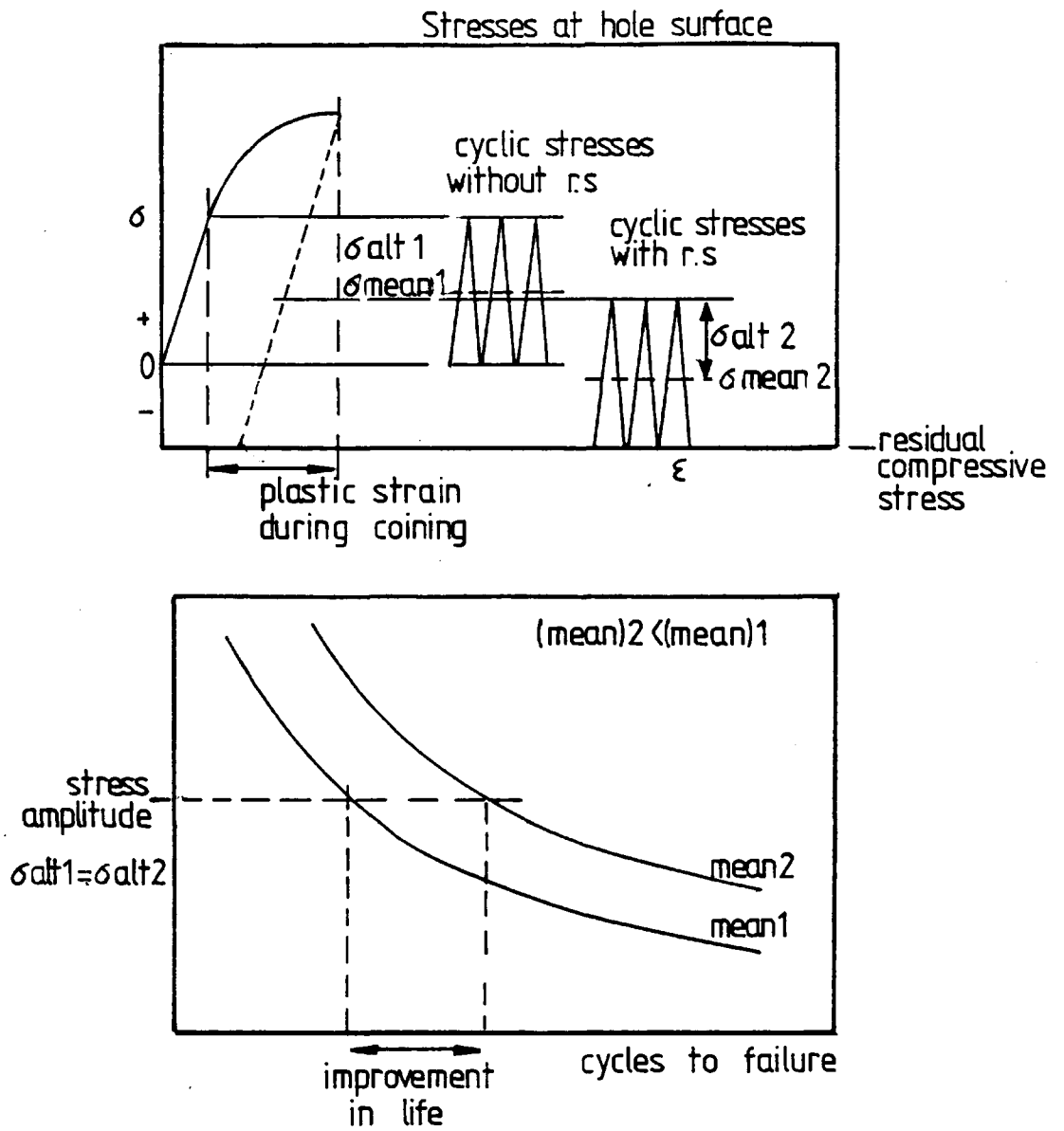


Relative Probability of Nucleation vs.  $D\sqrt{W}$  for Various Fatigue Intervals

cause stress relaxation. Speakman (52) supported this view and found that coining, a similar process to that used in reference (39) had a pronounced effect on the fatigue performance of aluminium alloy specimens containing open holes. He suggested that the improvement in life could be simply predicted by an adjustment of the stress level on the S/N curve to take into account the residual stress (Fig.4.9.).

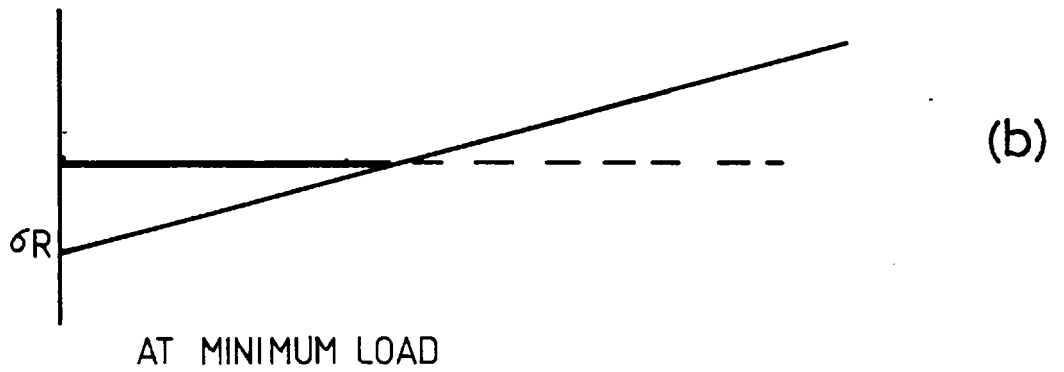
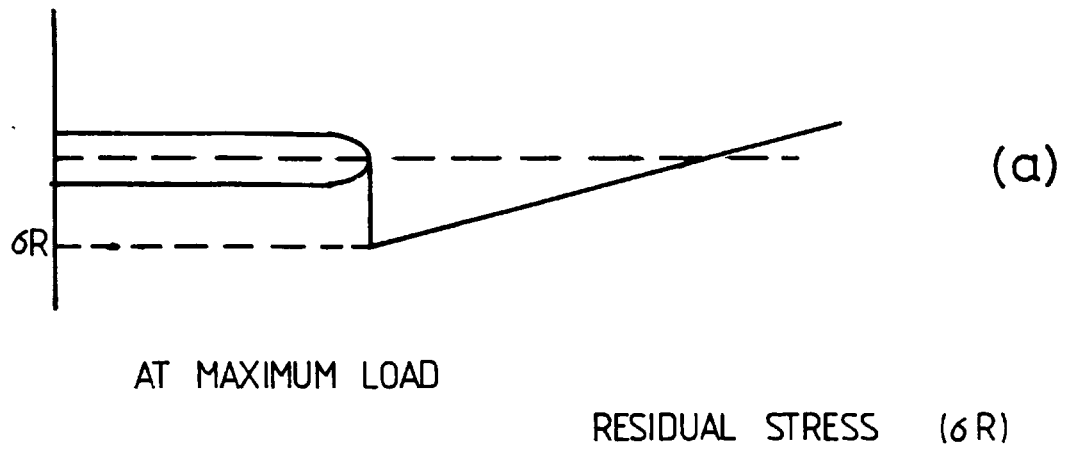
Leverant et al (53) made a study of the effect of machining and shot peening on crack initiation in Ti 6%Al 4%V, particularly from the viewpoint of residual stresses and surface topography. As machined specimens were found to have superior fatigue performance to those electropolished and stress relieved. The improvement was thought to be associated with microcrack growth retardation rather than crack nucleation as machined marks were found to act as crack nuclei. The effect of residual stresses on crack growth retardation has been clearly proven by Underwood et al (54) who found that not only were crack growth rates reduced in a surface compressive residual stress field but also as crack growth proceeded into underlying tensile regions. A simple superposition of stresses approach, similar to that suggested by Speakman, could be used to explain the effect of surface compressive stresses but the rather surprising effect in the tensile region was predicted by a consideration of residual stress redistribution ahead of the crack: The basis of their calculations of redistribution of stresses was that at minimum load the distribution was unchanged, since the crack could have no effect on compressive residual stress, (Fig.4.10). At maximum load however the residual stress was considered to redistribute as shown in Fig.4.10(a), leading to the maintenance of compressive residual stresses ahead of the crack.

The relative importance of residual stresses and deformation structure was investigated by Leverant et al (53) by testing heavily cold worked specimens. Little effect of cold work was found on fatigue properties, an observation which is in general agreement with other workers. In fact Laird (55) reviewed the subject and concluded that since the strains involved in PSB formation and crack propagation are very high (~100%) they are unlikely to be affected by prior deformation.



Improvement in Fatigue Life due to Coining

FROM SPEAKMAN [52]



Redistribution of Residual Stresses  
Ahead of a Crack Growing Through a  
Residual Stress Field

FROM UNDERWOOD ET AL [54]

The residual stress distribution was not observed by Leverant et al to 'shake down' and be removed during cycling, provided that the yield stress was not exceeded at the surface during testing. For example, in tests involving large compressive stresses, some stress relieving was observed since the additive residual and applied stresses exceeded the yield stress in the surface region. In contrast cycling in tension to similar peak loads had little effect.

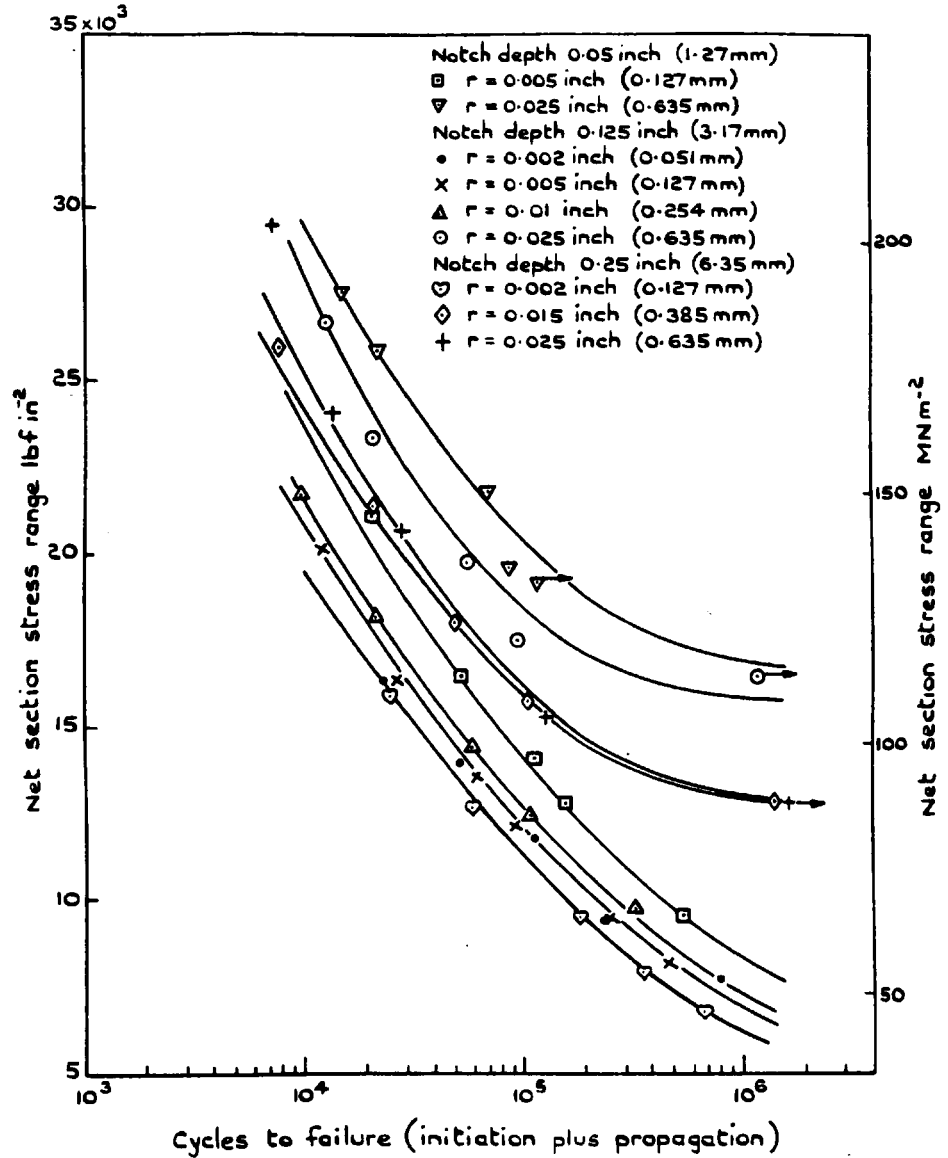
Under all conditions, Leverant et al found that crack initiation occurred at the specimen surface and hence, by testing stress relieved specimens they were able to investigate the effect of surface finish on initiation. Polished specimens were found to be inferior in terms of fatigue life to those as machined. It was found however, that the root radius of surface markings on polished specimens was much smaller than those as machined,  $2 \rightarrow 5 \mu\text{m}$  as opposed to  $50 \rightarrow 200 \mu\text{m}$ . The effect of notch root radius on initiation was demonstrated by Pearson (56) who found that while notch depth had an effect the dominating factor was root radius, (Fig. 4.II), supportive evidence for the results detailed above.

Forsyth (32) and Forsyth and Bowen (57) have obtained further information about crack initiation at machined or anodised surfaces in aluminium alloys: Forsyth found that crack initiation at drilled holes in RR58 could be inhibited at the hole surface due to a combination of surface deformation and residual stresses. Initiation was found to occur at a depth of  $\approx 50 \mu\text{m}$ ; this was related to a deformed layer depth of  $\approx 40 \mu\text{m}$ . Clearly surface finish would be unimportant in this situation. In the case of surface initiation Forsyth and Bowen concluded that the nature of surface markings was of importance: The most dangerous fatigue situations were felt to exist where surface defects were closely aligned to geometric stress concentrations. For example, Forsyth and Bowen found that surface anodizing pits formed effective initiation sites, but anodic film ruptures, aligned perpendicular to the stress axis, were more effective since they allowed the crack to initiate in long planar form.

#### I.4. Microcrack Growth.

As mentioned earlier, development of cracks up to 0.1mm in length

Fig. 4.11



The Influence of Notch Geometry on Crack Initiation

FROM PEARSON [56]

can consume most of the fatigue life of a component and it is therefore important to be able to describe crack growth in this regime. Many studies of fatigue crack growth have related growth rate to the crack tip stress intensity factor, but unfortunately this approach has been found to be invalid in the prediction of crack growth rates in the short crack ( $\sim 0.1\text{mm}$ ) regime. For this reason microcrack growth is often considered to be a part of the initiation process and crack growth to commence at lengths sufficient for linear elastic fracture mechanics to apply.

In order to predict the life of a component containing flaws, for example machining defects or inclusions, a number of workers have taken a different approach and have considered the flaws to behave as cracks whose growth can be predicted by fracture mechanics considerations and have therefore eliminated the initiation sequence. For example, Haslam (58) and Talug and Reifsnider (59) have based their analysis on the use of the equation

$$\Delta K_{th} = \Delta \sigma_{lim} \sqrt{\pi a_e}$$

Where:

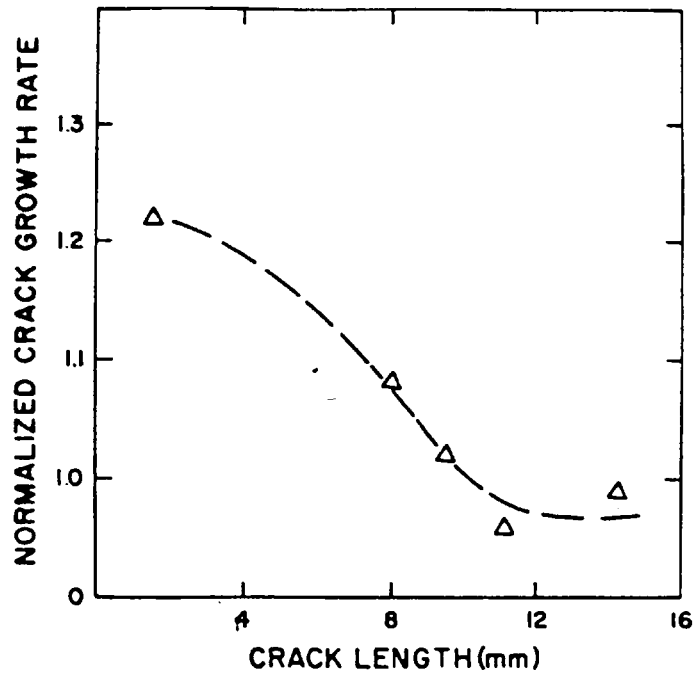
$\Delta K$  = the threshold stress intensity for growth of long cracks

$\Delta \sigma_{lim}$  = the fatigue limit

$a_e$  = the existing flaw size

The use of the equation is based on the premise that below the fatigue limit the stress intensity at the tip of a flaw, considering it as a crack, is below the threshold and therefore the flaw cannot grow and failure cannot occur.

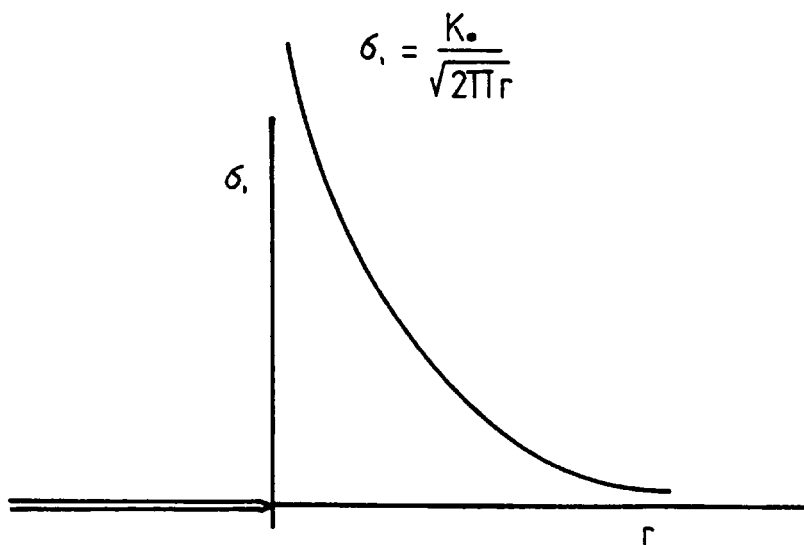
As noted by Pearson (60) however, very short flaws must grow at stress intensities below  $\Delta K_{th}$  or crack growth would not occur at applied stresses below the general yield. Both Pearson and Talug and Reifsnider investigated the growth of short cracks and found, as expected, that crack growth rates were higher than those predicted by extrapolation of long crack data (Fig.4.12). Talug and Reifsnider carried out a fracture mechanics analysis of short surface cracks and found that the proximity of the crack tip to the free specimen surface gave



Short Crack Growth Rates as a Function of Crack Length

FROM TALUG AND REIFSNIDER[59]

Fig. 4.13



Elastic Stress Field Ahead of an Infinitely Sharp Crack

rise to an increase in stress intensity, thereby partially explaining the observed effect. This evidence demonstrated that while the preexisting flaw size analysis may have some validity, the flaw size predicted is likely to be somewhat larger than observed. The analysis also implies a well defined threshold stress intensity, the existence of which in aluminium alloys is not well established. Kirby and Beevers (6I), for example, found that crack growth in the threshold regime was highly dependent upon environment and loading conditions and was difficult to specify accurately.

#### I.5. Fracture Mechanics Considerations.

In order to quantitatively investigate fatigue crack growth from the hole bore it is necessary to relate crack growth rate to a factor which describes the stress field at the crack tip. Generally the principles used in order to do this have been those of linear elastic fracture mechanics or L.E.F.M: The elastic stress field ahead of an infinitely sharp crack in a semi-infinite solid is described by:

$$\sigma_1 = \sigma \sqrt{a/2r} \quad (\text{Fig.4.I3})$$

Where:

$\sigma_1$  = stress perpendicular to crack

$\sigma$  = remotely applied stress

$a$  = half crack length

$r$  = distance ahead of crack in the plane of the crack

This can be expressed as:

$$\sigma_1 = \frac{K_0}{\sqrt{2\pi r}}$$

Where:

$$K_0 = \sigma \sqrt{\pi a}$$

$K_0$  is known as the crack tip stress intensity factor and can completely specify the amplitude (not distribution) of the stress field in the vicinity of the crack tip, since it is independent of  $r$  and depends only on crack length,  $a$ , and remotely applied stress  $\sigma$ .

The equation given above for  $K_0$  can only describe the situation for a crack in a semi-infinite solid. In the case of a crack initiated at the bore of a circular hole the value of  $K_0$  is affected by the presence of the elastic stress concentration factor ( $K_t$ ), equal to 3 in the case of a circular hole in a semi-infinite plate. (For finite width plate stress concentration factors see Fig.4.I4). In such a situation the crack tip stress intensity,  $K$ , is often quoted as:

$$K_1 = \frac{K_1}{K_0} \sigma \sqrt{\pi a'}$$

Where:

$K_1/K_0$  = stress intensity correction factor or normalised stress intensity factor.

$a'$  in this case equals half the crack length, including hole diameter.

In the simple case of a crack initiated at a free surface:

$$K_1 = 1.12 \sigma \sqrt{\pi c}$$

Where:

$c$  = total crack length

Similarly for very short cracks close to the hole bore the stress intensity factor approximates to:

$$K_1 = 1.12 K_t \sqrt{\pi c}$$

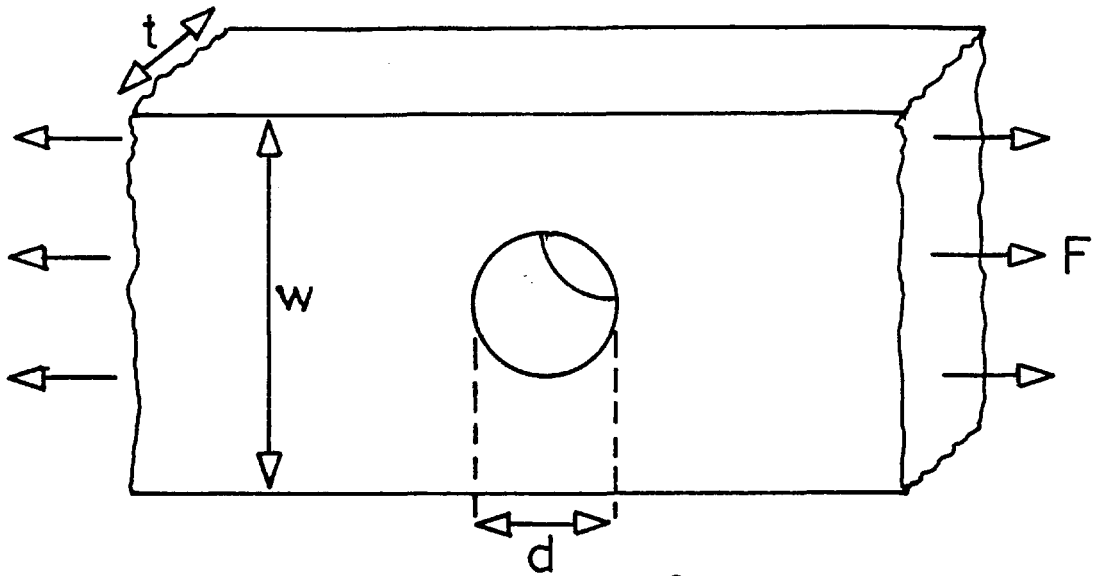
Where:

$K_t$  = elastic stress concentration factor

However, with increasing crack length, the influence of  $K_t$  diminishes and hence the correction factor  $K_1/K_0$  is not constant. Solutions for  $K_1/K_0$  in such situations have been calculated for example by Rooke and Cartwright (62) (Fig.4.I5).

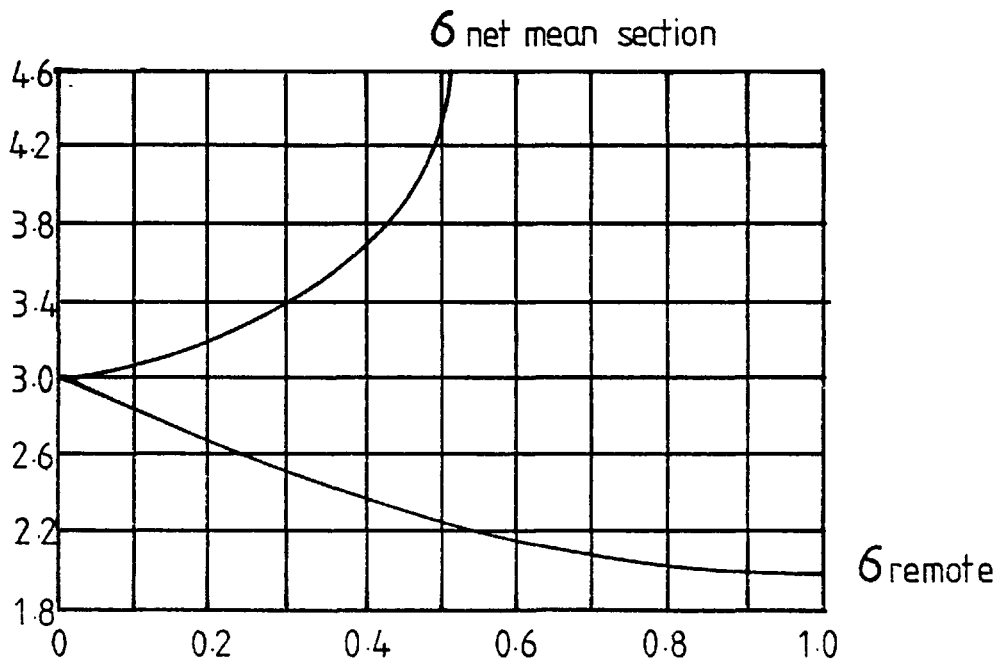
The solutions above apply for two dimensional or through crack situations as shown in Fig.4.I6(a), an unusual situation in the early stages of fatigue crack growth since cracks generally

Fig.4.14



$$\sigma_{\text{remote}} = F/wt$$

$$\sigma_{\text{net mean section}} = F/(w-d)t$$



Elastic Stress Concentration Factor  $K_t$

for a Circular Hole Diameter  $d$  in plate Width  $w$

Stress intensity factor for one or two cracks  
at a circular hole in a sheet subject to  
uniaxial tension - 2d solution

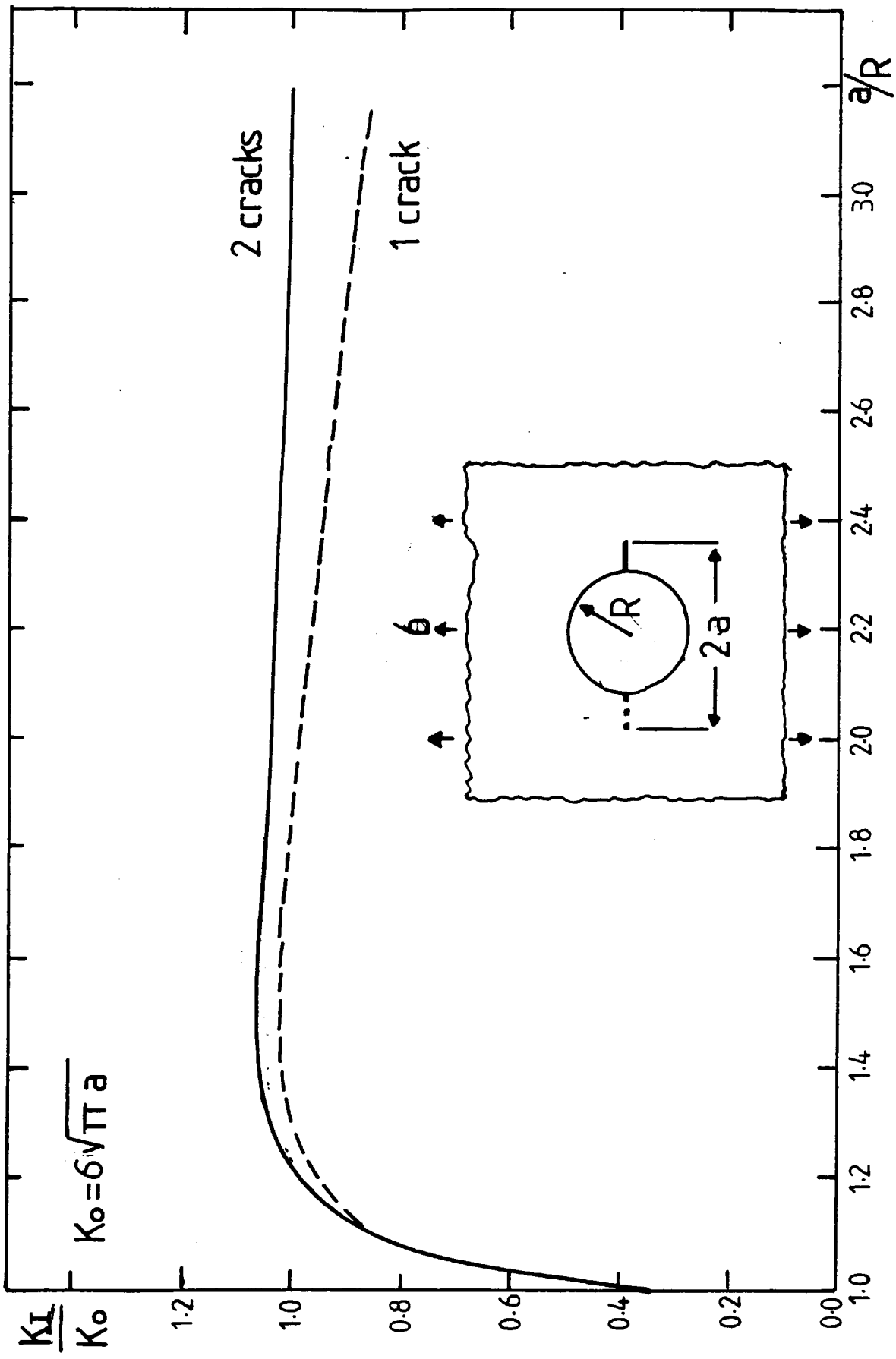
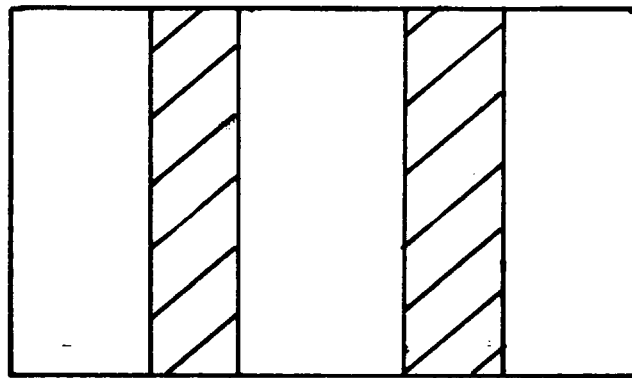
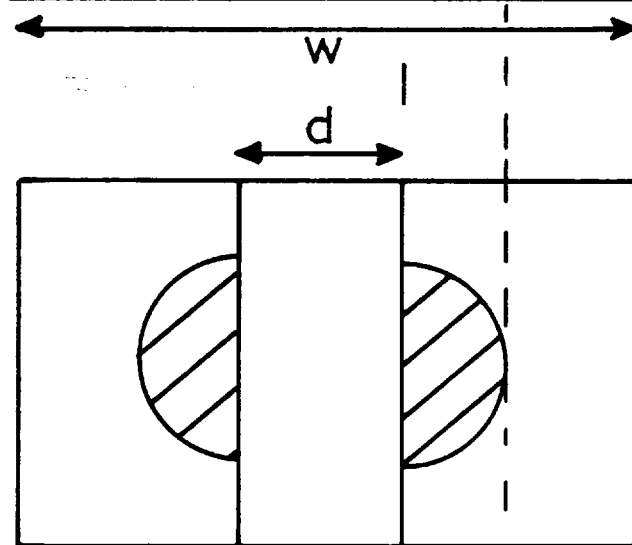


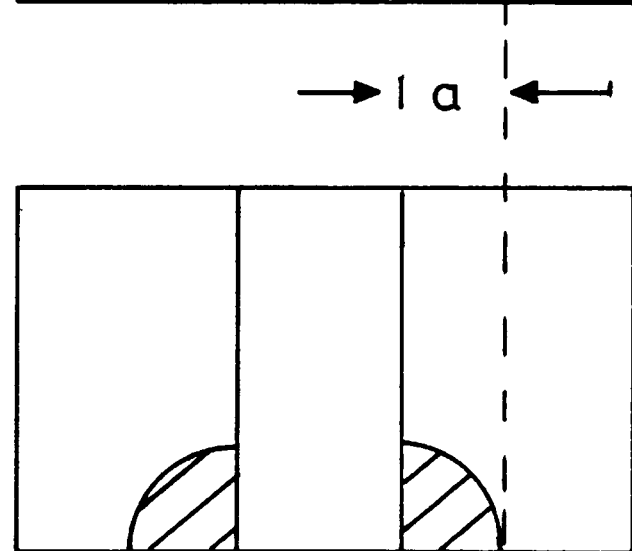
Fig. 4.16



(a)



(b)



(c)

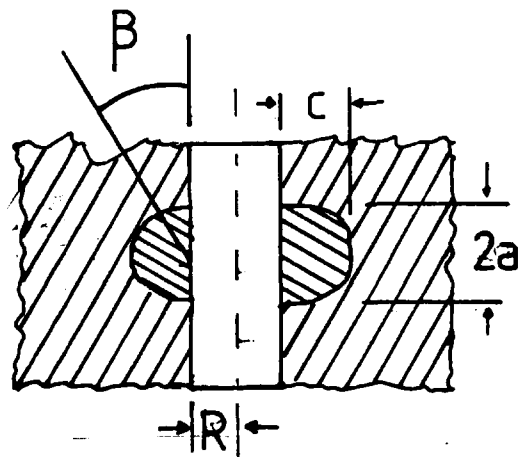
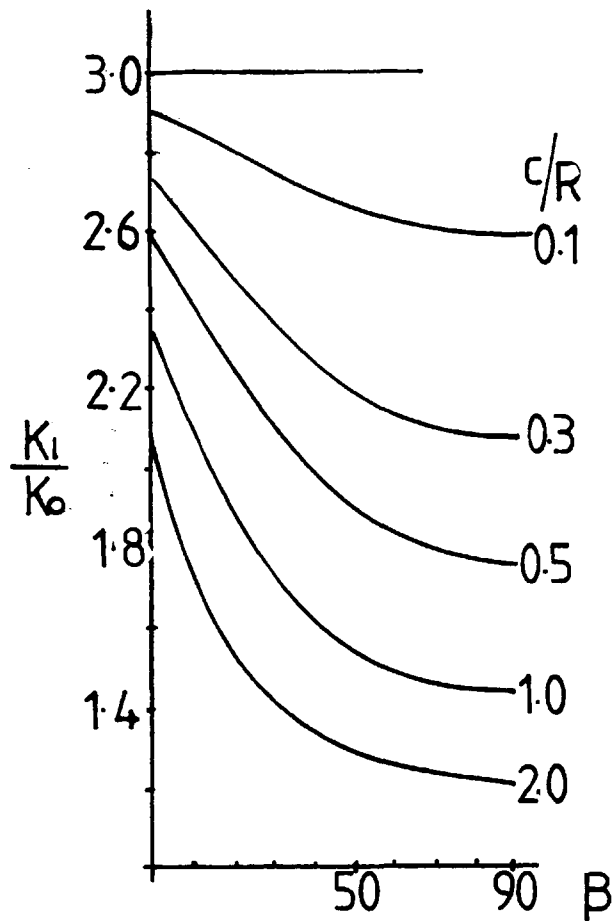
Possible Crack Configurations

initiate at a point and are either semi or quarter elliptical in shape in the early stages. The situation is now greatly complicated since cracks of equivalent length have different crack tip stress intensities from those calculated from two dimensional solutions, and stress intensity also varies along the crack front. In this case various possible routes can be followed to calculate  $K_1$ . The simplest involves the correction of through crack solutions using a crack front shape factor  $\phi$ : (63)

$$K_1 = \frac{K_1}{K_0 \phi} \sigma \sqrt{\pi a}$$

Values of  $\phi$  are available in the literature for various crack shapes. More sophisticated analyses have also been carried out for semi and quarter elliptical cracks at circular holes which give estimates of the variation in  $K_1$  along the crack front. Shah (64) for example, employed a standard mathematical route, while Raju and Newman (65) made use of finite element analysis. The results obtained by Shah are summarised in Fig.4.I7 and demonstrate that stress intensity is a maximum along the hole bore and hence crack growth would be expected to be most rapid in this direction.

Rather than carry out a detailed discussion here of the techniques used to calculate  $K_1$  in various situations it is proposed to calculate stress intensity/crack length calibrations for the various likely crack configurations in the actual specimen types used. The results of these calculations are shown in Appendix I.



Normalised stress intensity factor  
for two semi elliptical cracks at a hole  
in a thick plate

from Shah [64]

$K_0$  = stress intensity factor for  
=  $c/a$  ratio crack in infinite solid

## 2. EXPERIMENTAL RESULTS.

### 2.1. Hole Surface Topography and Subsurface Deformation Structure.

Surface roughness data obtained by British Aerospace showed that the drilled hole bores were generally somewhat rougher and varied more in quality than those having undergone the reaming process: The actual roughness data obtained (in  $\mu\text{m}$  about a centre line) was, average=37.4 $\mu\text{m}$  standard deviation=17.4 $\mu\text{m}$ , for the drilled holes. For the reamed holes, average=13.7 $\mu\text{m}$  standard deviation=8.3 $\mu\text{m}$ . Under SEM examination both types of hole bores showed parallel score marks, running in the direction of drill rotation, of similar magnitude (Fig. 4.18). The drilled holes, (a), also showed areas of more severe damage, with markings leading approximately perpendicular to the direction of drill rotation. These appeared to be a result of smearing and folding processes.

Evidence was also obtained of intermetallic particle damage in the surface layer in both types of hole but more commonly in the drilled case (Fig. 4.19). Intermetallic particles were observed in both surface layer thin foils (a) and in the surface itself (b). The particle observed in TEM would appear to have cracked during hole production rather than during electropolishing since electropolished, undeformed specimens did not show such cracking and the cracks extend into the aluminium matrix. The highly defective area visible in SEM (b) was found to be copper rich and is likely to be also a damaged intermetallic.

Microhardness testing, the results of which are plotted in Fig. 4.20, revealed a considerably hardened layer adjacent to the drilled hole bores with a peak V.P.N. of around 400. This compares with a bulk hardness of approximately 200. Despite the great scatter in experimental results, a clearly defined zone of increased hardness, diminishing to the bulk value at a depth of approximately 50 $\mu\text{m}$  below the surface, was observed. No such layer was found in the case of reamed holes; some slight increase in hardness was noted within 10 $\mu\text{m}$  of the hole bore but the increase was smaller than the scatter of experimental results and cannot therefore be re-

Fig. 4.I8. SEM observations of hole topography.

(a) drilled hole.

(b) reamed hole.

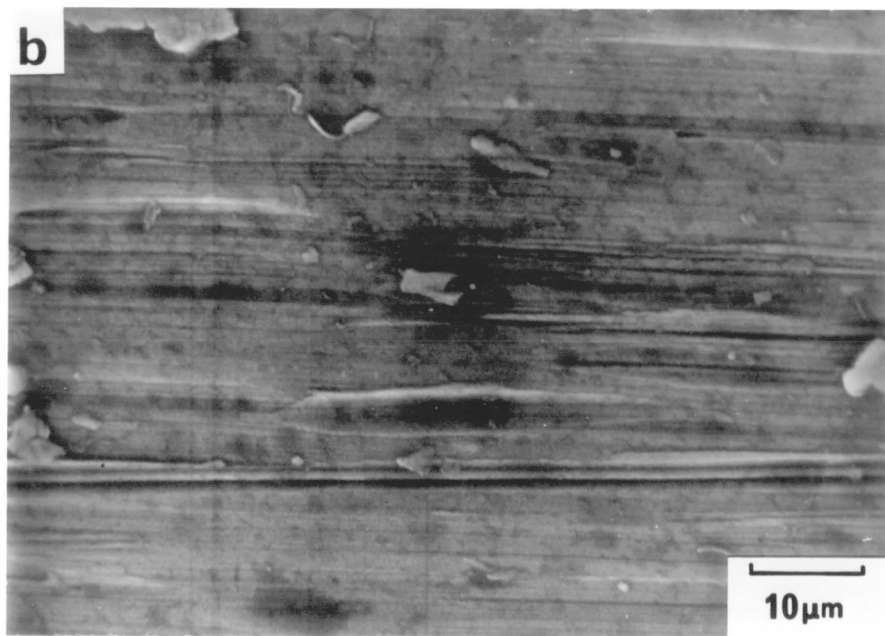
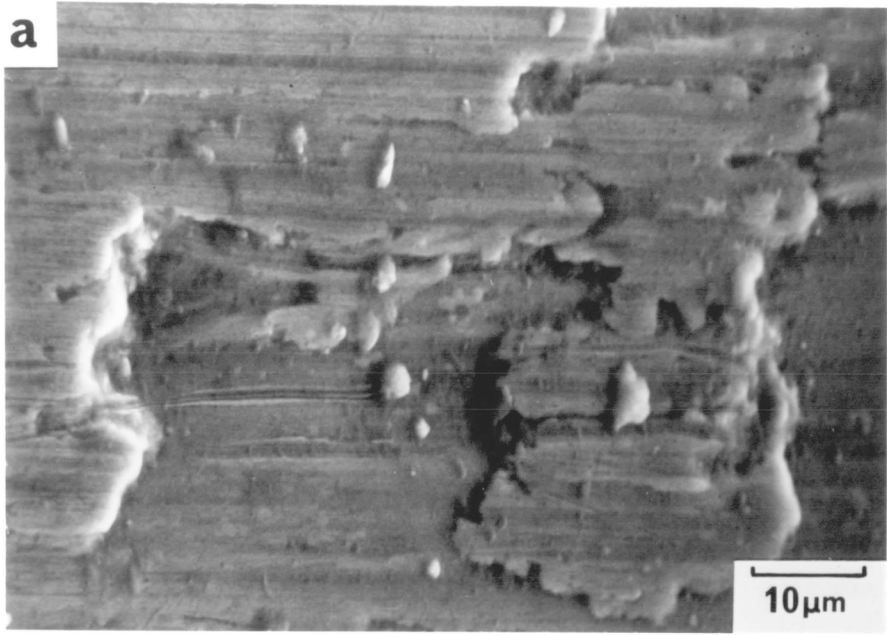
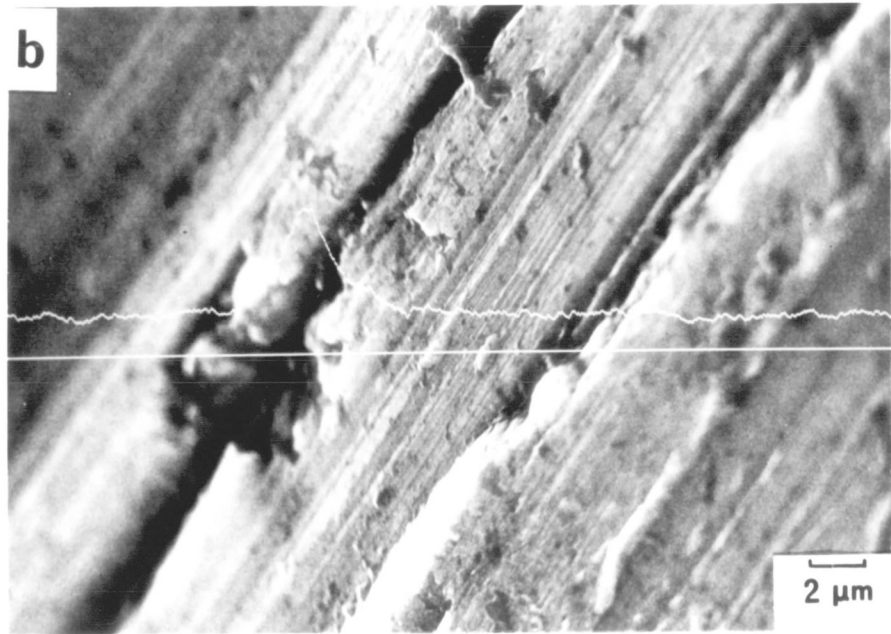
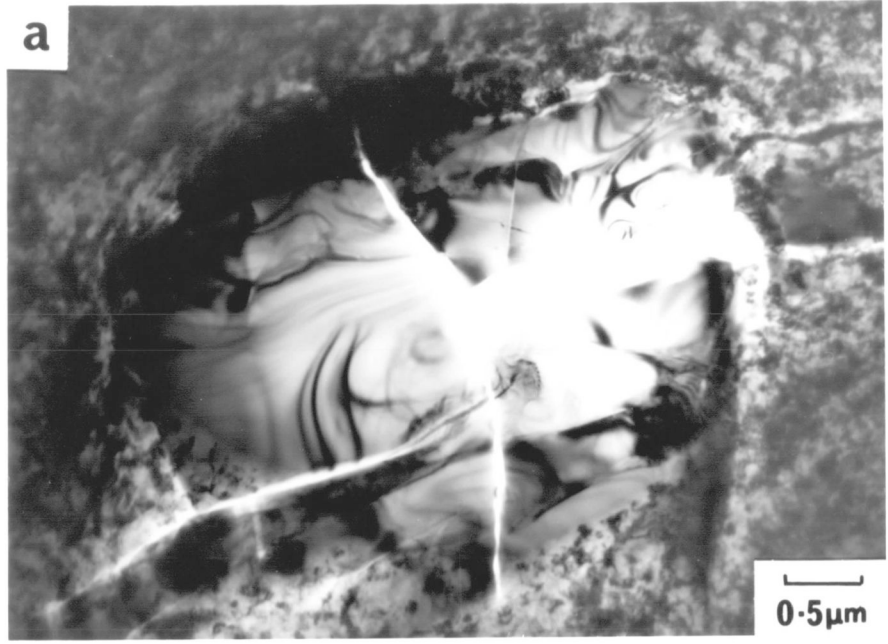


Fig. 4.I9. Damaged intermetallic particles lying in the hole surface layer.

(a) TEM bright field, hole surface foil, drilled hole.

(b) SEM micrograph of drilled hole surface. Elemental line scan shows copper concentration as measured by energy dispersive X-ray analysis.



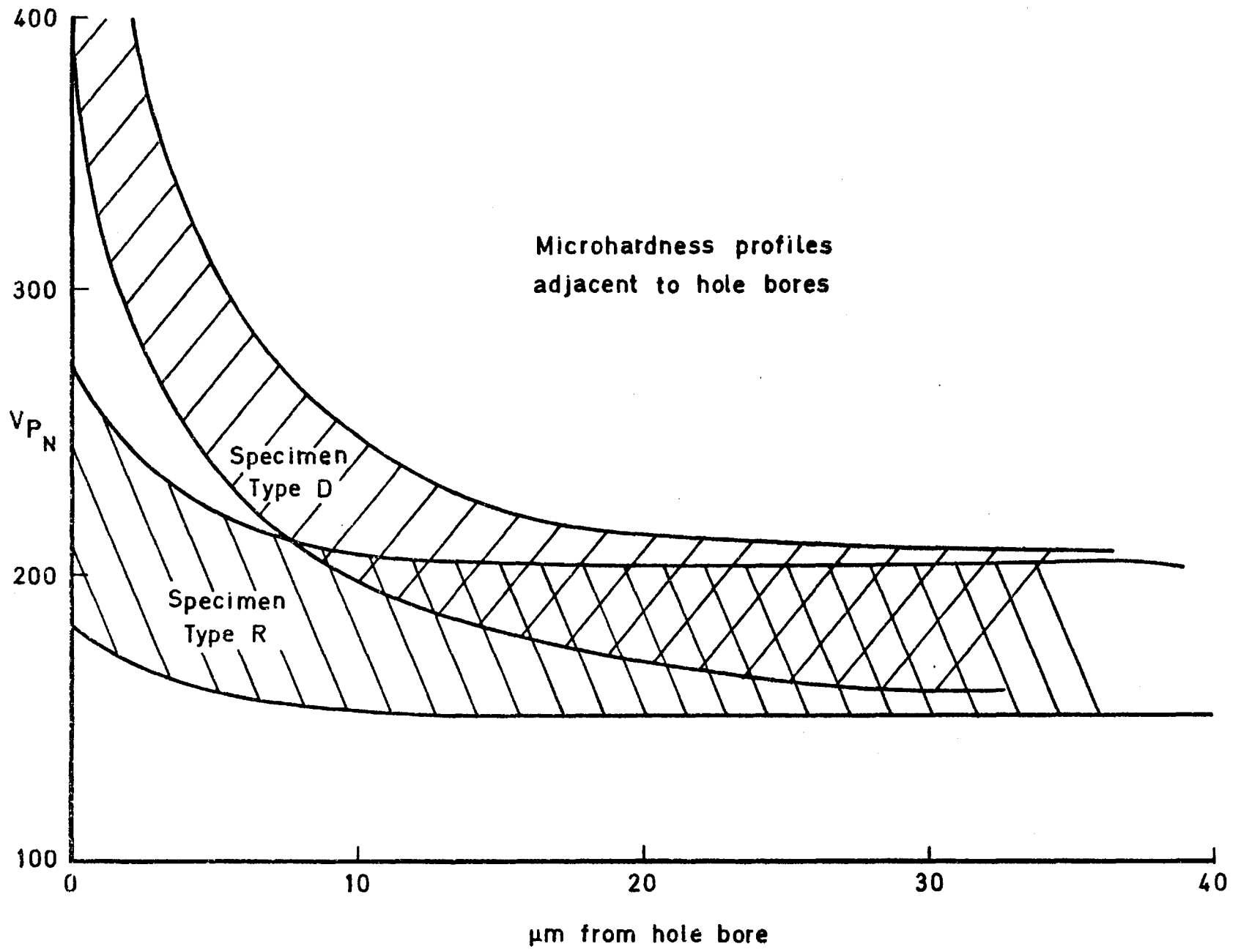


Fig 4.20

garded as conclusive.

The microhardness data were supported by metallographic observations in the light microscope of polished and etched specimens prepared perpendicular to the hole bore : A deformed zone was observed adjacent to drilled hole bores (Fig. 4.21). This zone was not observed at all points around the hole but was of maximum of 50 and 100 $\mu\text{m}$ . No such layer could be resolved next to holes produced by drilling and reaming operations.

The microstructure in the layer directly adjacent to the hole bores in the two cases was investigated by observation in the TEM of back polished thin foil specimens (Fig. 4.22). Clearly the material in this layer has undergone a radical transformation when compared to the initial alloy microstructure (Fig. 3.7), particularly in the drilled case, (a). Complete recrystallisation appeared to have taken place to a grain diameter of around 0.1 $\mu\text{m}$ . The original precipitate distribution was also found to be radically altered although some reflections in the SADP could be identified as corresponding to  $\eta$  phase ( $\text{MgZn}_2$ ). The actual particle distribution was not however determined. A clearly deformed structure was also observed in the reamed case, (b) although, as demonstrated by the arced SADP (produced with the same sized diffraction aperture as (a)), the structure consisted basically of recovered subgrains of low misorientation rather than randomly oriented grains as in the previous case. The precipitate distribution also appeared relatively undisturbed .

The microstructure adjacent to holes produced without lubricant was similarly investigated using TEM techniques: Here a more regular structure was produced (Fig. 4.23) again of ultrafine grains. Diffraction maxima were readily identified as corresponding to aluminium and  $\eta$  phase (Fig. 4.24). The  $\eta$  phase distribution was investigated using the micro-beam electron diffraction facility using a 20  $\text{\AA}$  spot size (Fig. 4.25). Using a scanning beam (a) a diffraction pattern similar to the SADP was produced and micro-beam diffraction patterns from points (b) and (c) could be identified as a  $\langle 112 \rangle_{\text{Al}}$  zone axis and a  $\langle \bar{1}2\bar{1}3 \rangle_{\eta}$  zone axis respectively. Using this technique  $\eta$  phase was found to be distributed in the form of

Fig. 4.2I. Optical micrograph of cross section through hole surface revealing deformed layer.

Fig. 4.22. TEM bright fields with corresponding SADP's:  
Hole surface microstructure.

(a) drilled hole.

(b) reamed hole.

(Holes bored to A.G.A.R.D. specification.)

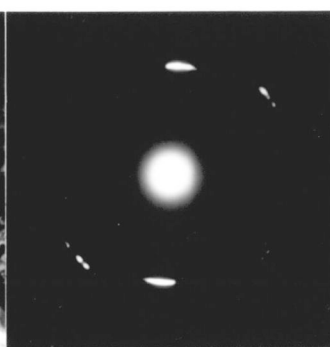
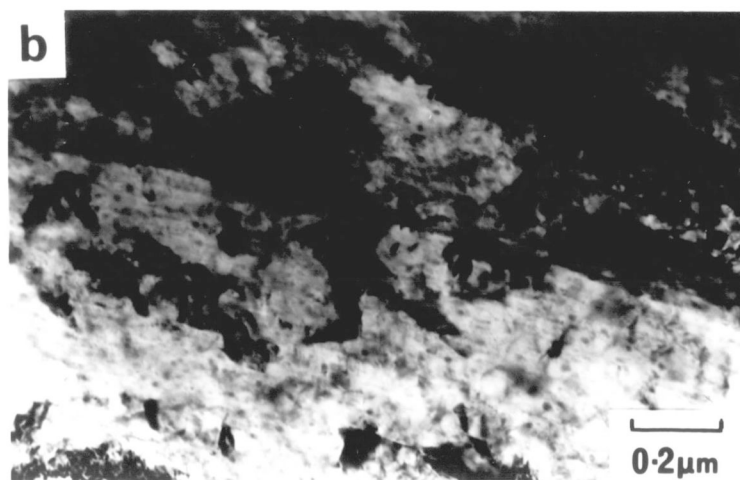
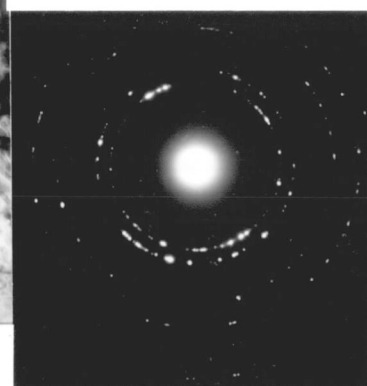
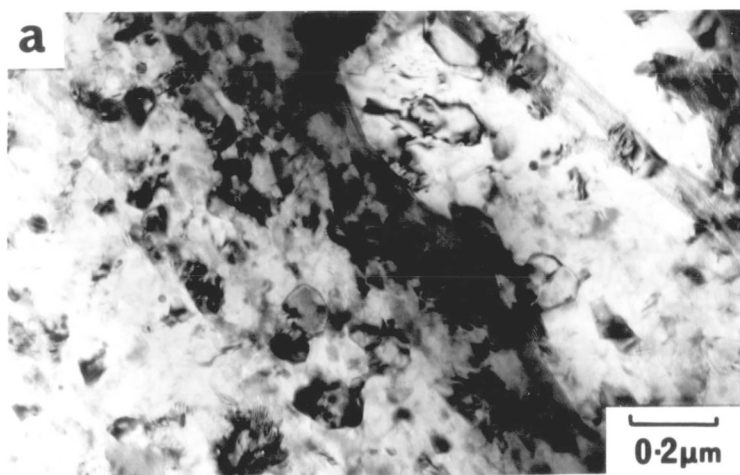
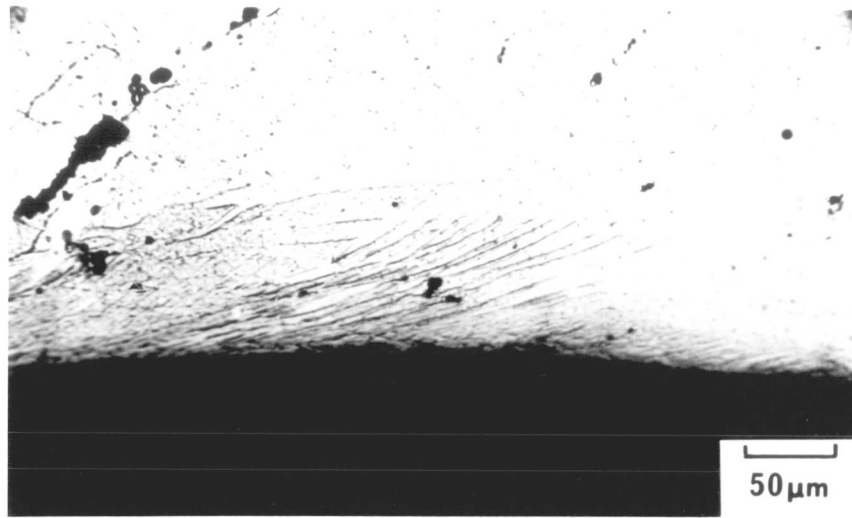


Fig. 4.23. Hole surface microstructure produced by drilling without lubricant: TEM bright field with corresponding SADP.

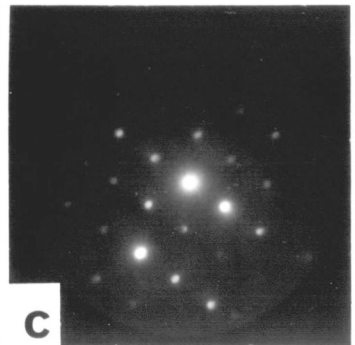
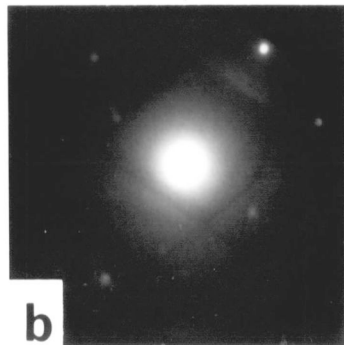
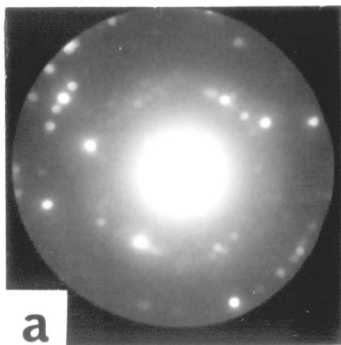
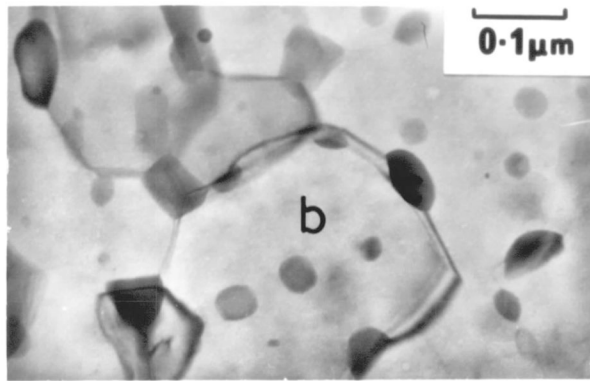
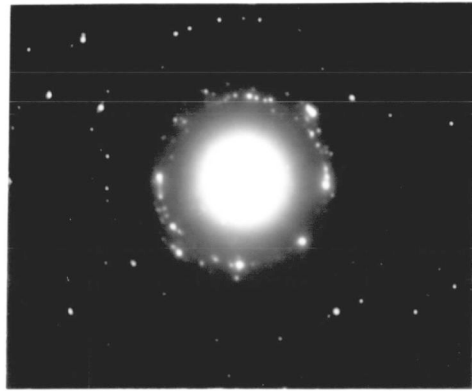
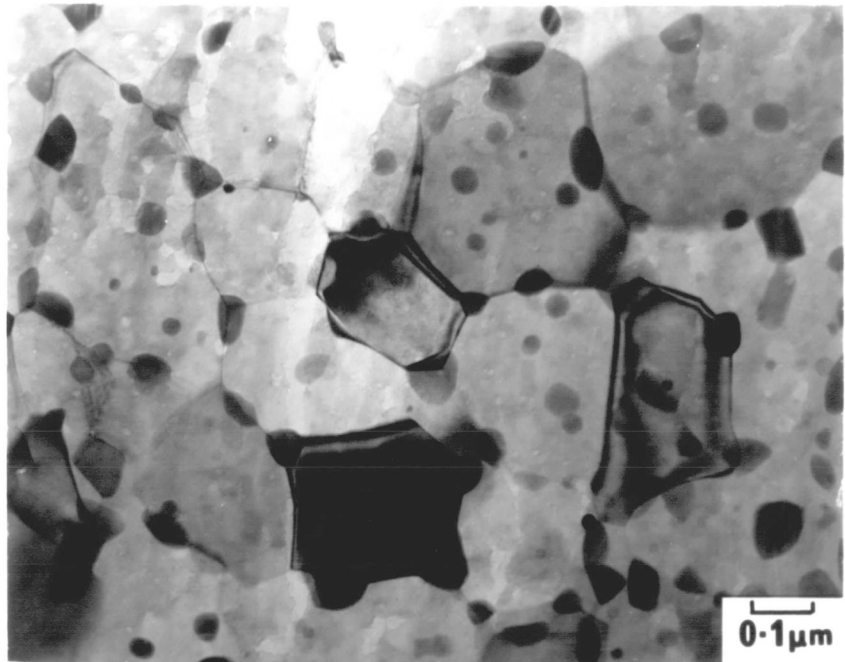
(For SADP analysis see Fig. 4.24 on p.99.)

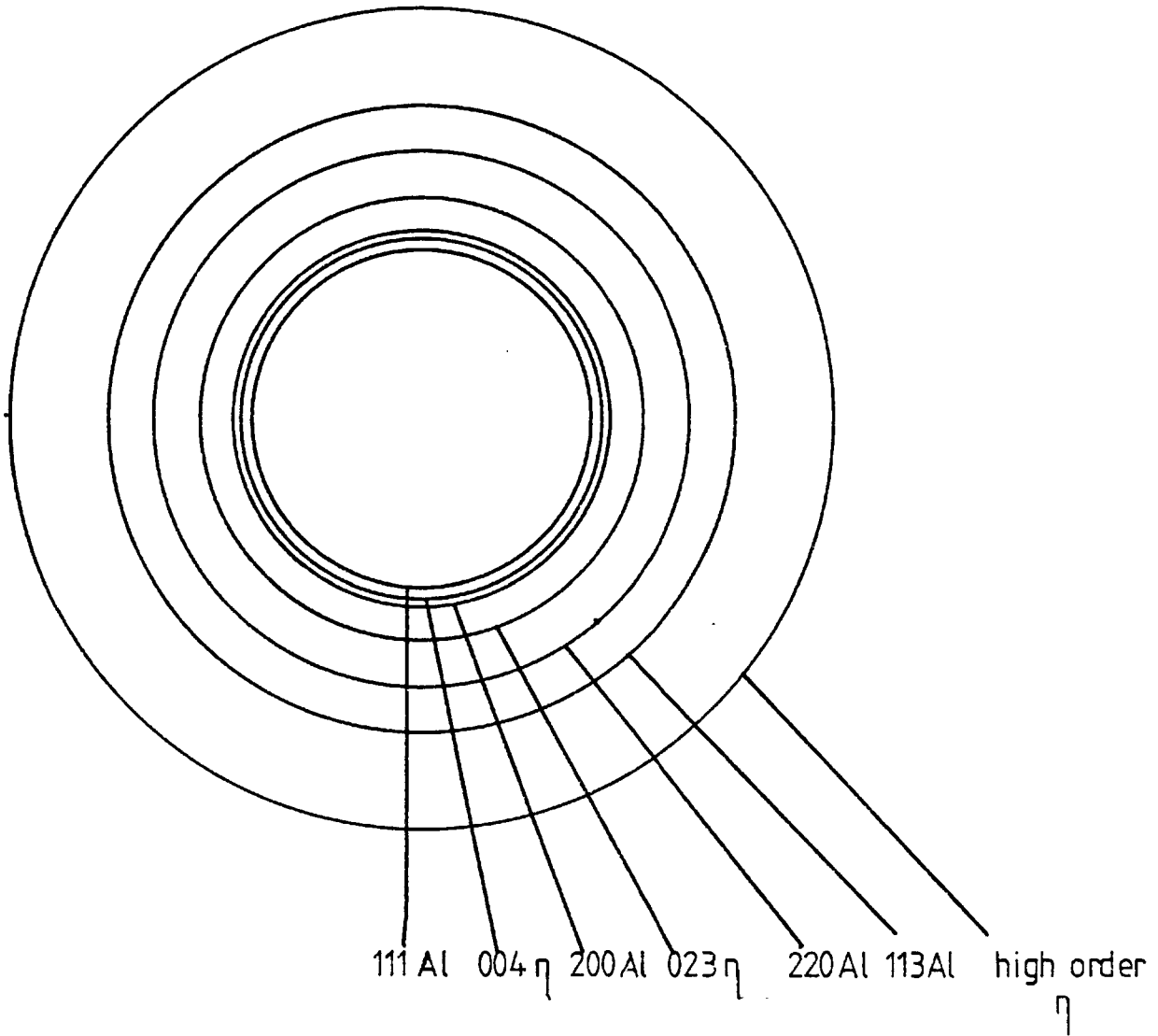
Fig. 4.25. Microbeam electron diffraction analysis of second phase particles.

(a) scanning beam pattern over entire area.

(b) micro-beam pattern from aluminium matrix  
(point (b))  $\equiv \langle 112 \rangle_{Al}$  zone axis.

(c) micro-beam pattern from particle (point  
(c))  $\equiv \langle \bar{1}2\bar{1}3 \rangle_{\eta}$  zone axis.





Analysis of SADP in Fig.4.23

comparatively large particles, principally at grain boundaries, a completely different distribution from that in the undeformed microstructure.

The specimens produced by methods which did not involve the deburring operation were found to have highly damaged burrs at the hole corner (i.e. the intersection of the hole with the specimen surface) (Fig. 4.26). The burrs were often found to be cracked at many points around the circumference but, in many cases, were almost continuous such that they formed an integral part of the test piece. These burrs were completely removed by the deburring operation to be replaced by a rounded corner, radius  $\approx 200\mu\text{m}$ , with a high quality surface akin to that of the reamed hole bores.

## 2.2 Fatigue Test Results.

The results of the fatigue testing programme are summarised in Tables 4.I to 4.V. Here, the number of cycles to failure is tabulated for each test, together with the peak applied stress, (Test piece codes used are as in Table 2.II). These results are then plotted in the form of S/N curves (i.e. peak applied stress versus log number of cycles to failure) (Figs. 4.27 to 4.30). The data obtained for the various hole preparations is then plotted in a series of comparative curves in order to allow direct assessment of the effect of hole preparation on fatigue life (Figs. 4.31 to 4.35). The S/N curves for the two A.G.A.R.D. hole qualities are shown in Fig. 4.31 and clearly a great improvement in fatigue life was found to exist in the high quality case. The improvement was observed over the whole range of peak stress with a shift in fatigue limit (peak stress for infinite life) from approximately 125 to 170 MPa, measured to the middle of each scatter band. Since both the reaming and deburring operations were involved in the production of the high quality holes (type RD) no conclusions could be made from these results about the relative importance of the two processes.

The effect of deburring was, however, demonstrated by the comparison of specimen type RD (A.G.A.R.D. high quality) with R and type DD with D (A.G.A.R.D. low quality) respectively (Figs 4.32 and 4.33). The deburring process was found to

Fig. 4.26. SEM observations of hole corner topography demonstrating the effect of deburring.

(a) deburred hole.

(b) non-deburred corner.

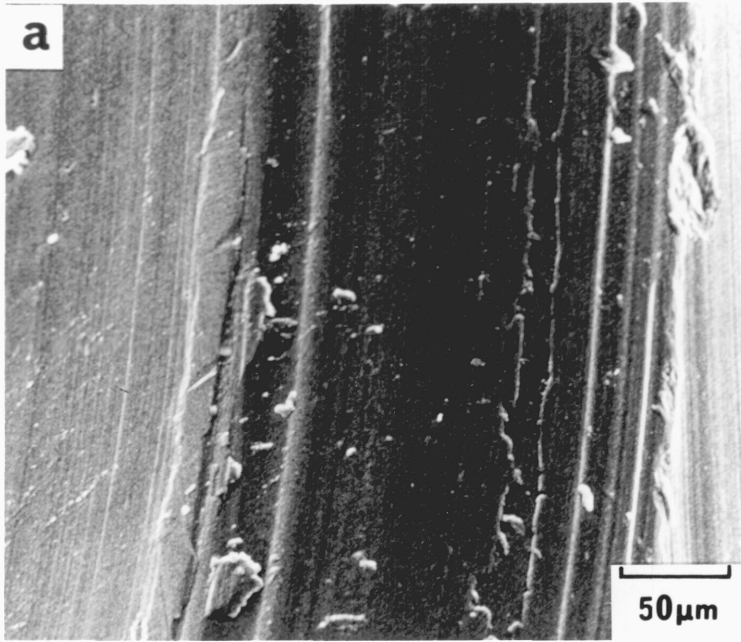


Table 4.I Specimen Type D - A.G.A.R.D. Low Quality Testing Details.

Specimen Number	Peak Stress MPa	Number of Cycles to Failure	Site of Crack Initiation
A I	130	Ran on	----
A 3	175	138 x 10 <sup>3</sup>	Corner
A 5	130	478 x 10 <sup>3</sup>	Corner
A 7	175	70 x 10 <sup>3</sup>	Corner
A 9	130	Ran on	----
A II	175	92 x 10 <sup>3</sup>	Corner
A I3	150	103 x 10 <sup>3</sup>	Corner
A I5	175	90 x 10 <sup>3</sup>	Corner
A I7	150	100 x 10 <sup>3</sup>	Corner
A I9	175	187 x 10 <sup>3</sup>	Corner
A 2I	150	229 x 10 <sup>3</sup>	Corner
A 23	175	113 x 10 <sup>3</sup>	Corner
A 25	150	215 x 10 <sup>3</sup>	Corner
A 27	175	84 x 10 <sup>3</sup>	Corner
A 29	150	478 x 10 <sup>3</sup>	Corner

All stresses shown are net mean section at hole.

Table 4.II Specimen Type RD - A.G.A.R.D. High Quality Testing Details.

Specimen Number	Peak Stress MPa	Number of Cycles to Failure	Site of Crack Initiation
A 2	150	$4.67 \times 10^6$	Bore
A 4	175	$849 \times 10^3$	Bore
A 6	150	Ran on	----
A 8	175	Ran on	----
A 10	200	$251 \times 10^3$	Bore
A 12	175	$16.3 \times 10^6$	Bore
A 14	200	$575 \times 10^3$	Corner
A 16	175	Ran on	----
A 18	200	$6.31 \times 10^6$	Corner
A 20	175	Ran on	----
A 22	200	$2.09 \times 10^6$	Corner
A 24	175	Ran on	----
A 26	200	$3.98 \times 10^6$	Bore
A 28	175	$2.89 \times 10^6$	Bore
A 30	200	$954 \times 10^3$	Corner

Table 4.III The Influence of Deburring on Life of Reamed Specimens, Testing Details.

Specimen Type	Specimen Number	Peak Stress MPa	Number of Cycles to Failure	Site of Crack Initiation
R	B I	175	$100 \times 10^3$	Corner
R	B 2	175	$135 \times 10^3$	Corner
RD	B 3	175	$93 \times 10^3$	Corner
R	B 4	175	$33 \times 10^3$	Corner
RD	B 5	175	$6.5 \times 10^6$	Bore
R	B 6	175	$229 \times 10^3$	Corner
RD	B 7	175	Ran on	----
R	B 8	175	$95 \times 10^3$	Corner
RD	B 9	175	Ran on	----
R	B 10	175	$175 \times 10^3$	Corner

Table 4.IV Specimen Type R - Testing Details.

Specimen Number	Peak Stress MPa	Number of Cycles to Failure	Site of Crack Initiation
B 11	150	Ran on	----
B 12	150	$553 \times 10^3$	Corner
B 13	150	Ran on	----
B 14	150	$208 \times 10^3$	Corner
B 15	150	Ran on	----
B 16	200	$56 \times 10^3$	Corner
B 17	200	$64 \times 10^3$	Corner
B 18	200	$39 \times 10^3$	Corner
B 19	200	$105 \times 10^3$	Corner
B 20	200	$65 \times 10^3$	Corner

Table 4.V Specimen Type DD - Testing Details.

Specimen Number	Peak Stress MPa	Number of Cycles to Failure	Site of Crack Initiation
C I	175	Ran on	----
C 2	200	526 x 10 <sup>3</sup>	Bore
C 3	200	684 x 10 <sup>3</sup>	Bore
C 4	175	Ran on	----
C 5	200	345 x 10 <sup>3</sup>	Bore
C 6	200	2.16 x 10 <sup>6</sup>	Bore
C 7	200	103 x 10 <sup>3</sup>	Bore
C 8	175	155 x 10 <sup>3</sup>	Bore
C 9	200	2.27 x 10 <sup>6</sup>	Bore
C 10	175	Ran on	----
C 11	190	636 x 10 <sup>3</sup>	Bore
C 12	190	300 x 10 <sup>3</sup>	Bore
C 13	190	133 x 10 <sup>3</sup>	Bore
C 14	190	3.54 x 10 <sup>6</sup>	Bore
C 15	190	Ran on	----
C 16	190	1.11 x 10 <sup>6</sup>	Bore
C 17	225	94 x 10 <sup>3</sup>	Corner
C 18	225	98 x 10 <sup>3</sup>	Bore
C 19	225	54 x 10 <sup>3</sup>	Bore
C 20	225	248 x 10 <sup>3</sup>	Bore
C 21	225	98 x 10 <sup>3</sup>	Bore

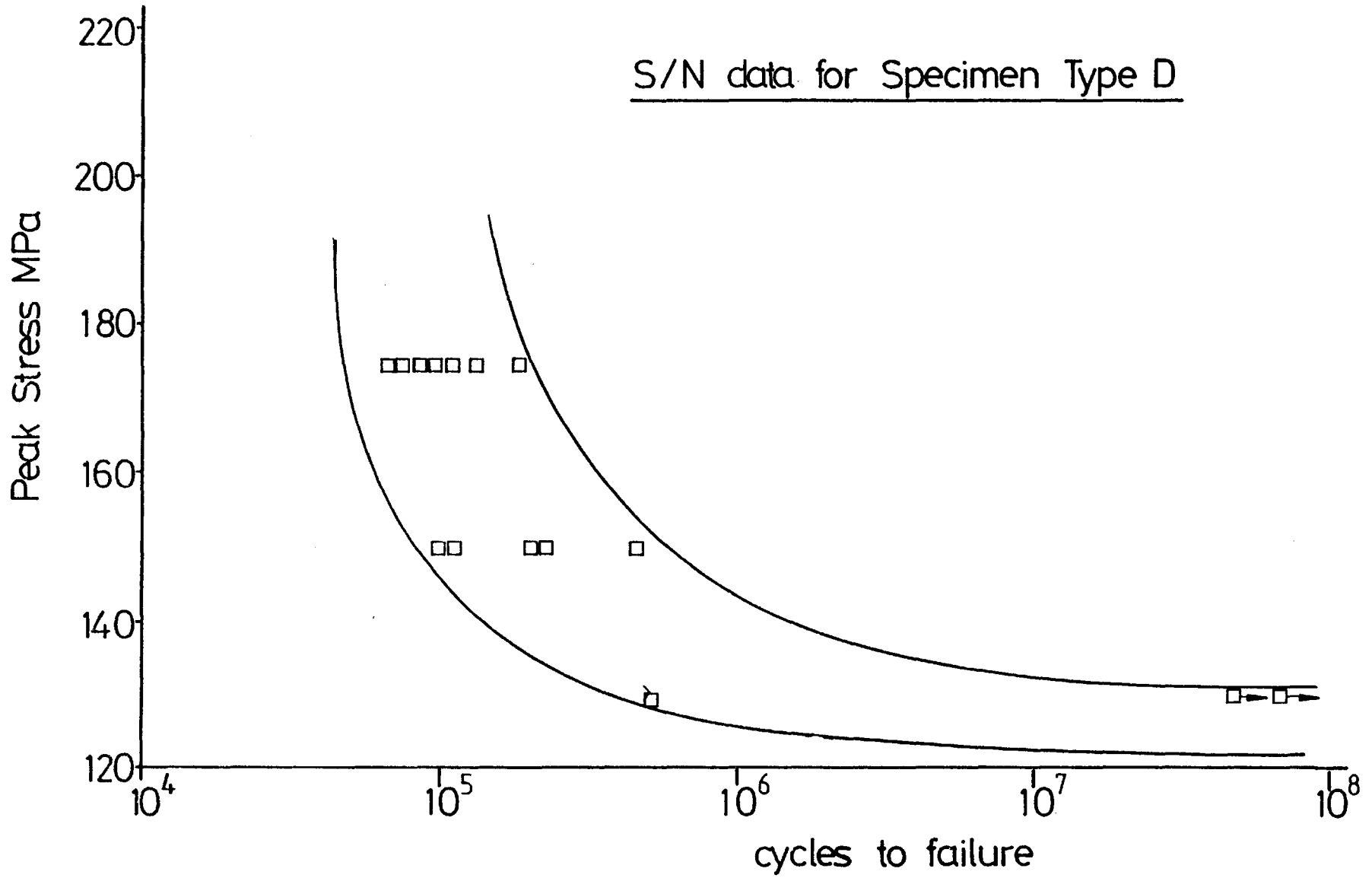


Fig. 4.27

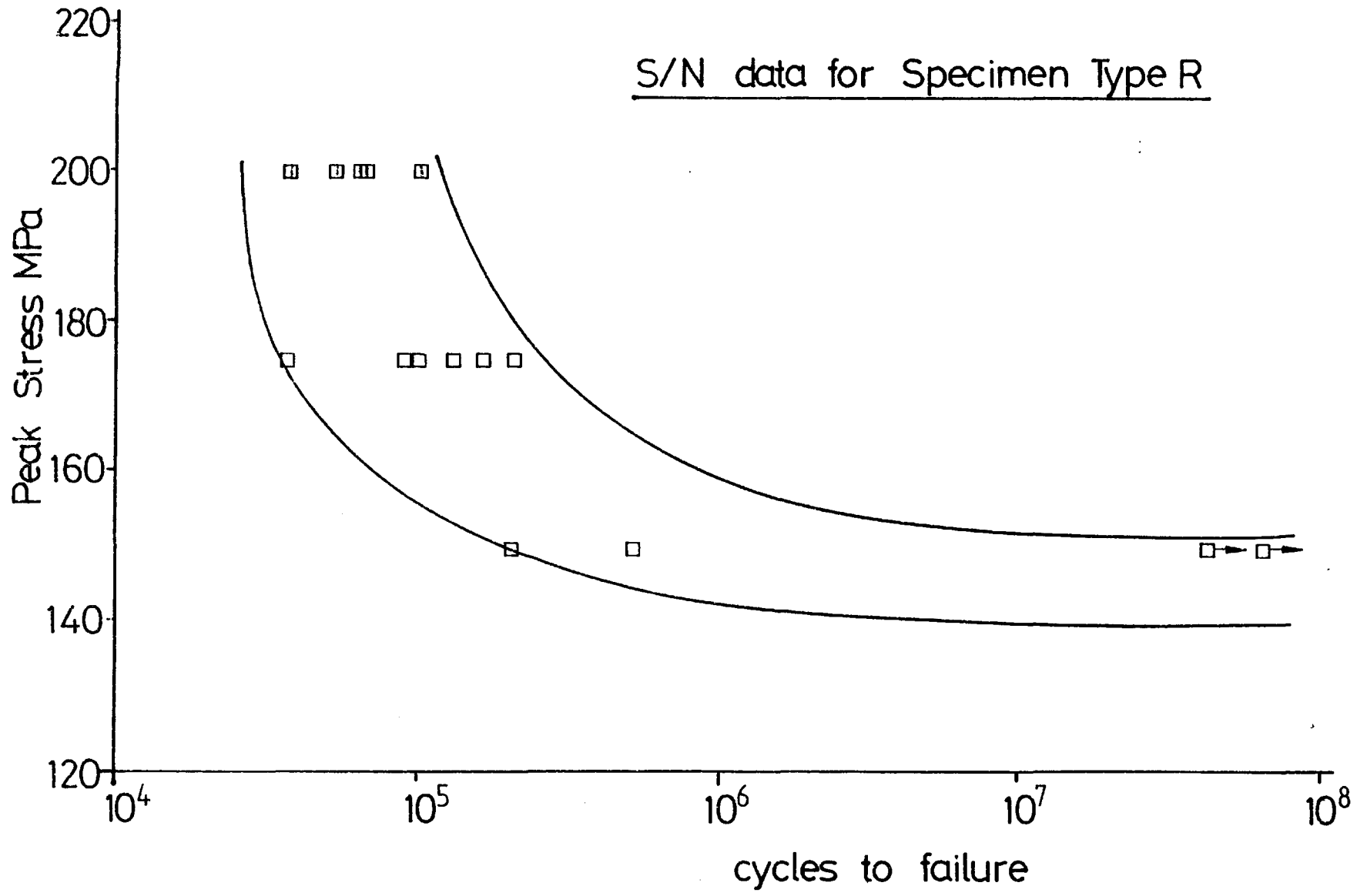


Fig. 4.28



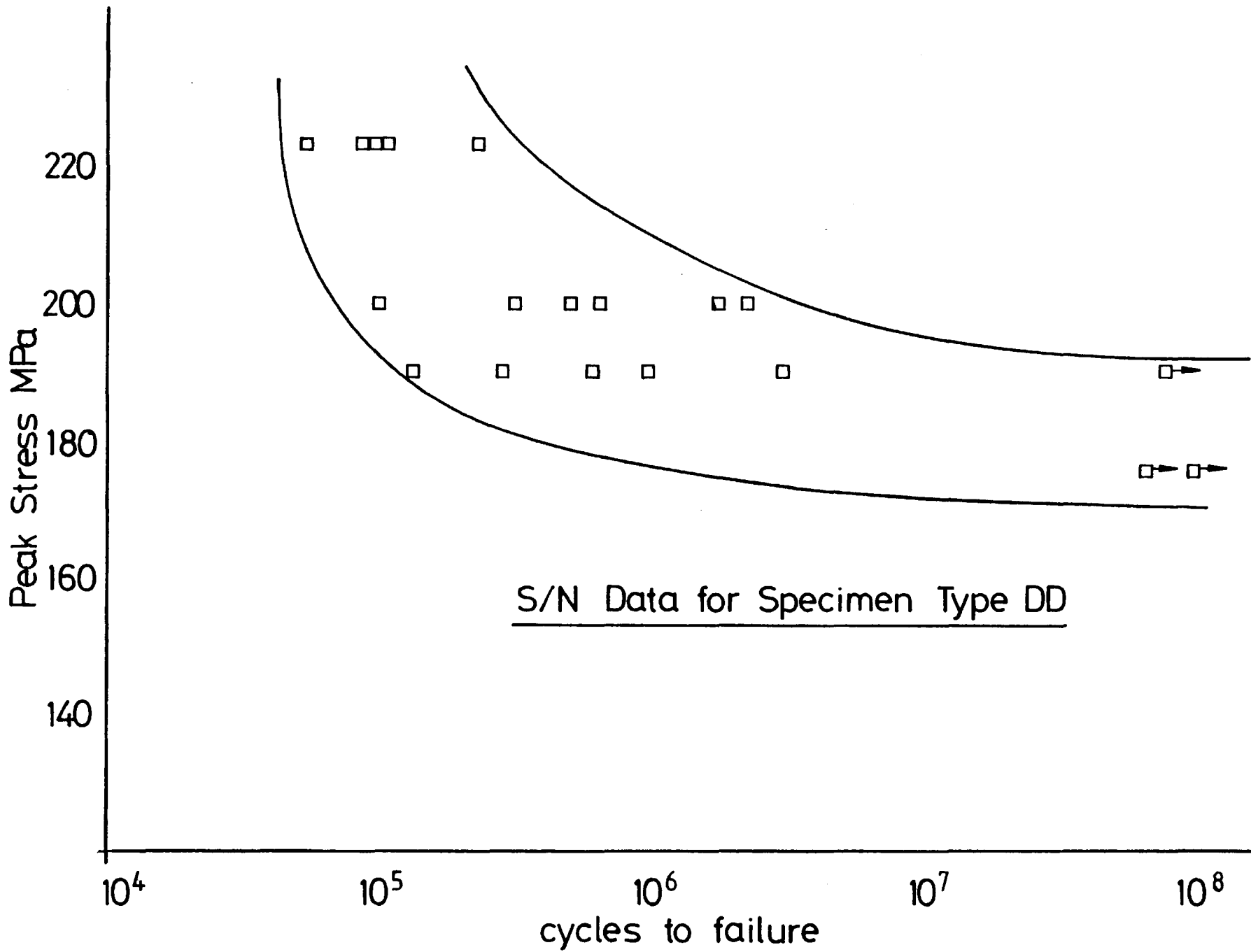
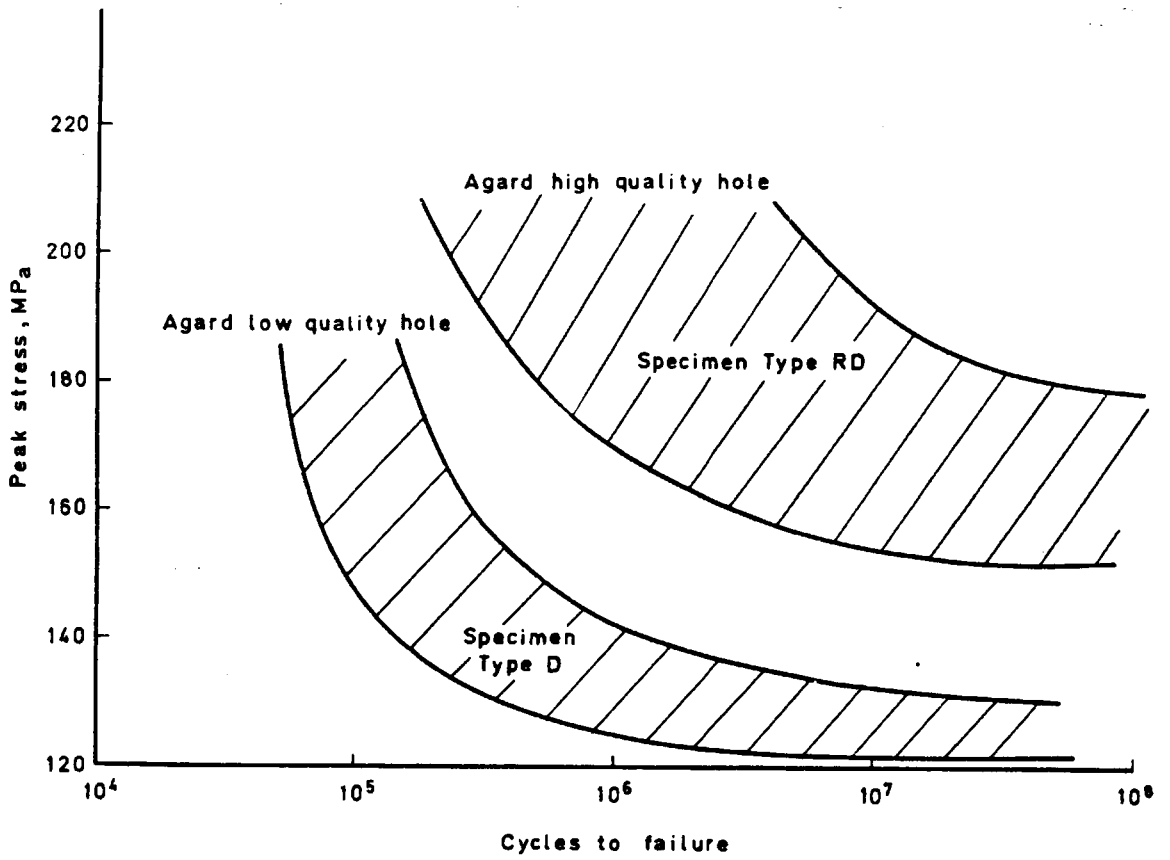
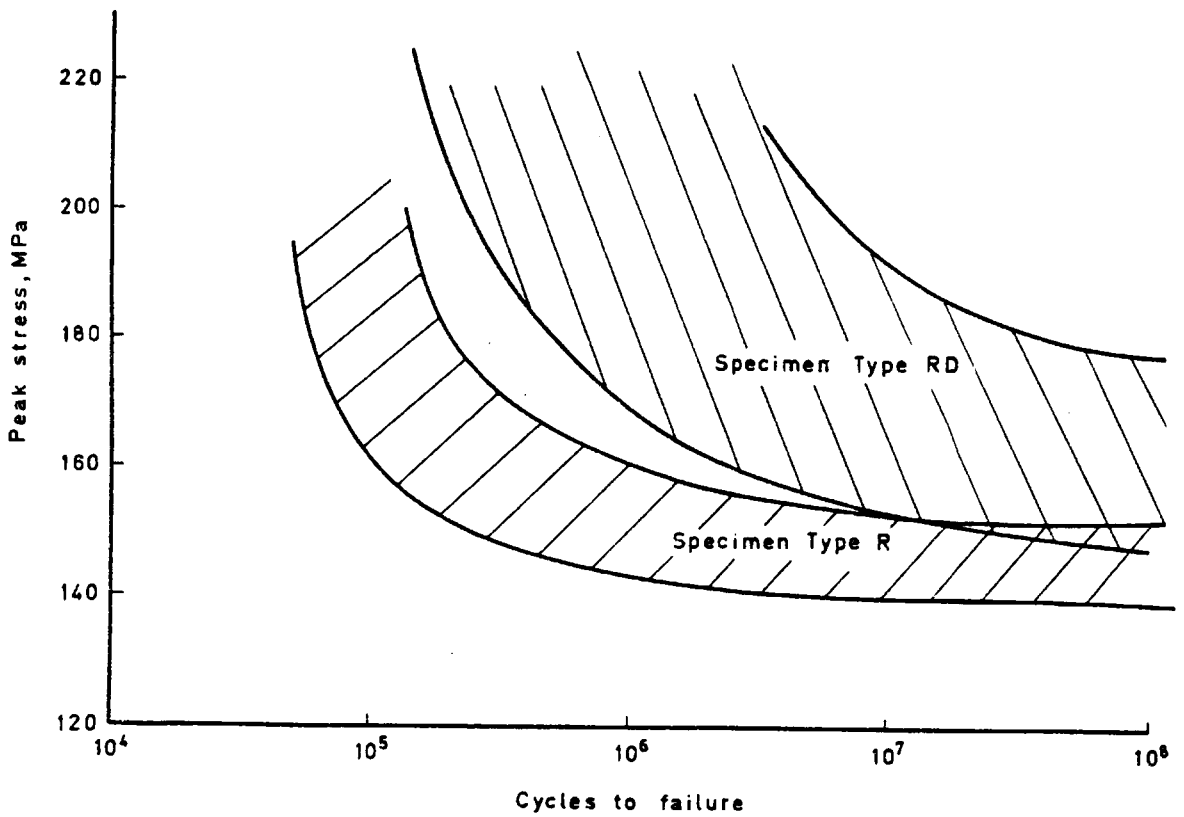


Fig.4.31



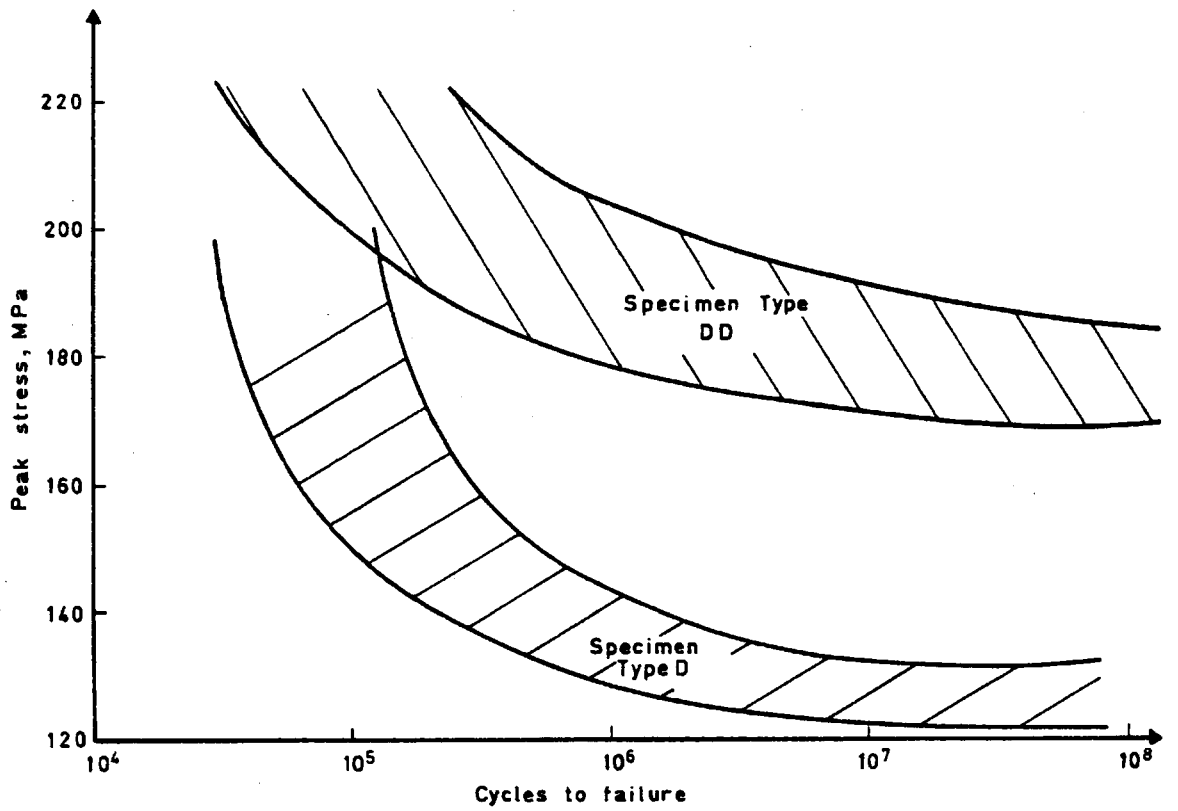
Comparison of S/N data, Specimen types RD and D

Fig.4.32



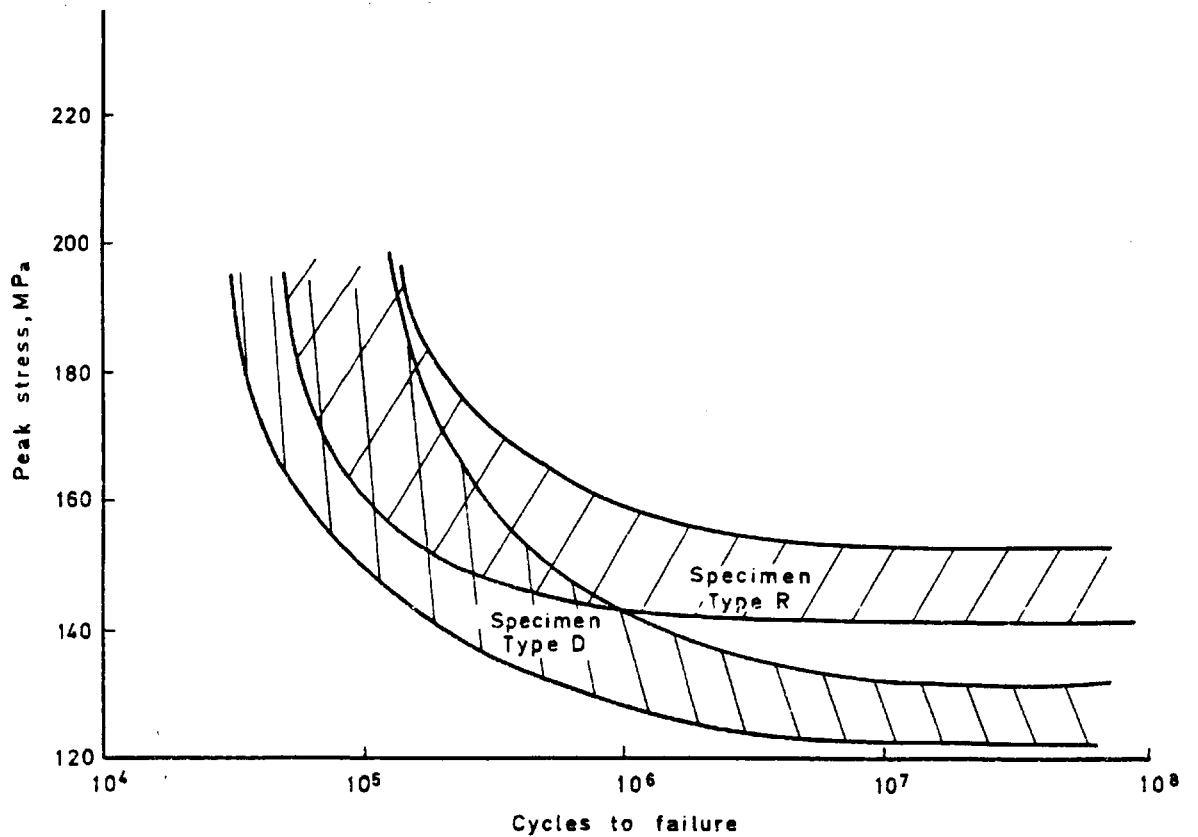
Comparison of S/N data, Specimen types RD and R

Fig.4.33



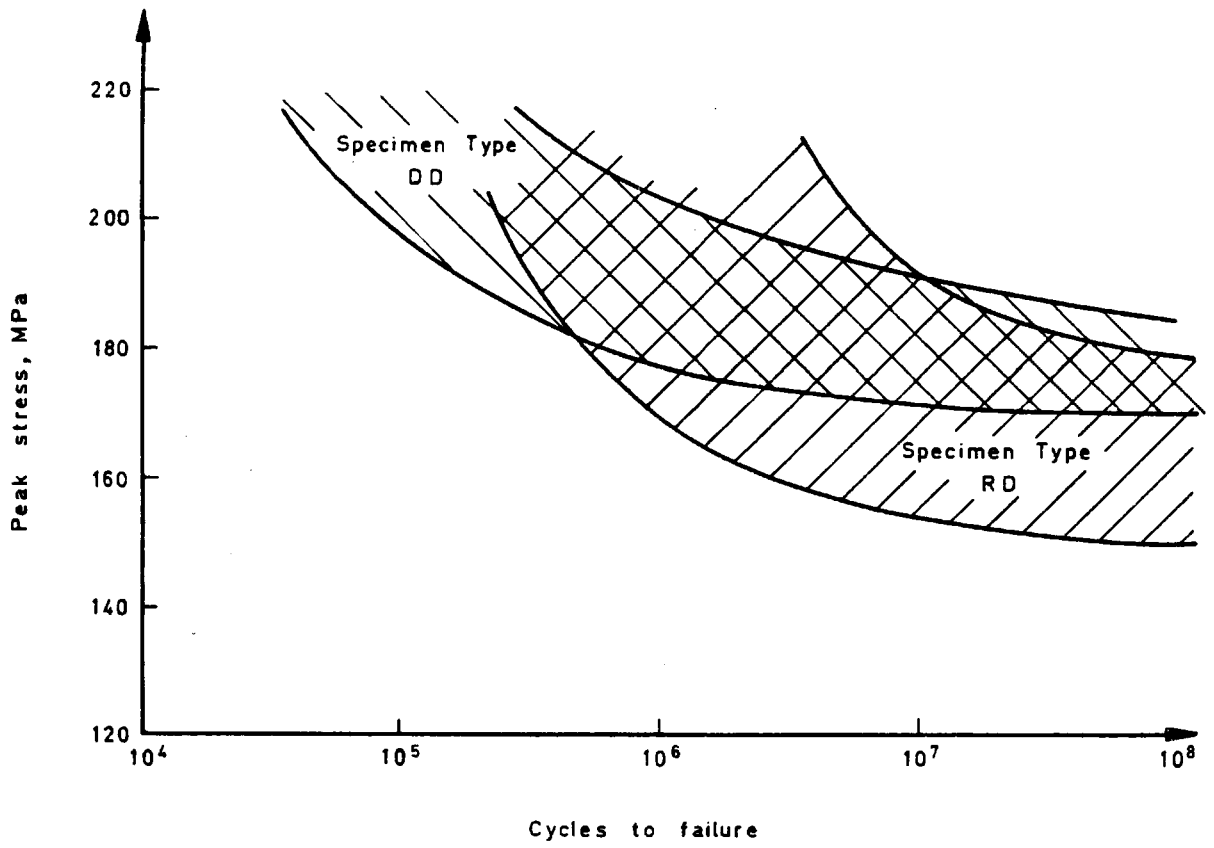
Comparison of S/N data, Specimen types DD and D

Fig.4.34



Comparison of S/N data, Specimen types D and R

Fig. 4.35



Comparison of S/N data, Specimen types DD and RD

have a marked beneficial effect on fatigue life in both cases with corresponding increases in fatigue limit. The effect was particularly marked in the drilled case (Fig. 4.33) with an increase from 130 to 180 MPa. Since results were obtained here from specimen batches produced at different times it was felt necessary to confirm the results by the deburring of reamed specimens from the same batch (Table 4.III). Once again, a large difference in life was observed at the peak stress chosen, 175 MPa, and deburred specimens were found to have lives similar to those in specimens of the same type in an earlier batch. (Table 4.II).

Specimens of both drilled and reamed types which did not undergo the deburring process showed more similar fatigue properties but some differences were noted, Fig. 4.34, specimens of type D being slightly inferior to those of type R.

Clearly since the deburring operation was found to dominate fatigue life any appraisal of the effects of bore surface preparation must be made by comparison of results obtained from deburred specimens. The results are shown in Fig. 4.35. Fatigue lives were generally found to be similar in the two cases over the whole range of applied stress although specimens of type DD were found to show a small improvement in fatigue limit of around 10 MPa.

### 2.3. Fractographic Observations.

All fatigue specimens which failed were routinely observed under the optical microscope and the position of the crack initiation site recorded. A very clear difference in position was noted between deburred and undeurred specimens. In undeurred specimens fatigue cracks were found in all cases to initiate at the hole corner, i.e. the intersection of the hole with the specimen surface (Tables 4.I and 4.IV). In the deburred cases cracks were found on a few occasions to initiate at the hole corner but the majority were found to initiate at a point along the hole bore (Tables 4.II and 4.V). In the case of specimen type RD bore initiation was found at low applied stress, but at the highest stress used, 200MPa, corner initiation was prevalent.

Observation of crack initiation sites in the SEM demonstrated clearly the involvement of corner burrs in initiation in specimens type D and R (Fig 4.36 (a) and (b)). Fig. 4.36 (c) and (d) show a specimen which was observed without breaking open. It is apparent, particularly in the stereo pair, that the burr was notched prior to testing and that crack initiation subsequently occurred at this point.

Fractographic observation of deburred specimens revealed quite different initiation behaviour and it was possible to determine the effect of hole surface quality on initiation. In the case of specimens type RD the initiation sites were generally found to be associated with large inclusions in the size range 5 to 50 $\mu$ m (Fig. 4.37). In many cases particle debonding appeared to have occurred leading to the inclusion remaining intact on one of the fracture surfaces (Fig. 4.37 (b) and (c)). However in some cases cracking of particles was observed (d).

Bore crack initiation in drilled specimens was not found to be associated with intermetallic particles. Here, multiple crack initiation was observed in approximately 25% of tests, this was rarely found in reamed specimens. Initiation sites were generally found to be associated with surface machining damage (Fig. 4.38). This damage varied in appearance from apparent areas of folding and smearing, (a) and (c), to others which appeared to be particles of some kind embedded in the surface (b). No initiation sites were found which could be associated with subsurface intermetallics as observed in type RD specimens.

While crack initiation did not appear to occur subsurface in type DD, in many cases a surface layer 10 to 50 $\mu$ m in depth was observed within which fracture morphology appeared to be quite different (Fig. 4.39). This layer was not observed adjacent to reamed hole surfaces.

As mentioned earlier crack initiation occurred in the majority of deburred cases along the hole bore. However, in a limited number of cases initiation sites were found at the hole corner but the fractography was quite different from non-deburred cases (Fig. 4.40). The initiation sites were not generally

Fig. 4.36. SEM observations demonstrating the involvement of corner burrs in crack initiation.

- (a) fatigue crack origin with associated burr, specimen type R.
- (b) as above, specimen type D.
- (c) specimen observed without breaking open, showing that a prior burr defect, arrowed, had resulted in initiation at that point.
- (d) stereo pair of area in (c).

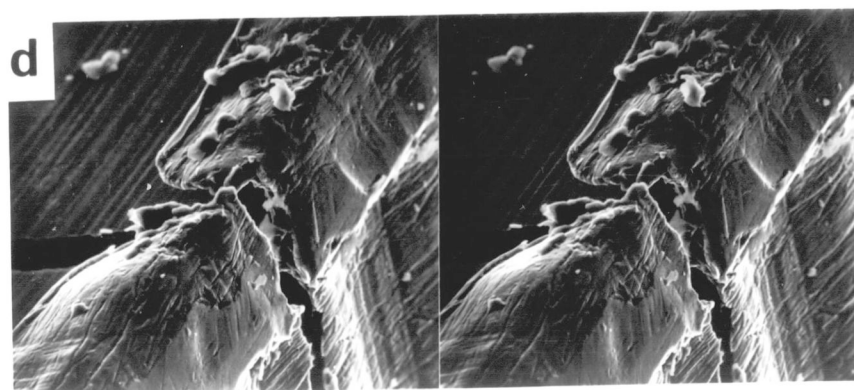
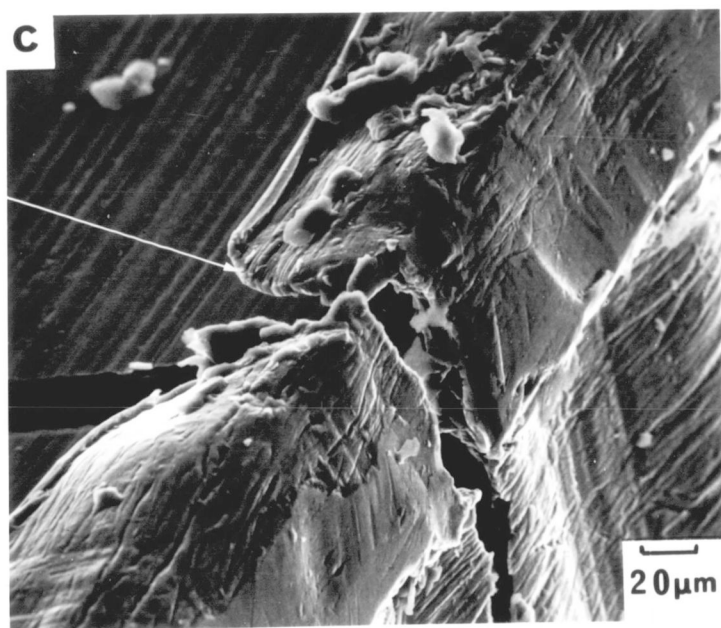
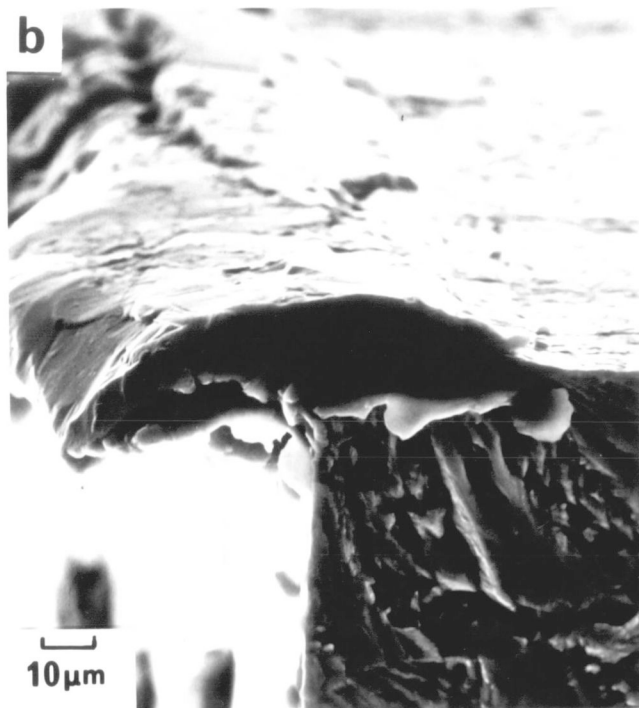
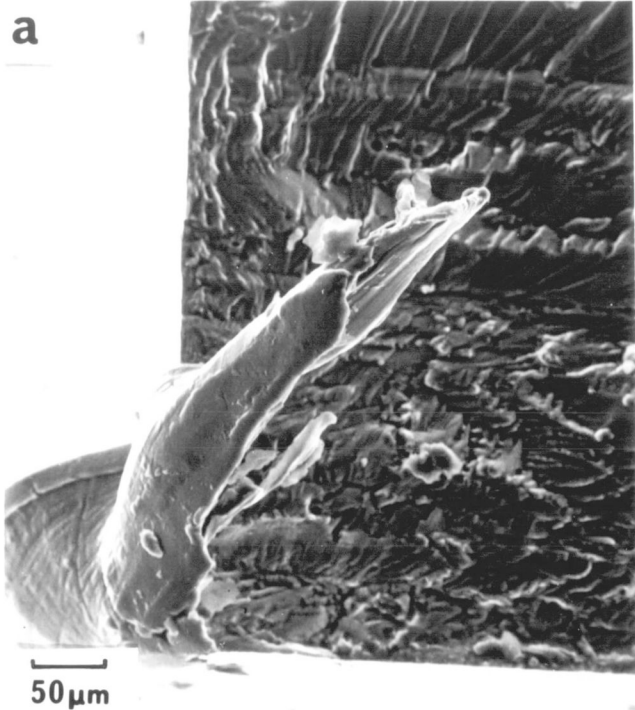


Fig. 4.37. SEM observations of crack initiation in specimens of type RD.

- (a) initiation site associated with large inclusion.
- (b) detail of above.
- (c) debonded inclusion at initiation site.
- (d) cracked inclusion acting as site for initiation.

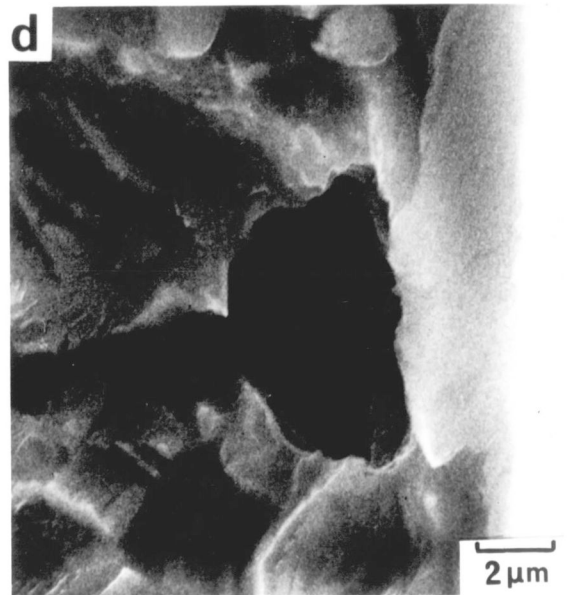
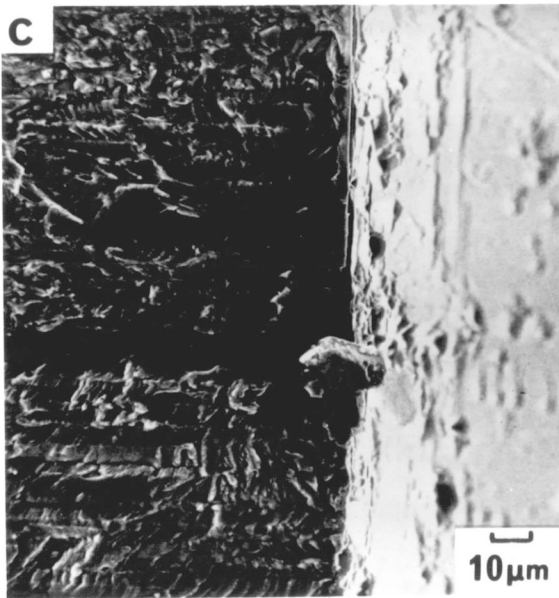
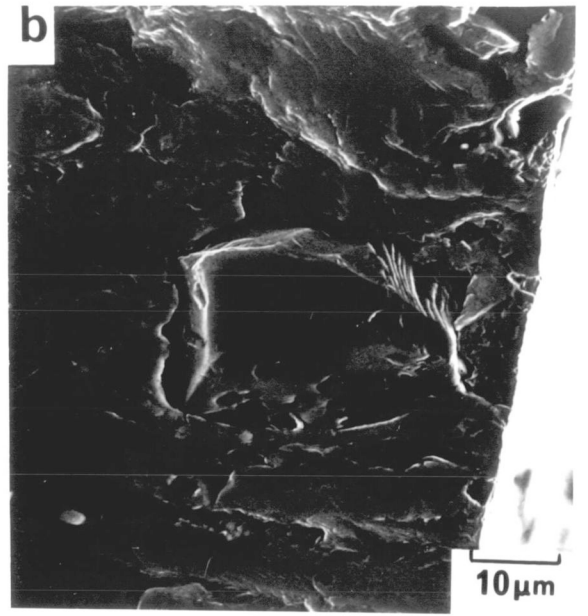
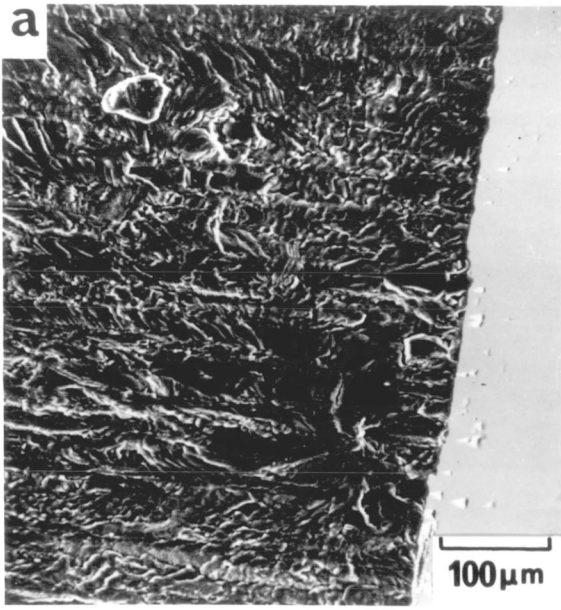


Fig. 4.38. Crack initiation sites in specimens of type DD, demonstrating the involvement of surface machining defects.

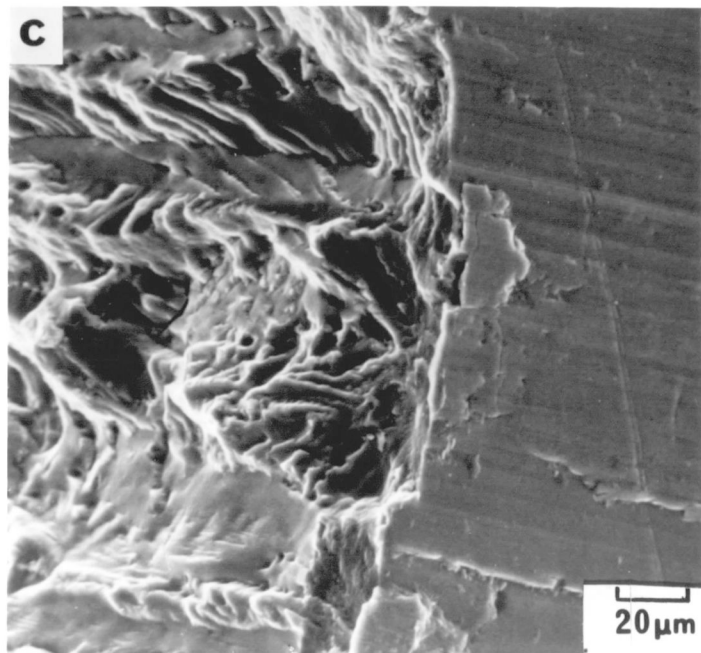
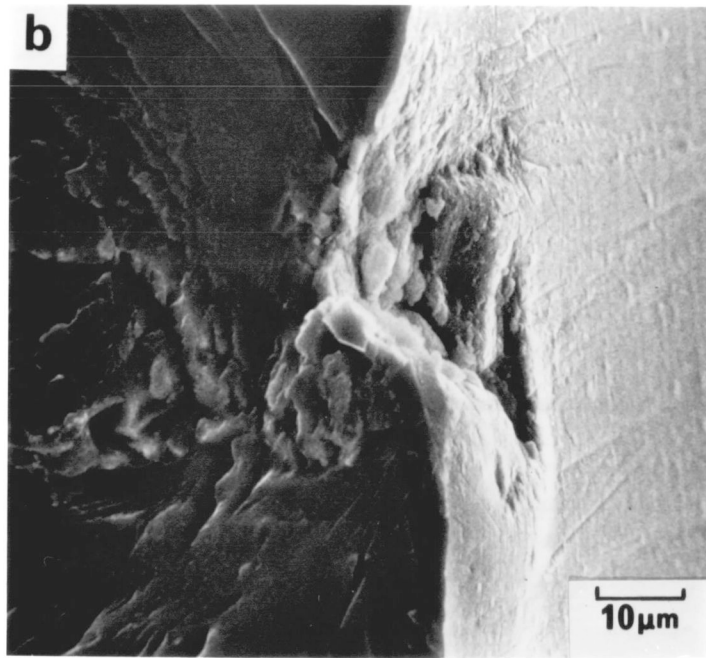
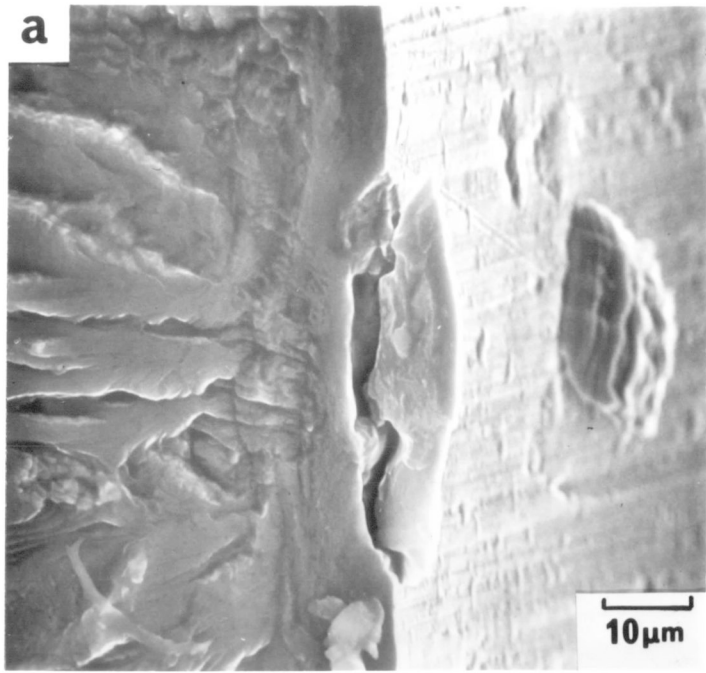


Fig. 4.39. Fractographic observations in region adjacent to initiation site in specimen type DD: Note differences in fractographic appearance in layer 10→20 $\mu$ m in depth (arrowed).

Stereo pair of the above.

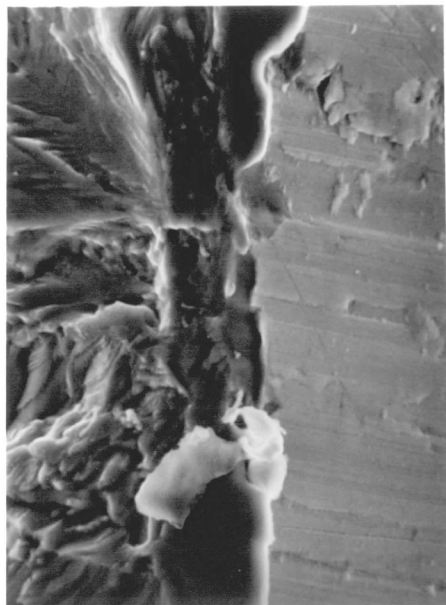
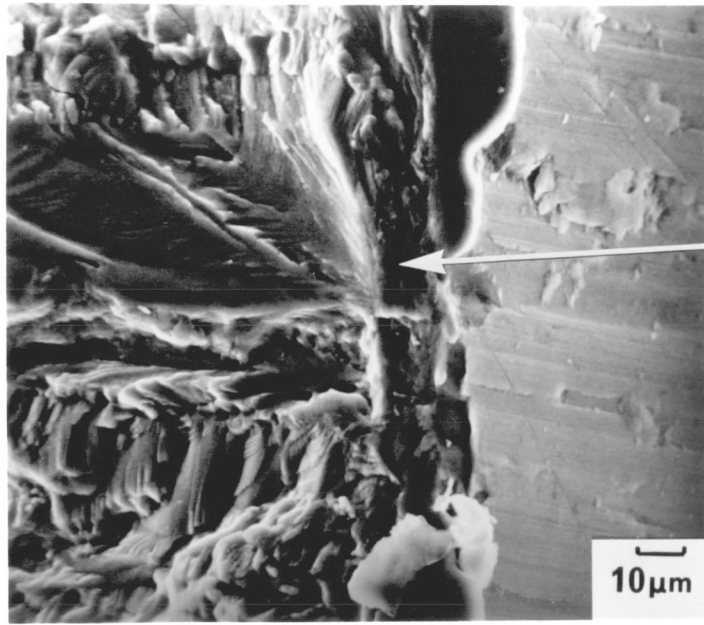
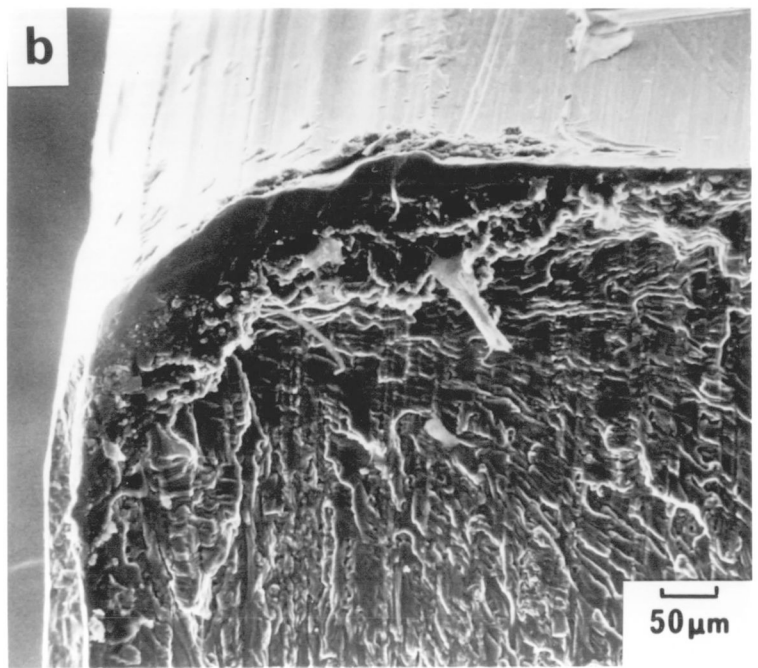
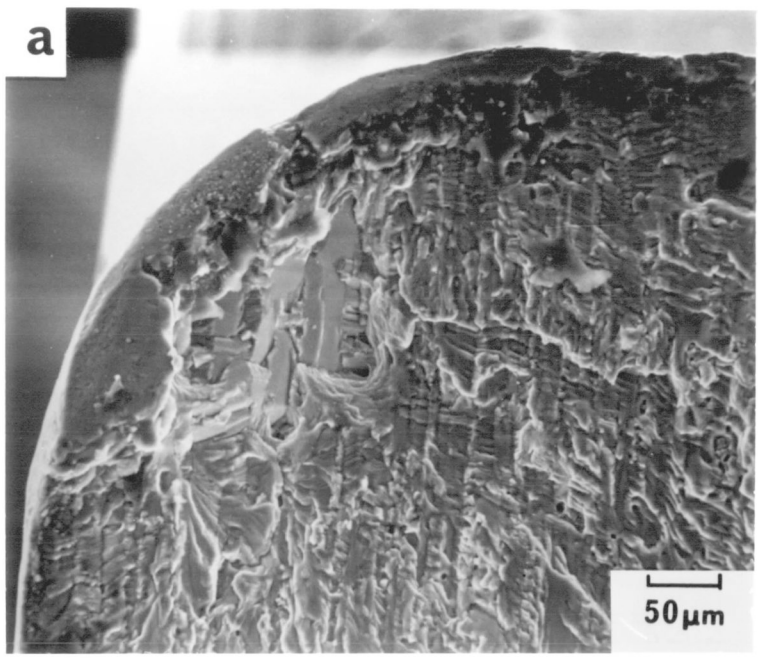


Fig. 4.40. Crack initiation at hole corner in deburred specimens

(a) type RD.

(b) type DD.



associated with any particular features but often showed a well defined surface lip with apparently subsurface initiation.

#### 2.4. Microcrack Growth.

The use of the high resolution SEM facility allowed the measurement of crack growth rate, via striation spacing, to be carried out at very short crack lengths. It was possible to detect striations with as small a spacing as  $0.04\mu\text{m}$ . By measuring these spacings at calibrated crack lengths (in the case of cracks initiated at the hole bore) it was possible then to relate the growth rate to stress intensity, via the stress intensity calibration detailed in Appendix I. Stress intensity was calibrated according to the maximum and minimum possible solutions given in Fig.AI in Appendix I. 2 different stress levels were chosen, 175 and 225 MPa, with both drilled and reamed surface preparations.

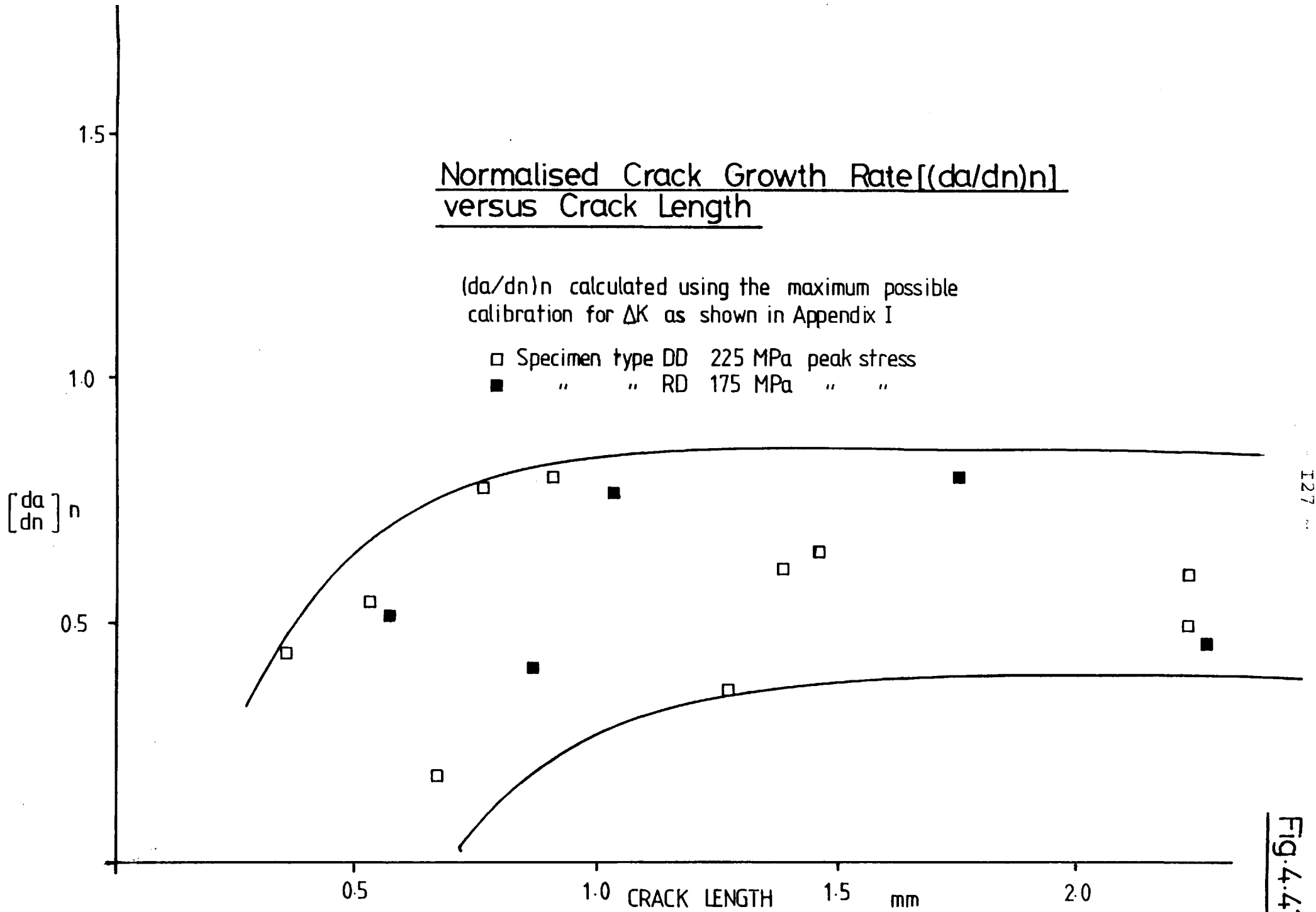
In the crack propagation study, striation spacing data were obtained over accurately determined stress intensity ranges ( $\Delta K$ ) (at a stress ratio  $R$  of 0.1) for long cracks i.e.  $>I_{cm}$  in length (Fig.5.5I) and therefore crack growth rates could be predicted for short crack lengths by extrapolation. The predicted and actual growth rates were then compared via the calculation of 'normalised' crack growth rate,  $x$ , which equals the measured value divided by the predicted growth rate. These results were then plotted against crack length. The results are shown in Figs. 4.4I and 4.42 for both the maximum and minimum stress intensity solutions. Clearly at long crack length the normalised growth rate should tend to 1, the fact that it was found to be somewhat less than 1 in the maximum case and greater than 1 in the minimum case can be attributed to inaccuracy in the stress intensity calibration at long crack lengths. In both cases however, the normalised crack growth rates showed a decrease at less than  $I_{mm}$ , implying that cracks of lengths less than  $I_{mm}$  were growing at rates lower than that predicted by linear elastic fracture mechanics, at least where striation spacing was taken as a method of growth rate measurement. The results did not show any variation with stress level. The specimen tested at 175 MPa peak stress showed identical results (within the large scatter) to those obtained from the specimen tested at 225 MPa.

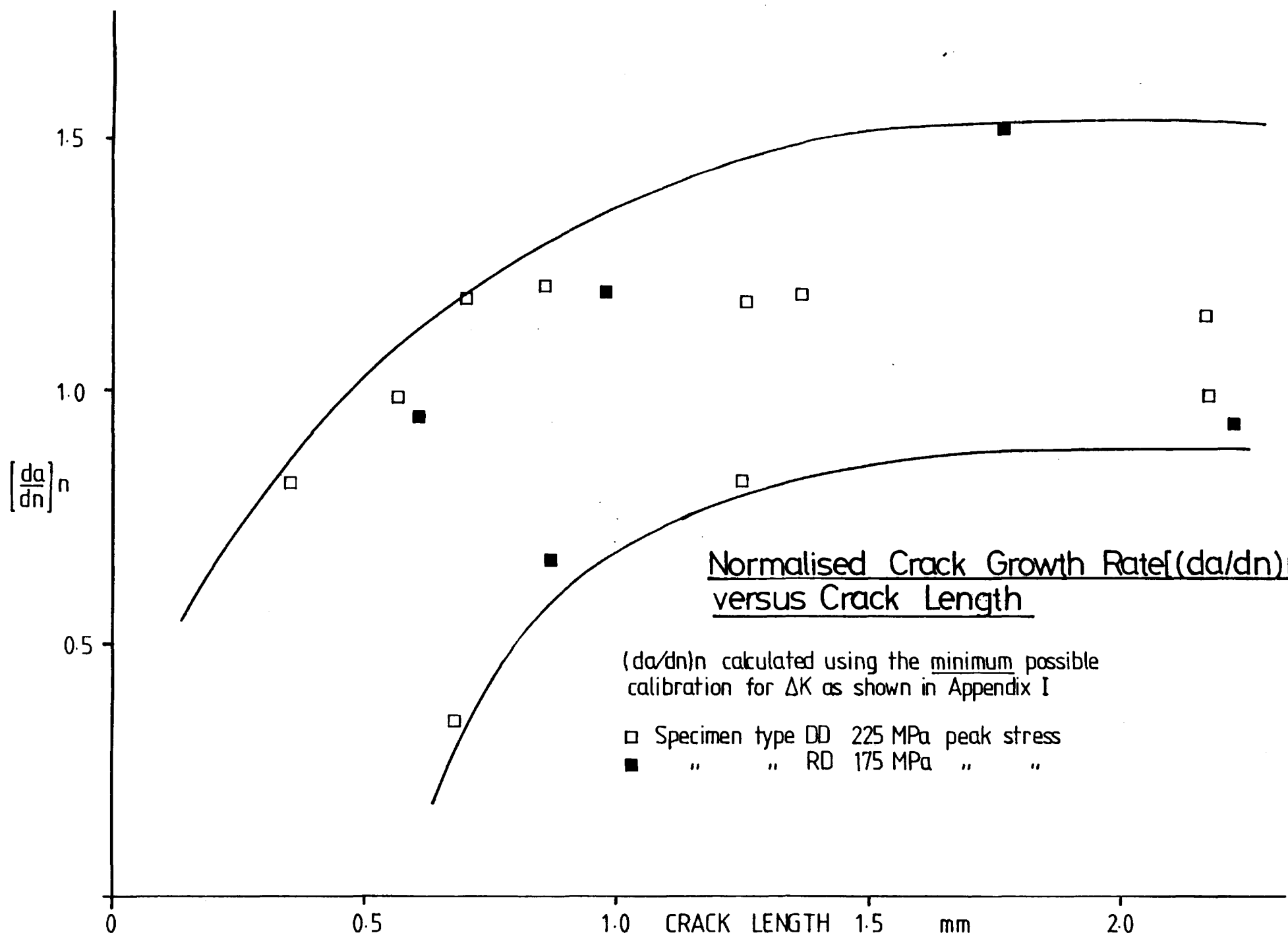
# Normalised Crack Growth Rate $[(da/dn)^n]$ versus Crack Length

$(da/dn)^n$  calculated using the maximum possible  
calibration for  $\Delta K$  as shown in Appendix I

- Specimen type DD 225 MPa peak stress
- " " RD 175 MPa " "

$[(da/dn)^n]$





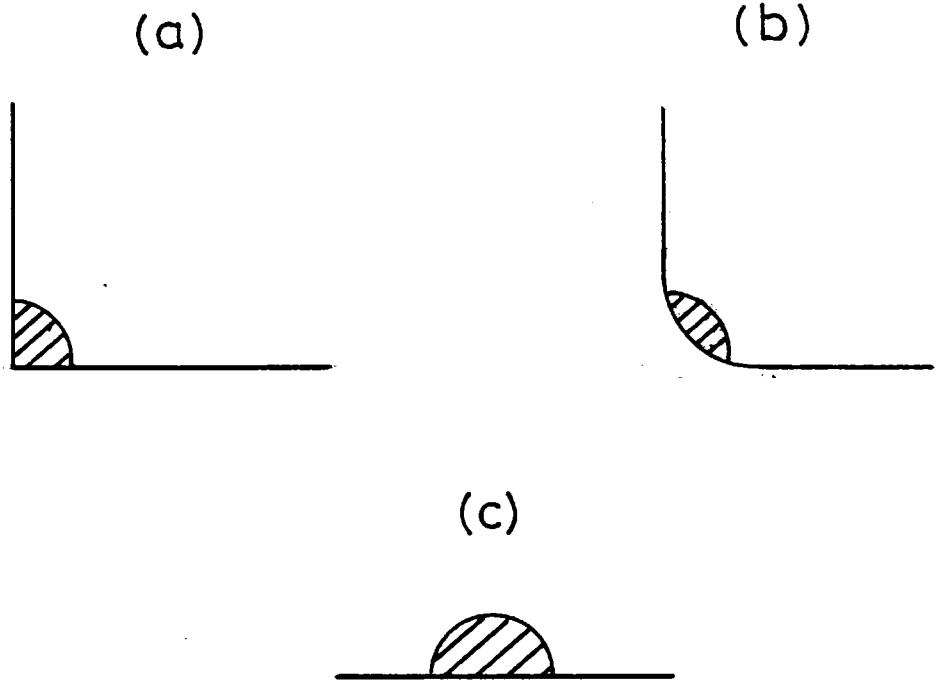
### 3. DISCUSSION.

#### 3.1 The Role of Hole Surface Topography in Fatigue Crack Initiation.

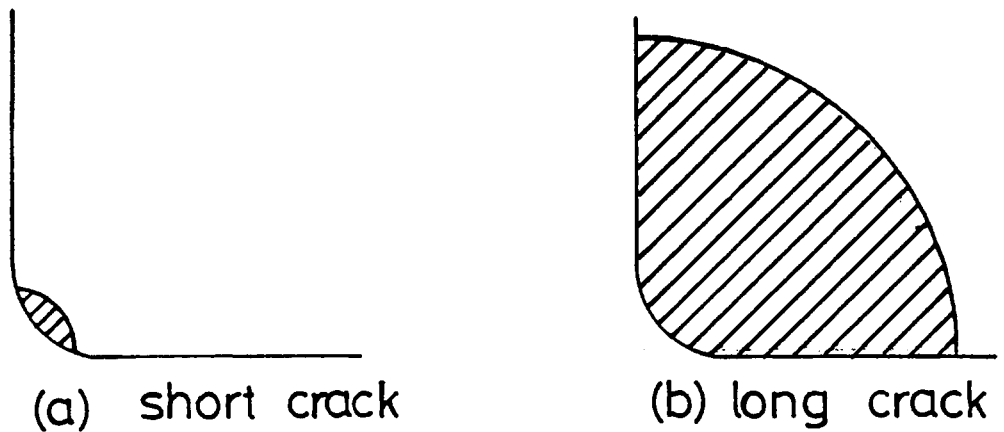
The large differences in fatigue life observed between test pieces with corner burrs and those having undergone the deburring operation (Figs. 4.32 , 4.33 ) would indicate that the deburring process has a dominating effect on crack initiation. The deburring operation used was demonstrated by SEM observation to have two effects on the hole corner topography: Firstly, the burrs were removed and secondly, a radiused corner was produced, radius equivalent to that of the cutting tool ( $\approx 200\mu\text{m}$ ), leading to a shape change at the corner.

The change in shape from right angle to radiused corner might be expected to have an effect on initiation via its effect on stress intensity at the tip of a microcrack. Consider a microcrack adjacent to the surface in the three different situations as shown in Fig. 4.43 . As calculated in Appendix I the crack tip stress intensity for the three crack configurations shown would be slightly different at equivalent crack lengths. This would be particularly the case between situations (a) and (c), (a) being higher owing to the influence of the two free surfaces on the crack. Situations (b) and (c) would be approximately equivalent, at least at short crack lengths where the radiused corner could be considered to be a plane surface. The result of this would be higher microcrack growth rates in situation (a) and therefore an overall reduction in fatigue life. It is possible to estimate the significance of the effect from the calculations in Appendix I: The maximum difference in crack tip stress intensity was calculated to be  $\approx 12\%$  between (a) and (c). It must also be emphasised that the effect would only be significant at very short crack lengths of the order of the corner radius (Fig. 4.44 ). Clearly at longer crack lengths the effect would be negligible.

A method of appreciating the size of the effect could be to use the minimum defect size analysis of Talug and Reifsnider (59) discussed in I.4. Here the equation employed was:



Three Possible Crack Configurations



Decreasing Influence of Corner Profile  
With Increasing Crack Length

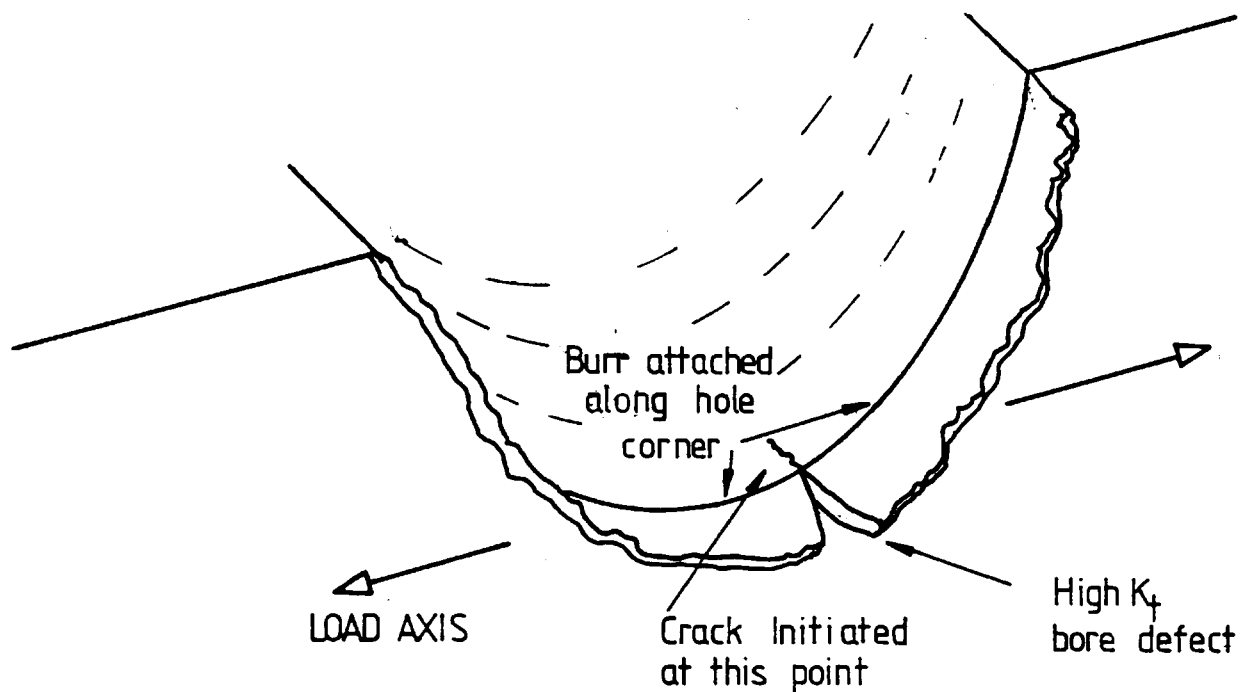
$$\Delta K_{th} = \Delta \sigma_{lim} \sqrt{\pi a_e}$$

If defects of equivalent size are considered present in the two situations and the 12% increase is taken into account in assessment of  $\Delta K_{th}$  clearly a maximum reduction in  $\Delta \sigma_{lim}$  of around 12% could be expected. Reductions in  $\Delta \sigma_{lim}$  have been observed to be from ~175MPa to 130MPa i.e. of the order of 30%. Hence the reduction in fatigue limit is very unlikely to be produced simply by a change in specimen shape.

The reduction in fatigue life must therefore be associated with the corner burrs themselves. This conclusion is certainly consistent with fractographic observations since crack initiation was found to occur exclusively at the hole corner in specimen types R and D. The burr involvement in initiation might be considered surprising since the burrs are not an integral part of the specimen itself but are regions of material attached to the corner. As noted in the SEM studies, however, burrs were found to be almost continuous around the hole corner and contained various defects (Figs.4.26, 4.36 ). A situation could then be visualised as shown in Fig.4.45 where the burr is attached over a significant length at the hole corner. The burr would in such circumstances be, to some extent, load bearing and hence a concentration of stress would be developed at the central notch in the burr shown. Such burr defects could act as extremely damaging sites from a fatigue viewpoint, since as shown in Fig.4.26 they were found to be equivalent to extremely sharp notches in many cases, notch root radius being a dominating factor as demonstrated by Pearson. Also, as demonstrated by Forsyth and Bowen (57), the orientation of such surface defects must be of great importance. Hence burr defects aligned approximately perpendicular to the stress axis would be most effective in causing a reduction in fatigue life.

Since the burrs produced at the hole corners were a result of the hole bore finishing operation some difference in initiation behaviour might be expected between test piece types R and D. A small difference was noted (Fig.4.34 ) reamed test pieces showing a slight improvement in fatigue

Fig.4.45



The Role of Burr Defects  
In Crack Initiation

properties presumably due to a reduction in the average size of the burrs.

In the case of deburred test pieces, types DD and RD, only a small difference in fatigue life was observed, the drilled (DD) showing a small improvement. Since crack initiation in those reamed (RD) was found to occur at intermetallic particles below the hole surface the surface topography itself can be considered to have no significant effect on initiation. In the drilled case, however, initiation was found to occur generally at the hole bore and here topography must be taken into consideration. Crack initiation sites appeared to be associated with the coarse markings attributed to smearing and folding, running approximately perpendicular to the finer circumferential grooves (Fig.4.38 ). These markings, owing to their geometric alignment, approximately perpendicular to the load axis, would be expected to act as preferred sites for crack initiation, due once again to the high elastic stress concentration developed. In fact the circumferential markings, observed on both drilled and reamed surfaces, would under the loading conditions used here, be expected to have little effect since they are aligned along the load axis. Hence the reaming operation, with resultant removal of the coarse transverse markings would be expected to inhibit bore initiation as generally observed. Crack initiation would then be transferred to the next most damaging defects, still under the influence of the elastic stress concentration factor due to the circular hole. In this case these were found to be most commonly intermetallic particles near to the surface.

It is perhaps rather surprising that test piece type DD showed slightly superior fatigue performance to RD, since the reaming operation removed the damaging surface smears. In order to explain this effect it is necessary to consider the influence of the boring operation on subsurface damage.

### 3.2 The Role of Subsurface Microstructural Damage in Fatigue Crack Initiation.

3.2.I Deformation Structure. Forsyth (32) in his earlier studies of hole drilling used microhardness measurements

to observe the increase in hardness in the layer adjacent to the hole (Fig. 4.1 ). In the present work similar observations were in general agreement with those of Forsyth. In the drilled case an approximately two-fold increase in hardness was observed adjacent to the hole bore, decaying to the bulk value at around 40 $\mu$ m depth. Optical metallography also revealed this deformed layer. In the reamed case a less well defined layer was found. The reaming operation removed  $\sim$ 0.25mm from the drilled hole surface and hence the original deformed layer, produced by drilling, must be completely removed by this operation. The small increase in hardness at the surface must therefore be due to the deformation occurring during reaming. It is felt that the reduction in the extent of deformation is a result of the lower feed rate and depth of cut involved in the reaming operation.

The surface layer TEM observations allowed the marked surface hardening to be related to deformation structure. Particularly in the case of unlubricated drilling operations evidence was found for a great increase in surface temperature during drilling (Fig. 4.23). The  $\eta$  precipitate distribution was found to be quite different from that in the original alloy and was typical of a structure heated to a temperature greater than that necessary for  $\eta$  phase dissolution followed by cooling. This dissolution and re-precipitation reaction would by necessity have to occur extremely rapidly, and by reference to the ternary equilibrium diagram Fig. 3.1 , surface temperatures of approximately 500 $^{\circ}$ C would be necessary for such a process. The random orientation of grains of extremely small size ( $\sim$ 0.1 $\mu$ m diameter) observed at the surface must imply a process involving complete recrystallisation. The recrystallised grains were found to be completely free of dislocation debris: Using the earlier studies of deformation structure during hot working, reviewed by Jonas et al (36) as a reference, the most likely deformation process must be one of dynamic recovery during deformation followed by static recrystallisation, involving a very high density of sites for nucleation. The grain size produced is much smaller than any observed during controlled high strain rate deformation studies and must imply the development of an extremely high dislocation density during deformation giving many sites for the nucleation of

recrystallisation. It would be impossible to predict the strain rates involved, but as detailed in the Literature Review, strain rates as high as  $5 \times 10^4 \text{ s}^{-1}$  have been postulated to occur under machining conditions. The development of a structure of this type can therefore be predicted.

All drilling and reaming operations carried out to standard specifications involved the use of a drilling lubricant. This clearly had some effect on the surface layer microstructure as demonstrated by the TEM observations. The drilled hole surface microstructure appeared to be basically similar to that produced without lubricant but was less well defined. An equiaxed, ultrafine, grain structure was again found which must imply a recrystallisation process. Tsuchida et al (38), as discussed earlier, concluded that lubricants reduced friction and hence surface layer heating, a finding which is in accord with the present findings:  $\eta$  phase, while apparently present in the surface layer was not found in the form of coarse particles as in the unlubricated case, which is consistent with lower surface temperatures during drilling.

Forsyth (32) attributed the large increase in hardness at the surface of a drilled hole to a reduction in grain (subgrain) size, by applying a Hall-Petch type of equation of the form:

$$H = H_0 + K'd^{-\frac{1}{2}}.$$

Where  $H_0$  and  $K'$  are constants and  $d$  = grain diameter.  $H_0$  being related to  $\sigma_i$ , the lattice friction stress in the true Hall-Petch equation:

$$\sigma_y = \sigma_i + Kd^{-\frac{1}{2}}.$$

In order to apply this equation the assumption must be made that  $\sigma_i$  (i.e.  $H_0$ ) is negligible in comparison to the effect of grain size, whereupon:

$$H = K'd^{-\frac{1}{2}}.$$

A reduction in grain size from  $\approx 0.1 \mu\text{m}$  would then result in a 7 fold increase in hardness, somewhat larger than the two

fold increase observed. It is believed however, that the ultrafine grain structure is confined to a very narrow layer at the hole surface, the true hardness of which could not be assessed, even using microhardness techniques. Forsyth made the further assumption that hardness is proportional to yield stress: If such an assumption is made here a yield stress in the surface layer of  $\approx 900 \text{ MNm}^{-2}$  would be expected, far greater than could be produced by normal hot working routes and obviously a result of high strain, high strain rate, deformation occurring during drilling in the surface layer.

Adjacent to the reamed holes, a less severe deformation structure was found, consistent with the smaller increase in hardness in the surface layer. The reaming operation clearly involves less microstructural damage over a region only  $\approx 10 \mu\text{m}$  in depth at the hole bore.

As discussed in the Literature Review, the amount of strain necessary to crack large intermetallic particles can be as low as 3 to 5% (45). In the present situation strains at least an order of magnitude higher than this must be involved and any intermetallic particles lying within  $50 \mu\text{m}$  of the hole bore would be expected to be fractured or debonded during boring operations. Cracked particles were in fact noted adjacent to both drilled and reamed holes, supporting this view (Figs. 4.19 , 4.37).

### 3.2.2 The Relationship Between Surface Deformation and Crack Initiation.

As detailed in the Literature Review, there are three areas which may be of significance here:

- (a) The formation of crack nuclei by intermetallic cracking or debonding.
- (b) The inhibition of microcrack growth due to the presence of deformation structure.
- (c) The influence of the residual stress distribution produced as a result of surface layer deformation which may promote or inhibit crack initiation depending on its nature (tensile or compressive in the hoop direction) and its stability.

It is now proposed to discuss these factors with reference to the features of the deformation structure discussed earlier, and possibly explain the differences in crack initiation behaviour between the two deburred test piece types (DD and RD).

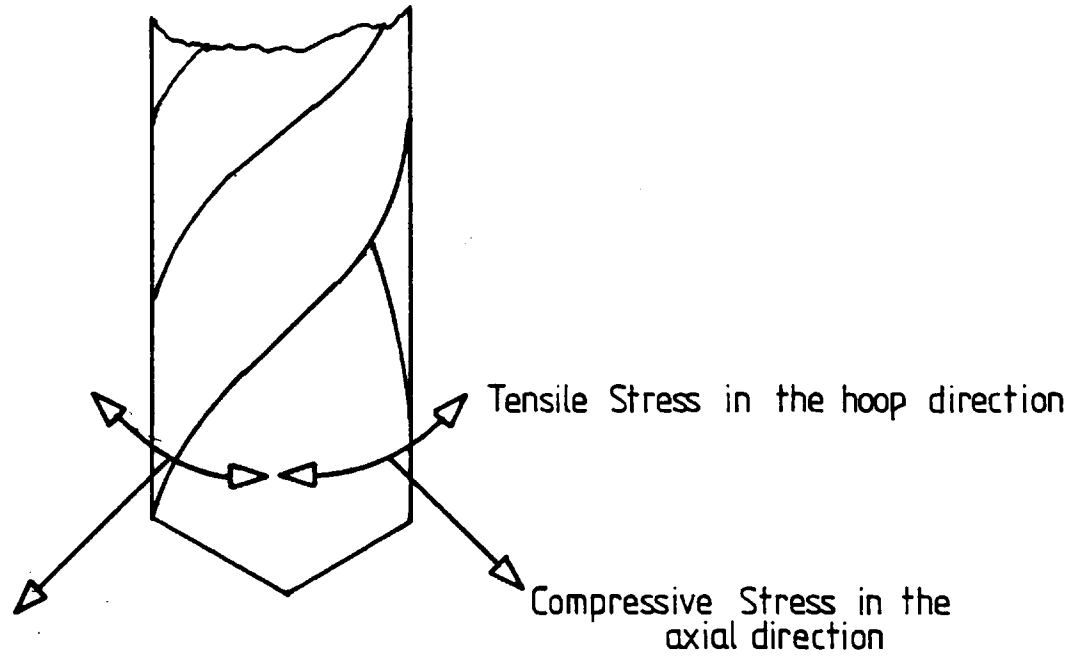
The observation of intermetallic particle initiation in most reamed test pieces manifestly demonstrates the involvement of these large inclusions in crack initiation. Initiation occurred via particle debonding in many cases although cracked particles were also observed. The theory of crack initiation at particles proposed by Chang et al (49) involves firstly the formation of dislocation pile-ups by cyclic plasticity giving rise to particle cracking. This stage may not be necessary in the case of particles lying within the deformed layer due to precracking during deformation. The second stage of microcrack development in the alloy matrix may however remain a necessary stage, although as shown in Fig.4.I9 precracking was found to extend beyond the particle into the matrix in some cases. Such precracked particles would appear therefore to be particularly damaging sites from a crack initiation viewpoint.

Intermetallic particle damage would be expected, bearing in mind the observations of surface deformation, to be more prevalent in the drilled case and certainly such particles were observed. It is rather surprising therefore that initiation at particles was only observed in reamed specimens and not in drilled. Two possible explanations can be proposed: Firstly that more damaging sites for initiation exist at the drilled hole bore, or secondly, that particle initiation is inhibited in some way. Crack initiation in drilled specimens was, as discussed earlier, found to occur at surface machining marks and hence these must be the most damaging sites adjacent to drilled holes. However, the overall fatigue performance was not found to be influenced greatly by the presence of these surface flaws and in fact showed a slight improvement in fatigue limit. By implication some other factor must be inhibiting crack initiation adjacent to drilled holes. It is argued that the important factor is the inhibition of microcrack development due to a combination of deformation structure and resultant residual stresses. General

opinion expressed in the literature is that cold working and deformation structure per-se has no effect on fatigue behaviour since the prior strains involved are very low compared to those involved in crack initiation and growth. However, as demonstrated earlier, the surface layer strains involved in drilling are enormously high and the very marked increase in flow stress would be expected to inhibit dislocation motion..

Residual stresses developed in the surface layer must also be taken into consideration. Leverant et al (53), for example, found a marked effect of compressive residual stresses on microcrack development from shot peened surfaces. Underwood et al also noted that this effect persisted to a much greater depth than expected (Fig. 4.10). Forsyth (32) considered that residual stresses might be removed due to relaxation during cycling but Leverant et al believed that this would only be so if the yield stress, including the residual effect, was exceeded at the surface during cycling. This would be most unlikely in this case of cycling in tension, assuming, of course, a compressive residual stress.

Tsuchida et al (38), as detailed in Fig. 4.5, found that compressive surface residual stresses were only produced by machining processes involving well lubricated cuts and a low cutting speed, with a low feed rate and depth of cut also having some effect. During the drilling operation used here it would be very difficult to predict the residual stresses: The drill rotation speed of 2000 rpm is equivalent to a cutting speed of approximately 41m/min, a low cutting speed in comparison to those employed during turning by Tsuchida et al. However, the depth of cut can be considered to be very large and surface heating, believed to give rise to tensile residuals by Tsuchida et al, was in evidence. It is argued however, that unlike turning operations there may be another stress consideration; that of expansion of the hole during drilling (Fig. 4.46) giving rise to tensile strains in the hoop direction in a similar manner to that produced during coining operations. This would of course give rise to compressive residual stresses. The fatigue life results would certainly imply a reduction in microcrack



Stresses Exerted During Drilling  
due to Hole Expansion

development rate adjacent to drilled holes and it is felt that surface compressive residual stresses must have a role to play in this process.

Metallographic evidence indicating an influence of the deformed layer on the early stages of crack growth was found on the fracture surface (Fig. 4.39). The fracture surface was found to exhibit a different morphology in a surface layer approximately 50 $\mu$ m in depth, exactly equivalent to the depth of the deformed layer. No such region was observed adjacent to reamed holes. Compressive surface stresses under some circumstances can lead to subsurface initiation due to the presence of a subsurface tensile residual. Subsurface initiation was in fact observed by Forsyth (32) adjacent to drilled holes but no clear evidence for it was obtained here.

### 3.3 The Growth of Short Cracks.

Using the HRSEM short crack (<Imm in length) growth rates were investigated via striation spacing. The growth rates were then related to crack tip stress intensities using the calculations in Appendix I. Using the long crack data obtained as part of the propagation study normalised crack growth rates were calculated in a manner similar to that of Talug and Reifsnider (59). Rather surprisingly, it was found, even using the minimum possible  $\Delta K$  calibration (giving the maximum possible crack growth rate) that normalised crack growth rates decreased at short crack lengths to values as low as 0.3 (Figs. 4.41, 4.42). This means that the measured crack growth rates are lower than those predicted by the use of L.E.F.M. analysis and long crack growth rate data. This observation is in opposition to the earlier studies of Talug and Reifsnider and also Pearson (60) who noted increases in crack growth rates at short crack lengths over those predicted.

There are three possible explanations for the discrepancies between results:

- (a) The use of striation spacing data gives a difference in crack growth rate from that de-

terminated optically (as by Pearson) at short crack lengths.

- (b) The effect is a real one and crack growth rates are reduced below those predicted by L.E.F.M.
- (c) The calibration of stress intensity breaks down at short crack lengths.

The observations made in the crack propagation studies indicate that while discrepancies do exist between striation spacing and macroscopic crack growth rate there is no systematic effect which would lead to striations giving an underestimate of true rate at short crack lengths. In fact at  $\Delta K < 10 \text{ MNm}^{-3/2}$ , the range of importance here, striation spacings were found to give an overestimate of macroscopic rate as measured optically.

In the present study crack growth rates have been measured along a growth direction approximately perpendicular to the hole bore. Pearson however, measured optically the rate of growth of cracks at the base of a shallow notch along the specimen surface, i.e. along a direction at right angles to that in the present study. The analysis of stress intensity carried out by Shah (64) indicated an increase in  $\Delta K$  along the specimen surface and hence crack growth rates along the hole bore would be expected to be somewhat greater than into the bulk. It is argued that at very short crack lengths this effect may be particularly marked. Crack growth rates measured along the surface might therefore be expected to be somewhat higher than those into the bulk. While this effect may explain the discrepancies between the present work and the previous studies of, for example, Pearson, it cannot successfully predict why normalised crack growth rates of less than one have been found.

Crack growth in the surface layer may be influenced by surface compressive residual stresses, even to a considerable depth, as demonstrated by Underwood et al (54). The microstructural studies conducted in the present work indicate that any residual stress distribution is likely to be very different in the drilled and reamed specimen types. The fact that crack growth rates at short crack lengths were identical

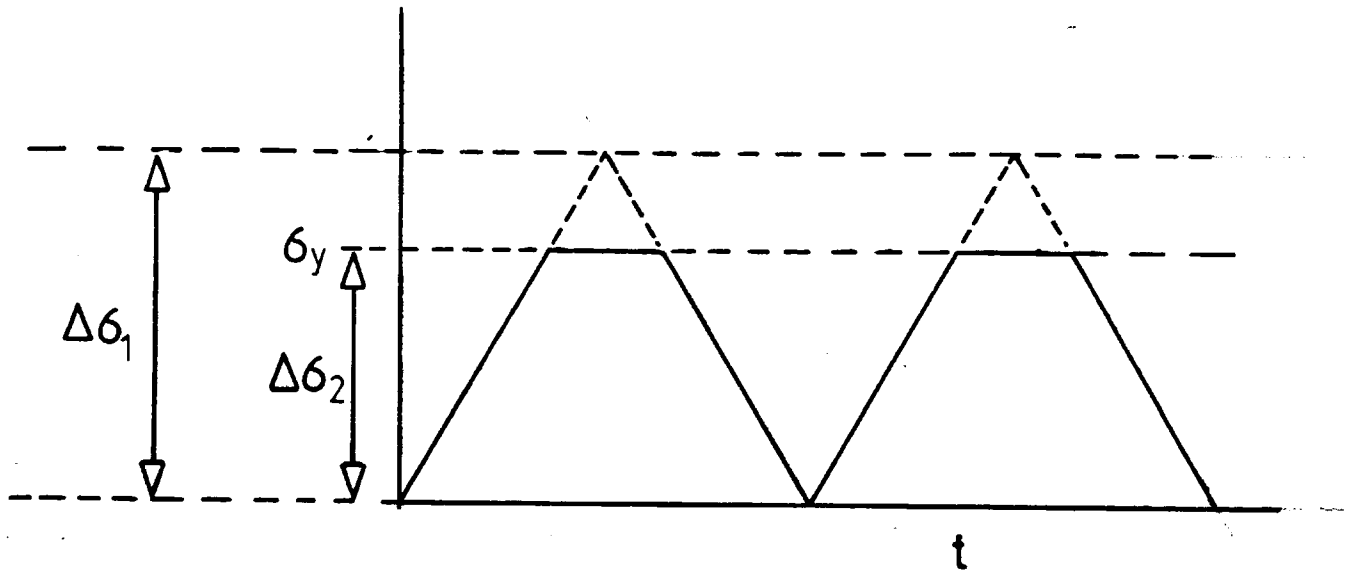
(within experimental scatter) would indicate that the residual stresses are not of significance. (This result does not invalidate the earlier proposal of inhibition of micro-crack development due to residual stresses since much shorter crack lengths, of the order of the depth of the deformed layer, are involved in that case).

The results obtained from the drilled specimens were from tests carried out at 225MPa peak net mean section stress: Assuming a  $K_t$  of approximately 2.3 (Fig.4.I4) this implies a maximum surface stress of >500MPa, which is somewhat in excess of the yield stress. It could be argued therefore that surface yielding results in a reduction in  $\Delta K$  (Fig.4.47 ). Unfortunately, results obtained at net peak stress of 175MPa could not be subject to such an effect so it is unlikely that surface yielding is the controlling factor.

The third, and perhaps most likely, explanation of the effect is that the stress intensity calibration breaks down at these short crack lengths. It is notable that the calibrations for  $\Delta K$  in Appendix I are based upon solutions which make use of ratios of, for example, crack length to hole diameter (62). Such ratios allow the solutions to be applied both to short and long cracks in various specimen configurations, but it is possible that they are only valid in comparatively long crack situations. The break down of L.E.F.M. analysis may therefore explain the present results. It is worth noting that while previous workers used basically similar methods to calculate  $\Delta K$  for short cracks they were concerned with crack growth from surface notches rather than from the centre notch (circular hole) involved here.

Discrepancies of this kind clearly imply that the method of minimum defect size analysis to predict fatigue limit must be used very carefully. However, the changes in normalised crack growth rate observed here and previously never exceed a factor of  $\sim 3$ , the lowest value observed here being 0.3 and the highest by Talug and Reifsnider 1.2. Hence the use of the equation:

$$\Delta K_{th} = \Delta \sigma_{lim} \sqrt{\pi a_e}$$



$\Delta\sigma_1$  = stress range without yielding

$\Delta\sigma_2$  = stress range with yielding

$$\Delta\sigma_1 > \Delta\sigma_2$$

Possible Reduction in Stress Range  
due to Surface Layer Yielding

may have some validity. It is possible to test the equation using inclusion initiation in specimen type RD as an example: The fatigue limit  $\Delta\sigma_{lim}$  was here approximately 155MPa ( $\sigma_{max\ lim} = 170\text{MPa}$  at  $R = 0.1$ ). Hence using a threshold of around  $2\text{MNm}^{-3/2}$  (a very approximate value from Kirby and Beevers (6I))

$$2 = 170\sqrt{\pi a_e} \quad \text{hence} \quad a_e \approx 40\mu\text{m}.$$

Intermetallic particles, which acted as sites for initiation in these specimens were found to range in size from 10 to 100 $\mu\text{m}$ , so clearly this simple approach can give an estimate of the initial defect size assuming the particle to be equivalent to a crack.

#### 3.4 Technological Significance.

The basic fatigue testing data obtained here show that the deburring operation has the controlling influence on fatigue life and that the reaming operation is superfluous. In fact the drilled and deburred test pieces (DD) showed a slight improvement over (RD). Hence under the loading conditions employed here the ideal hole preparation process is one of drilling followed by deburring. It must be emphasised however, that these results strictly only apply to situations where the drilling direction is perpendicular to the primary load axis in alternating tension. It is likely however, that the deburring operation would be beneficial under all loading conditions. Leverant et al (53) demonstrated that, under loading conditions employing large compressive stresses, 'shake down' of compressive residual stresses was observed. If the assumption is made therefore, as seems likely, that there is a residual stress involvement in the inhibition of initiation adjacent to drilled holes, there might be a degradation of performance in drilled specimens, under compressive applied loads. Further tests would be necessary to check this effect.

From the viewpoint of aircraft manufacture the apparently ineffectual reaming process (with possible qualification of compressive loading conditions) could be removed from hole

preparation: At present bored holes in critical or high load situations are often reamed, with the aim of inhibiting fatigue crack initiation. The present results indicate that this is unnecessary.

The deburring operation, while giving significant improvements in properties, may be difficult to apply in certain situations: Many holes are bored through several components clamped together, or in configurations where access to the rear surface of the component is impossible. Hence deburring would not be possible without the disassembly of many components. At the present time it is not possible to deburr internal faces of components where access is precluded: It may be possible however, to develop machine tools to conduct such operations, the great improvement in fatigue properties would certainly make such a development worthwhile.

PART 5. CRACK PROPAGATION STUDIES.

THE MICROSCOPIC MECHANISMS OF FATIGUE CRACK PROPAGATION  
IN HIGH STRENGTH ALUMINIUM ALLOYS: LITERATURE REVIEW.

I.1 Introduction

Fatigue fracture has been studied for a great number of years using various increasingly sophisticated metallographic techniques. Zappfe and Worden (66) were amongst the earliest workers to make such an investigation using optical metallography and noted various stages of crack growth, one delineated by regular surface markings, which were called striations, and one earlier apparently striation free stage. Forsyth and Ryder (67,68) investigated the fracture surface in more detail and introduced the terms 'Stage I' and 'Stage II' to describe the first and second stages, the first being defined as crack growth on planes of high shear stress and the second as growth on planes of high tensile stress. Stage I was shown by these workers to be associated generally with initiation and the formation of slip bands prior to cracking. Under mode I loading, stage II was found to consume most of the fracture and it is this stage that is of principal concern here.

Forsyth and his coworkers, Ryder and Stubbington (69,70,71) found that test environment had great influence on crack growth, particularly moist environments in the case of the Al-Zn-Mg alloys used in their studies. Their early evidence has led to a large number of different models to explain the manner in which a fatigue crack grows and the influence of the test environment on that growth. The mechanisms fall roughly into two categories, those involving a ductile mode of crack extension and those in which crack growth occurs in a partially brittle manner. An even larger number of mechanisms have been put forward to explain the formation of fatigue striations, which are particularly well marked on the fracture surfaces of aluminium alloys. In the following sections the two crack extension modes are discussed, together with an appraisal of striation formation processes.

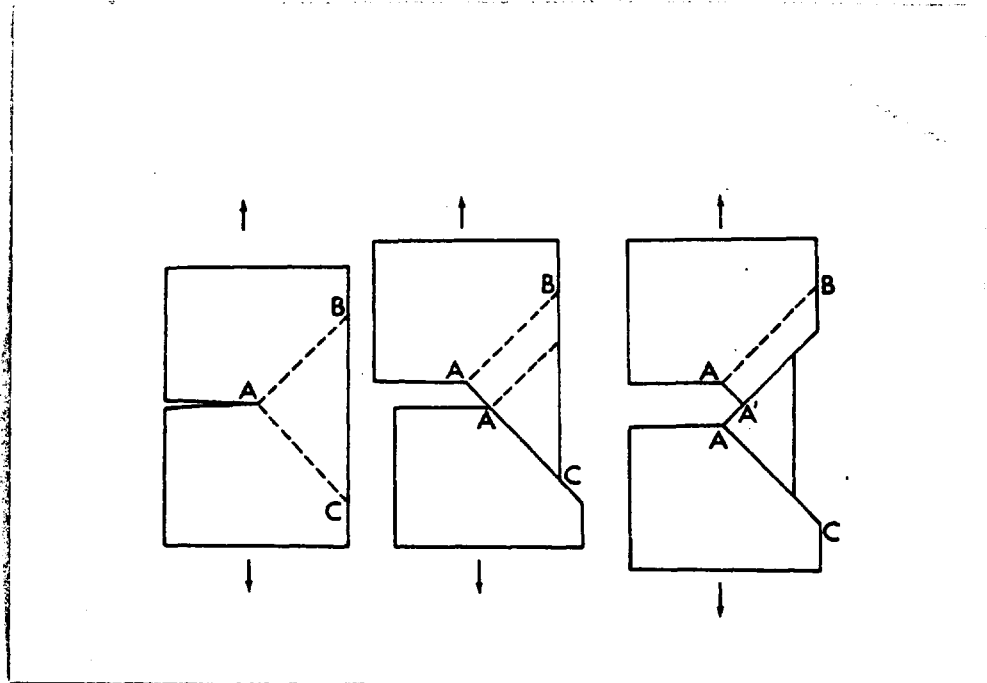
## I.2.Ductile Crack Propagation

Forsyth and his coworkers noted that under corrosive test conditions stage II crack growth occurred on crystallographic planes. They proposed therefore that under these conditions crack extension must include a cleavage component. This suggestion did not receive a great deal of early support since most workers could not believe that the aluminium alloys studied could fail by cleavage under any circumstances. One of these early critics was Laird (72) who proposed that a 'quasi-cleavage' mechanism might operate in which dislocation motion leads to crack advance, with slip system symmetry leading to crystallographic crack planes.

This type of model was further developed by Pelloux (73) who considered a fully plastic notched single crystal to represent a crack tip. He developed a theory for crack propagation based upon an alternating shear process, in which as work hardening occurred on a single slip system at the crack tip, shear was transferred to an opposite, similar, slip system, (Fig.5.I). Using this basic premise Pelloux predicted that a crack would tend to follow an  $\{100\}$  or  $\{011\}$  crack plane in an F.C.C. metal with an  $\langle 0\bar{1}1 \rangle$  crack tip direction. He supported his theory with an etch pitting experiment on fracture surfaces of aluminium alloys tested in laboratory air.

More direct evidence for alternating shear mechanism has since been provided by Neumann and his coworkers (74,75). In situ observation was made of crack propagation in single crystal copper and Fe 3wt% Si using both light microscopy and SEM. Polished specimens were used and slip activity was observed via surface slip steps. In these rather elegant studies clear evidence was presented to demonstrate the alternating shear process, and crystallographic studies were also made. It was shown that in copper a macroscopically flat fracture surface could only be obtained with an  $\{001\}$  crack plane and a  $\{110\}$  crack tip direction - supporting Pelloux's earlier theory.

I.2.1 The Influence of Test Environment. A criticism often levelled at the ductile growth model, is that it cannot



Notched Single Crystal Analogue  
of a Fatigue Crack

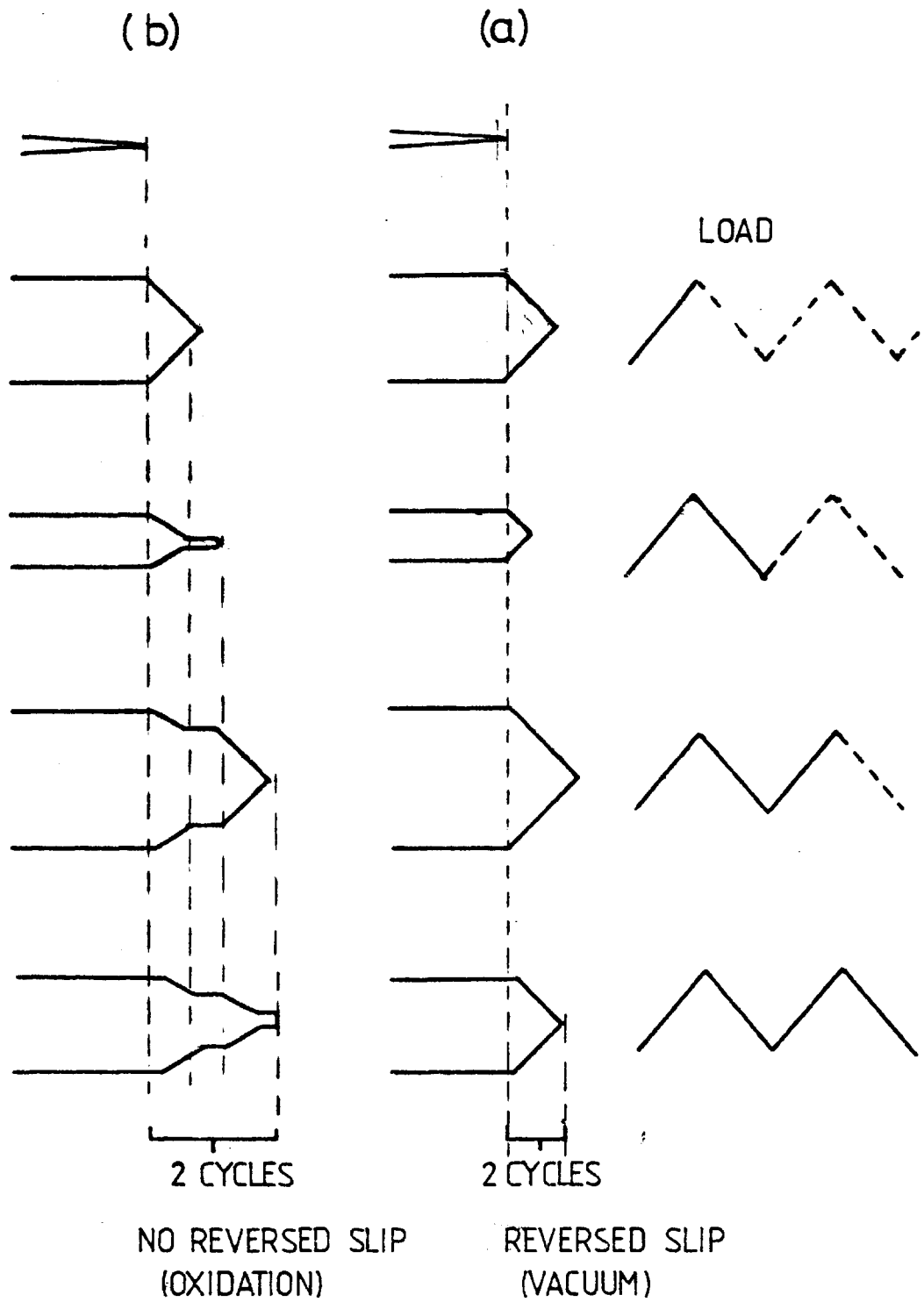
FROM PELLOUX [73]

adequately explain the increase in crack growth rates in corrosive environments. Three suggestions have been made to explain the effect: (a) Interference with otherwise reversible slip by surface oxidation. (b) Prevention of crack tip rewelding. (c) Bulk oxide interference with slip processes.

The suggestion that a reversible slip process was responsible was originally made by Pelloux (73). He proposed (again using the notched single crystal analogue) that as crack opening occurred a crack tip profile as shown in Fig. 5.2 was produced. Pelloux then suggested that in vacuum slip could occur in the opposite direction during crack closure, (Fig. 5.2(a)). In air however the oxidation of the newly formed fracture surfaces prevented the reversal, leading to enhanced crack growth rates (Fig. 5.2(b)). In aluminium alloys it has clearly been demonstrated by Grosskreutz (76) that slip character can be markedly altered by surface oxidation. Here, surface slip band formation during cyclic loading was found to be much enhanced by surface oxidation; many dislocation dipoles were observed close to the specimen surface and the explanation proposed was that oxidation of the emerging slip steps prevented slip reversibility. This evidence has been taken to lend support to the Pelloux model. However Grosskreutz in a further study (77) found that the mechanical properties of the surface film, already present on the specimen surface, were very much improved in vacuum, Young's Modulus being enhanced by a factor of 4. His explanation for this phenomenon was that adsorbed water vapour weakened the film in laboratory air leading Grosskreutz to believe that his earlier results might have been explicable by this film strengthening rather than by slip step oxidation.

A mechanism for crack growth rate enhancement in moist environments was suggested by Hartman (78) based upon the changes in elastic properties of the oxide film and was supported by the findings of Grosskreutz detailed above. Wei (79) was, however of the opinion that the oxide film, being only a few monolayers in thickness, could not possibly have a significant effect and he therefore discounted the theory.

Fig. 5.2



Mechanism of environmentally enhanced crack growth

FROM PELLOUX (73)

The second explanation for environmental enhancement of growth rate which overlaps rather with the slip reversibility suggestion, implies that partial rewelding of the crack surfaces can occur during the compressive part of the fatigue cycle in vacuum and that surface oxidation may prevent this if tests are carried out in air (80).

The early work of Wadsworth and Hutchings (81) demonstrated that surface oxidation could have an effect on crack growth rates, in this case in pure copper, and some more recent work by Fuhlrott and Neumann (82) lent some support to a rewelding model: Fatigue tests were carried out on pure copper in both air and vacuum and it was found that holding times in compression reduced the crack growth rate in vacuum but had no effect in air.

Critics of this mechanism have included Laird and Smith (83) who noted that inert gases such as nitrogen were as effective as vacuum in reducing crack growth rates, although they believed that adsorption of an inert gas would have an effect if rewelding were occurring. More recent evidence obtained by Bowles (84) showed that under normal loading conditions (i.e. without large compressive stresses) the crack faces produced in a high strength aluminium alloy made contact only at a very few discrete points. A re-welding process seems unlikely to play a significant role therefore in most circumstances.

The third model, also based on surface oxidation and proposed by Shen et al (85), involves the possibility that surface oxidation affects dislocation escape from the surface during crack opening. They suggested that the inhibition of the alternate shear process enhanced the formation of voids and cavities ahead of the crack, as blunting was inhibited, thereby increasing crack growth rates. Cavity formation was originally proposed by Wood et al (86) and has been observed using TEM techniques in pure aluminium (87) and therefore remains a possible explanation. There is however no evidence in the case of high strength aluminium alloys to suggest that void formation can occur near the crack tip except where these voids are associated with large inter-

metallic particles (57).

In conclusion the available evidence suggests that these mechanisms of environment influenced crack growth have some relevance in explaining for example the effect of oxygen on copper (81) and dry oxygen on aluminium alloys (88). However these mechanisms do not adequately account for the dramatic effect of water vapour on fatigue crack growth in aluminium alloys.

A number of workers have studied this effect, for example Bradshaw and Wheeler (88), and water vapour has been found to enhance crack growth rates by up to a factor of 10 (78). For a rewelding/slip interference mechanism to explain the effect the ad hoc suggestion must be made that the greater thickness of oxide formed by the reaction of moist air with the newly formed crack surfaces (89) leads to more complete rewelding/slip interference than the thinner oxide layer formed by dry oxygen. This suggestion does not seem to have gained great support and as a number of workers have pointed out, the initial rates of reaction, which may well be of greatest importance, have been found to be approximately equal in pure aluminium (90). Bradshaw and Wheeler (88) also found that water vapour in suspension in nitrogen was equally effective in increasing crack growth rates as moist oxygen - this would not be expected if oxide layer thickness were the controlling factor. Clearly the ductile cracking mechanisms while explaining concisely some environmental effects break down in their explanation of the effect of water vapour.

### I.3 The Influence of Water Vapour on Crack Propagation:

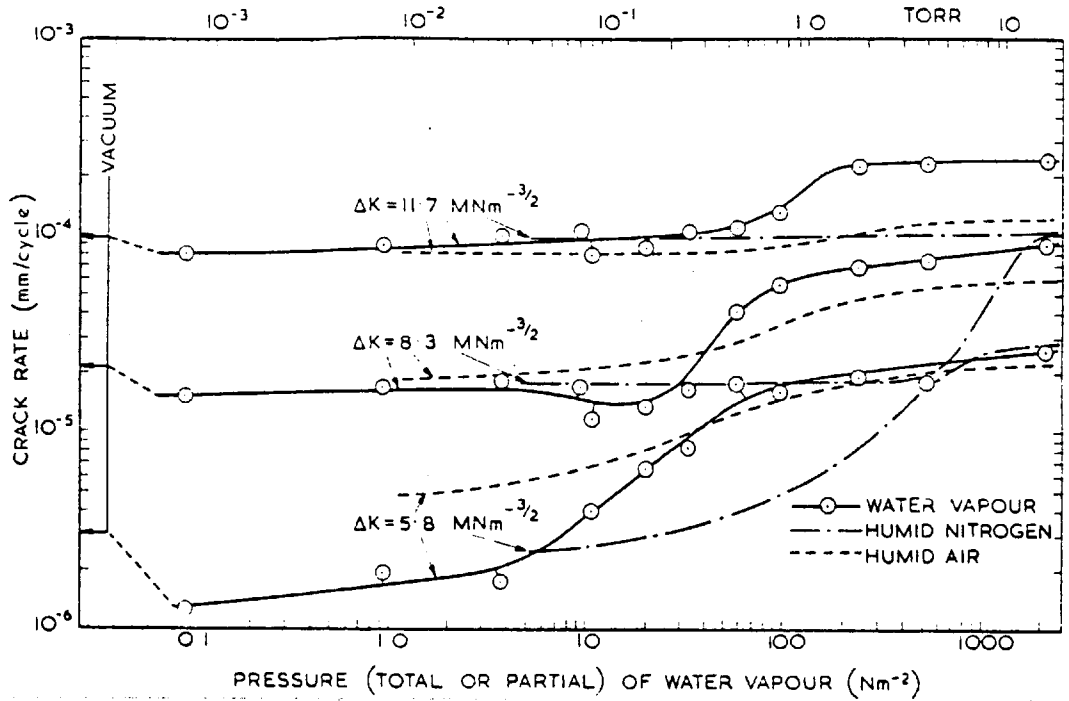
#### I.3.1 Combined Fracture Mechanics Surface Chemistry Studies:

In order to determine the effect of water vapour on crack propagation in a quantitative manner, and thereby qualify the mechanism of crack growth, a number of workers have carried out studies in which crack propagation was studied under carefully controlled conditions of environment, stress intensity, and test frequency.

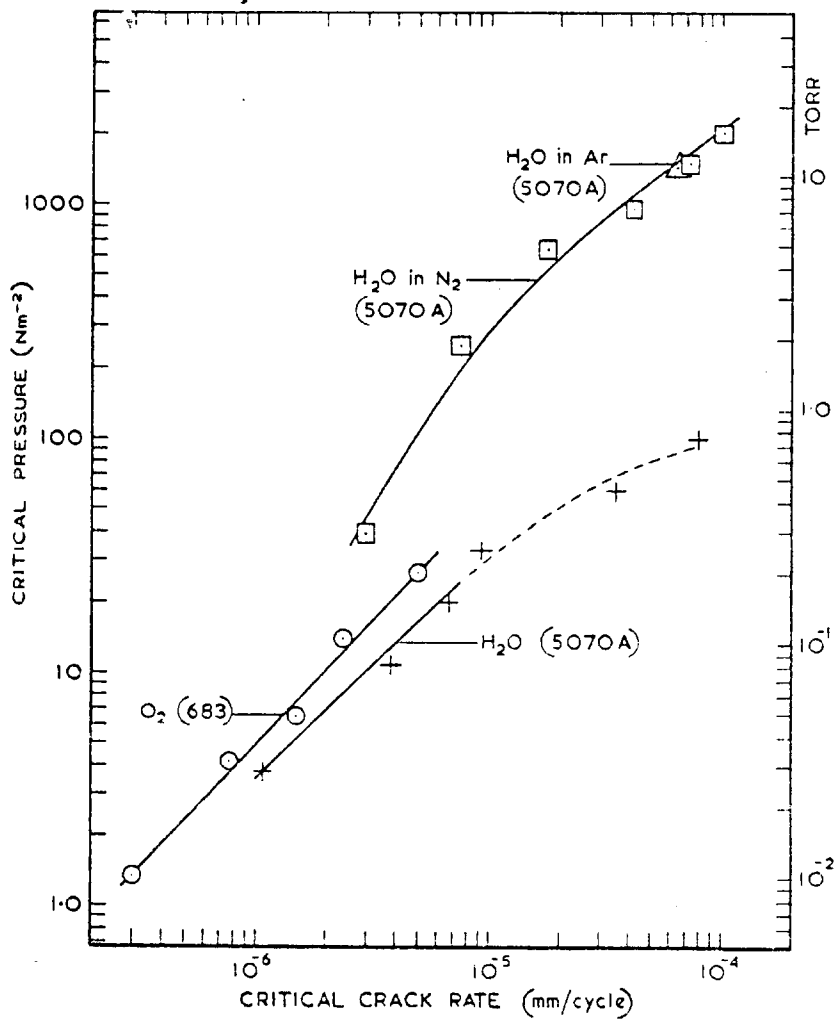
Wadsworth and Hutchings (81) were amongst the earliest

workers to carry out such studies and demonstrated that only gaseous species which reacted with the crack surface have any effect and that gold was unaffected. They also found, rather suprisingly, that water vapour and oxygen were similar in their effect on aluminium alloys. However a number of years later Hartman and Jacobs (91) pointed out that Wadsworth and Hutchings had measured total pressures of laboratory air, rather than the partial pressure of water vapour, to specify the effect of water vapour and therefore the marked effect was masked. Hartman and Jacobs and also Broom and Nicholson (92) were able to detect the marked effect of moist air in increasing crack growth rates and the latter noted in fact that dry oxygen had little effect on endurance while laboratory air reduced it by a factor of 5. They concluded therefore that water vapour was the only component of normal laboratory air affecting endurance and suggested a mechanism involving the diffusion of hydrogen ions, produced by surface reaction, into the region ahead of the crack.

Bradshaw, and later Bradshaw and Wheeler (93,88) continued these studies in a more carefully defined manner, since they measured crack growth rates rather than endurance and also controlled water vapour partial pressure and test frequency. They found that if crack growth rate at constant  $\Delta K$  was plotted against partial pressure a characterisic S shaped curve was produced, see Fig.5.3, with a certain pressure above which no further environmental enhancement of growth rate was observed. They found that  $P_c$  depended on  $\Delta K$  and was in fact related to crack growth rate, ( Fig.5.3(b) ) a critical crack rate existing equivalent to each critical pressure.  $P_c$  was found to be dependent on test frequency a 100 fold increase in test frequency resulting in a 100 fold increase in  $P_c$ . Bradshaw (93) originally suggested that  $P_c$  represented a pressure at which surface creation rate during crack growth was equivalent to surface coverage rate by gaseous species (assuming monolayer coverage). However adsorption rate calculations carried out by Bradshaw gave an under estimate of  $P_c$  of  $10^3$ . Snowden (94) accounted for this discrepancy by considering the crack to be a capillary; capillary flow was therefore considered to limit the rate



(a) Influence of Water Vapour Pressure on Crack Growth Rate in 2618 (DTD 5070 A)



(b) Relationship Between Critical Growth Rate and Critical Pressure AFTER BRADSHAW+WHEELER [88]

of supply of gaseous species to the crack tip. Bradshaw, however, carried out similar calculations and considered capillary effects to be negligible; he suggested that perhaps multiple adsorbed layers were necessary.

The discrepancy between observed and theoretical pressures was reduced by Achter (95) who modified the adsorption calculations; Bradshaw had considered the time available for adsorption in one cycle to be  $1/2f$  where  $f$ =cyclic frequency. The factor of two was included as no new crack surfaces were considered to be produced during crack closure. Bradshaw termed this value 'exposure' and made use of it in calculations of  $P_c$ , along with the area of crack surface exposed during this period which was determined from growth rate. Achter modified these calculations by making the premise that adsorbed species could only have an effect if they were adsorbed while the crack was actually growing and that adsorption must occur onto the surface up to a distance of one atomic spacing behind the crack tip. His calculations yielded an equation for  $P_c$  of:

$$P_c = 2 \times 10^4 \frac{da}{dn} \text{ torr}$$

at 100 Hz where  $da/dn$  = growth rate in cm/cycle. This was modified by Horden (96) to give:

$$P_c = 2 \times 10^2 \frac{da}{dn} f.$$

where  $f$  = cyclic frequency. Bradshaw and Wheeler's experimental observations gave:

$$P_c = 4 \times 10^2 \frac{da}{dn} f.$$

These theoretical calculations reduced the discrepancy therefore and as Achter pointed out his calculations were based on a sticking coefficient of unity: This has been shown by Jona (90) to be a large over estimate: for example values as low as  $10^{-2}$  have been observed. The conclusion made by both Bradshaw and Wheeler, and Achter, was that rate of adsorption appeared to be related to crack growth rate enhancement and therefore the action of surface layers

was deemed responsible rather than some other bulk process such as the hydrogen ion diffusion suggestion of Broom and Nicholson. Bradshaw and Wheeler cited their evidence that at high frequencies (100 Hz) crack growth rates were equal to those at low frequency (at sufficiently high water vapour pressures) to emphasise this point.

All of the studies reported so far have based their adsorption rate calculations on purely theoretical considerations: Recently, however, using Auger electron spectroscopy (AES) and X-ray photo electron spectroscopy (XPS) it has been possible to actually monitor the rate of reaction of water vapour with a clean metal surface. Such a study in an aluminium alloy (2219-7851) has been made by Wei et al (97). The reaction results are shown in Fig.5.5. The exposure required for a normalised oxygen Auger signal of 1.0 which signifies the completion of the surface reaction was found to equal  $10^{-2}$  pa.s. (1 torr=133pa.s.). Wei et al also monitored crack growth rates in a similar way to Bradshaw and Wheeler and obtained results as shown in Fig.5.4 -here the critical exposure ( $P_{H_2O}/2f$ )  $8 \times 10^{-1}$  pa.s. This discrepancy cannot be explained by sticking coefficients since Auger results accounted for this factor. Wei et al reverted to the capillary flow explanation and made some sophisticated calculations based on Knudsen flow parameters. They obtained an expression for  $P_{H_2O}$  at the crack tip of:

$$\frac{dp}{dt} = \underbrace{-\frac{K \cdot d\theta}{V}}_A + \underbrace{\frac{F \cdot (P_o - P)}{V}}_B$$

P = pressure of gas at the crack tip

Po = external pressure

F = Knudsen flow parameter

$\theta$  = extent of surface reaction

K = constant

V = a control volume related to  $\frac{da}{dn}$

Part A of the equation relates to surface reaction rate and part B to the rate of supply. Clearly if  $\frac{dp}{dt} = 0$  or became

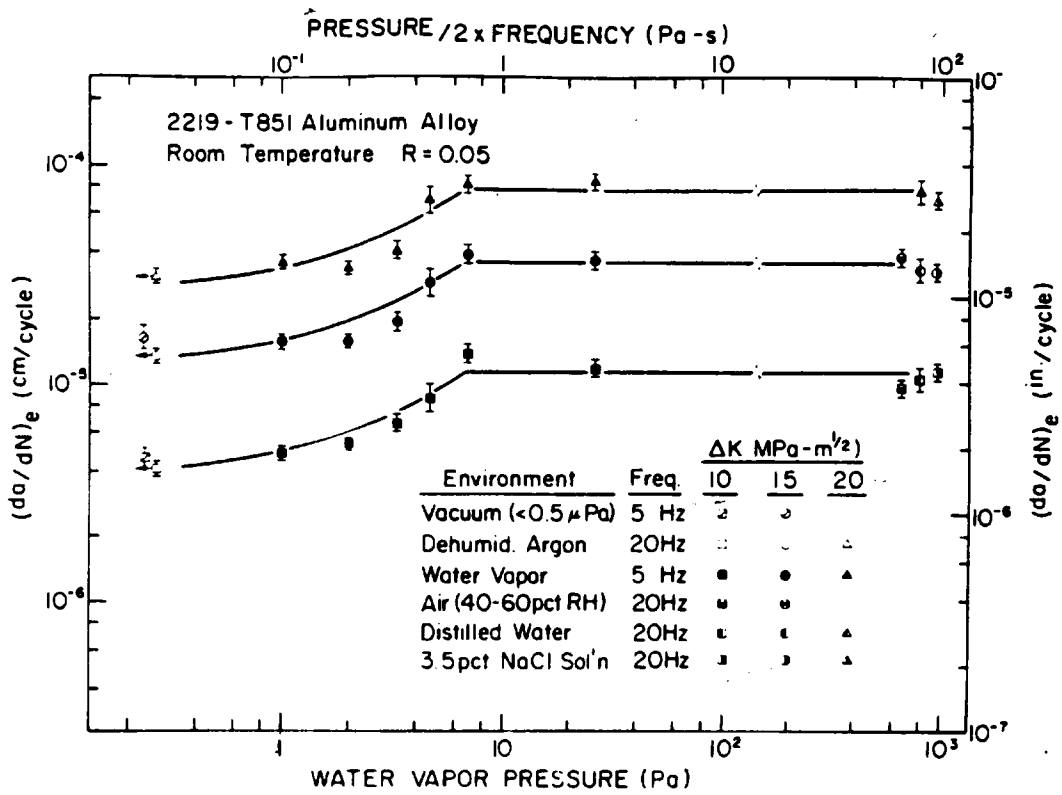


Fig 5.4. The Influence of Water Vapour Pressure on Fatigue Crack Growth Rate

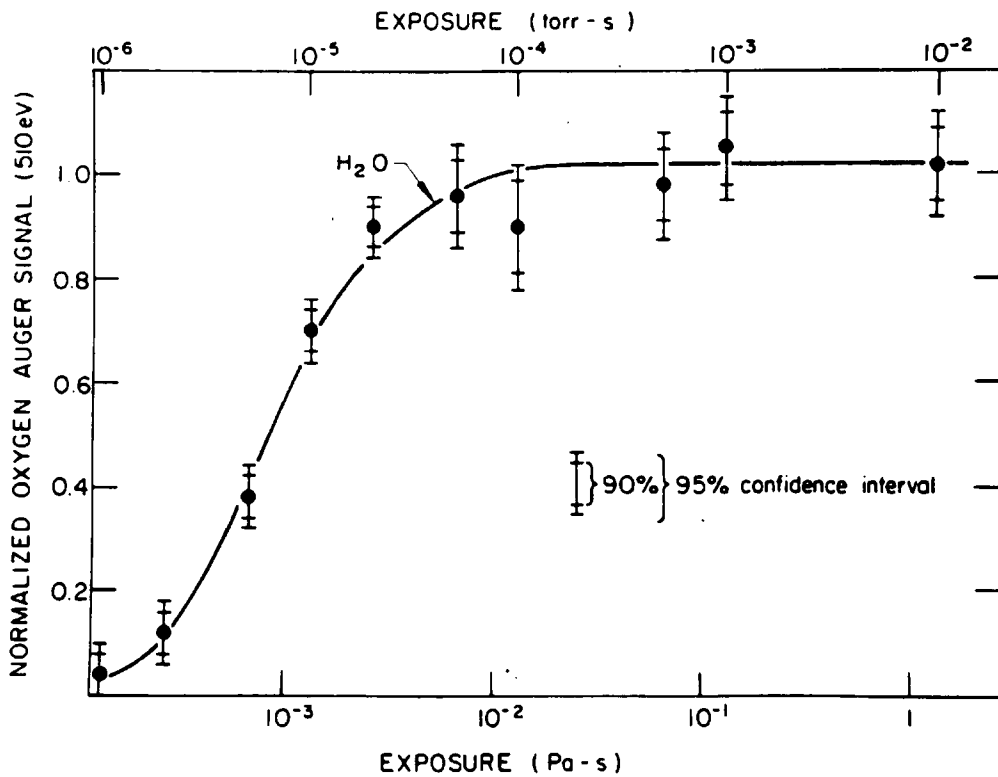


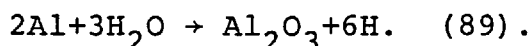
Fig 5.5. Water Vapour / Aluminium Reaction Kinetics

negative then environmental enhancement of crack growth would cease due to insufficient available species. Using various realistic values of the constants in their equation Wei et al succeeded in fitting their model to the experimental results with some accuracy.

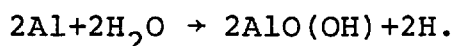
The conclusion from all the fracture mechanics/surface chemistry studies carried out to date appears to be that the two factors controlling environmental enhancement of growth rate are surface reaction/adsorption rate and probably transport of species along the crack.

I.3.2 Surface Reactions. In the previous section reference has been made briefly to various possible mechanisms of environment sensitive cracking: Before discussing these in any more detail it is proposed to give a brief summary of the likely crack tip reactions.

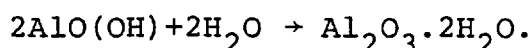
In a dry oxygen environment the standard oxidation reaction occurs leading to the formation of alumina ( $\text{Al}_2\text{O}_3$ ). Booker (89) noted that this layer was limited to a few angströms in thickness at room temperature. The thickness of the surface layer increased to 50-100<sup>0</sup>Å in the presence of water vapour in small quantities, in which case the reaction was thought more likely to be:



In the presence of greater concentrations of water vapour the production of hydroxides and hydrated oxides has been found possible viz:

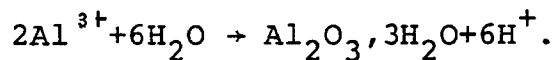


followed by:



Obviously the production of large thicknesses of oxide and hydroxide found in moist conditions must involve migration of ionic species through the film. As Mott (98)

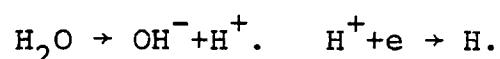
pointed out, very large thicknesses of oxide could only be produced by anodising where  $\text{Al}^{3+}$  ions must pass through the film and electrons were removed via the external circuit. Mott therefore was of the opinion that at room temperature the reaction proceeded almost exclusively via this route. This suggestion was taken up by, for example, Montgrain, Scamans and Swann (99), who proposed at the surface oxide film, the reaction:



For this reaction to proceed  $\text{Al}^{3+}$  ions must have passed through the film leading to a build up of electrons at the metal-oxide interface. Draley and Ruther (100) proposed that protons then migrated through the film to recombine with electrons giving atomic hydrogen. According to Montgrain, Scamans and Swann this recombination could occur at the interface or some distance into the bulk, leading to a build up of hydrogen in the metal matrix (Fig.5.6); a fact which may be of great significance in explaining environmental cracking, as discussed later.

A number of workers have carried out studies of stress corrosion cracking (S.C.C.) and corrosion fatigue under conditions of both anodic and cathodic polarisation. Since some of these studies are discussed in detail later it is useful to note at this stage the modification of surface reactions under polarisation.

Under conditions of anodic polarisation electrons produced by the reaction  $\text{Al} \rightarrow \text{Al}^{3+} + 3\text{e}$  are carried away by the external circuit and therefore the anodic reaction is preferred and hydrogen evolution is suppressed. Alternatively under cathodic conditions electrons are provided, promoting the hydrogen evolution reaction:



In the stress corrosion literature enhanced crack growth rates under anodic conditions have been attributed to increased dissolution at the crack tip by a number of

Metal	Oxide	Water
$\text{Al} \rightarrow \text{Al}^{3+} + 3\text{e}^{-}$ $\text{e}^{-} + \text{H}^{+} \rightarrow \frac{1}{2}\text{H}_2$	$\text{Al}^{3+} \rightarrow$ $\leftarrow \text{H}^{+}$ $\text{O}^{\ominus}$ $\text{e}^{-} \rightarrow$	$\text{H}^{+}$ $\text{O}^{\ominus}$ $\text{H}^{+}$

Species Transport and Reactions at  
The Metal-Oxide-Water Interface

FROM DRALEY AND RUTHER (100)

workers and have formed the basis for the anodic dissolution models for S.C.C. Since hydrogen evolution is ideally reduced, hydrogen embrittlement has been discounted. However, corrosion reactions at the crack tip have been found to lead to acidification of the solution and enhanced hydrogen evolution (IOI). Conversely, cathodic polarisation has been found to reduce crack growth rates, a fact which has again been made use of in arguments against hydrogen embrittlement. However, Bernstein and Thompson (IO2) found that cathodic polarisation reduced the permeability of hydrogen through the metal matrix and suggested therefore that while hydrogen evolution was enhanced, the penetration of hydrogen ahead of the crack was inhibited. Further evidence has also been provided which shows that crack tip conditions may be very different from those at the surface of a polarised specimen: Ataye and Pickering (IO3) and Harris and Pickering (IO4) found, for example, that it was possible to detect Fe ions in crevices during cathodic charging of iron specimens. They also noted hydrogen evolution under similar circumstances if specimens were anodically polarised.

The conclusion which must be made from these studies is clearly that great care must be taken in assessing data obtained concerning crack growth under electrically polarised conditions.

#### I.4 Brittle Crack Propagation

I.4.1 Experimental Evidence: As mentioned earlier, Forsyth and his coworkers (70) proposed a cleavage involvement in stage II crack propagation in an Al-7.5%Zn-2.5%Mg alloy in salt solution. They used both etch pitting and back reflection Laue techniques and observed a general fracture plane close to {001}; since specimens polished back from the fracture surface were used, the actual plane of separation could not be accurately determined. These proposals did not receive a great deal of support initially but more recently crystallographic fracture facets have been observed in aluminium alloys under conditions of both liquid metal embrittlement and transgranular S.C.C. For example, an

{001} fracture plane was noted in gallium wetted single crystals of pure aluminium by Westwood et al (I05). An {011} fracture plane was however observed in an Al-5%Zn-2.5%Mg alloy tested under sustained load in an aqueous NaCl solution by Bursle and Pugh (I06). Here a surface trace analysis was used to predict the fracture plane from fractographic observations. A good deal of evidence exists in both of these cases to suggest cleavage failure.

A {011} fracture plane has also been found for fatigue crack growth in 7075 T6 under laboratory air conditions by Bowles and Broek (I07). Their observations were made using a TEM technique hence crystallographic evidence was limited to electron transparent areas which owing to the specimen preparation technique were approximately parallel to the general plane of fracture. More significantly, Bowles and Broek noted regularly spaced deformation bands extending below the fracture surface, separated by areas of low dislocation density. Their original conclusion was that these bands were produced as dislocations rearranged into subgrains during deformation at maximum load. Bowles (84), however, in a more recent study has reinterpreted his earlier results and suggested that the deformation band structure was a result of brittle/ductile transition occurring during each cycle and caused by environmental interaction. This conclusion was supported by Wanhill (I08) who carried out a similar study under vacuum test conditions and found no such band structure; here an almost continuous dislocation network was observed below the fracture surface.

Any cleavage component in fracture would imply that less plastic deformation must accompany crack growth, resulting in a smaller plastic zone at the crack tip at the same stress intensity ( $\Delta K$ ). Petit et al (I09) showed that the plastic zone was almost twice as large in vacuum as in laboratory air at the same stress intensity providing further convincing evidence for an environmentally influenced cleavage component in fatigue crack growth.

I.4.2 Theoretical Considerations. The principles under which normally ductile materials might fail by cleavage

have been developed by a number of workers, notably Kelly et al (II) and Rice and Thomson (III): Kelly et al suggested that a crack can propagate by cleavage if  $R$ , the ratio of the normal stress ( $\sigma$ ) to the applied shear stress ( $\tau$ ) ( $R=\sigma/\tau$ ) is greater than the ratio of the theoretical tensile stress ( $\sigma_{CR}$ ) to shear strength ( $\tau_{CR}$ ). The term 'theoretical' refers to perfect crystals. The physical basis of the theory is that as a crack is loaded it will propagate by cleavage if  $\sigma_{CR}$  is achieved at the crack tip at a lower applied stress than that required for dislocation motion and shear  $\tau_{CR}$ . Clearly a decrease in the ratio  $\sigma_{CR}/\tau_{CR}$  can potentially lead to a ductile/brittle transition.

Rice and Thomson were in dispute with the consideration detailed above. They disagreed particularly with the implication that if the applied shear stress at the crack tip exceeds  $\tau_{CR}$  then crack propagation occurs by shear. They proposed that a crystal can only shear if  $\tau_{CR}$  is exceeded across an entire plane running through the crystal. They therefore put forward a more sophisticated model for cleavage crack propagation involving the stability of dislocations at the crack tip. The basis of this model is that there exists a distance from the crack tip,  $\epsilon_C$ , at which a straight dislocation is under conditions of unstable equilibrium. If  $\epsilon_C$  is less than the core radius of a dislocation then dislocations are spontaneously emitted from the crack tip and the shear mode of crack propagation is found exclusively. A simple expression for  $\epsilon_C$  was obtained:

$$\epsilon_C = \mu b / 10\gamma$$

$\mu$  = shear modulus  
 $b$  = Burgers vector  
 $\gamma$  = surface energy

By calculating  $\epsilon_C$  for a range of materials Rice and Thomson were able to show that if dislocations have a high core radius and  $\mu/\gamma$  is low i.e.  $< 7.5 \rightarrow 10$  then cleavage cannot occur - the general situation in F.C.C. metals such as aluminium. They did however introduce the possibility that environmental reactions or elemental segregation

could lead to a reduction in  $\gamma$  and a ductile/cleavage transition.

Since  $\sigma_{CR}$  in the Kelly et al model is also related to  $\gamma$  by a form of Griffith equation the two models are similar in their predictions of embrittlement effects. Mechanisms based on a reduction in  $\gamma$  have however been criticised in the past since surface energy is known to contribute only to a small extent to the total fracture energy in most ductile materials. The total work to fracture designated  $G_{IC}$  by Irwin (II2) (in plane strain) is known to be of the order of  $10^3 \text{ J/m}^2$  while  $\gamma$  is around  $1 \text{ J/m}^2$ . In the terminology of Orowan (II3)  $G_{IC} = 2\gamma + W_p$  where  $W_p$  is a plastic work term. It has been argued that a reduction in  $\gamma$  even to 0 could have little effect on  $G_{IC}$ . However if the physical processes occurring are considered, a reduction in  $\gamma$  to 0, i.e. a reduction in bond strength to 0, must lead to the complete absence of any plastic work.  $\gamma$  and  $W_p$  must be considered as dependent upon one another not exclusive. Such dependence has been proven in the case of steels, embrittled by metallic impurity segregation: McMahon and Vitek (II4) showed that a 95% reduction in fracture toughness was achieved by a reduction in cohesive energy of only 10%. Clearly, therefore, a fairly modest change in bond strength can lead to a very large change in work to fracture demonstrating that while plastic deformation must accompany brittle fracture the amount of such deformation and hence the energy absorbed during fracture is critically dependent on surface energy ( $\gamma$ ).

I.4.3 Embrittlement Due to Environmental Interaction. The principles under which normally ductile materials can fail in a brittle manner is clearly well established from a theoretical viewpoint. Any embrittlement mechanism can involve a lowering of  $\gamma$  via bond strength, as predicted by both theoretical models, or possibly by an increase in  $\tau_{CR}$ , the shear flow stress, via a dislocation locking reaction. The embrittlement theories developed based on these principles fall into two broad categories: Those involving surface adsorption and reaction alone, and those involving penetration of some species, notably hydrogen,

into the lattice ahead of the crack. The mechanisms have been investigated experimentally by a large number of workers both in their relation to S.C.C. and fatigue, and reference must be made to the literature referring to both areas in their discussion.

I.4.4. Embrittlement Via Dislocation/Corrosion Product Interaction. Embrittlement has been attributed to an increase in flow stress, due to an interaction between dislocations and corrosion product, in a relatively small number of studies, for example that of Stoltz and Pelloux (II5). Mechanistically they proposed that corrosion of the crack surfaces as they were exposed inhibited dislocation escape from the surface, preventing crack blunting and leading to cleavage failure. The mechanism can be related back to a reduction in  $\sigma_{CR}/\tau_{CR}$  in the Kelly et al model via an increase in  $\tau_{CR}$ . In fact this mechanism overlaps with those discussed earlier in which dislocation/oxide interaction was thought to lead to enhanced growth rates via void formation ahead of the crack. Stoltz and Pelloux attempted to confirm their proposals using a test in which the specimen polarisation was reversed every few load cycles. Tests were carried out on the commercial alloy 7075 in a 3.5% NaCl solution. These tests showed that under cathodic polarisation crack propagation rates were much reduced and the crack followed a plane approximately perpendicular to the stress axis. Under anodic conditions crack growth rates were increased and a fracture plane was followed which was not perpendicular to the stress axis, a fact which was attributed to cleavage. Since anodic polarisation was thought to promote the dissolution reaction and cathodic polarisation hydrogen evolution, Stoltz and Pelloux discounted hydrogen embrittlement mechanisms, which are discussed later. However as discussed earlier in the section I.3.2 the electrode potential at the crack tip may be very different from that at the specimen surface and the effect of cathodic polarisation on hydrogen permeation may also be important. Great care must therefore be taken in the interpretation of these results.

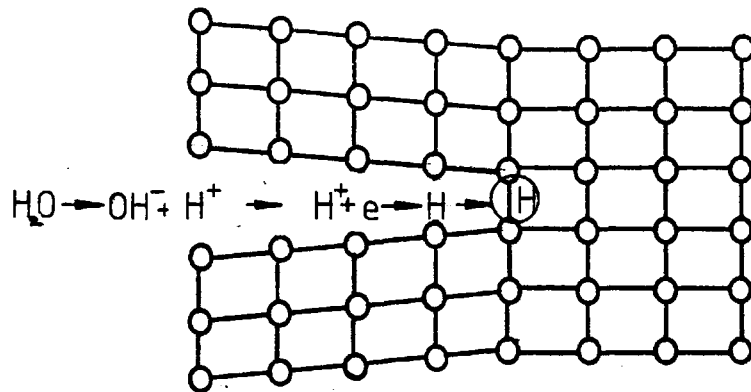
I.4.5. Hydrogen Embrittlement Mechanisms. The liberation of hydrogen at a crack tip under any conditions where the  $H^+$  reduction reaction is possible has formed the basis of a great

deal of debate concerning the significance of hydrogen as an embrittling agent. The general principle is that hydrogen interacts with interatomic bonds at the crack tip leading to intergranular decohesion or transgranular cleavage. Hydrogen embrittlement appears to be recognised as a likely contributory factor in both S.C.C. and corrosion fatigue, (see recent reviews by Bernstein and Thompson (II6) and Duquette (II7)) there is however no consensus about the actual mechanism by which this occurs. Two general mechanisms have been postulated, one based on the adsorption of hydrogen at the crack tip and the other involving bulk embrittlement via hydrogen penetration into the lattice ahead of the crack.

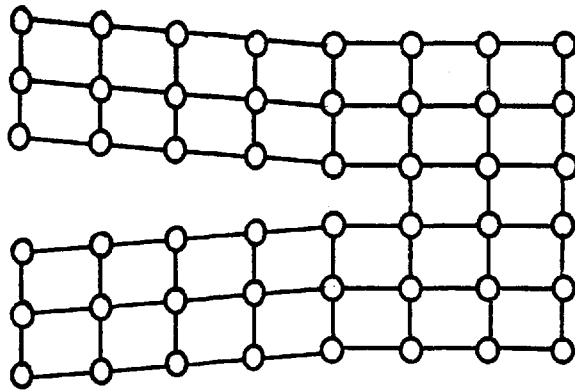
Hydrogen embrittlement by adsorption is based on the premise that atomic hydrogen, liberated by crack tip reaction, is adsorbed onto and interacts with strained bonds at the crack tip (Fig. 5.7). The mechanism which was originally proposed a number of years ago by Petch and Stables (IIS) is thought to be continuous; as a bond at the crack tip breaks another is exposed, adsorption takes place and the process is repeated.

The mechanism has gained a great deal of support in the corrosion fatigue literature since, unlike bulk embrittlement processes, it does not involve penetration of hydrogen into the matrix. The rates of reaction and transport of water can therefore be the only embrittlement controlling factors. As discussed earlier in section I.3.1 the results of the fracture mechanics/surface chemistry studies are consistent with these factors being rate controlling.

In a recent study, Bowles (84) attempted to prove that a hydrogen embrittlement mechanism was operative during crack propagation in aluminium alloys in moist air environments and that this occurred via an adsorption process: His experimental technique involved cycling in frequency blocks at frequencies of 0.01 and 20 Hz consecutively. A test environment of 10 p.p.m. water vapour in air was used ( $p_{H_2O} = 7.6 \times 10^{-3}$  torr). A simple calculation based on the critical pressure data obtained by Wei et al (97) (Fig. 5.4) yields the result that in this atmosphere at the  $\Delta K$  levels used, crack propagation at 0.01 Hz ought to occur in a 'brittle' manner, while at 20 Hz little



hydrogen  
adsorbed onto  
thereby weakening  
crack tip bonds



bonds rupture,  
crack advances,  
process repeats.

Schematic Representation of  
the Adsorption Embrittlement Mechanism

environmental effect should be observed. It would be expected therefore that if a surface reaction mechanism such as any of those involving shear mode cracking or the Stoltz/Pelloux type were operative, an increase in frequency from 0.01 → 20 Hz would result in an immediate change in fracture mode. Bowles, however, found that the change was not immediate and that a transition band of characteristically 'brittle' cracking was found before loss of environmental influence. The band was found to be  $\sim 1.7\mu\text{m}$  wide in 7075 T6 and to be independent of the number of cycles at the low frequency and stress intensity.

Bowles surmised that his results could be explained by one of two effects: he suggested that diffusion of hydrogen ahead of the crack during the slow cycles could lead to the transient band, but since the band width was independent of the number of slow cycles he dismissed this idea. (If a large number of low frequency cycles were applied then there would be available more time for hydrogen diffusion to occur ahead of the crack.) His final explanation put forward to explain the transient band behaviour involved surface diffusion of hydrogen: Bowles calculated that while surface diffusion of water was insufficiently fast to keep pace with the crack at 20 Hz hydrogen would be able to achieve this at crack growth rates of up to  $0.4\mu\text{m}/\text{cycle}$ ; higher than that observed in his tests. He therefore suggested that hydrogen, produced during the low frequency cycles diffused along the crack surfaces causing embrittlement via adsorption until it was used up, reaction and water transport rate being insufficiently fast to generate sufficient hydrogen to render the process continuous.

A number of workers have been critical of the adsorption or 'stressorption' mechanism both in its application to S.C.C. and fatigue. Some of this criticism has been fundamental in nature. For example, Thompson and Bernstein (II6) in a recent review state; "for hydrogen to effectively embrittle a material it must be present in the host lattice; there is no unequivocal evidence that surface hydrogen is an embrittling agent."

Experimental evidence which cannot be readily explained by an adsorption mechanism has been provided by Scamans (II9)

in intergranular and Bursle and Pugh (I06) in transgranular S.C.C. of aluminium alloys. In both studies regular arrest markings or striations were observed which suggested that crack propagation was discontinuous under constant load. Clearly an adsorption mechanism implies a 'bond by bond' embrittlement process which, these authors claimed, would be likely to give discontinuous propagation only on an atomic scale. They therefore proposed a bulk embrittlement mechanism in which an embrittled zone existed ahead of the crack through which the crack propagated, followed by blunting, arrest and re-embrittlement.

In fatigue, several studies involving crack propagation under varying load cycle wave shapes have provided some results which cannot easily be reconciled with an adsorption mechanism. For example, Barsom (I20) in his studies of corrosion fatigue crack propagation in high strength steels found that load dwells at maximum tensile load had no effect on crack growth rate. Selines and Pelloux (I2I) quantified the effect of wave shape on crack growth in aluminium alloys and found that growth rates were dependent upon the rise time of the cycle. They therefore concluded that embrittlement was dependent on the time during which plastic deformation was occurring at the crack tip during each cycle. They were unable to relate the time dependence to an adsorption process, unless, they suggested, some kind of film rupture process was involved. The results of Barsom are also of interest here because it must be the case that if the crack is maintained at the maximum stress intensity ( $K_{max}$ ) and adsorbing species such as hydrogen are available then the embrittlement process should continue and the crack should continue to grow. This is clearly not the case and one of the fundamentals of fatigue is of course that if load is held at  $K < K_C$  (or  $K_{ISCC}$  in the case of corrosion fatigue) crack growth does not continue.

Fracture mechanics studies of the effect of cyclic frequency on crack growth in aluminium alloys by Bradshaw and Wheeler (38) demonstrated that under fully embrittled conditions, i.e. at gas pressures above  $P_C$ , cyclic frequency had comparatively little effect on growth rate. This further supports the earlier wave shape results, since, one would expect that if an

adsorption embrittlement mechanism is operative then during the time that the crack tip stress intensity is greater than some critical cleavage value crack growth should be continuous, for example, at one half the frequency at the same  $K_{max}$  the crack growth rate ought to be doubled.

In conclusion, while a good deal of evidence exists to support an embrittlement mechanism based purely on adsorption, in particular the coordinated fracture mechanics/surface chemistry studies reported earlier, there are several features of crack growth both in S.C.C. and corrosion fatigue which are not readily explicable. These studies which have noted discontinuous cracking and no load dwell dependence, tend to suggest some mechanism which involves crack growth through an embrittled zone, followed by blunting and crack arrest.

Embrittlement via hydrogen actually dissolved in the metal matrix was originally proposed by Troiano (I22) and has attracted a great deal of research attention in subsequent years. A comparatively recent development of this theory was provided by Oriani (I23): He postulated that in regions up to a few atomic radii from the tip of a crack, a region in which interatomic bonds are subject to a considerable elastic strain, atomic hydrogen collected and reduced the cohesive strength below the applied tensile stress. A situation then existed in which transgranular cleavage or intergranular decohesion could occur.

Direct evidence that precharging specimens with hydrogen can lead to intergranular brittle failure has been provided by a number of workers: For example by Guest and Troiano (I24) who cathodically precharged specimens and Christodoulou and Flower (I25) who thermally precharged Al-Zn-Mg alloy specimens by exposure to superheated steam. The results of these studies are difficult to explain by a mechanism other than one involving hydrogen predissolved in the matrix.

Predissolved hydrogen can also have similar effects on fatigue as discovered by Smith, Jacko and Duquette (I26) They found that cathodic precharging had a significant effect on the fatigue life of specimens of 7075 T6 and high purity Al-Zn-Mg

alloys. This reduction in life was partially recovered by an intermediate annealing treatment suggesting some solid solution effect. Since surface finish has a great effect on fatigue life careful steps were taken to eliminate corrosion induced surface pits. The results should therefore be valid although it would have been more directly informative to measure crack growth rates rather than fatigue life. Once again, however, the results are difficult to explain by any mechanism other than one involving bulk embrittlement; failure in this case was however predominantly transgranular.

In their early studies of fatigue in aluminium alloys Forsyth and his coworkers concluded from metallographic observation that in moist environments crack extension occurred by an initially brittle process followed by blunting. This conclusion has been backed up by the more recent studies of Bowles (84): Bowles made use of a plastic crack infiltration technique which clearly demonstrated that initial crack extension was accompanied by very little plastic deformation and that blunting then occurred leading to a blunted crack at maximum crack opening. These studies together with those reported earlier of discontinuous cracking in transgranular S.C.C. all suggest that the crack grows through an embrittled zone ahead of the crack, a model in fact proposed by Bursle and Pugh (106) to explain discontinuous cracking in S.C.C.

From the fracture mechanics viewpoint Selines and Pelloux (121) were able to relate overall crack growth rates to their component parts by

$$\frac{da}{dn} \text{ total} = \frac{da}{dn} \text{ corrosion} + \frac{da}{dn} \text{ mechanical}$$

If a two stage process is considered involving an initial brittle phase, followed by blunting this interpretation is a most useful one:  $\frac{da}{dn}$  mechanical was taken to be the crack growth rate in dry argon, and therefore was not thought to involve any environmental effect.

In conclusion therefore it seems that a number of experimental observations suggest a two stage brittle-ductile transition

process occurring during each increment of crack growth involving the formation of an embrittled zone directly ahead of the crack; the embrittled zone being a result of hydrogen concentration. In order for such a mechanism to operate however it is necessary to describe the process by which hydrogen is transported into and collects in this region.

I.4.6. Hydrogen Transport and Distribution. The main criticism levelled at the application of a bulk embrittlement mechanism to fatigue has centred around hydrogen transport. For a bulk embrittlement mechanism to occur it must be possible for hydrogen to be transported ahead of the crack at a rate equal to that of crack growth. In the case of intergranular S.C.C. in aluminium alloys grain boundary hydrogen diffusivity, which is relatively high, has been invoked to explain the effect and it has been shown that crack growth rates can be related to diffusion rate (I27). The crack path in the case of fatigue in commercial alloys is, however, predominantly transgranular and here the mechanism is more difficult to apply since lattice diffusion of hydrogen in aluminium is extremely low (I28, I29).

Van Leeuwen (I27) and also Montgrain Scamans and Swann (99) have assumed that diffusion rates of hydrogen in aluminium can be described simply by  $(X=(Dt)^{\frac{1}{2}})$  at room temperature ( $X$ =diffusion distance,  $D$ =diffusivity,  $t$ =time). These workers were however involved with grain boundary diffusivities. A number of workers have measured the diffusivity of hydrogen in aluminium but vast discrepancies exist between the results. Two often quoted diffusivities are those of Eichenauer and Pebler (I28),  $D=0.21 \exp(-10900/RT)$  and Ransley and Talbot (I29),  $D=1.12 \times 10^{-5} \exp(-33500/RT)$ . Both groups however measured diffusivities at temperatures of the order of  $500^{\circ}\text{C}$  and all data for room temperature has been obtained by extrapolation from high temperatures. Such extrapolations give diffusivities of  $10^{-8}$  and  $10^{-19} \text{ cm}^2/\text{sec}$ . Bowles for example obtained a value of  $2 \times 10^{-16} \text{ cm}^2/\text{sec}$  by extrapolation of data obtained by Eborall and Ransley (I30). Clearly while the actual diffusivity may lie within this vast range at room temperature the actual mobility of hydrogen cannot be stated with any accuracy.

Christodoulou(I3I) was able to make an estimate of hydrogen diffusivity at low temperatures (I20°C) by measurement of pre-exposure embrittlement times, which were taken to represent the time for penetration of hydrogen through the specimen thickness. His calculations yielded a diffusivity of around  $10^{-8} \text{ cm}^2\text{sec}^{-1}$ , the upper limit of the high temperature extrapolations, and his results were in agreement with earlier studies by Ells and Evans (I32) However as discussed by Shewman (I33) grain boundary diffusion has been found to dominate the overall diffusion rate, particularly at low temperatures and hence, low temperature hydrogen diffusion data is likely to be an estimate of grain boundary hydrogen mobility rather than lattice diffusion within the grains, which is more appropriate here.

Using the above data it is possible to estimate the distance which hydrogen might diffuse during one load cycle. Using the two extremes of diffusivity and the simple  $X=(Dt)^{\frac{1}{2}}$  relationship these distances can be tabulated for various cyclic frequencies.

Table 5.I .

		X			
		$D=10^{-19} \text{ cm}^2\text{s}^{-1}$		$D=10^{-8} \text{ cm}^2\text{s}^{-1}$	
f Hz	t s	cm	Å	cm	µm
0.01	100.0	$10^{-8}$	1.0	$10^{-3}$	10.0
0.1	10.0	$10^{-9}$	0.1	$10^{-4}$	1.0
1.0	1.0	$10^{-10}$	0.01	$10^{-5}$	0.1
10.0	0.1	$10^{-11}$	0.001	$10^{-6}$	0.01
100.0	0.01	$10^{-12}$	0.0001	$10^{-7}$	0.001

Clearly since cyclic growth rates are of the order of 0.1 → 1µm/cycle D would have to be increased by at least a factor of 100 in order for hydrogen to penetrate ahead of a crack growing at a frequency of 100 Hz, even assuming the upper limit of diffusivity. It therefore appears that a bulk embrittlement mechanism involving simply lattice diffusion of hydrogen is quite impossible, a conclusion which has also been reached by Bowles (84).

If a bulk embrittlement process is taking place, then some more rapid mechanism of hydrogen transport must be operative. The most likely possible mechanism appears to be one of dislocation transport: The concept that hydrogen can be transported by dislocations was first put forward by Bastien and Azou (I34). They proposed that hydrogen could be swept in Cottrell Atmospheres in a similar way to carbon in iron. Bastien (I35) then progressed to show that the rate of dislocation transport could be related to experimental data on the strain rate and temperature dependence of S.C.C. in steels. This correlation, which was obtained as long ago as 1951, originally attracted very little attention and only recently has the possible significance of dislocation transport been realised.

Evidence has appeared in recent years which demonstrates that dislocation transport is operative in aluminium and its alloys. For example Foster, Jack and Hill (I36) found that the points of exit of tritium from precharged pure aluminium specimens were related to regions of plastic deformation. They found that under straining an effective diffusivity of up to  $10^5$ x higher than that found by extrapolation of the high temperature data was achieved. Further investigation by Donovan (I37) eliminated the possibilities of anomalous effects due to local heating or deformation induced release of surface adsorbed hydrogen and made the suggestion that dislocation transport might be of importance in the environmental cracking of aluminium alloys.

A quantitative relationship between hydrogen embrittlement and dislocation transport has been developed by Tien et al and Tien (I38, I39, I40). They developed the Cottrell Atmosphere model of hydrogen transport and attempted to calculate the dislocation velocity above which hydrogen atoms are dumped and transport cannot occur. They proposed an equation to give this critical velocity  $V_c$ :

$$V_c = \frac{D_H \cdot F_c}{KT}$$

where  $D_H$  = hydrogen diffusivity and  $F_c$  the critical force on the dislocation due to the presence of hydrogen above which hydrogen is dumped.  $F_c$  was calculated to be  $=E_b/30b$  where  $E_b$  = the hydrogen binding energy and  $b$  the Burgers vector. Using these equations Tien and his coworkers progressed to calculate the maximum hydrogen penetration distances during different periods of plastic deformation. Rather than measuring absolute distances they calculated the ratio of dislocation enhanced distance to that predicted by random walk diffusion and the results are shown in Table 5.II for various materials. Their calculations showed that the enhancement,  $X_c/X_D$  ( $X_c$  = dislocation transport distance.  $X_D$  = random walk diffusion distance ) was approximately given by  $X_c/X_D = 10^2 \sqrt{t_p}$  where  $t_p$  = the duration of plastic deformation for  $D_H = 10^{-10} \text{ cm}^2/\text{second}$  (an intermediate estimate of diffusivity of hydrogen in aluminium). In the case of fatigue  $t_p = 1/f$  where  $f$  = cyclic frequency and therefore  $X_c/X_D = 10^2 f^{-1/2}$ . So for no dislocation enhancement of hydrogen penetration a cyclic frequency of around  $10^4 \text{ Hz}$  is implied.

Clearly the possibility that dislocation transport could lead to enhancement of hydrogen penetration ahead of the crack is a real one although since all quantitative assessments involve the lattice diffusivity of hydrogen in aluminium, which is basically unknown at room temperature, the actual magnitude of the effect cannot really be estimated. From a more physical viewpoint Tien et al have discussed some of the possible implications of dislocation transport: They suggested that appreciable transport can only occur via mobile dislocations and that as dislocations become tangled and form networks hydrogen may be dumped and may build up in interstitial sites in significant quantities, and may also segregate to particles, grain boundaries etc.

#### I.5. Fractographic Features.

Fatigue striations, which are particularly well defined in the case of aluminium alloys, have received a great deal of research attention since they yield important information about the mechanisms of crack growth. They are also of great technological importance since they can give an assessment of local crack growth rate and can therefore play an important part in the

Table 5.II. Penetration Depth Ratios for  $\sqrt{Dt}$  vs. Dislocation Sweep-in Transport of Hydrogen in Fe and Ni Based Alloys.

t(sec)	f	$X_C/X_D$	$X_C/X_D$
		Fe-Base	Ni-Base
Ihr	ICPH	$4.4 \times 10^4$	$4.4 \times 10^2$
60	ICPM	$1.8 \times 10^4$	$1.8 \times 10^2$
I	IHz	$2.4 \times 10^3$	$2.4 \times 10^1$
$2 \times 10^{-2}$	60Hz	$3.0 \times 10^2$	$3.0 \times 10^0$
$1 \times 10^{-3}$	IKHz	$7.4 \times 10^1$	$7.4 \times 10^{-1}$
$1 \times 10^{-4}$	10KHz	$2.2 \times 10^1$	$2.2 \times 10^{-1}$
		$D_H \approx 10^{-6} \text{ cm}^2 \text{ s}^{-1}$	$D_H \approx 10^{-10} \text{ cm}^2 \text{ s}^{-1}$

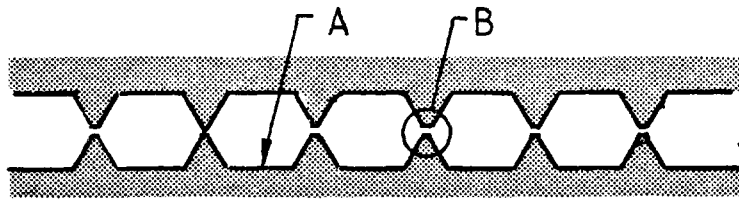
After Tien (I38)

investigation of in service fatigue failures ( 2 ). In the subsequent sections it is proposed to discuss some of the numerous mechanisms which have been put forward to predict their formation and also to discuss some of the more general features of fatigue fractures in aluminium alloys.

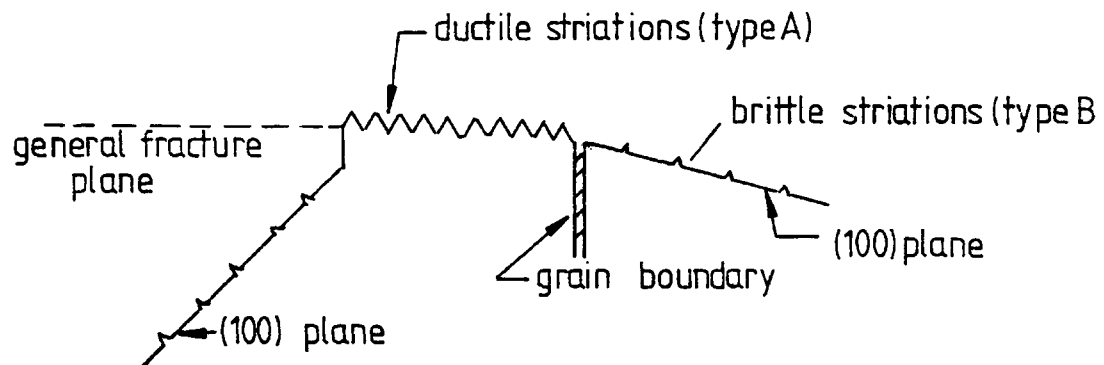
I.5.I. Mechanisms of Fatigue Striation Formation. A very large number of mechanisms have been proposed to describe the formation of fatigue striations. Most of these mechanisms have been based on ductile, shear mode, mechanisms of crack propagation, and only a few have included the possibility of brittle crack extension. It is obvious that striation formation must involve plastic deformation so many of the mechanisms are also reconcilable to a brittle/ductile crack propagation mode.

The first mechanism put forward to explain the formation of fatigue striations, that of Forsyth and Ryder (68), did in fact involve such a brittle/ductile transition process: The striation profile proposed is shown in Fig.5.8 and involves the formation of flat fracture facets by brittle growth separated by raised portions, marking regions of plastic deformation. The ductile markings were proposed to mark the limit of crack extension in one cycle and striation spacing was therefore believed to be directly related to cyclic crack growth rate.

In subsequent work Stubbington (70) and Forsyth (71) noted the presence of striations of two different profiles in the case of Al-Zn-Mg alloys: The first, type (A) was observed to be of sawtooth profile with the second, (B), similar to that originally proposed by Forsyth and Ryder but in fact a mirror image, the fracture surface being traversed by slots rather than ridges (Fig.5.9 ). The latter were found to be more prominent on corrosion fatigue fractures and were therefore termed brittle. This type of striation was also found on crystallographic fracture facets, (70), which were taken as evidence for cleavage, as discussed earlier. Sawtooth, type A, striations were found on non crystallographic areas of fracture and were therefore described as 'ductile'. It was suggested that both types of striation might occur

Fig. 5.8

Striation profile as suggested by Forsyth and Ryder [68]. Brittle fracture is indicated at A with ductile fracture at B

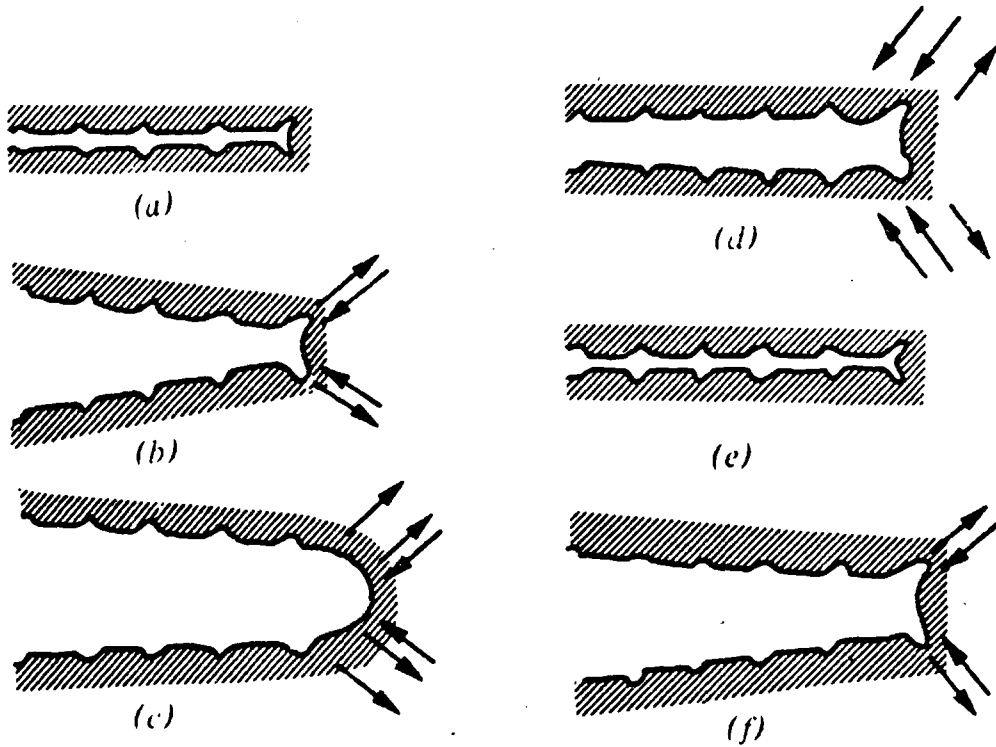
Fig. 5.9

Striation types A and B as visualised by Stubbington [69]

together on a single fracture surface, in adjacent areas as represented diagrammatically by Stubbington (70), (Fig.5.9).

The influence of test environment on striation formation in aluminium alloys has been demonstrated by a number of workers. For example Meyn (142) found that fatigue striations were not apparent on vacuum fatigue fractures. His evidence was not however regarded as conclusive: Ritter and Wei (179) were able to observe striations on the fracture surfaces of Ti 6%Al 4%V tested in vacuum and suggested that the resolution of Meyn's electron replica observation technique would be insufficient to detect striations at the crack growth rates involved. Later Wanhill (108), using electron replica techniques was able to resolve some surface markings on vacuum fatigue fractures so the possibility exists that striations are not purely an environmental effect. It should be noted however that the markings observed by Wanhill were very different in profile from those found on specimens fractured in laboratory air.

A number of striation formation mechanisms have been proposed based purely on shear modes of crack growth. The first of these, which does not imply any environmental influence on striation formation was the widely accepted plastic blunting process (P.B.P.) as proposed by Laird and Smith (83) and later refined by Laird (72). The model was based on observations of high strain fatigue crack growth in pure metals such as nickel and is simple in concept: Fig.5.10. The basis of the process is that work hardening at the crack tip during crack opening prevents the reversal of dislocation motion during closure leading to the double eared notch profile at minimum load. The model has the advantage that it can predict the formation of striations in non crystalline materials such as polymers but it has been criticised in its application to metals in that in its simplest form it does not involve any crystallographic considerations. Laird in his development of the model did however suggest that cracks may follow  $\{001\}$  planes in F.C.C. metals owing to the symmetry of slip systems at the crack tip-; a proposal similar to those of Pelloux (73) and Neumann (74) discussed earlier in section I.2. Further criticism has been levelled at the model from an environmental viewpoint since clearly even if



Schematic representation of the plastic blunting process of fatigue crack propagation in the Stage II mode: (a) zero load; (b) small tensile load; (c) maximum tensile load of the cycle; (d) small compressive load; (e) maximum compressive load of the cycle; and (f) small tensile load in the succeeding cycle. The double arrowheads in (c) and (d) signify the greater width of slip bands at the crack in these stages of the process. The stress axis is vertical.

Striation Formation as visualised by Laird[72]

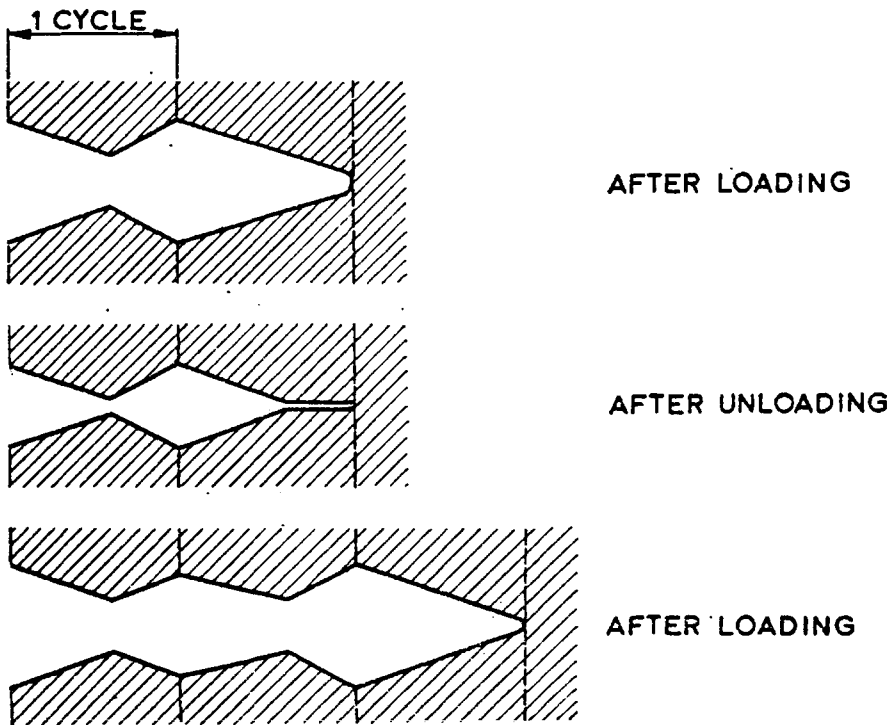


Fig. 5.11

Striation Formation as visualised by Schijve[40]

striations are present in vacuum they are very different from those found in laboratory air.

The Laird and Smith model of striation formation obviously most easily relates to the formation of type B striations, using the Stubbington terminology. Hertzberg (143) claimed however that all striations found on fatigue fractures of engineering materials at realistic crack growth rates (i.e. not high strains) were of a sawtooth profile, type A, and that any results to the contrary were a shadowing artifact of the electron replica techniques used. He then suggested a possible mechanism for the formation of this type of striation based upon the assumption that the two striation flanks were parallel to two operative slip systems at the crack tip i.e. segment of {111} planes. In such an orientation the overall fracture plane could, he suggested, be a {001} with the striation flanks at  $\sim 55^\circ$  to it. The mechanism was not developed in great detail but presumably the alternate activation of the two operative slip systems was thought to be responsible for striation formation.

A model for the actual deformation processes occurring at the crack tip leading to the formation of type A striations was suggested by Schijve (40) Fig. 5.II, who believed that crack tip resharpening occurred during crack closure. His suggestions formed the basis of the mechanisms developed by Pelloux (73) and Bowles and Broek (107). As discussed earlier Pelloux considered crack propagation to occur by an alternating shear process and crack surface oxidation to lead to growth rate enhancement in oxidising atmospheres. The striation formation process developed by Pelloux was similarly based around crack surface oxidation. The prevention of reversal of slip on planes passing through the crack tip due to oxidation, was postulated to lead to slip on a number of parallel systems, Fig. 5.2, giving rise to striation formation. In vacuum, the lack of oxidising species was taken to prevent this process leading to the non occurrence of striations in vacuum. With reference to his model of fatigue crack growth, Pelloux predicted that the striations would lie along  $\langle 110 \rangle$  directions.

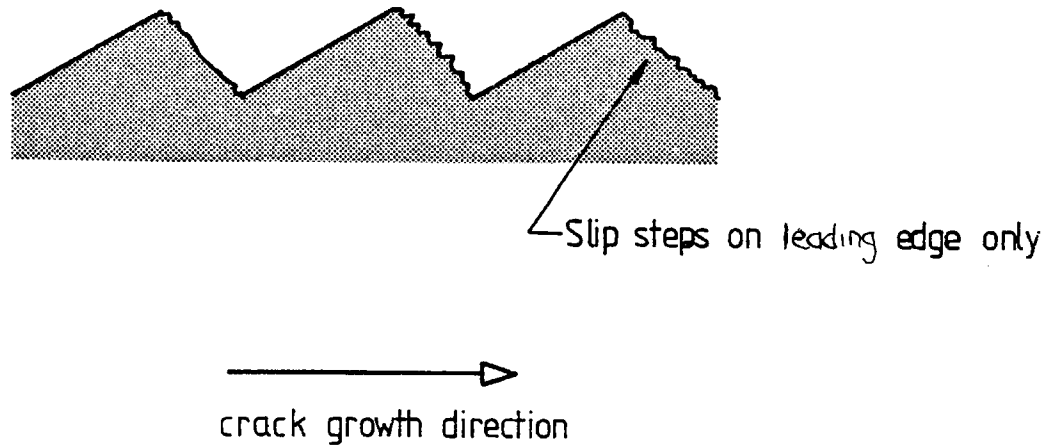
Experimental evidence for this kind of mechanism has been

provided by Neumann (74) in pure copper single crystals. The crack tip profile was observed during loading and unloading at high plastic strain and shapes very similar to those predicted by Pelloux were observed. Clearly such studies in commercial aluminium alloys would be quite impossible and supportive evidence has been limited to crystallographic studies using etch pitting techniques (73,107) and the TEM studies carried out by Bowles and Broek (107): As mentioned earlier Bowles and Broek noted a fracture plane close to  $\{011\}$  using TEM techniques. They also noted using shadowed replicas, that slip steps were to be found on the leading edges of striations (type A) (Fig. 5.12) and developed the Pelloux model to describe this. They also found using the TEM that subgrain bands lay approximately below the peak and leading edge of the striations and ascribed this to deformation occurring during crack closure.

This mechanism has the advantage that supportive evidence exists in its application to high strength aluminium alloys while that of Laird has only been actually proven at relatively high plastic strains in 'model' materials such as pure nickel. Common to both metals is the assertion that the striation formation occurs during crack closure, but the Bowles and Broek mechanism can only successfully predict the type A striation profile and Laird's only type B.

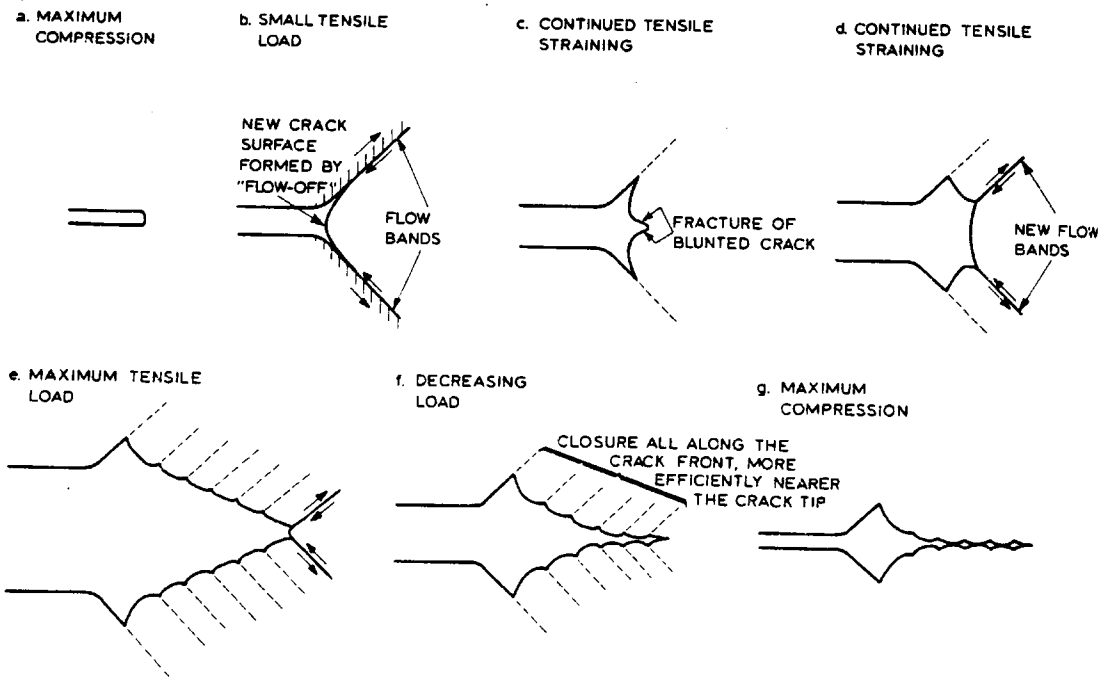
A totally different view has been taken of striation formation by Tomkins (144) and Tomkins and Biggs (145). They studied striation formation in pure aluminium and various polymers at very high plastic strains using light microscopy. They proposed a mechanism which is fundamentally different from all the others. The mechanism is summarised in Fig. 5.13. It involves plastic flow on shear bands as the crack is loaded leading to the formation of the double eared notch shown. If work hardening is exhausted before maximum crack opening displacement is reached, fracture can occur at the crack tip leading to a repeat of the process and the formation of a secondary striation. This implies that more than one striation might form in one cycle although Tomkins and Biggs stated that the first striation would be much more apparent. Evidence was presented in their publications to suggest the occurrence of

Fig. 5.12



Detailed Striation Profile as observed by Bowles and Broek[107]

Fig. 5.13



The Tomkins and Biggs [145] Model of Striation Formation

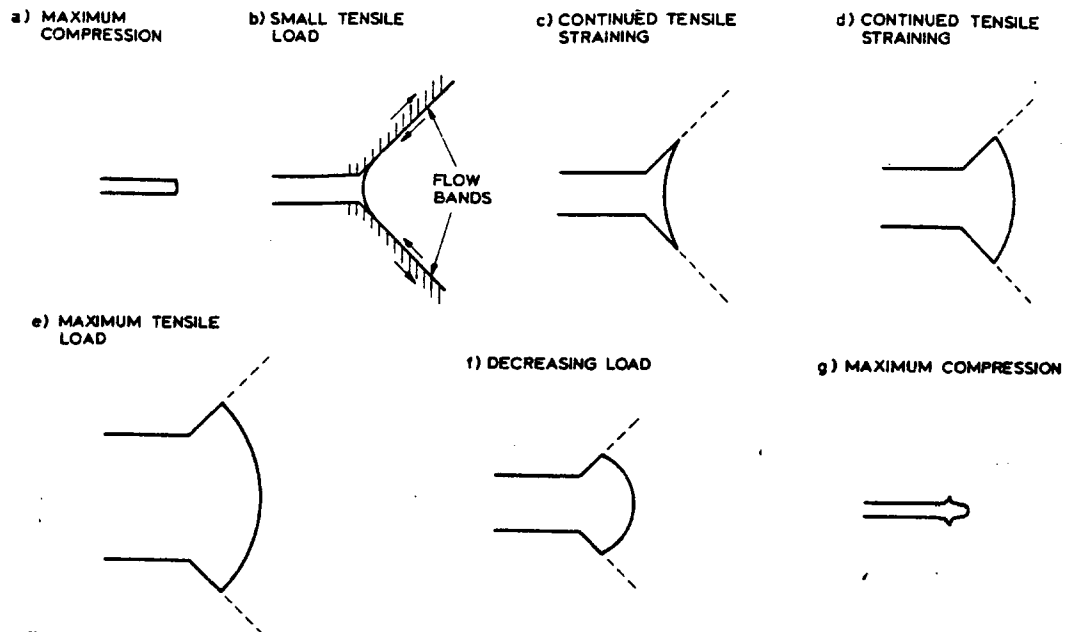
this process during low cycle fatigue at high plastic strain in the materials investigated. Tomkins and Biggs did not however claim that this mechanism could be applied to the high cycle fatigue regime.

Such a mechanism has been applied to high strength aluminium alloys by Wanhill (I08). He studied fatigue crack propagation in 2024 and 7075 alloys in air and vacuum. Using a programme load sequence and electron replica techniques to investigate the fractures he was able to relate a heavy type B striation to a large tensile load excursion, he therefore invoked the Tomkins and Biggs model. He also developed the model to include environmental effects: Wanhill proposed that in laboratory air adsorbed species promoted stage 2 of the Tomkins and Biggs model - fracture at the tip of the blunted crack - while in vacuum this tended not to occur leading to a sequence shown in Fig.5.I4 and much reduced growth rates. Wanhill observed complex ripple markings on vacuum fatigue fracture surfaces, the formation of which he explained by this process.

Wanhill's application of the model has received a certain amount of criticism, particularly from Laird and De la Veaux (I46) They invoked the evidence of McEvily (I47) that the slot in the type B striation was produced during crack closure. Once again, however, this evidence was obtained by observing crack growth in model systems in the high plastic strain range and may not be applicable.

Recently, observation has been made by Bowles of the crack tip profiles produced during crack growth in high strength aluminium alloys using a crack infiltration technique. The results obtained are in agreement with the predictions of Laird, that crack closure leads to the formation of the double eared notch.

In conclusion, there seems to be no general consensus about the mechanism of striation formation and the profile of the striation produced. Most mechanisms are based around observation at high plastic strains, where the effect of any environmental process may be reduced. Two types of striation have been observed but no mechanism has been found which can



Modification of the Tomkins and Biggs  
Model for Crack Growth in Vacuo  
(after Wanhill [108])

successfully predict the formation of both types and the circumstances under which they are produced.

I.5.2. General Features. A recent study has been made by Forsyth and Bowen (57) of the general fracture surface appearance produced during stage II crack growth in laboratory air environment in the commercial AL-Zn-Mg-Cu alloy 7I78. At  $\Delta K \approx 5 \text{ MNm}^{-3/2}$ ,  $R=0.1$  a network was found of approximately normally oriented flat facets with each facet corresponding roughly to a grain. At slightly higher  $\Delta K$  ( $\sim 7 \text{ MNm}^{-3/2}$ ) this structure gave way to a series of parallel markings running along the direction of the crack growth and termed 'river markings'. Structures apparently similar to this were also observed by Cina and Kaatz (148) who described them as 'ridges'. They were unable to resolve striations on these ridges and hence attributed their formation to a mechanism of crack growth not involving striation formation. Forsyth (71) in his earlier studies attributed the formation of fracture facets to crystallographic fracture in the case of corrosion fatigue, striations were however resolved on these facets. With increasing stress intensity, ( $\Delta k > 10 \text{ MNm}^{-3/2}$ ,  $R=0.1$ ). Forsyth and Bowen noted that intermetallic particles began to be incorporated in the fracture surface. This involvement showed itself first by the appearance of chevron markings with intermetallics lying at the point of the chevron. This was followed at higher stress intensity by isolated fracture regions associated with the particles. These were not however believed to be regions of ductile tearing, rather regions of fatigue crack growth under conditions influenced by the presence of the particle.

Ductile dimples formed by fibrous tensile failure in the region of intermetallics was noted at  $\Delta K > 20 \text{ MNm}^{-3/2}$  ( $R=0.1$ ). These dimples and voids were found to be much deeper than the irregular plateaux produced at lower  $\Delta K$  but were linked by regions of cyclic crack growth.

## I.6. The Influence of Metallurgical Variables.

I.6.I. Precipitate Distribution. In the previous sections, a broad outline has been given of the mechanisms of fatigue crack growth in aluminium alloys under mildly corrosive conditions. The possibilities of crack growth involving both

shear and cleavage components have been noted, and clearly dislocation motion has a significant part to play. It may be entirely responsible for crack growth or be involved via plastic blunting of an initially brittle crack and/or dislocation transport of hydrogen.

As detailed in Part 3, high strength aluminium alloys such as 7010 and 2024 contain in their normal heat treated condition small ( $<0.1\mu\text{m}$ ) coherent or semi-coherent particles produced by precipitation hardening. These particles are principally  $\eta'$  and  $\eta$  ( $\text{MgZn}_2$ ) in the case of 7000 series alloys and GPB zones and S ( $\text{CuMgAl}_2$ ) in 2000 series alloys. The conditions under which peak strength can be achieved in these alloys have been extensively detailed, see for example Fine (149) for a recent review. While very large increases in yield strength have been achieved by age-hardening it has been found that increases in fatigue endurance are relatively modest (Table 5.III). For example the ratio of ultimate tensile stress (U.T.S) to fatigue endurance limit (unnotched) increases dramatically with ageing in 7075. Compare for example the alloy 5086 in cold worked condition: While having a much lower tensile stress, in terms of fatigue properties the two are identical. The poor ratio has been found to be particularly the case in peak aged materials such as 7075 T6. The explanation for this has generally been that when precipitate particles are small glide dislocations can cut particles during plastic deformation. While this may be a condition resulting in high yield stress it leads to a low rate of work hardening since dislocations can continue to pass through cut particles. Thus deformation is localised into groups of a few active slip planes and bands are formed, a condition described as 'planar slip'.

This effect has been investigated in fatigue by a number of workers, both from the point of view of crack initiation and the cyclic stress-strain response. In the early work of Stubbington and Forsyth (42) the localisation of slip and formation of cyclic slip bands was found to be prevalent in peak aged Al-Zn-Mg ternary alloys and was inhibited by over-ageing. Slip band formation was found to lead to the production of extrusions and intrusions on the specimen surface

Table. 5.III.

			YS	TS	FL	FS/TS
Precipitation	2024	O	11000	27000	13000	0.48
Hardened		T3	50000	70000	20000	0.29
		T4	47000	68000	20000	0.29
	7075	O	18000	33000	17000	0.51
		T6	73000	83000	23000	0.28
Work	5083	O	21000	42000	22000	0.52
Hardened	5083	H32I	33000	46000	22000	0.48
	5086	O	17000	38000	21000	0.55
	5086	H34	37000	47000	23000	0.49

FL = fatigue limit

TS = tensile strength

From Fine (I49)

which were a precursor to crack initiation. Hence the poor endurance limit of peak aged material was attributed to slip band formation. The cyclic stress-strain response has also been related to slip band formation by Sanders and Starke (155). Here a reduction in cyclic yield stress was found during the cycling of peak aged alloys, whereas underaged alloys in particular exhibited cyclic hardening. This effect was shown to be associated with the formation of slip bands.

The actual process of cyclic slip band formation has been attributed to two possible effects. Firstly, as noted earlier precipitate cutting was found in peak aged material and Forsyth and Stubbington suggested that the repeated cutting of particles during cycling led to their falling below the critical size and to their resolution. Hence softened bands were formed and strain was further localised. The second possibility, suggested by Lynch and Ryder (150) was that local overageing might occur due to dislocation enhanced diffusion. In the Al-Zn-Mg-Cu alloy 7050, a recent rather interesting study of this process has been carried out using differential scanning calorimetry (DSC) by Papazian et al (151). These workers discovered that in an underaged condition precipitate dissolution was found to occur during cycling with no evidence for overageing. In an overaged condition however the alloy exhibited limited further ageing during cycling with no apparent reversion. It was concluded therefore that in the overaged condition the  $\eta$ (MgZn<sub>2</sub>) particles could not be sheared.

As mentioned previously most fatigue studies of the formation of slip bands and interaction of precipitates with dislocations have centered around crack initiation and cyclic stress strain response. However some workers have attempted to relate these processes to stage II crack propagation. For example, Lynch (152) suggested that plastic deformation around a stage II fatigue crack might also involve precipitate resolution and slip localisation, thereby leading to increased crack growth rates in alloys containing shearable precipitates. In fact Lynch proposed that glide on intersecting slip systems at the crack tip gave rise to the formation of a precipitate free slip band on a bisecting plane ahead of the crack and hence to crack growth on this plane. Clearly these suggestions

are based around a ductile mode of crack growth and hence the precipitate reversion enhancement of crack growth would be expected in dry environments. Lin and Starke (I54), however, found that decreasing the Cu content in an Al-Zn-Mg-Cu alloy and producing a microstructure of readily shearable precipitates (see Part 3 for a discussion of the influence of copper on precipitation) gave rise to a reduced crack growth rate under dry conditions. These workers believed that slip band formation led to crack branching thereby explaining the effect. Hence the validity of a theory of crack growth rate enhancement due to precipitate cutting would appear to be in some doubt.

The influence of the planar slip tendency on mechanisms of embrittlement has received a good deal of attention in relation to S.C.C. but most of this work has been concerned with dislocation pile-up leading to crack initiation (I53) which is of no concern here. In fact the beneficial effect of copper additions on S.C.C. in Al-Zn-Mg alloys has been attributed to this process.

In a recent study Lin and Starke (I54) showed that copper content had the effect of reducing fatigue crack growth rates in moist environments. Hence they were of the opinion that the formation of intense slip bands at the crack tip associated with precipitate cutting gave rise to an increase in the dislocation transport of hydrogen ahead of the crack; dislocations moving more easily within the slip bands. Hence the possibility of precipitate distribution involvement in the embrittlement mechanism itself is a real one.

I.6.2 Large Inclusions and Grain Structure. The large inter-metallic inclusions found in commercial high strength aluminium alloys are well known to influence fracture toughness as discussed in Part 3. They have also been found to have some effect on fatigue crack propagation: Sanders and Starke (I55), for example, found that in the case of 7050, heat treatments resulting in large ( $\approx 10\mu\text{m}$  diameter) particles of  $\text{S}(\text{CuMgAl}_2)$  increased fatigue crack growth rates. Albrecht et al (I56) also noted a similar effect due to chromium rich particles in the alloy 7075. The plate-like particle morphology was considered important in this case. Broek (I57) concluded, however

that their effect would only be appreciable at high  $\Delta K$  where particles were associated with ductile tearing. This would be expected from the fractographic observations of Forsyth and Bowen discussed earlier, since particles were often incorporated into fracture at high  $\Delta K$ . Broek's conclusion that at intermediate  $\Delta K$  large inclusions would have little effect was supported by his own experimental results and also those of El Soudani and Pelloux (I58).

Forsyth and Bowen found that grain size had little effect on growth rates in laboratory air in the alloy 7I78 and their findings have been generally supported by other workers. Changes in crack propagation behaviour have been attributed to grain shape in some circumstances: For example, Lynch and Ryder (I50) discovered that cracks followed an intergranular path in a high purity Al-Zn-Mg ternary alloy with an approximately equiaxed grain structure. However, exclusively transgranular cracking in the transverse direction was noted in a commercial alloy of elongated grain structure. The change in failure mode was attributed to the tortuous crack path that would have been necessary for an intergranular crack path.

## 2. EXPERIMENTAL RESULTS.

### 2.1. Introduction.

The majority of results which have been obtained concern crack propagation in 7010 T76 with a laboratory air environment (relative humidity approximately 50%) and at a stress ratio (R) of 0.1. It is therefore proposed to detail the observations made of fracture under such conditions, followed by an appraisal of the effect of loading conditions and test environment. The results obtained from 2024 T3 are also presented here.

### 2.2. General Fracture Appearance.

The observations made of the fracture surfaces at low magnification in the SEM are summarised in Figs. 5.15 and 5.16. Both stress intensity and grain structure were found to have an effect on the fracture appearance: At low stress intensity range,  $\Delta K < 10 \text{ MNm}^{-3/2}$ , particularly in the case of the centre notched specimen types, the surface appearance was one of elongated facets running along the direction of crack growth. These facets were admixed with less regular areas of fracture with increasing  $\Delta K$  and large intermetallic particles ( $> 10 \mu\text{m}$  diameter) became increasingly evident on the fracture surface. These regions, as the maximum stress intensity  $K_{\text{max}}$  approached  $K_{\text{IC}}$  ( $\sim 35 \text{ MNm}^{-3/2}$ ), were in turn interspersed with regions of ductile tearing. At  $\Delta K = 26 \text{ MNm}^{-3/2}$ , however, (Fig. 5.15(c)) the greater proportion of the fracture surface consisted of (Fig. S36) fatigue fracture delineated by striations rather than ductile dimple fracture. The faceted structure was by this stage completely absent. Facets were found to be influenced greatly by grain orientation, (Fig. 5.16): The crack growth direction in the initiation type centre notched specimens was both transverse to and along the long transverse (L-T) grain axis (Fig. 5.17). Abrupt changes in the faceted structure were observed along lines corresponding to the planar grain boundaries, which, as discussed in Part 3(2.1), were found to be well marked. In the case of the C.T design specimens crack growth occurred along the L-T direction and the structure was less well marked. In all cases the overall plane of fracture was approximately perpendicular to the load axis, excluding final shear failure which occurred at an angle of about  $45^\circ$  as

Fig. 5.I5. General appearance of fracture surfaces, laboratory air failure, R=0.I. Centre notched specimen type.

(a)  $\Delta K(\text{mean}) = 6\text{MNm}^{-3/2}$ .

(b)  $\Delta K(\text{mean}) = 16\text{MNm}^{-3/2}$ .

(c)  $\Delta K(\text{mean}) = 25\text{MNm}^{-3/2}$ .

Crack growth directions arrowed.

Fig. 5.I6. The influence of grain structure on general fracture appearance.  $\Delta K \approx 15\text{MNm}^{-3/2}$ . R=0.I.

(a) crack growth along L.T. direction C.T. design specimen.

(b) crack growth along S.T. direction, centre notched specimen.

Crack growth directions arrowed.

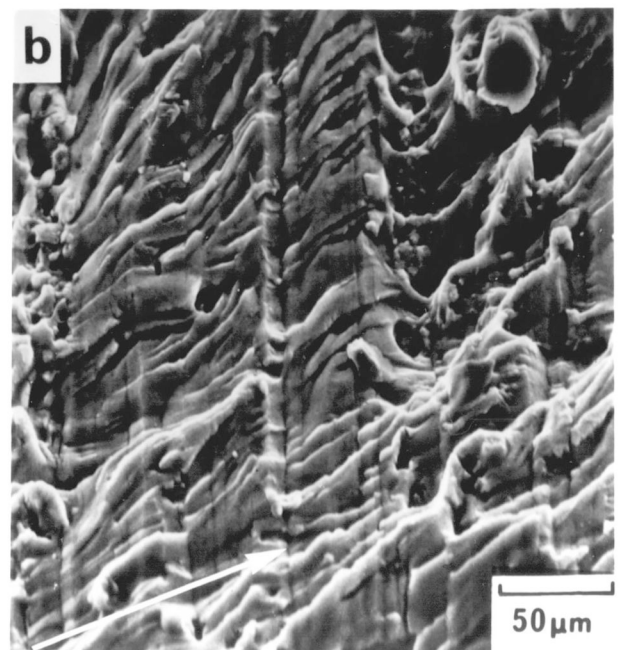
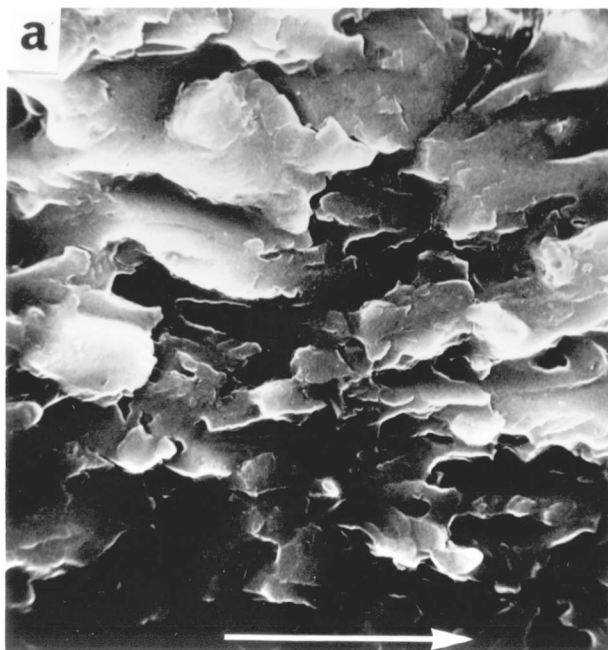
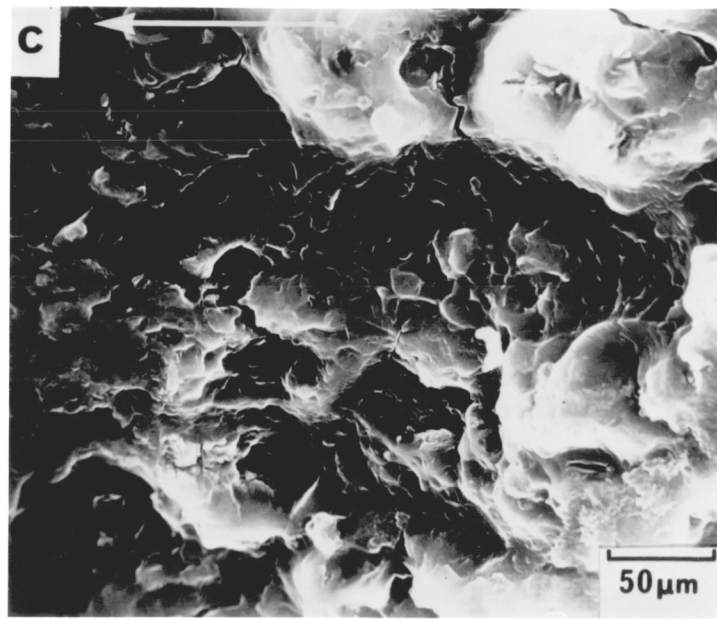
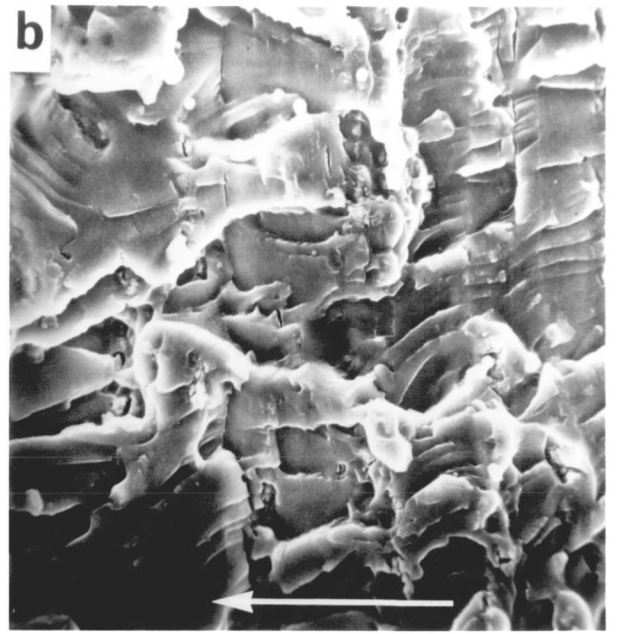
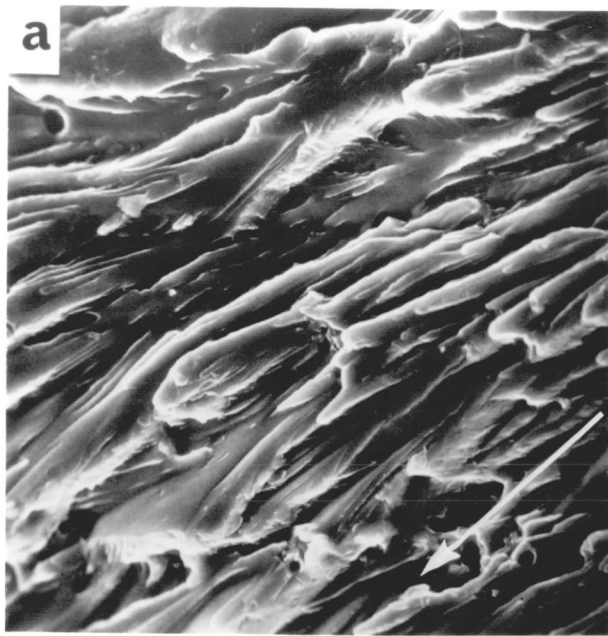
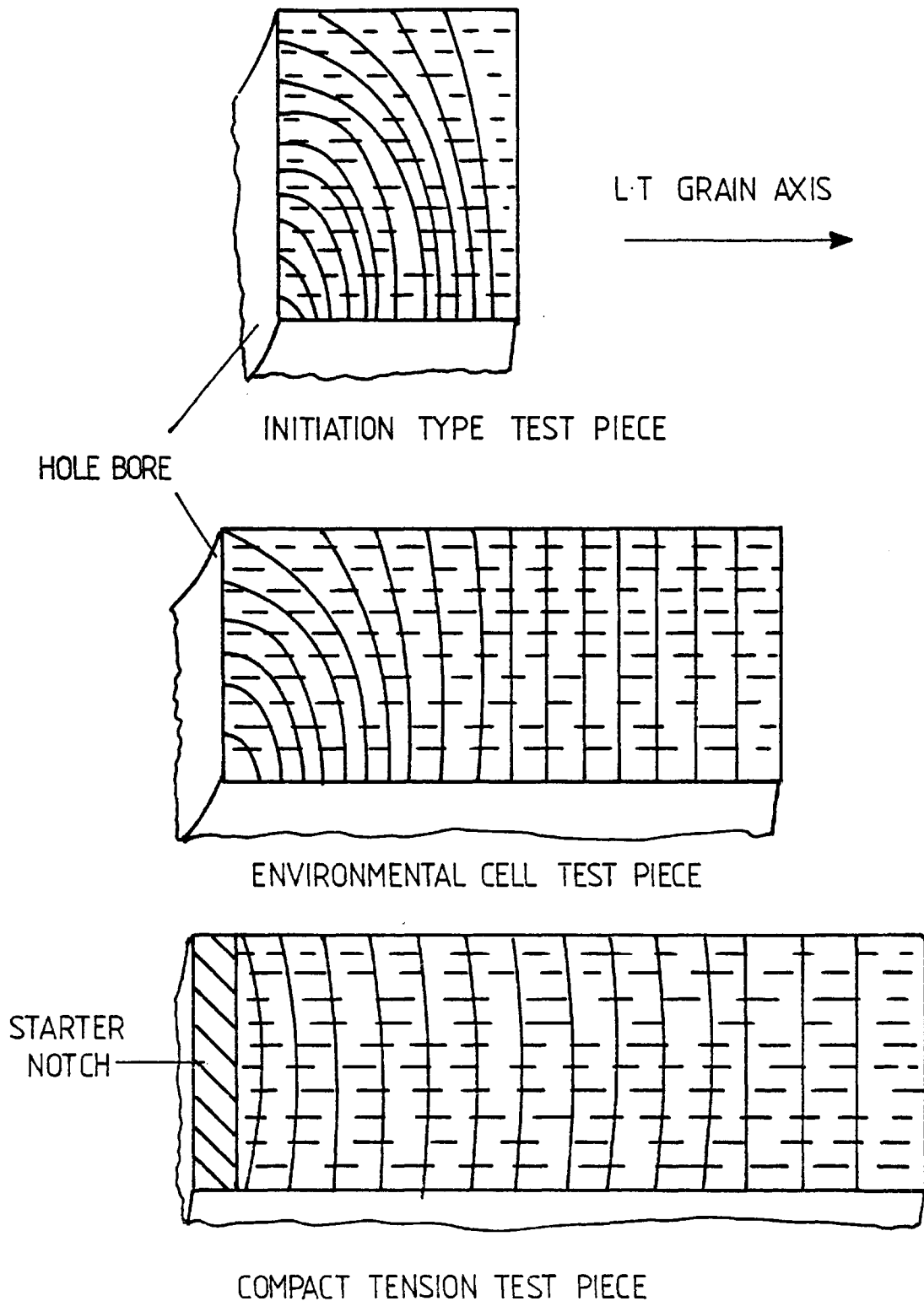


Fig. 5.17



The Relationship Between Crack Front Direction and Grain Structure

expected. No effect of test frequency was observed on the fracture appearance.

### 2.3. High Resolution Fractography.

The high resolution (HRSEM) studies were based around the observation of fatigue striations. In the vast majority of cases, striations were of one of two types, quite different in appearance. Type A (Fig.5.I8) were found to be of a saw-tooth profile with slip steps on the leading edge (i.e. the edge facing away from the crack origin). The opposite edge was found to be generally featureless under all circumstances. Type B striations (Fig.5.I9) consisted of essentially parallel fracture facets separated by parallel sided slots. The inter-striation facets were apparently smooth and featureless.

Fatigue striations were not found to cover the whole of the fracture surface, even under conditions where stable crack jumps would not be expected (i.e.  $K_{max} \ll K_C$ ). Areas were found to be free of any markings even at high tilt angles where any topographic contrast would be maximised. Striation free regions were found adjacent to areas of well marked striations (Fig.5.20). No evidence was found to suggest contact of opposing fracture surfaces and associated fretting.

Striations of types A and B were found over the whole range of  $\Delta K$  and at all test frequencies employed. The types of fracture facet upon which the two types were observed were found to differ however. Type A striations were generally found to occur only on irregularly shaped facets and were particularly well marked on areas inclined at a steep angle to the overall plane of fracture (Fig.5.20). Stereoscopic observations showed the featureless edge of the striations to be approximately perpendicular to the viewing direction while the edge delineated by slip markings was at a steep angle to it. It must be emphasised, however, that type A striations were not found exclusively on these steeply angled facets. While type B striations were also observed on regions of this type they were found to occur, to the exclusion of type A, on the elongated facets described earlier (Fig.5.2I). Each facet was found to be covered with type B striations which

Fig. 5.I8. Type A fatigue striations with stereo pair of corresponding area HRSEM image. Crack growth direction arrowed.

Fig. 5.I9. Type B fatigue striations with stereo pair of corresponding area HRSEM image. Crack growth direction arrowed.

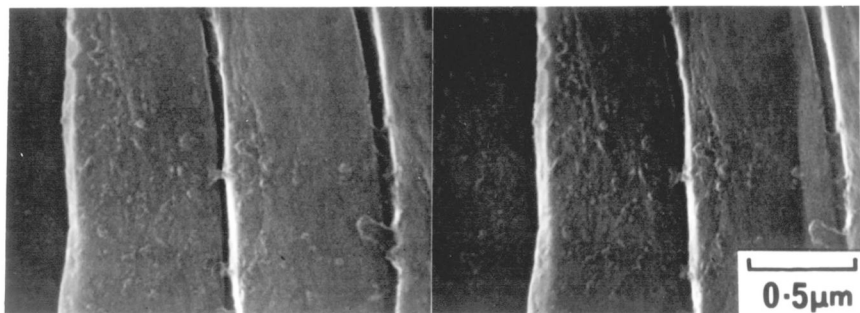
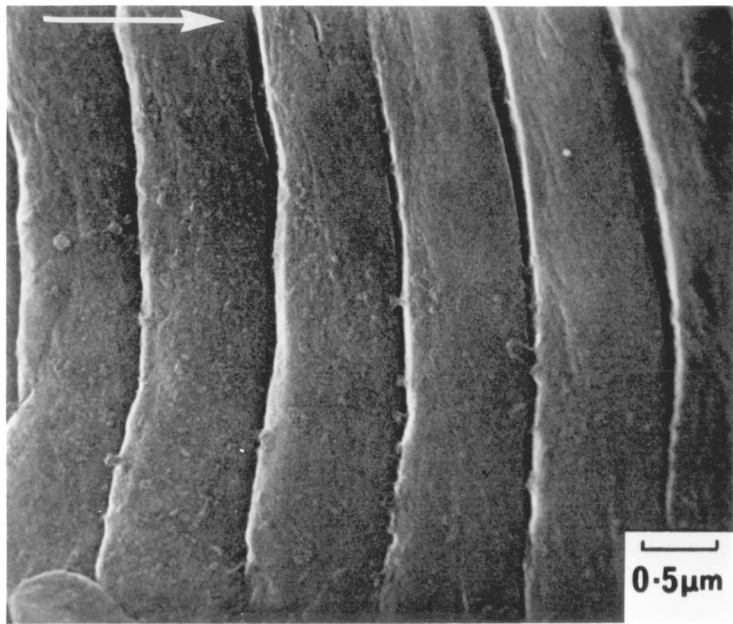
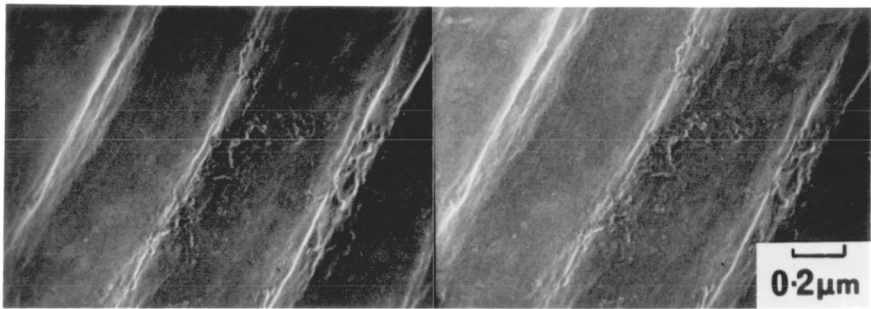
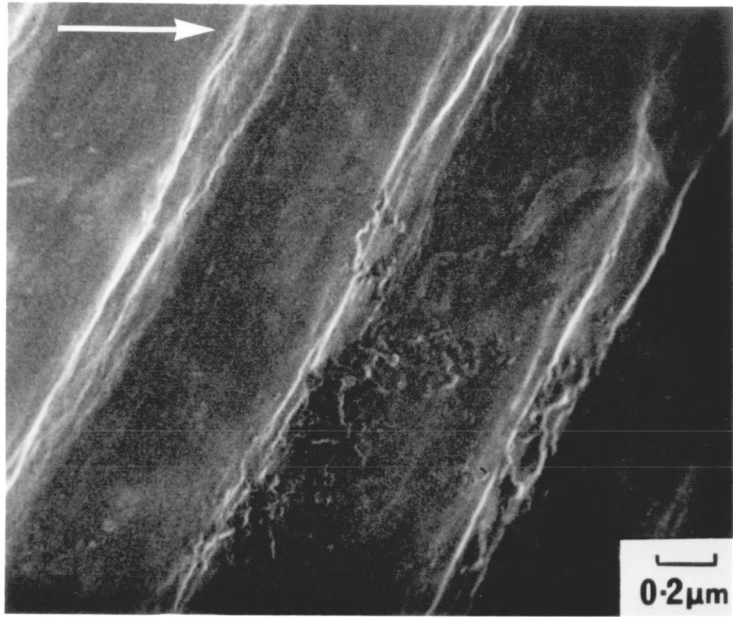
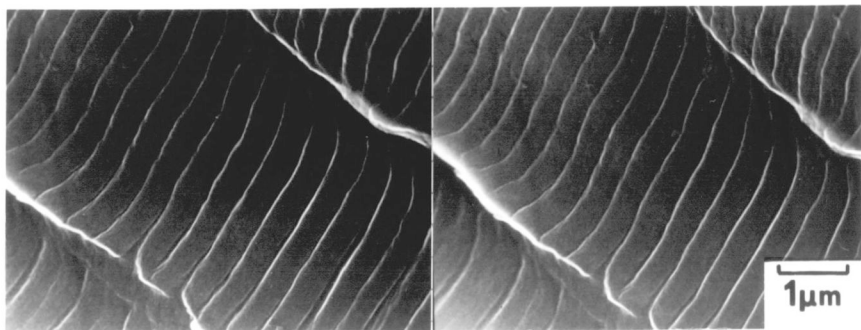
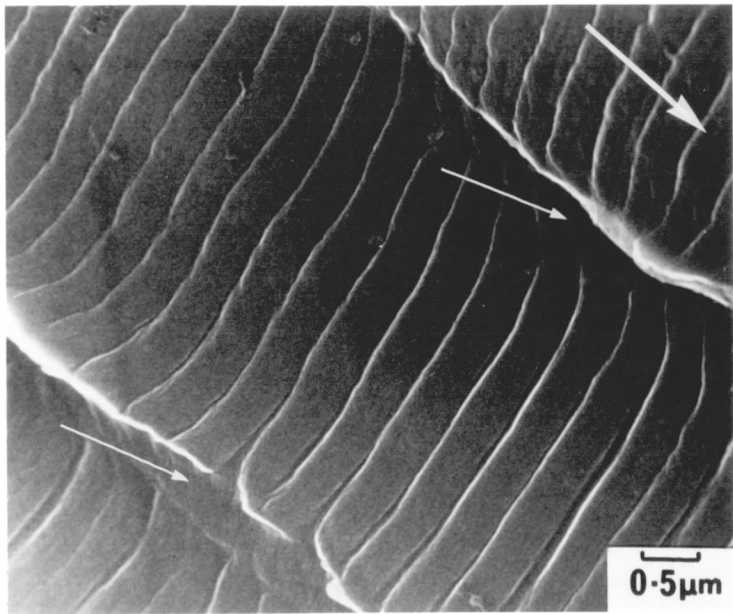
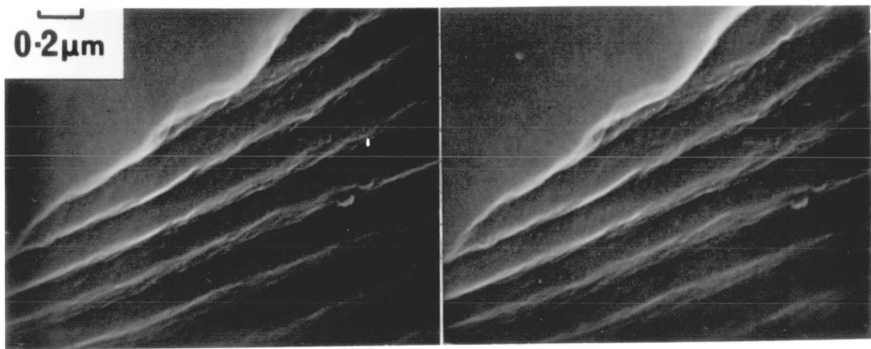
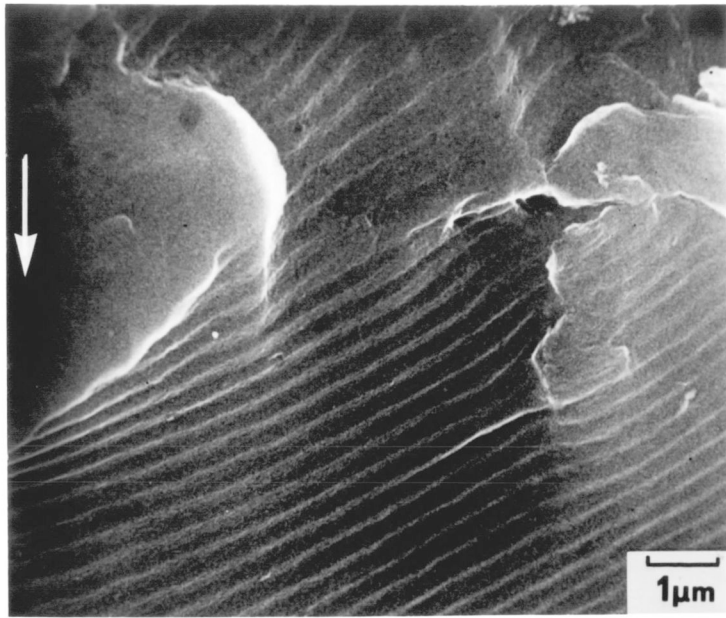


Fig. 5.20. Typical area of type A striations with stereo pair of corresponding area, HRSEM image. Note also upper, striation free, region. Crack growth direction arrowed.

Fig. 5.2I. Typical area of type B striations with stereo pair of corresponding area, HRSEM image. Crack growth direction arrowed.



were often separated by regions of tearing along the facet boundaries.

Striations were generally observed to lie perpendicular to the overall crack growth direction. Rotations of up to  $30^{\circ}$  were observed in some cases between adjacent areas of fracture (Fig.5.22). Striation fronts were often found to be curved, giving the impression, especially in the type B case, of a curved fracture surface. Careful stereoscopic observations, however, showed the inter-striation regions to be planar and parallel to one another, the striation slots themselves being curved. The inter-striation regions were often at an angle to the overall plane of fracture such that a staircase structure was developed as shown schematically in Fig.5.23.

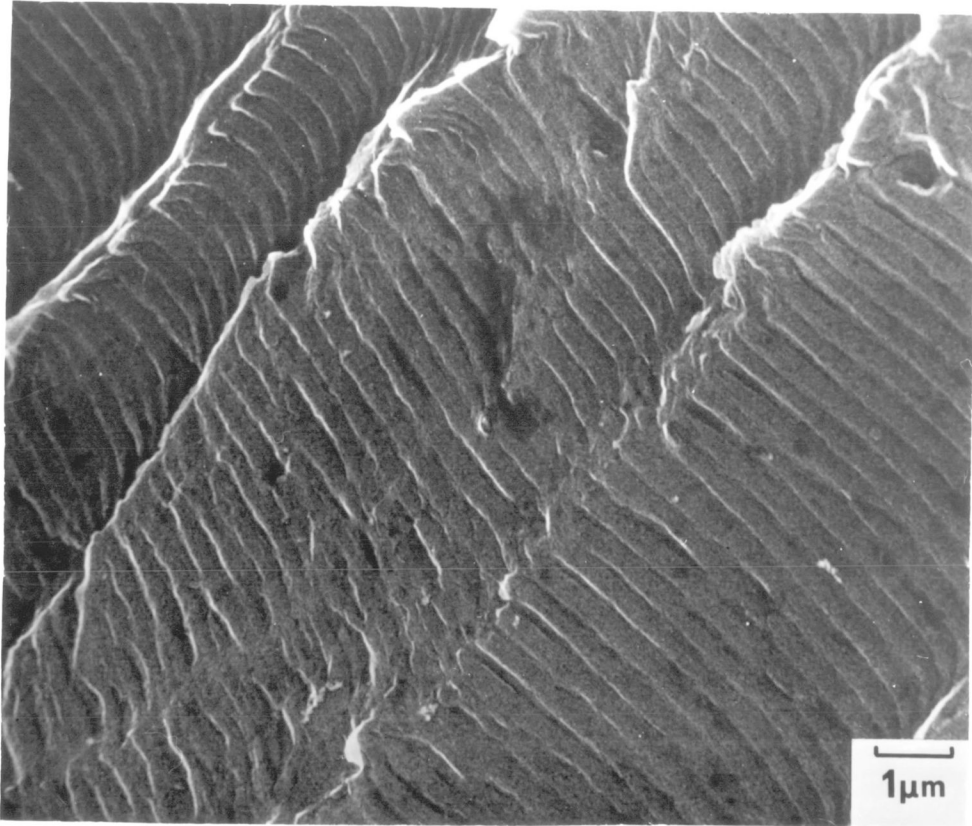
Using the high resolution fracture surface matching technique it was possible to observe the correspondence of striations on opposing fracture surfaces. Matching areas were obtained showing striations of types A and B and the rather surprising results are reproduced in Figs.5.24-5.26. Type B striations were often found to match with their own kind (Fig.5.24) although opposing faces did not normally show equal amounts of striation topography, striated regions matching almost striation free regions in many cases. Type A striations were not necessarily found to correspond to the same type of striation on the opposite fracture surface (Figs.5.25,5.26). In fact in this case type A striations on fracture surface (a) were found to correspond to type B striations on fracture surface (b). It would be impossible to state that this was exclusively the case since only a limited number of corresponding areas were observed.

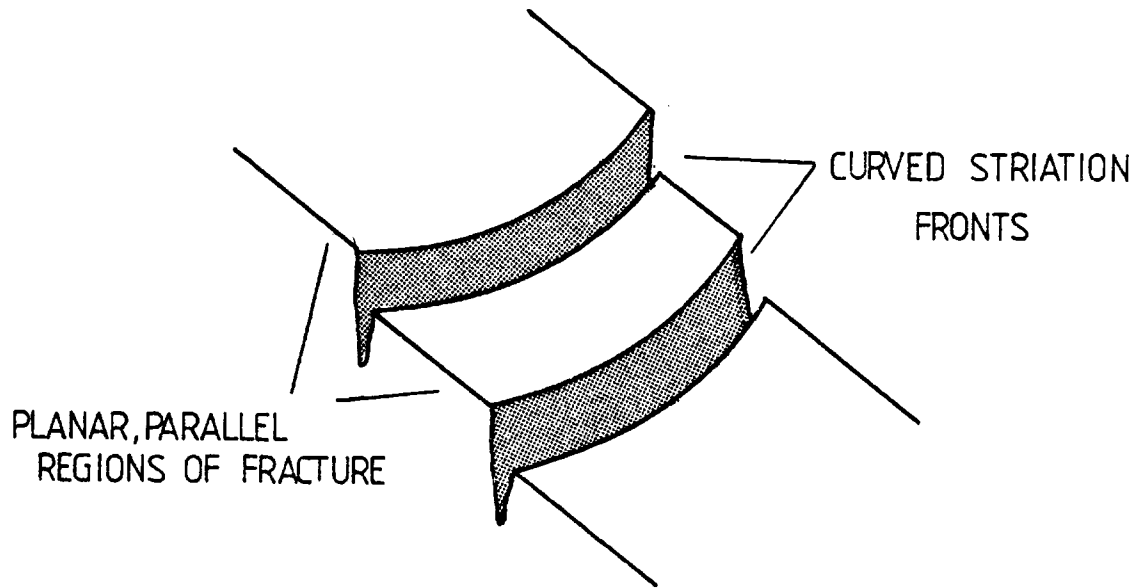
Further confirming the interrelation between profiles an intermediate type of striation was also observed on a very few occasions, (Fig.5.27). Here features corresponding to both types of striation could be found, the 'type B' slot corresponding to the trough in the type A striation.

#### 2.4. TEM Observations.

Observation in TEM of type I thin foils yielded information about both the crystallography of fracture and the deformation

Fig. 5.22. General area of striations showing striation front curvature and rotations between adjacent areas.





'Staircase' Structure-:  
Type B Striations

Fig. 5.24. High resolution fracture surface matching of type B striations.

(a) matching areas.

(b) detail from the central portion of each.  
(The pair of micrographs on the right hand side of the page are printed in reverse in order to facilitate matching of images.)

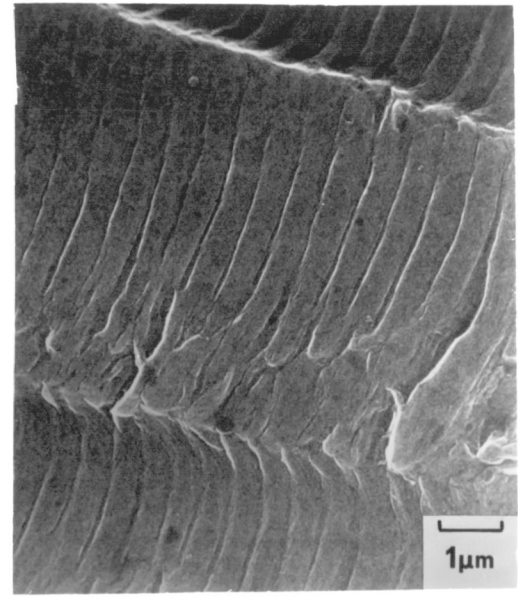
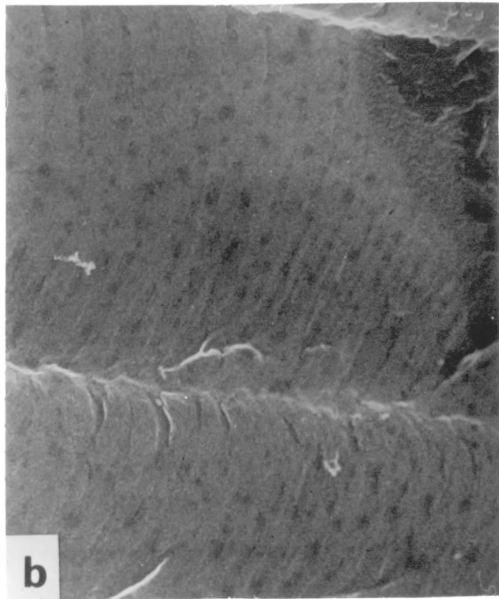
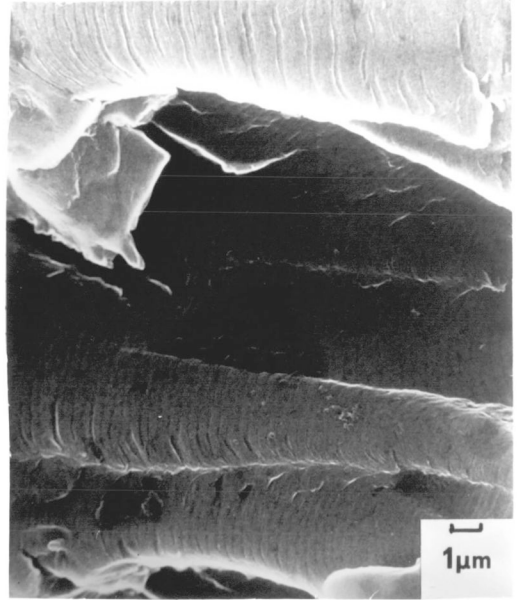
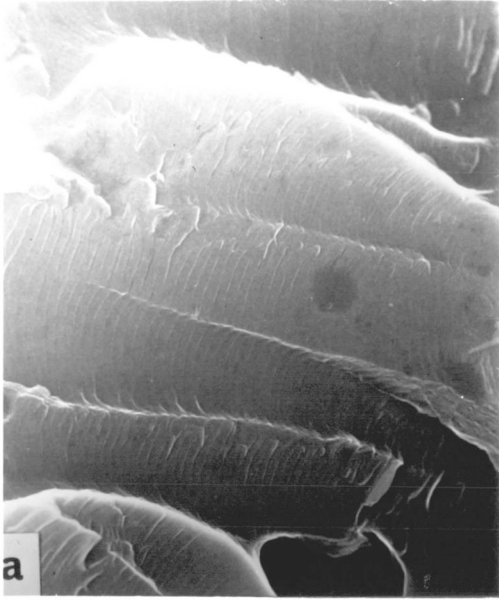


Fig. 5.25. High resolution fracture surface matching of striation types A and B. Matching areas, regions of interest arrowed.

Detail from arrowed regions in upper micrographs showing type A striations on surface (a) corresponding to type B striations on surface (b). Crack growth directions arrowed. (Stereo pairs of these regions are shown in Fig. 5.26.)

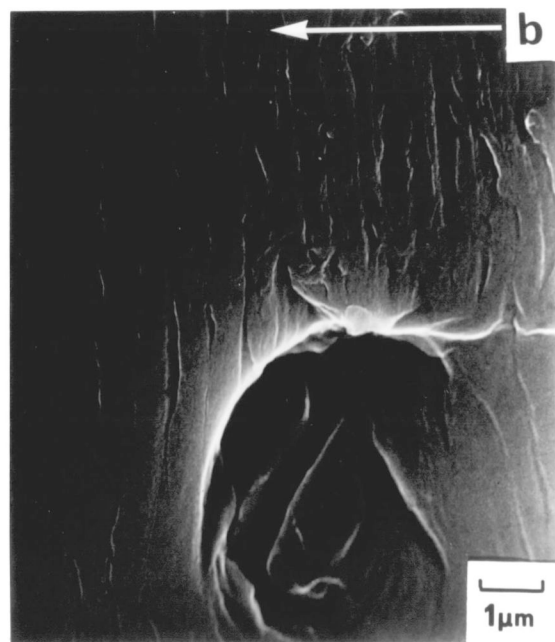
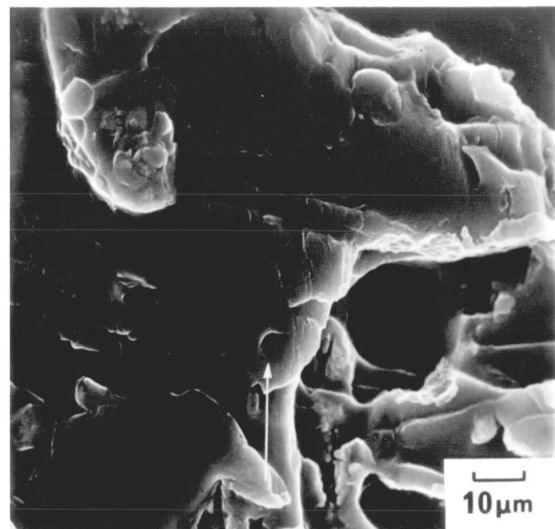
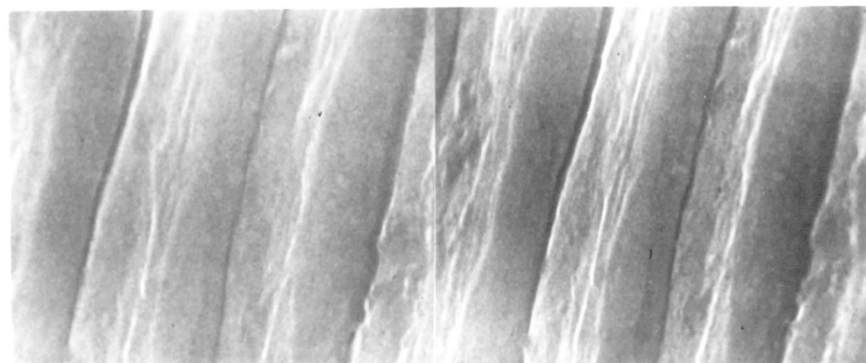
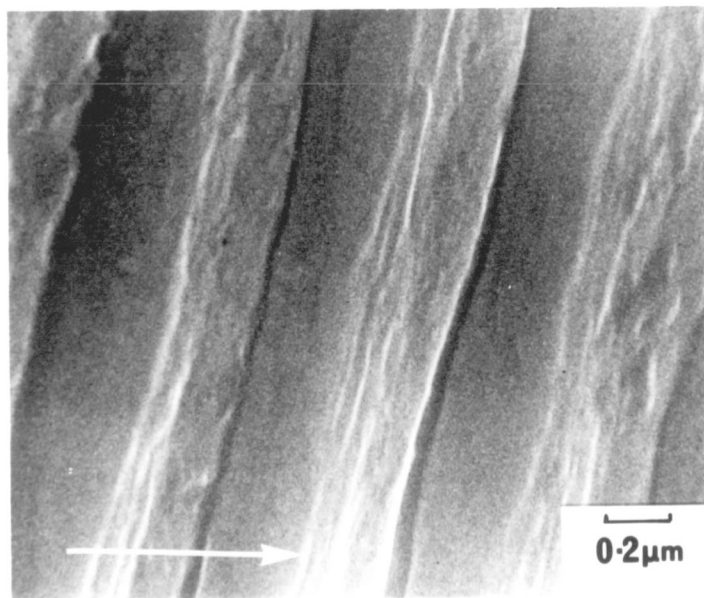
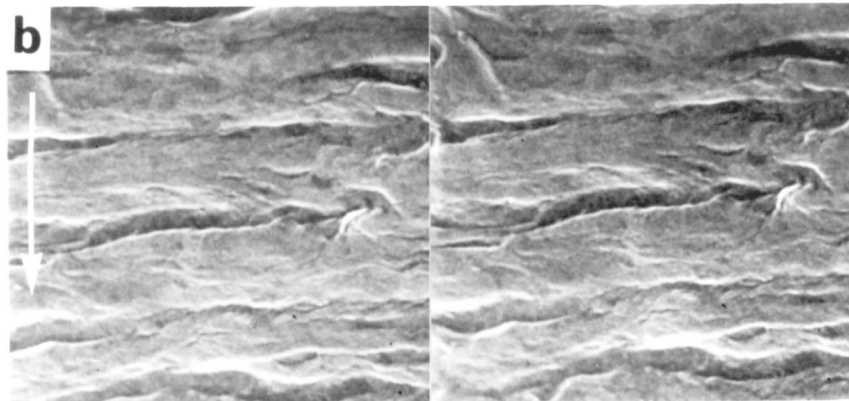
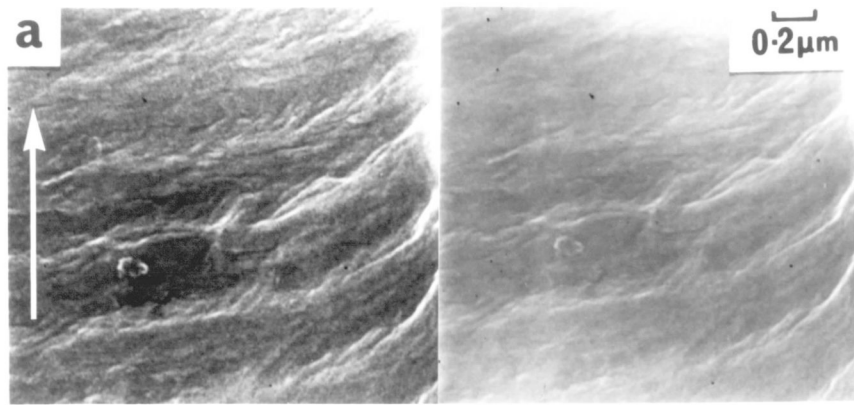


Fig. 5.26. Stereo pairs of regions in Fig. 5,25; crack growth directions arrowed.

Fig. 5.27. HRSEM image with corresponding stereo pair showing an intermediate type of striation with features relating to both types A and B.



structure associated with crack growth. The basic observations are summarised in Fig.5.28. A highly regular structure of bands of deformation separated by regions of low dislocation density was observed. The deformation bands were found to be highly imperfect and consisted basically of recovered subgrains. Rotational Moiré fringes were visible in many cases (Fig.5.28(b)), and a simple analysis of the fringe spacing yields subgrain rotations of less than  $1^\circ$ . These observations were supported by the electron diffraction data which showed arcing of reflections. In all cases selected area diffraction patterns (SADP's) produced with the foil in an untilted condition showed a zone axis close to  $\langle 011 \rangle$ . The surface of the thin foil must be expected to be approximately perpendicular to the electron beam in this situation so these results imply a fracture surface close to  $\{011\}$  in electron transparent areas. The line of intersection of the deformation bands with the foil surface was found in the majority of cases to be close to the  $\langle 11\bar{1} \rangle$  direction. This was not, however, the case exclusively and  $\langle 100 \rangle$  and  $\langle 01\bar{1} \rangle$  directions were observed together with apparently non-crystallographic directions.

The deformation bands were found to be separated by regions of low dislocation density with a visibly undisturbed precipitate distribution. Extensive tilting produced no evidence of substructure in these regions. The precipitate distribution also appeared to be unaltered within the deformation bands since with the bands tilted out of contrast no regular change in precipitate distribution was evident.

The band structure was particularly well revealed by high resolution dark field microscopy (Fig.5.29). By tilting about the line of intersection of the bands with the foil surface it was possible to obtain more information about the nature of the bands. With the foil untilted the bands were found to present a relatively narrow image and by tilting, this image could be broadened until the band images overlapped. Tilting in the opposite direction allowed the band images to be decreased in width slightly although difficulties were experienced in maintaining suitable contrast under these conditions. The deformation bands were found therefore

Fig. 5.28. TEM observations carried out on plane section (type I) thin foil specimen.

- (a) bright field micrograph showing regular deformation band structure. Specimen untilted ( $\Delta K \approx 15 \text{ MNm}^{-3/2}$ ,  $R=0.1$ ).
- (b) detail of the above with corresponding SADP. (Zone axis  $\approx \langle 011 \rangle$ )

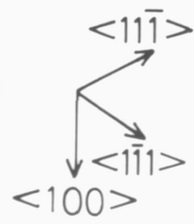
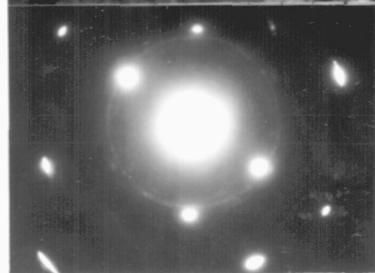
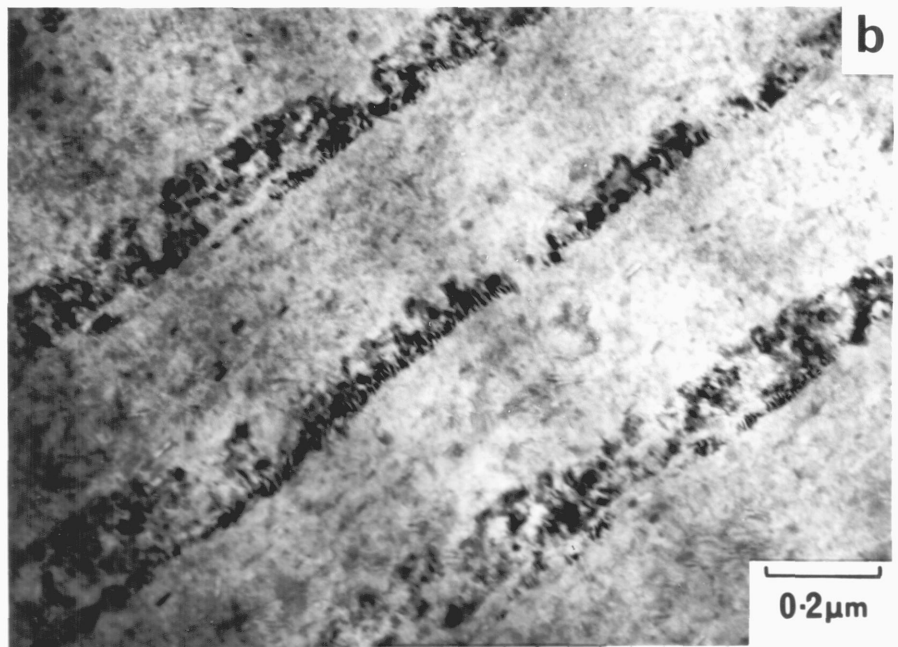
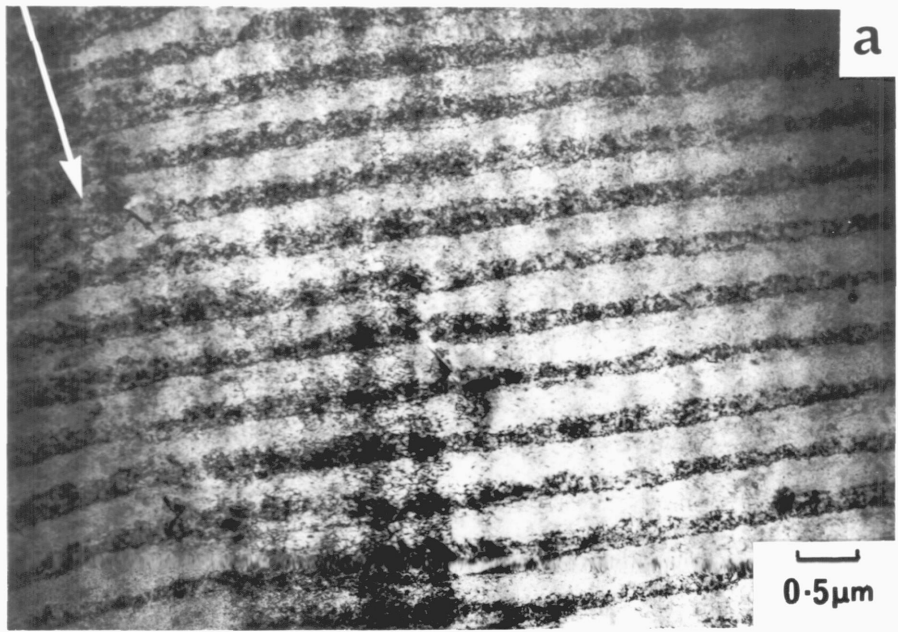
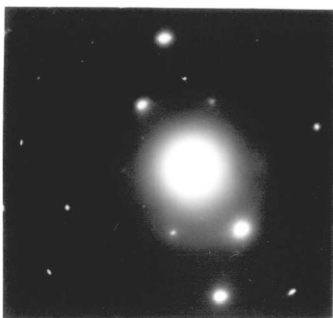
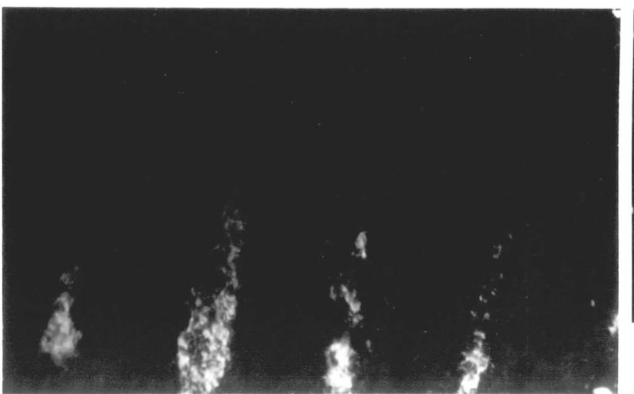
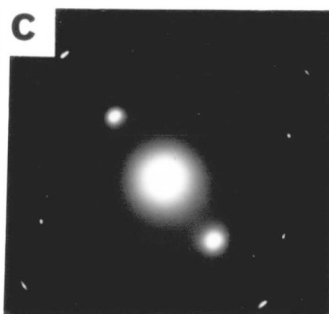
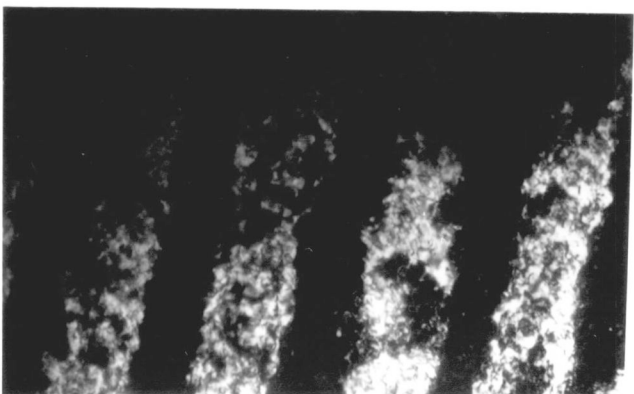
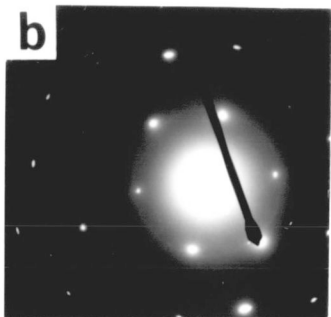
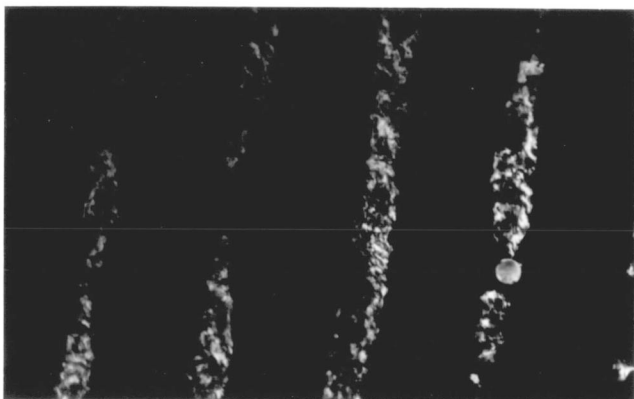
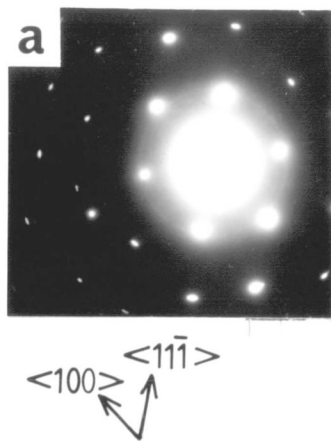
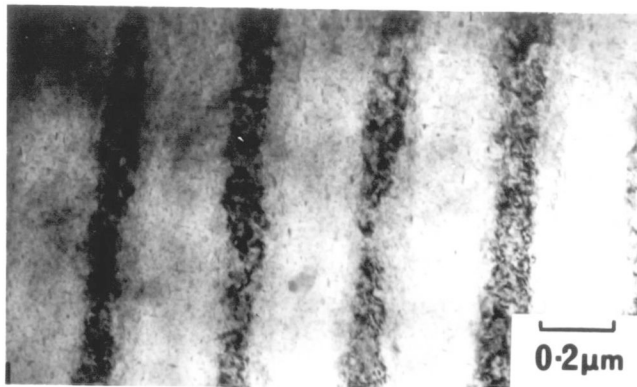


Fig. 5.29. TEM observations of deformation band structure carried out at different specimen orientations.

- (a) bright field micrograph with corresponding SADP, specimen untilted. (Zone axis  $\approx \langle 011 \rangle$ )
- (b) high resolution dark field (HRDF) of same area, specimen untilted, reflection arrowed in SADP.
- (c) HRDF and SADP, specimen tilted  $15^\circ$  c.w. about an axis approximately parallel to the trace of the bands in the foil plane.
- (d) as above, specimen tilted  $5^\circ$  a.c.w.



to be of width around  $0.1\mu\text{m}$  in the case of an inter-band spacing of  $0.3\mu\text{m}$ . The bands appeared to be somewhat irregular in thickness however and ran through the foil at an angle to the surface of greater than  $60^\circ$ .

More details were obtained concerning the dislocation structure by the observation of type II, cross section, thin foil specimens in the HVEM operating at 500 kV. Very limited areas of electron transparent material were produced in electropolished specimens, but it was possible to examine material at distances of less than  $1\mu\text{m}$  from the original fracture surface. (Fig. 5.30). The deformation bands were again visible, extending only to a limited distance of around  $1\mu\text{m}$  below the fracture surface. No information was obtained, from electropolished specimens, of crack tip dislocation structures, the overlapping of fracture surfaces merely giving the impression of a crack termination in Fig. 5.30(b). In terms of electron transparency the ion-beam thinning preparation technique was much more successful. The fracture surfaces were again preserved, but unfortunately a great number of artifacts were produced (Fig. 5.31). Apparent overageing during thinning was found (compare the precipitate size here with Fig. 3.7) and substantial heating during thinning would appear to have occurred. Account must be taken of this therefore in interpretation of substructural information. The deformation bands could not be observed, presumably owing to thermally induced recovery. A region of subgrains was observed to extend to a distance of approximately  $0.5\mu\text{m}$  ahead of the crack (at  $\Delta K = 14\text{MNm}^{-3/2}$ ,  $R=0.1$ ). This region would imply the presence of an area of high dislocation density in the original unmodified state.

### 2.5. Combined HRSEM and TEM Observations.

By observation of type I thin foils in the HRSEM and TEM modes it was possible to obtain information both about surface topography and underlying substructure and crystallography. Unfortunately areas showing marked surface topography are by their nature unlikely to give suitable thin areas for observation and the success rate of this technique was extremely low. However, it was possible to obtain this type of information from areas showing a number of different surface topographies.

Fig. 5.30. Observations of cross section (type II),  
thin foil specimens prepared by electropol-  
ishing. HVEM bright fields at 500Kv. ( $\Delta K$   
 $\approx 14\text{MNm}^{-3/2}$ , R=O.I.)

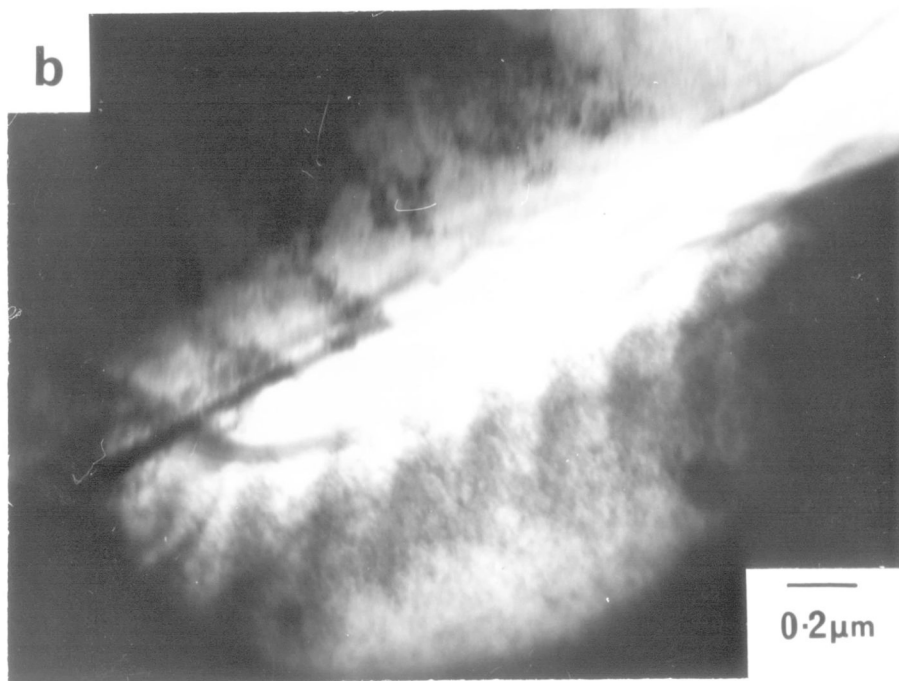
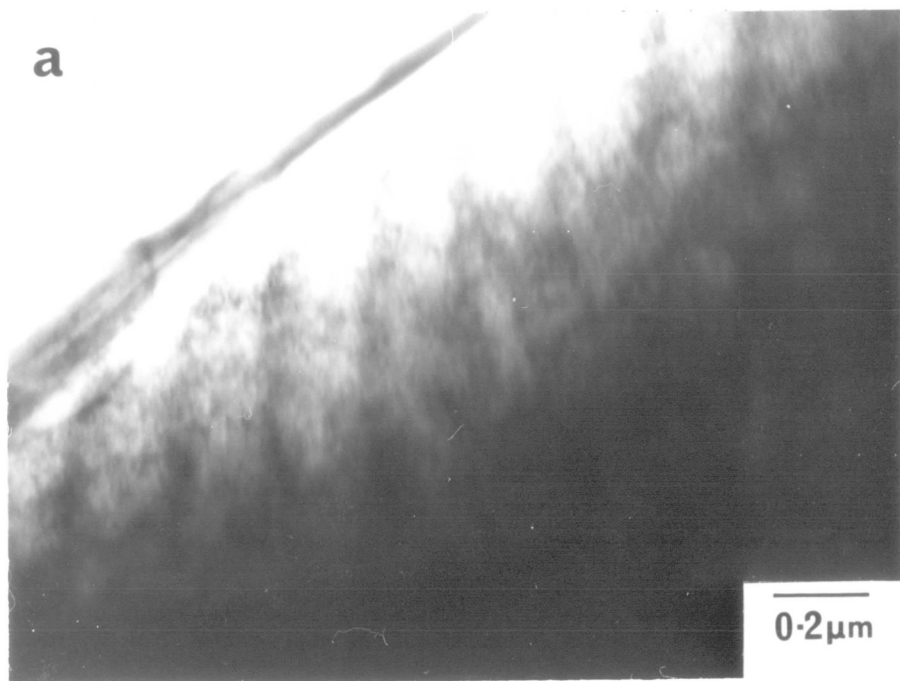
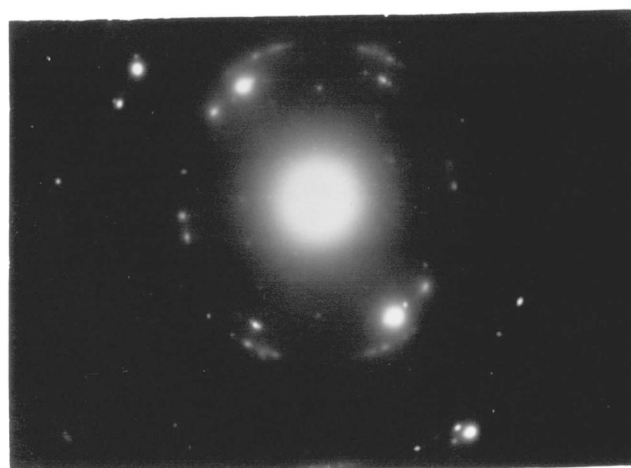
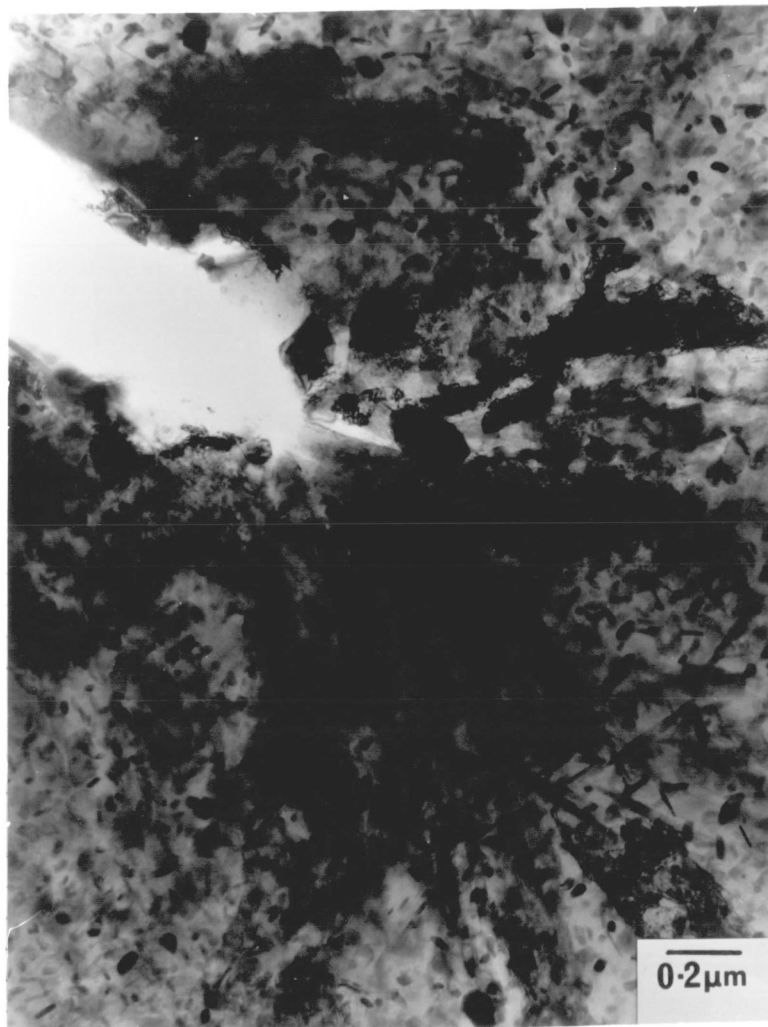


Fig. 5.3I. Observations of cross section (type II) thin foil specimen prepared by ion-beam thinning, section through crack tip. HVEM bright field 500Kv with corresponding SADP from region  $\approx 1\mu\text{m}$  diameter, adjacent to crack tip.



The deformation band structure was found to exist over areas showing no apparent striations on the surface and, for example, the area in Fig.5.28 was such a region. The relationship between the deformation band structure and striation topography in the case of type A striations is shown in Fig.5.32 . The deformation bands which, in this example, intersected the surface approximately along a  $\langle III \bar{I} \rangle$  direction, were found to lie directly below the leading edge of the striations, i.e. the edge angled away from the fatigue crack origin. The fracture surface as shown in the stereo pair was approximately perpendicular to the electron beam in this case. The deformation band-striation relationship in the case of type B striations is shown in Fig.5.33. Here, the deformation bands, visible in TEM, were observed directly ahead of the slots visible in SEM. The bands again intersected the surface along a  $\langle III \bar{I} \rangle$  direction in this particular case. Further observations in thicker specimens showed that the bands extended beneath the striation slots but were not observed on the opposite side of the slot from that shown in Fig.5.33 under any circumstances. In both cases therefore the deformation band structure was found to be related directly to the fatigue striations as shown schematically in Fig.5.34 .

As noted earlier the band structure was found to be extremely regular in all the electron transparent areas. The only exception to this was in areas containing intermetallic particles, which, as well as disturbing the striation topography, gave rise to a break up of the band structure in their vicinity (Fig.5.35). In this case it can clearly be seen that as the crack approached the intermetallic the deformation structure became less regular and was accompanied by a correspondingly irregular fracture surface in a region up to approximately  $2\mu\text{m}$  ahead of the particle. It is notable that the particle appeared to exert an influence on the deformation structure only over a very limited length of crack front, the band structure in adjacent areas being relatively undisturbed. As expected the band structure returned to the regular pattern as soon as the crack had propagated beyond the particle.

#### 2.5.I. Crack Growth at High and Low Stress Intensity Ranges.

Crack growth in the region  $\Delta K$   $20\text{MNm}^{-3/2}$  was readily investigated

Fig. 5.32. Combined TEM/HRSEM observations on plane section (type I) thin foil; region exhibiting type A striation topography.

- (a) HRSEM image, crack growth direction arrowed.
- (b) TEM bright field, at 100Kv, of corresponding area with SADP, specimen untilted. (Zone axis  $\approx \langle 011 \rangle$  .)
- (c) Stereo pair of area in (a) (rotated  $90^\circ$  a.c.w.)

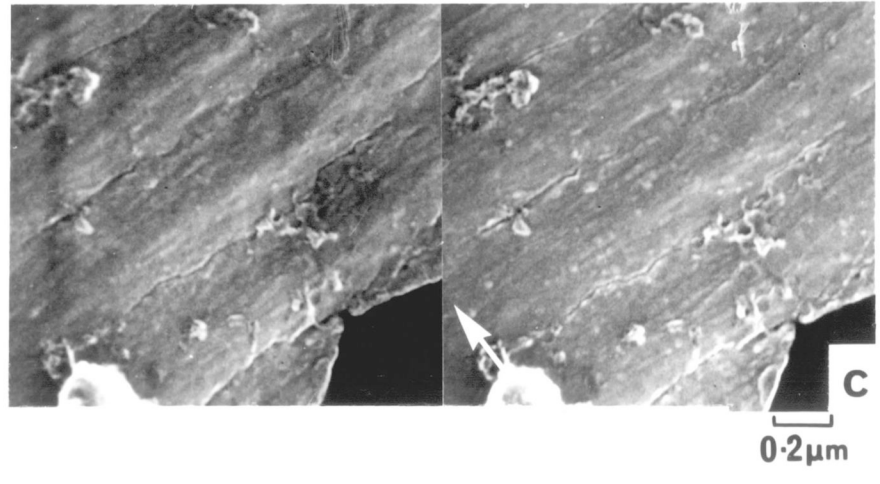
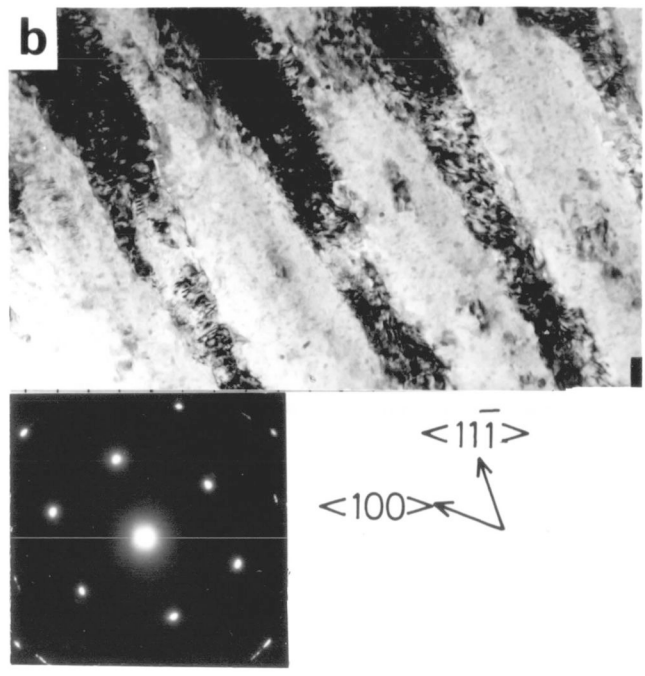
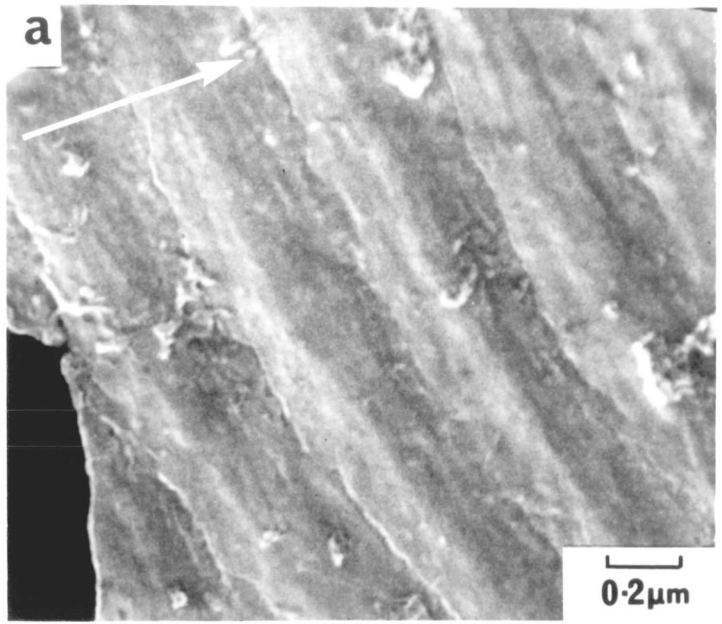
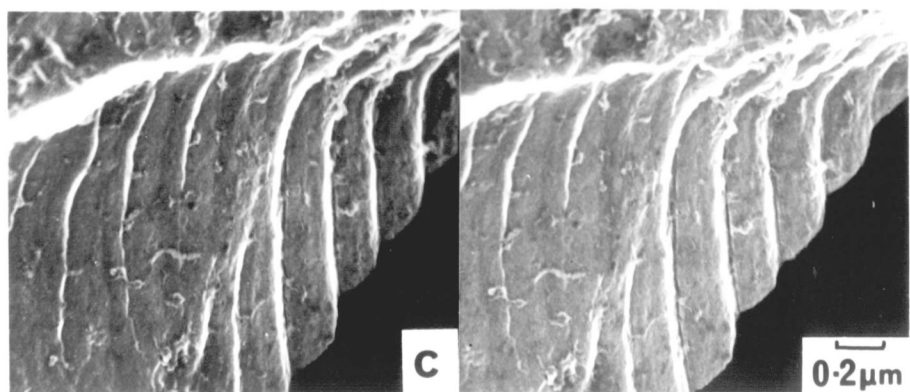
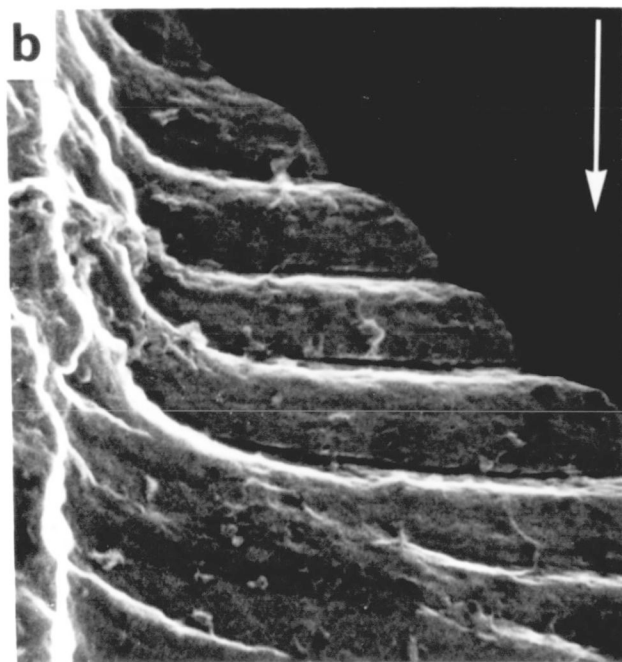
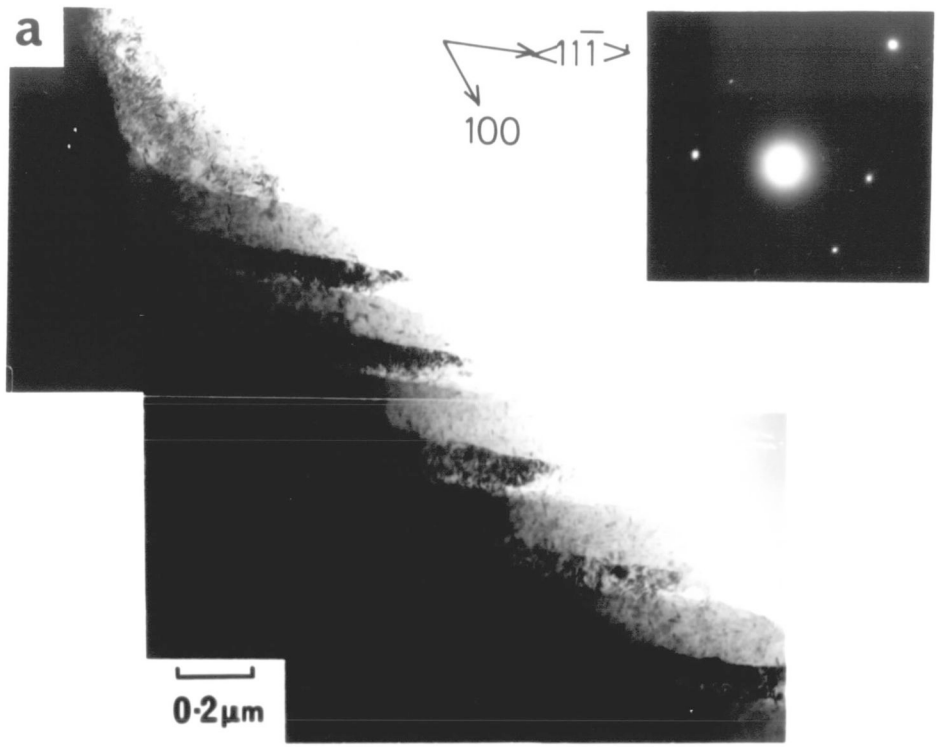
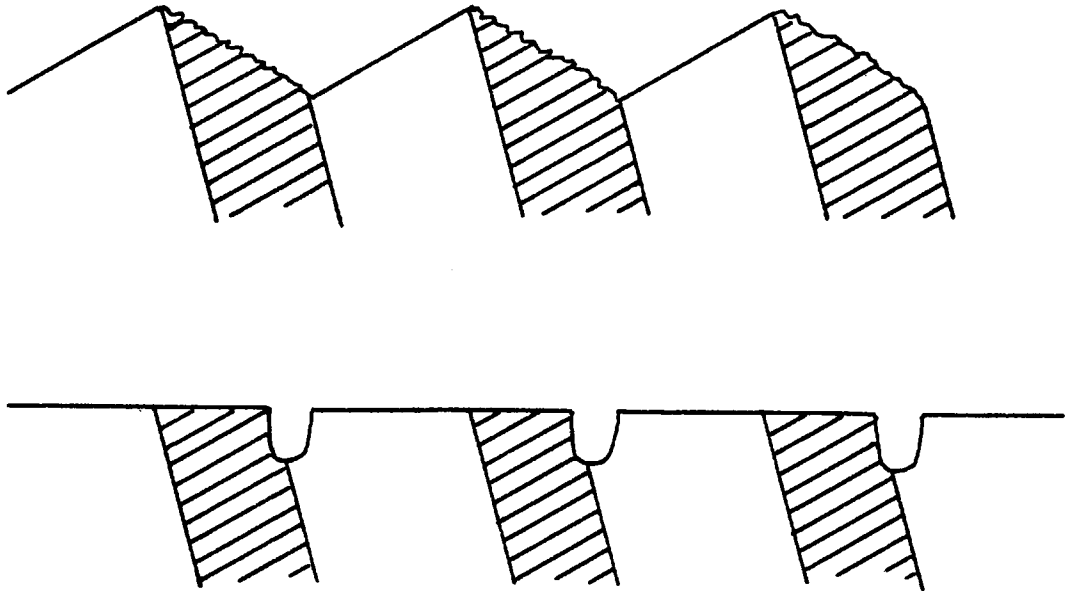


Fig. 5.33. Combined TEM/HRSEM observations on plane section (type I) thin foil; region exhibiting type B striation topography.

- (a) TEM bright field, 100Kv, with corresponding SADP, specimen untilted. (Zone axis  $\approx \langle 011 \rangle$  .)
- (b) HRSEM image of corresponding area, crack growth direction arrowed.
- (c) Stereo pair of area in (b) (rotated  $90^\circ$  c.w.).



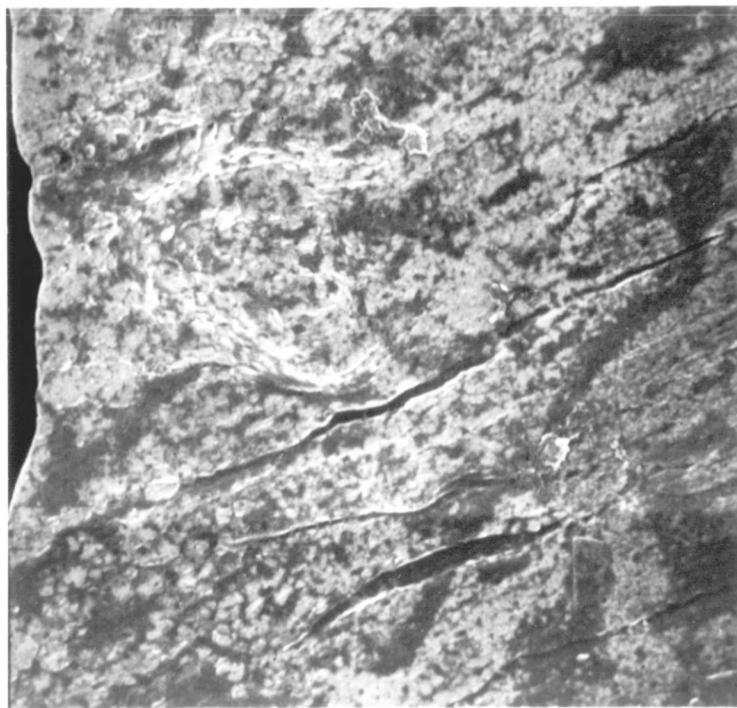
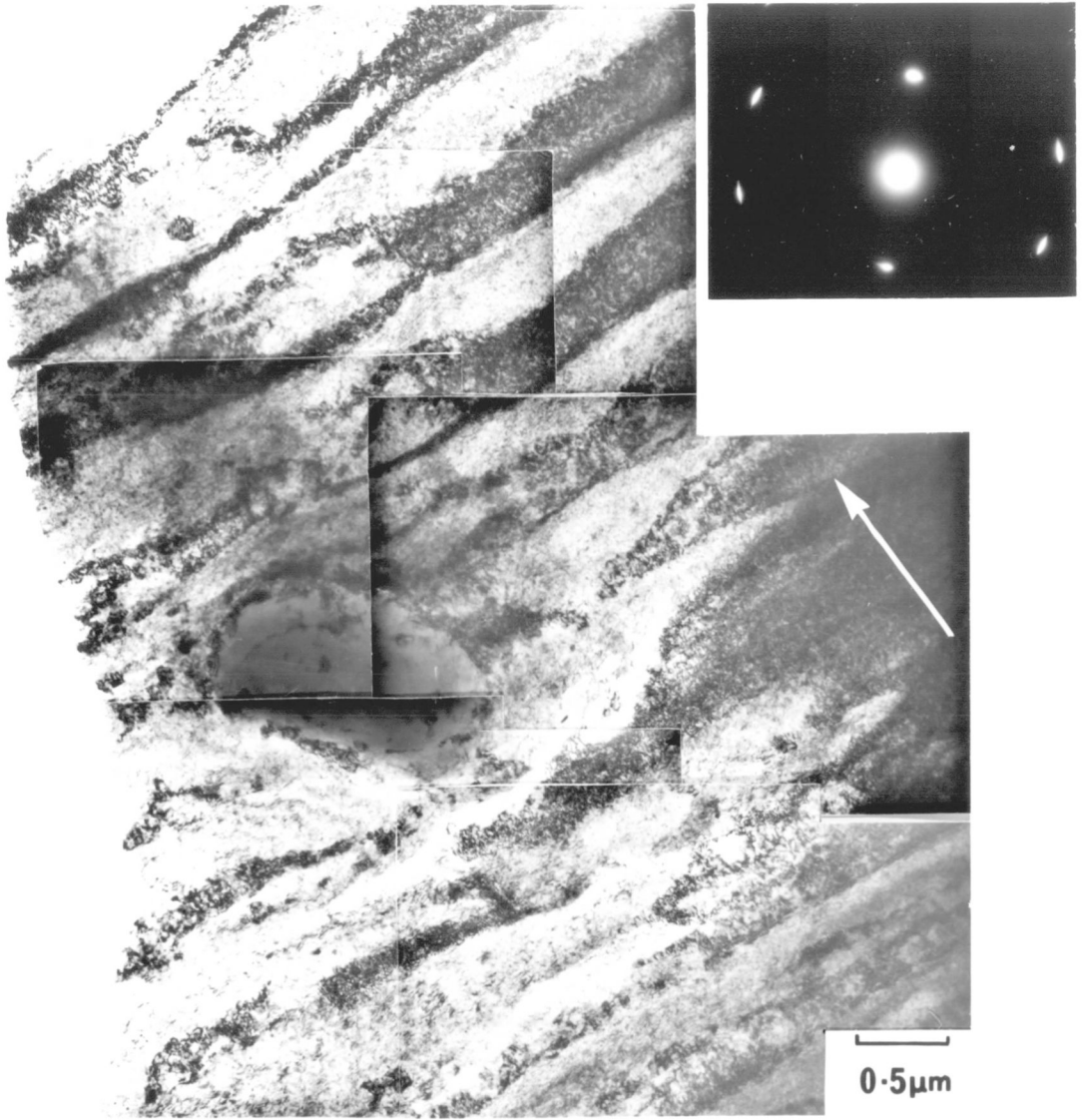


Deformation Band / Striation  
Relationship

Fig. 5.35. Combined TEM/HRSEM observations on plane section (type I) thin foil; region containing a large inclusion incorporated in to the fracture surface.

Series of TEM bright fields, 100Kv, with corresponding SADP from region  $\approx 1\mu\text{m}$  diameter, directly beneath the inclusion, specimen untilted. Crack growth direction arrowed.

Corresponding HRSEM image showing disturbance of striation topography.



fractographically since fatigue striations were found to be extremely well marked. Both types of striation were observed and a commonly observed feature was the formation of secondary cracks corresponding to type B striations as shown in Fig.5.36. Great changes in striation topography were noted between adjacent areas and relatively striation free areas were observed. Abrupt topographical changes were often found to be associated with grain boundaries, arrowed in Fig.5.36.

Type I thin foil observations were much more difficult at high  $\Delta K$ , since, owing to the extremely rough fracture surface, thin areas were rarely produced. An example of such an area is shown in Fig.5.37. The deformation band structure under these conditions was found to be basically unchanged. The bands were extremely well marked and somewhat irregular in width. The fracture plane remained, however, close to  $\{011\}$ . Clearly the width of the deformation band image must depend on foil thickness but, by observing foils of similar thickness to those of lower  $\Delta K$  fracture in the same orientation, it was noted, qualitatively, that the deformation bands were considerably wider when related to those of the lower  $\Delta K$  fractures.

In the very low stress intensity range ( $\Delta K < 10 \text{ MNm}^{-3/2}$ ) difficulties in striation observation were encountered in SEM since striation topography was not well marked and spacing was very small. In fact very high tilt angles were necessary in order to observe the striations. It is significant, however, that they were found to be present (Fig.5.38(b)). They appeared to be somewhat irregular in nature on many facets, as shown here, and it was impossible to determine the striation profile. The spacing of these markings was, however, found to be consistent with extrapolation of striation spacing data obtained at higher  $\Delta K$  and can therefore be considered to be true striations rather than some kind of slip markings.

It was not possible to observe striations of spacing less than  $400 \text{ \AA}$  observed here although the spatial resolution of the HRSEM is theoretically an order of magnitude higher than this. This may, however, be simply a result of the vertical height of striation features falling below the resolution limit rather than the non-occurrence of striations.

Fig. 5.36. SEM image of region exhibiting type B striations at  $\Delta K \approx 25 \text{ MNm}^{-3/2}$ . Note striation splitting in central region and abrupt change in striation topography at grain boundaries (arrowed). Crack growth direction also arrowed.

Fig. 5.37. TEM observations of deformation band structure at high  $\Delta K$  ( $\approx 27 \text{ MNm}^{-3/2}$ ). Series of TEM bright fields, 100kV, with corresponding SADP, specimen untilted. (Zone axis  $\approx \langle \text{OII} \rangle$ .) Crack growth direction arrowed.

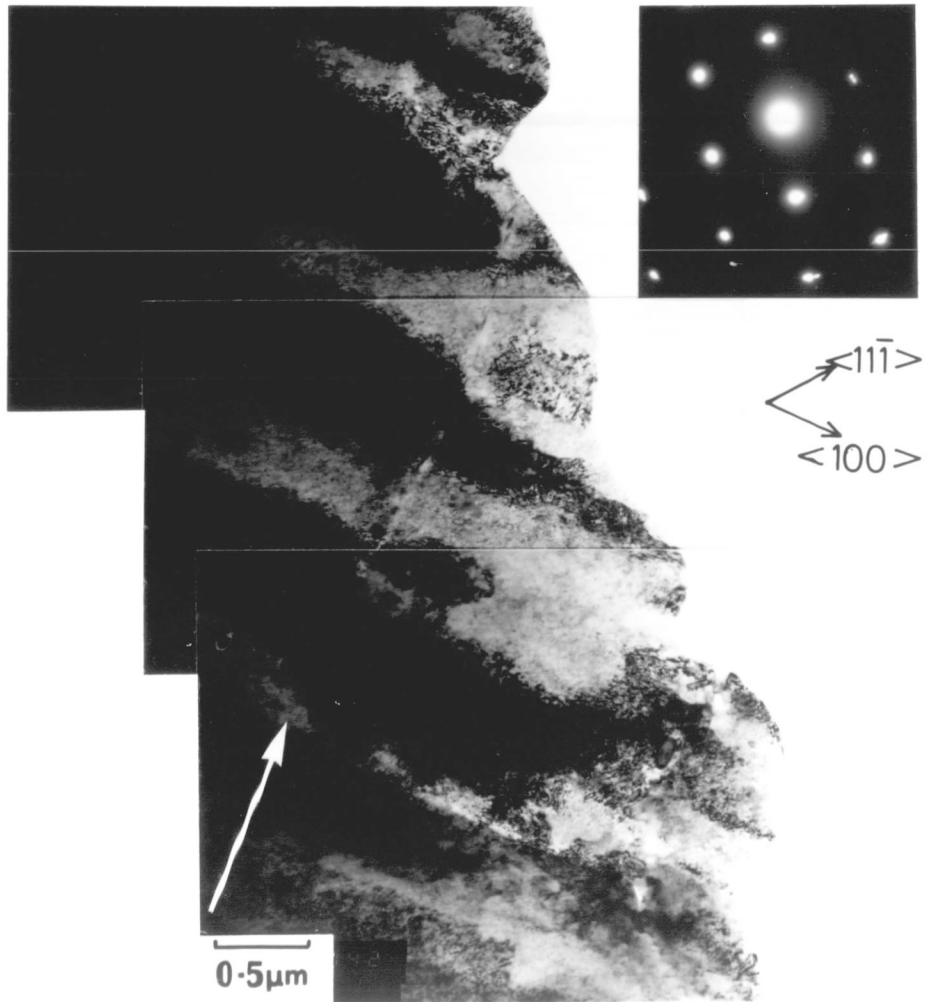
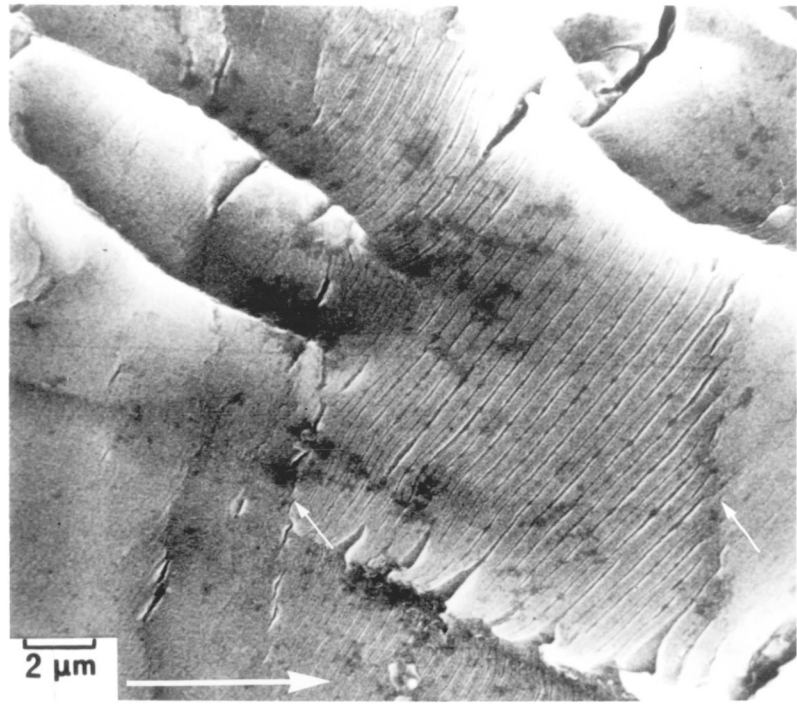
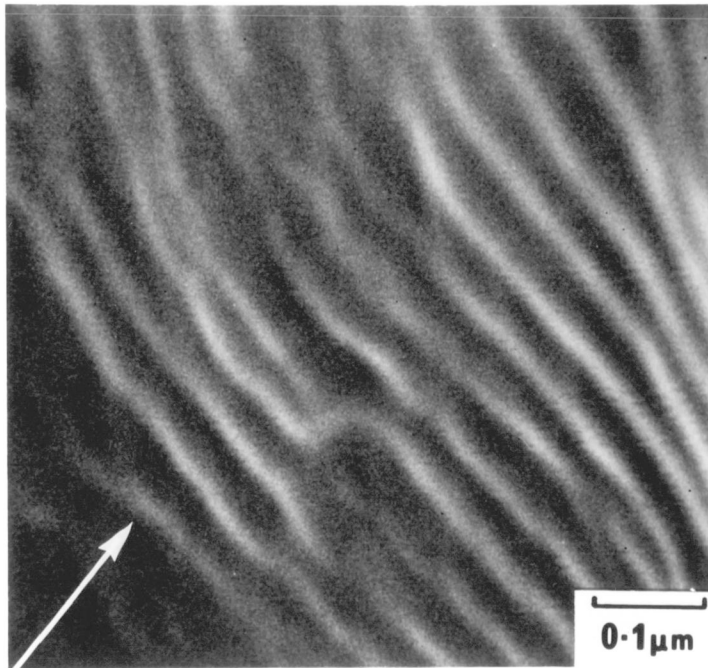
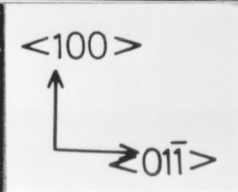
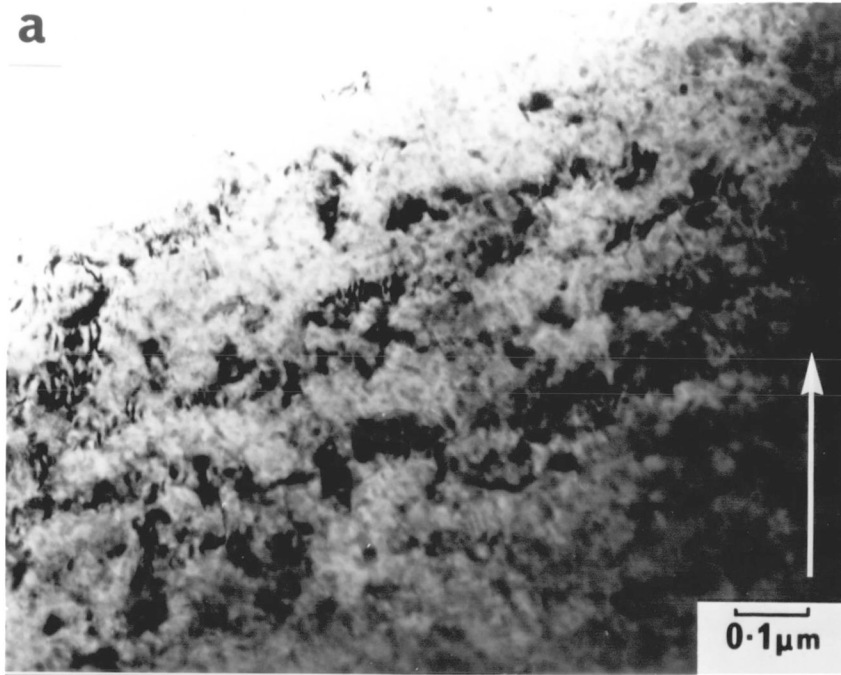


Fig. 5.38. TEM and HRSEM observations (not corresponding areas) of striations and deformation band structures at low  $\Delta K$  ( $\approx 6 \text{ MNm}^{-3/2}$ ,  $R=0.1$ ).

- (a) plane section foil, TEM bright field, 100Kv, with corresponding SADP. (Zone axis  $\approx \langle 011 \rangle$ ). Crack growth direction arrowed.
- (b) HRSEM image of striations. Crack growth direction arrowed.

a



The TEM observations of type I foils yielded information about the nature of the deformation band structure although the bands were difficult to resolve since the lattice distortion due to the bands appeared to be slight. Ill defined bands were however observed as shown in Fig.5.38(a) with a line of intersection with the fracture surface of  $\langle OII \rangle$  in this case and, once again, an approximately  $\{OII\}$  fracture plane. The band spacing was found to be around  $500 \text{ \AA}$ , corresponding approximately to the striation spacing at equivalent  $\Delta K$  ( $\approx 6 \text{ MNm}^{-3/2}$ ).

### 2.6. The Effect of Stress Ratio.

Type I thin foils were prepared from specimens tested at stress ratios of  $R=+0.5$  and  $R=-0.3$ . These were examined to investigate the effect of peak stress intensity ( $K_{\max}$ ) on the deformation band structure. The deformation sub-structures observed were, however, consistent with fracture at similar  $\Delta K$  at  $R=0.1$  rather than at similar  $K_{\max}$ . For example, Fig.5.39 shows a region of fracture at  $R=-0.3$   $\Delta K=25 \text{ MNm}^{-3/2}$ ,  $K_{\max}=19 \text{ MNm}^{-3/2}$ . The structure observed here can be compared to Fig.5.40 which shows fracture at  $R=0.5$   $\Delta K=12 \text{ MNm}^{-3/2}$ ,  $K_{\max}=25 \text{ MNm}^{-3/2}$ . Despite  $K_{\max}$  being somewhat lower in the former, the deformation bands clearly show evidence of more deformation accompanying crack growth. Peak stress intensity would therefore appear to have little effect on the band structure. The overall crack plane crystallography was also found to be unaffected, being close to  $\{OII\}$  in both cases. The two types of striation were observed on the fracture surfaces produced at both  $R=0.5$  and  $-0.3$ . Striations were found to be consistent with those observed at  $R=0.1$  at equivalent  $\Delta K$ . Hence, well defined striations were rarely observed at  $R=0.5$ , since large areas of ductile tearing were found at  $\Delta K \approx 15 \text{ MNm}^{-3/2}$  as  $K_{\max}$  approached  $K_C$  ( $\approx 35 \text{ MNm}^{-3/2}$ ).

### 2.7. Programme Load Tests.

HRSEM observations of type B fatigue striations produced using the simple load programme showed conclusively that each striation was related to one load cycle (Fig.5.41). Striation slots showing a narrow image (arrowed) were found to occur in pairs separated by groups of three wider striation slots. The narrow striation slot images were found to be followed by correspondingly narrow inter-striation regions, while the

Fig. 5.39. Deformation band structure associated with crack growth at  $R=-0.3$   $\Delta K \approx 25 \text{MNm}^{-3/2}$ ,  $K_{\text{max}} \approx 19 \text{MNm}^{-3/2}$ . HVEM bright field image at 500Kv with corresponding SADP, specimen untilted. (Zone axis  $\approx \langle 011 \rangle$ ).

Fig. 5.40. Deformation band structure associated with crack growth at  $R=0.5$ ,  $\Delta K \approx 12 \text{MNm}^{-3/2}$ ,  $K_{\text{max}} \approx 25 \text{MNm}^{-3/2}$ . HVEM bright field, 500Kv with corresponding SADP, specimen untilted.

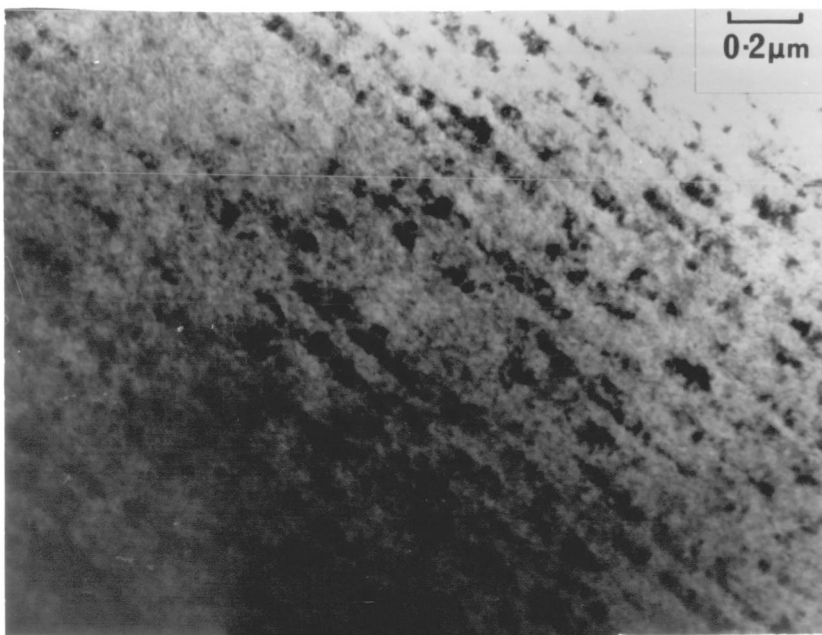
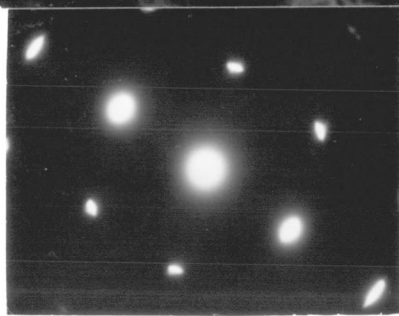
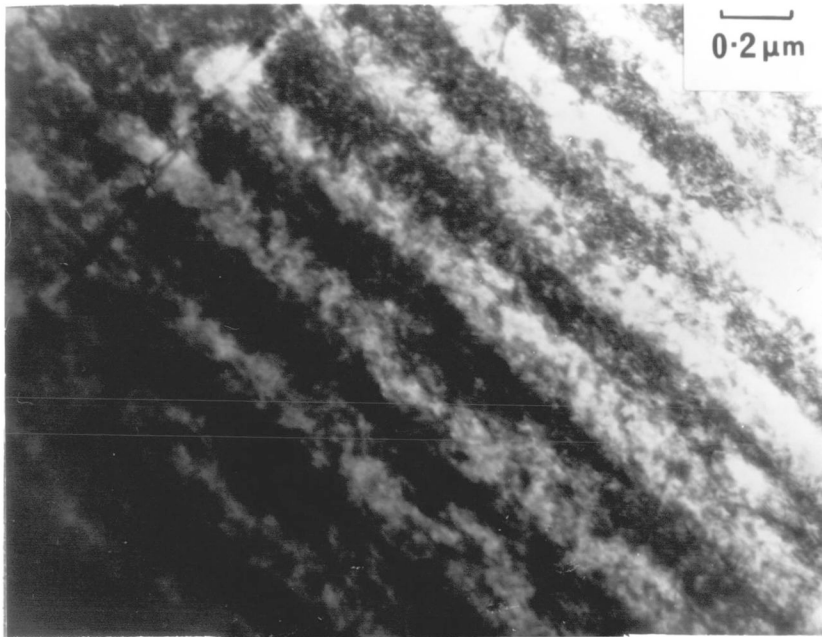
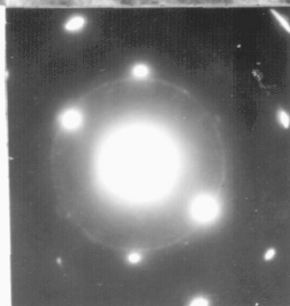
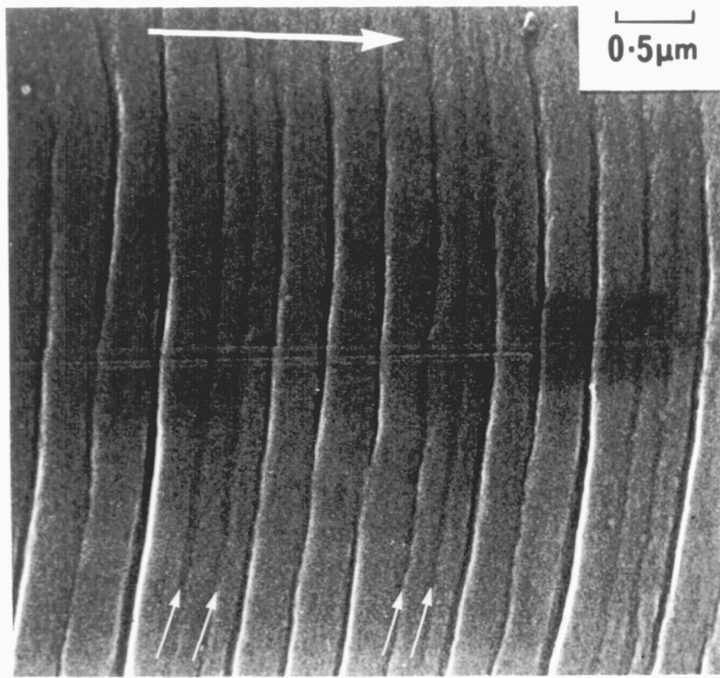


Fig. 5.41. HRSEM observations of type B striations produced during crack growth under programme loading conditions. Narrow striation images and crack growth direction arrowed.

Fig. 5.42. Deformation band structure produced during crack growth under programme loading conditions. TEM bright field, 200Kv, with corresponding SADP, specimen untilted. (Zone axis  $\approx$ <OII>.) Ill-defined bands and crack growth direction arrowed.



groups of three well defined striations were followed by broad interstriation regions. These observations can be readily related to the load programme (Fig.2.6 ).

It was also possible to conduct thin foil observations on type I thin foils prepared from these specimens and here the effect of varying  $\Delta K$  was again apparent (Fig.5.42): Well defined deformation bands were observed in groups of three, separated by pairs of ill-defined bands (arrowed). Quite evidently therefore, deformation bands can be related to  $\Delta K$  and are formed on a cycle by cycle basis. It was not possible to obtain electron transparent areas showing a clear relationship between deformation bands and surface striations but Fig.5.43 shows an HRSEM image corresponding to Fig.5.42. The narrow striation images appear to correspond to the ill-defined bands and vice versa.

#### 2.8. Fatigue Crack Growth in the Alloy 2024 T3.

A similar but less rigorous HRSEM and TEM study was made of crack propagation in 2024 T3 using a laboratory air environment, a stress ratio of 0.1 and a frequency of 0.2 Hz. The type I thin foil observations showed a deformation band structure similar to that observed in 7010 T76 with a crack plane once again close to  $\{011\}$  (Fig.5.44). The trace of the deformation band in the foil surface was also found to be along a number of crystallographic and non-crystallographic directions, as in 7010 T76. A number of differences in structure between 2024 T3 and 7010 T76 were, however, observed:

- (a) A greater degree of overall deformation appeared to be associated with crack growth at approximately equal  $\Delta K$ . The electron diffraction data showed obvious diffraction reflection streaking in low order reflections. Patterns produced with the same sized selected area aperture in 7010 did not exhibit such streaking even at very high  $\Delta K$  (c.f. Fig.5.37).
- (b) The deformation band structure was generally less regular than that observed in 7010 T76.
- (c) Small intermetallic particles, many of which were present in this alloy, were found to be incorporated

Fig. 5.43. HRSEM image of area corresponding to Fig. 5.42.  
Narrow striation images and crack growth  
direction arrowed.

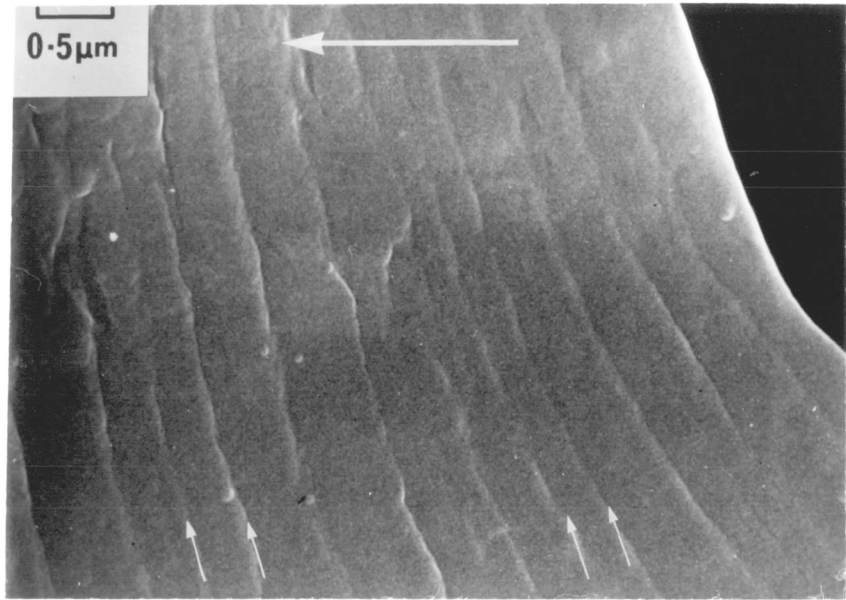


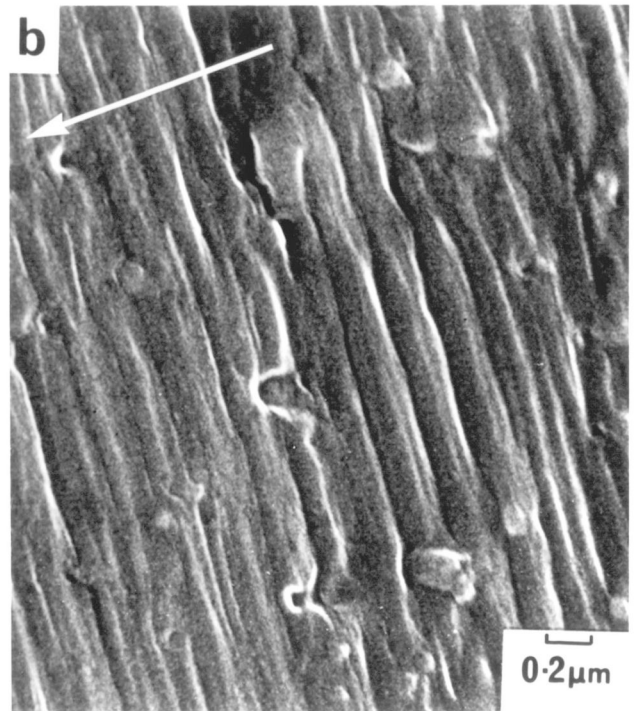
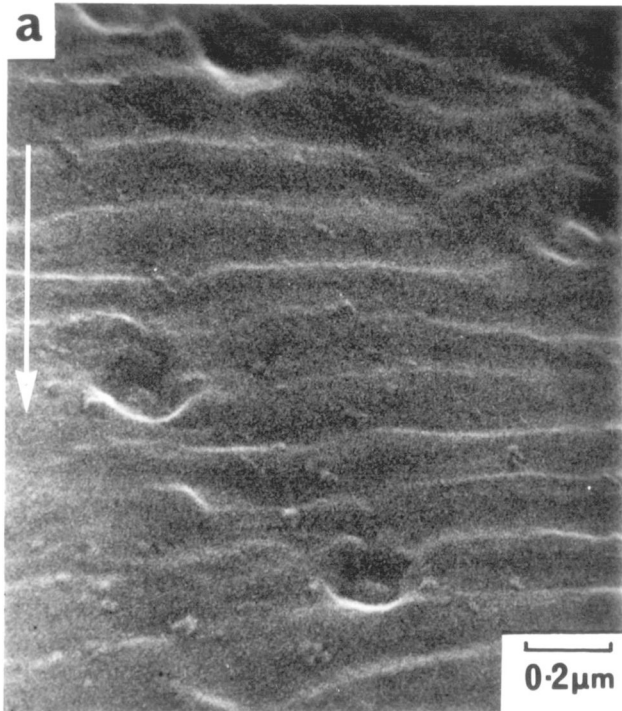
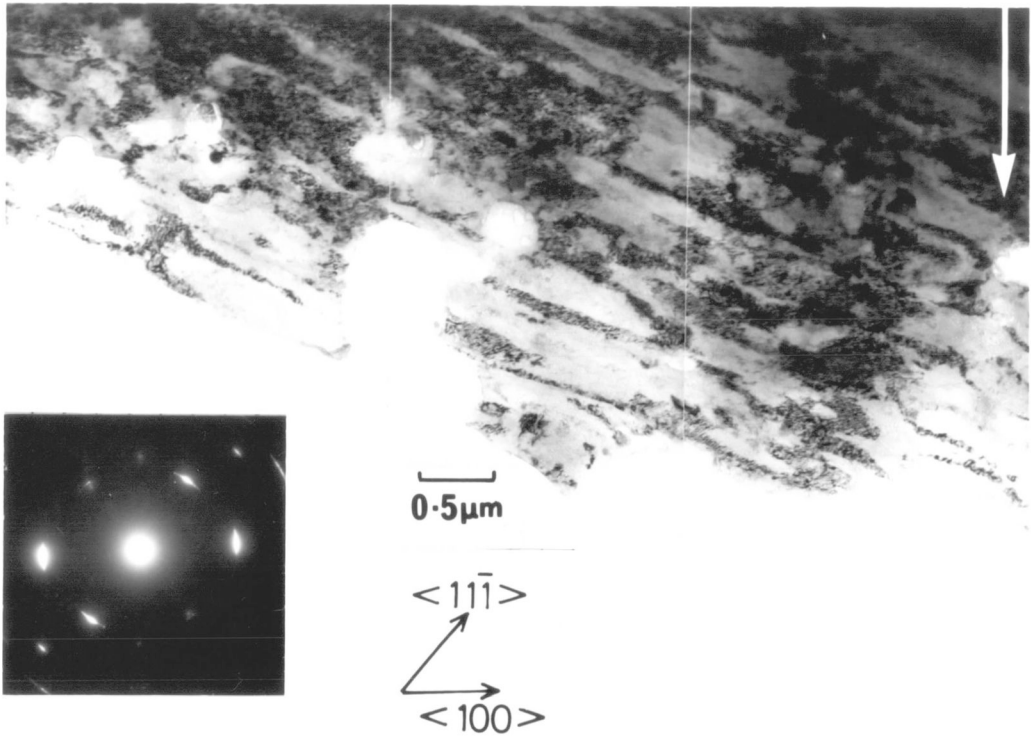
Fig. 5.44. Plane section (type I) thin foil observations of crack growth in a laboratory air environment in the alloy 2024 T3.  $\Delta K \approx 25 \text{ MNm}^{-3/2}$ ,  $R=0.1$ . TEM bright field, 100kV, with corresponding SADP, specimen untilted. (Zone axis  $\approx \langle 011 \rangle$ ). Crack growth direction arrowed.

Fig. 5.45. HRSEM images of typical striation topographies found on fracture surfaces of the alloy 2024 T3.

(a) type A striations,  $\Delta K \approx 12 \text{ MNm}^{-3/2}$ ,  $R=0.1$ .

(b) type B striations,  $\Delta K \approx 20 \text{ MNm}^{-3/2}$ ,  $R=0.1$ .

Crack growth direction arrowed.



in the fracture and appeared to be associated with irregularities in the band structure (Fig.5.44 ).

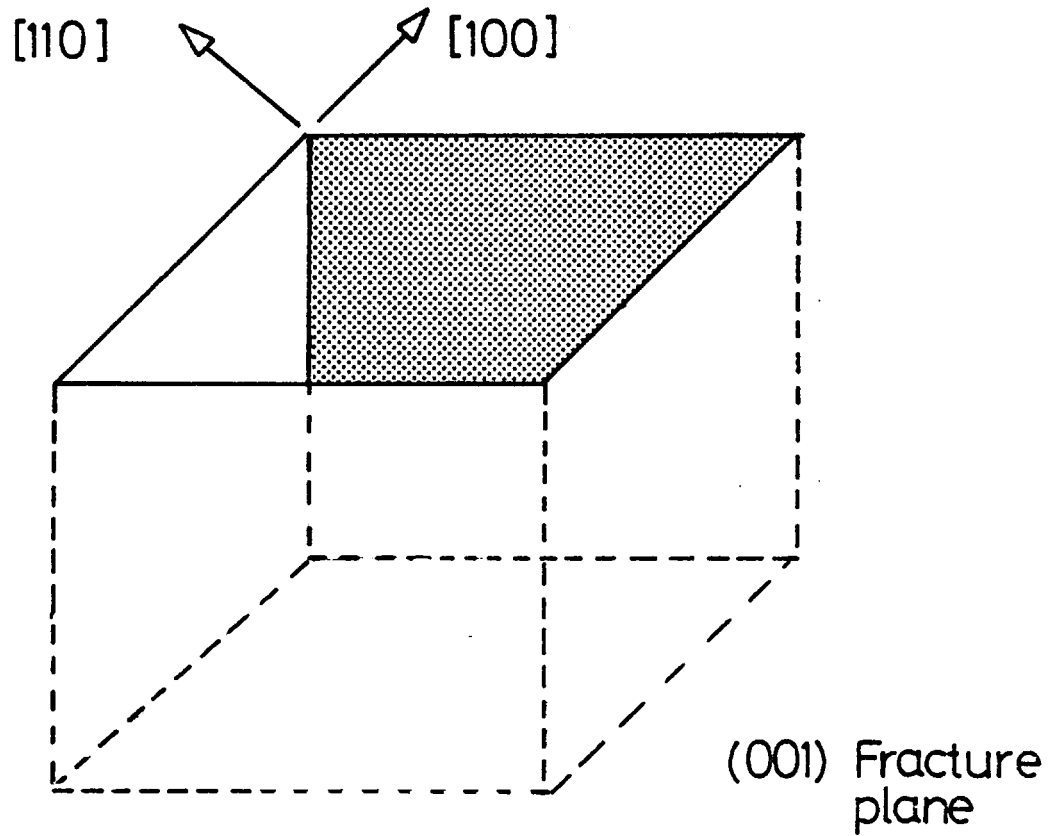
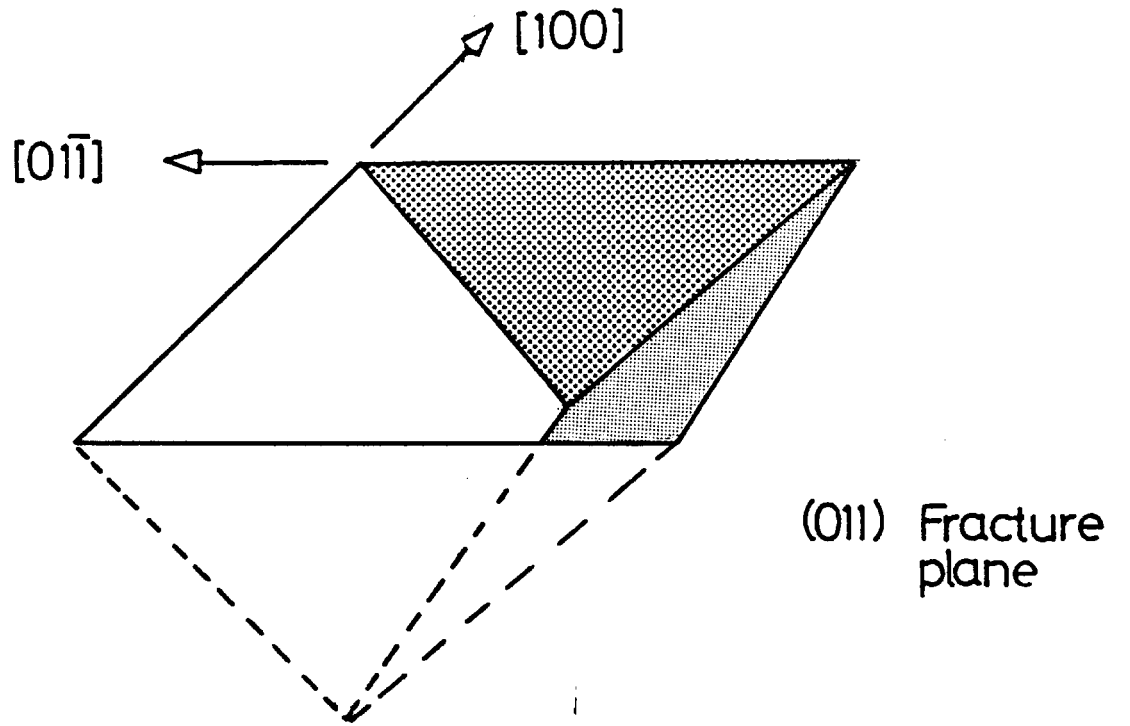
The HRSEM studies (Fig.5.45 ) confirmed the influence of intermetallics on crack growth. Both types of fatigue striation were observed but both were found to be less regular with evidence of a great deal more plastic deformation accompanying crack growth. Impressions in the fracture surface, produced by incorporation of intermetallics were clearly visible at all times even at low  $\Delta K$  (Fig.5.45(a)).

### 2.9. Etch Pitting Studies.

Selected area diffraction studies, whilst providing evidence of a crack plane close to  $\{OII\}$ , were not sufficiently sensitive to determine accurately the actual plane of separation and were limited to electron transparent areas. These observations of crack plane crystallography were therefore extended by the use of the etch pitting technique. Previous workers have reported that the etchant used attacked  $\{OOI\}$  planes and hence square pits would be expected on an  $\{OOI\}$  surface and rectangular pits with sloping bases on an  $\{OII\}$  surface (Fig.5.46). Combined HRSEM/TEM observations of etched thin foils has allowed pit shape to be compared to electron diffraction data (Fig.5.47). In the case of an  $\{OII\}$  foil surface, etch pits were found to be approximately square in shape but had sloping bases. The edges of the pits were found to be crystallographic and of  $\langle OII \bar{I} \rangle$  and  $\langle IOO \rangle$  as expected. Pits on  $\{OOI\}$  planes were also square in section but showed parallel sides and hence had a different depth profile from pits on  $\{OII\}$ .

The results of these observations demonstrated the difficulty which might be found in distinguishing  $\{OOI\}$  and  $\{OII\}$  pits since both were approximately square in shape in two dimensions. Stereoscopic techniques were therefore used for all observations of etch pits on fracture surfaces in order that the pit depth profile could be determined. The results of these observations are shown in Figs.5.48 and 5.49. Some areas of irregular etchant attack were found particularly at high  $\Delta K$ . However, many areas showed etch pits which were of the shape shown in Fig.5.48, an area showing no apparent striation topography. These pits are clearly characteristic of  $\{OII\}$  when observed stereo-

Fig. 5.46



Etch Pit Morphology

Fig. 5.47. Combined TEM/HRSEM observations of etched thin foil specimen.

- (a) HRSEM image showing pit profile.
- (b) corresponding TEM bright field, 100kV, with SADP, specimen untilted. (Zone axis  $\approx \langle 011 \rangle$ .)

Fig. 5.48. Etched fracture surface. HRSEM stereo pair showing  $\{011\}$  pits.

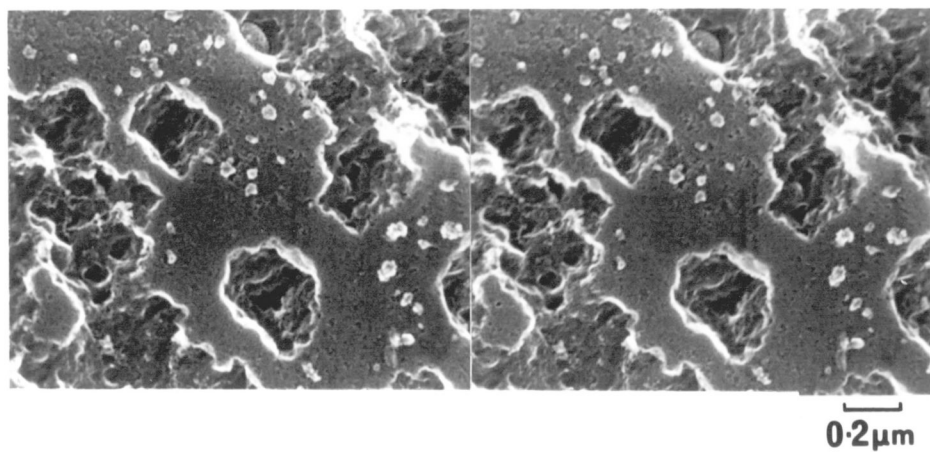
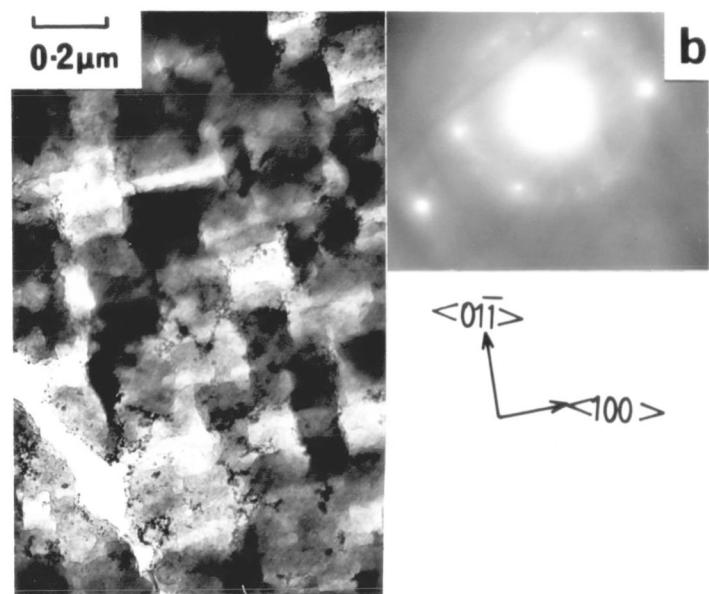
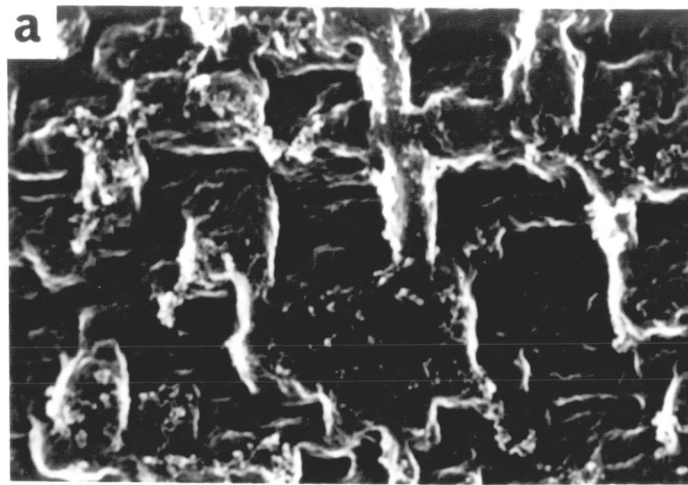


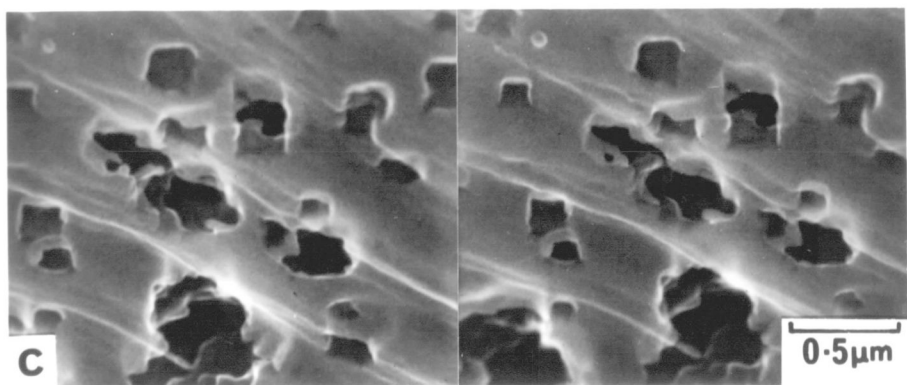
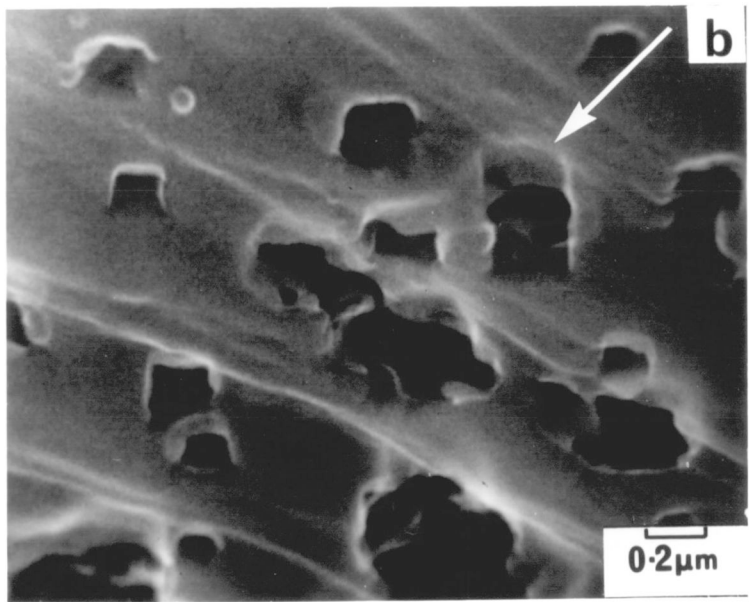
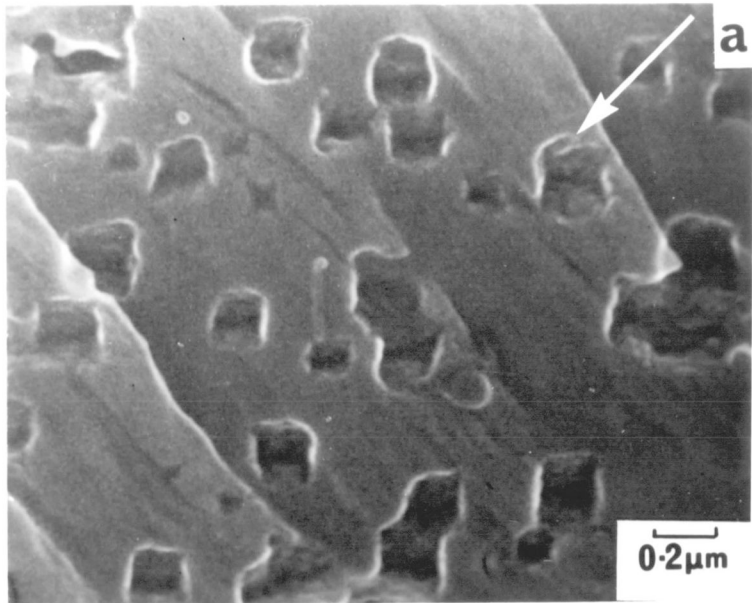
Fig. 5.49. Etch pitted fracture surfaces showing the two striation profiles.

(a) type B striations.

(b) type A striations.

(c) stereo pair of area in (b).

Crack growth direction arrowed.



scopically. All pits observed were found to be of this type although the profile was not in all cases as clearly defined. Pits were observed on areas showing both type A and type B striation profiles (Fig.5.49). In the case of type B striations pits were found over the whole surface in various orientations with respect to the striations, indicating a range of striation directions. For example, Fig.5.49(a) shows an approximate  $\langle III \bar{I} \rangle$  striation front; this was in fact the most commonly observed direction. In the case of type A striations  $\{OII\}$  pits were found to occur only on the trailing edges of the striations (Fig.5.49(b), i.e. the areas showing no evidence of slip activity. Once again various rotations of pit relative to striation were observed although an approximately  $\langle III \bar{I} \rangle$  direction was found to be most common.

#### 2.IO.Measurement of Crack Growth Rate From Striation Spacing.

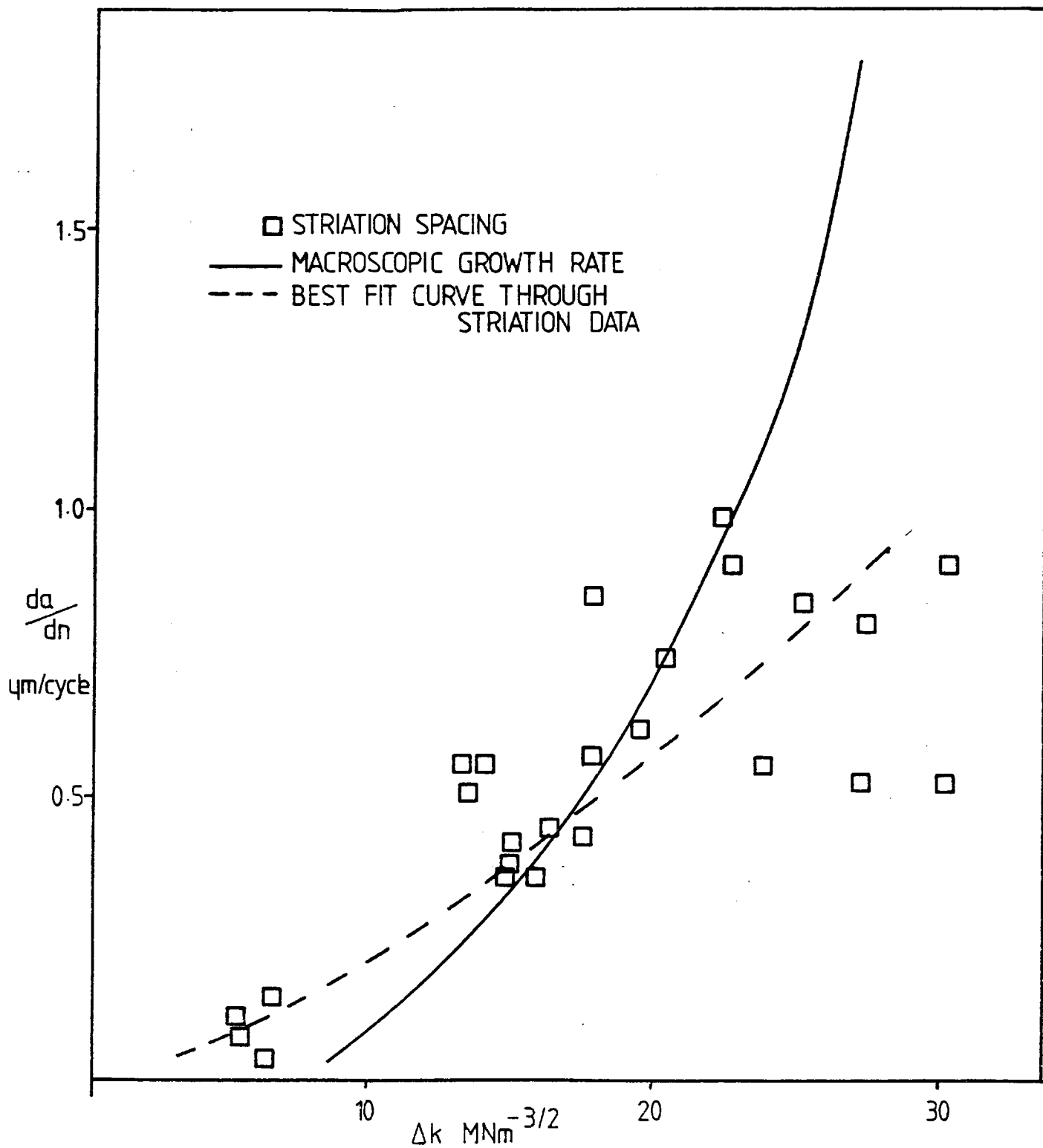
The striation spacing results obtained from C.T. design specimens were plotted versus  $\Delta K$  and are shown in Fig.5.50. At low  $\Delta K$  where fatigue striations were not often clearly apparent deformation band spacings obtained from TEM observations were also used. At low  $\Delta K$ , striations were generally found to give an overestimate of the macroscopic crack growth rate, assuming cycle by cycle growth. At low to medium  $\Delta K$  ( $10 \rightarrow 15 \text{ MNm}^{-3/2}$ ) average striation spacing was found to approximate to macroscopic growth rate. At higher  $\Delta K$ , however, a great discrepancy was observed between the two, striation spacing generally underestimating crack growth rate.

Plotting the results on a log scale (i.e.  $\log da/dn$  v  $\log \Delta K$ ) reveals a slope for striation data of approximately 2. Hence striation spacing can approximately be given by the equation:

$$\text{Striation Spacing} = \text{const.} \Delta K^2 \quad (\text{Fig.5.5I})$$

#### 2.II.Crack Growth in Dry Environments.

Crack propagation was studied in dry argon and oxygen environments, both containing less than 10 ppm water vapour at a test frequency of 100 Hz. The general fractographic appearance was found to be quite different from laboratory air tests in both cases (Figs. 5.52, 5.53). The faceted



Comparison of Macroscopic Crack Growth Rate with Striation Spacing

Comparison of macroscopic crack growth rate with striation spacing (plotted on Log scale)

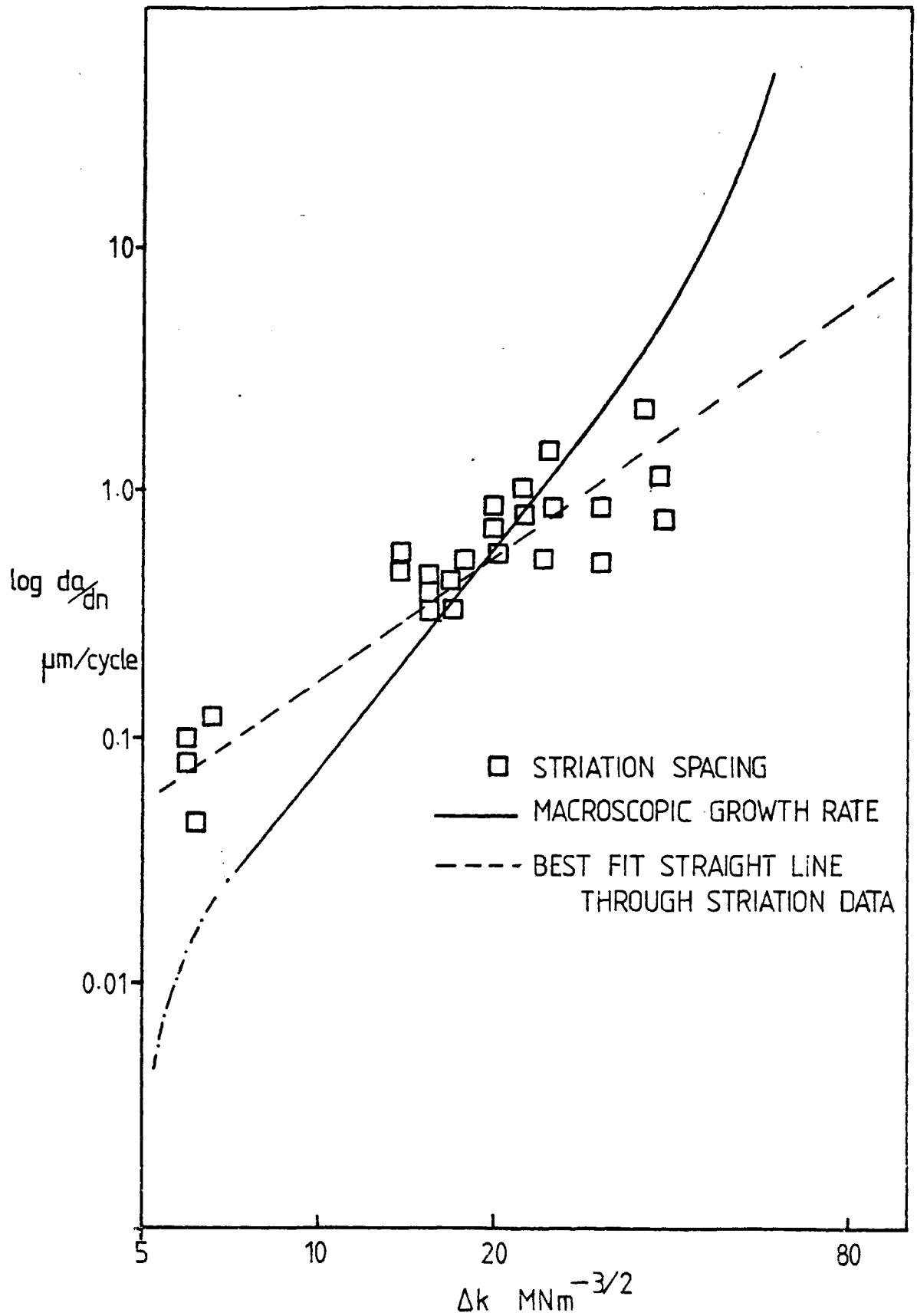


Fig. 5.52. Fractographic observations of crack growth in a dry oxygen test environment.

(a) general fracture appearance

$$\Delta K \approx 11 \text{ MNm}^{-3/2}, R=0.1.$$

(b) general fracture appearance

$$\Delta K \approx 26 \text{ MNm}^{-3/2}, R=0.1$$

(c) detail from (b) showing region of striation like features.

(d) stereo pair of striation like features in (c).

Crack growth directions arrowed.

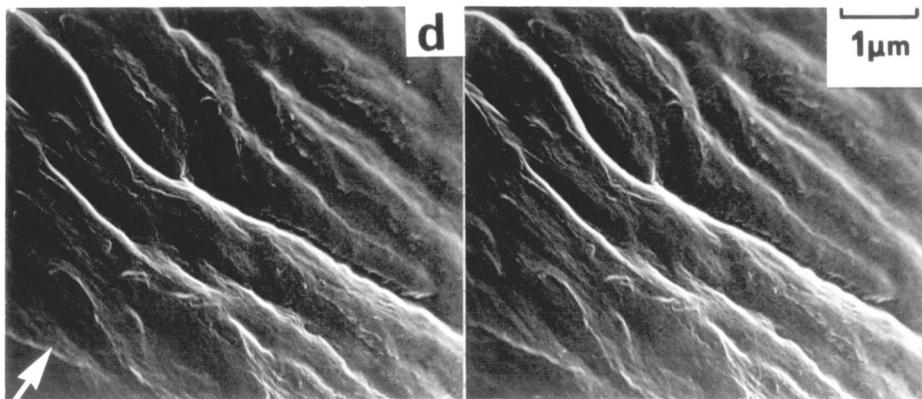
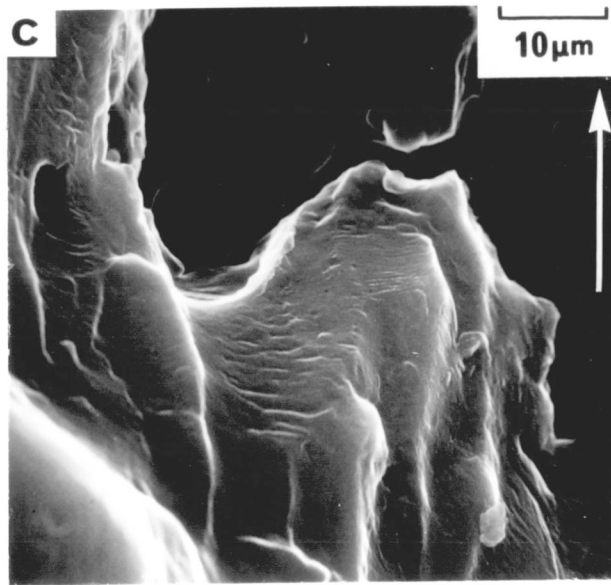
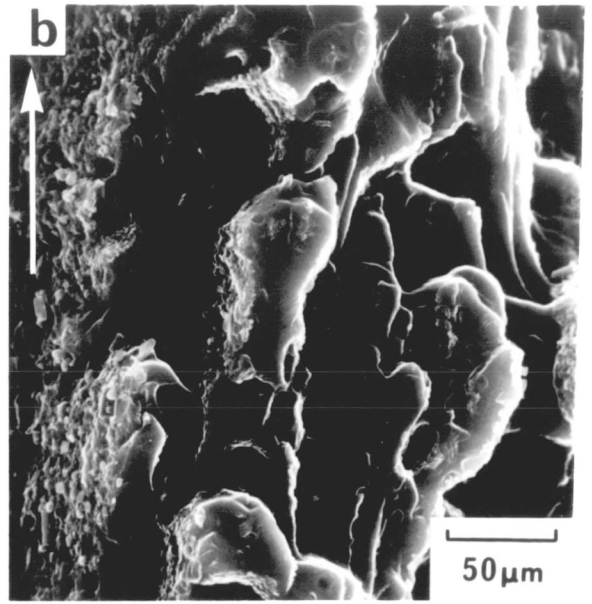
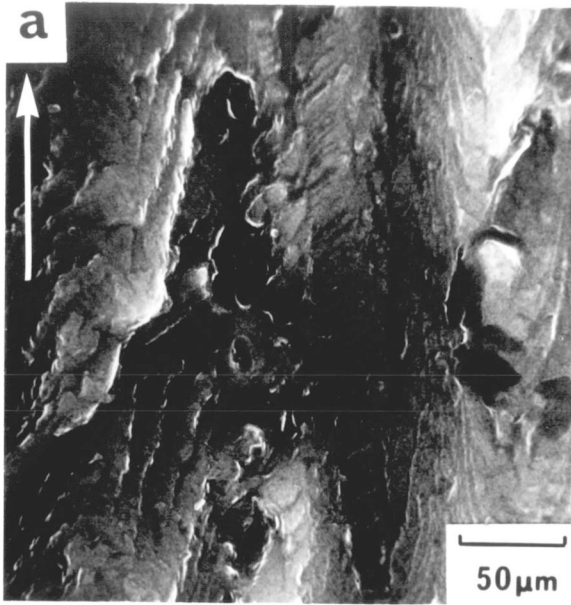


Fig. 5.53 Fractographic observations of crack growth in dry argon test environment.

(a) general fracture appearance

$$\Delta K_{(\text{mean})} \approx 15 \text{MNm}^{-3/2}$$

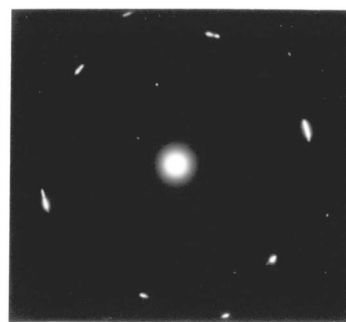
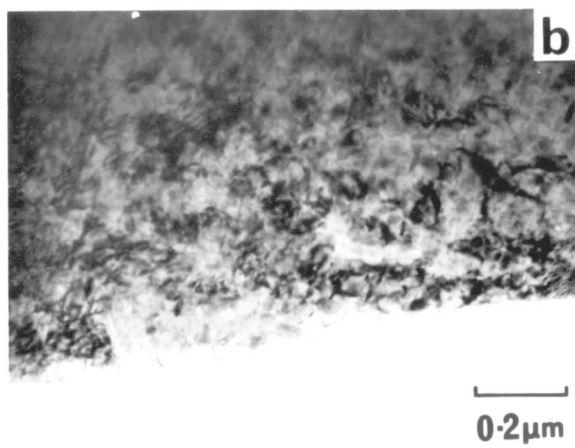
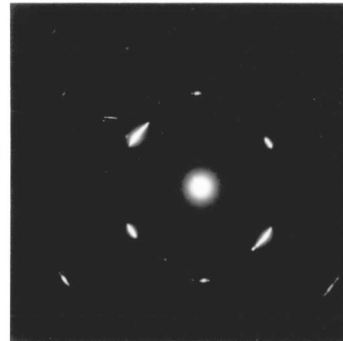
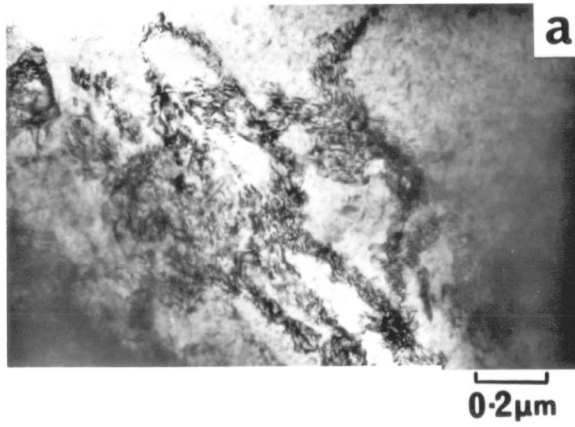
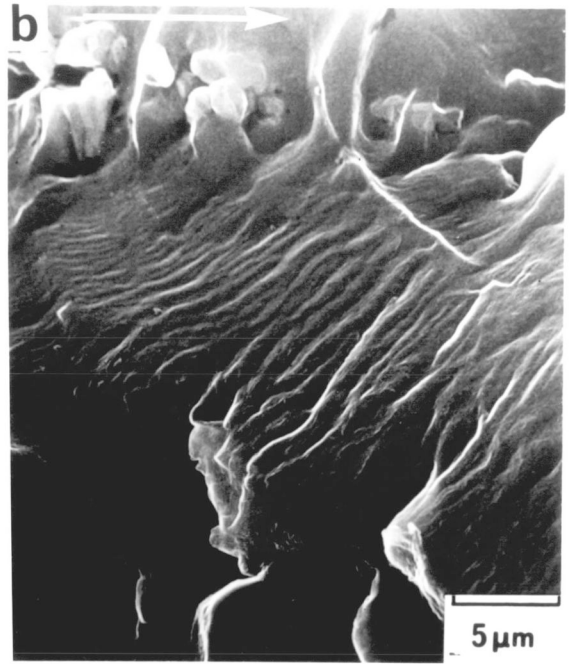
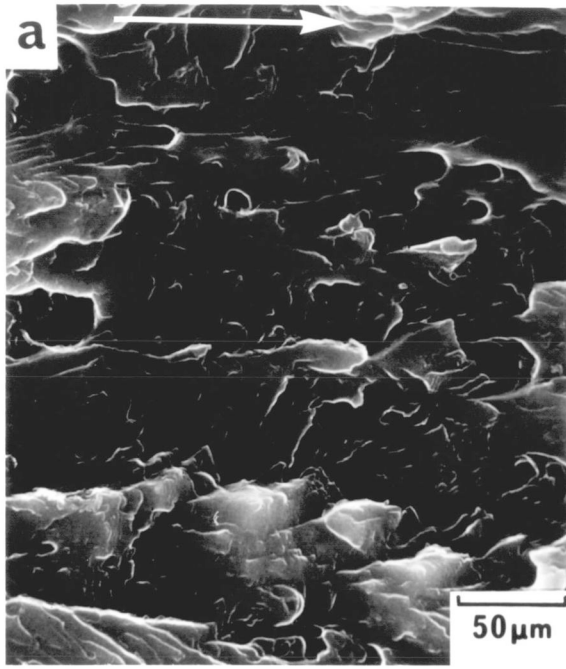
(b) striation like features at high  $\Delta K$

$$(\approx 27 \text{MNm}^{-3/2})$$

Fig. 5.54. TEM observations of plane section (type I) thin foil, specimens prepared from 'dry' fractures.

(a) dry argon test environment TEM bright field, 100KV, with corresponding SADP specimen untilted. (Zone axis  $\approx \langle \text{OII} \rangle$ .)

(b) dry oxygen test environment TEM bright field, 100KV, with corresponding SADP, specimen untilted (Zone axis  $\approx \langle \text{III} \rangle$ .)



structure observed in laboratory air tests was found to be absent at low  $\Delta K$  and the roughness of the fracture surface was found to be much higher.

Only at high  $\Delta K$  ( $>25\text{MNm}^{-3/2}$ ) could any features be observed which could be considered striations (Fig.5.52(c)) and as shown in the stereo pair these coarse markings were found to be far less regular than striations previously observed and of no particular profile. No differences in fractographic appearance could be distinguished between oxygen and argon environment.

Type I thin foil observations, (Fig.5.54) also revealed a completely different structure from that found in laboratory air fractures and once again no differences could be found between the two dry environments. Fracture planes did not follow any crystallographic orientation and even in areas where an  $\{011\}$  surface was observed (Fig.5.54(a)) no dislocation band structure could be found. The microstructure generally appeared to be one of uniformly high dislocation density.

### 3. DISCUSSION OF RESULTS.

#### 3.1 Introduction.

It is proposed here to carry out a discussion of the experimental results in relation to those obtained in previous studies reported in the literature. The discussion is broken down into five major parts: In the first, a mechanism of cyclic crack growth is developed, taking into account environmental considerations. In the following four sections the basic mechanism is discussed in relation to, (a) the formation of fractographic features, (b) the overall mode of failure, (c) the influence of loading conditions on crack growth and (d) the importance of metallurgical variables.

#### 3.2 The Mechanism of Crack Growth.

3.2.1 The Crystallographic Fracture Plane. In the preceding section results were presented which demonstrated the fatigue crack path in laboratory air to be in many areas crystallographic in nature. Both selected area electron diffraction and micro-etch pitting techniques demonstrated a fracture plane close to {OII} in all areas of crystallographic fracture. Under 'dry' test conditions no single crystallographic plane was found to lie close to the plane of fracture.

A number of other workers have made observations of crystallographic fatigue crack growth in aluminium alloys (70,73,107) and under conditions of stage II crack growth the most commonly observed fracture planes have been {OOI} and {OII}. In alloys similar in composition to 7010 and 2024 an {OOI} fracture plane has been exclusively observed by Pelloux (73) and Stubbington (70), both workers using etch pit observations and Stubbington also employing a Laué back reflection X-ray technique. Bowles and Broek (107) used an etch pitting technique similar to Pelloux and observed an {OOI} fracture plane in 7075 T6, but, using electron diffraction, an {OII} plane was found in most electron transparent regions. There appears therefore to be some agreement and some discrepancy between the present work and previous studies since here an {OII} plane was observed using both electron diffraction and etch pitting techniques.

There are two possible explanations for the differences between results obtained in the various studies, the first involving the limitations of the etch pit and Laué techniques and the second involving alloy texture. The observations made by Stubbington were carried out on electropolished fracture surfaces and hence it is possible that the actual plane of separation was not accurately determined. No such explanation is possible in the case of Pelloux's and Bowles and Broek's etch pitting studies, since here the actual fracture surfaces were used. Shadowed transmission replicas were however made in both cases to allow observation of etch pit shape and, as demonstrated in the present work by the high resolution SEM observations (Fig. 5.48), the etch pits produced were approximately square in two dimensions, even on {OII} surfaces. Careful stereoscopic observation of the pit base was necessary to differentiate {OOI} and {OII} pits. It is possible therefore that {OII} pits, the three dimensional shape of which would be impossible to determine accurately from shadowed replicas, were mistakenly identified as {OOI} in previous studies. This could certainly explain the rather surprising discrepancy in the results of Bowles and Broek between electron diffraction and etch pit data.

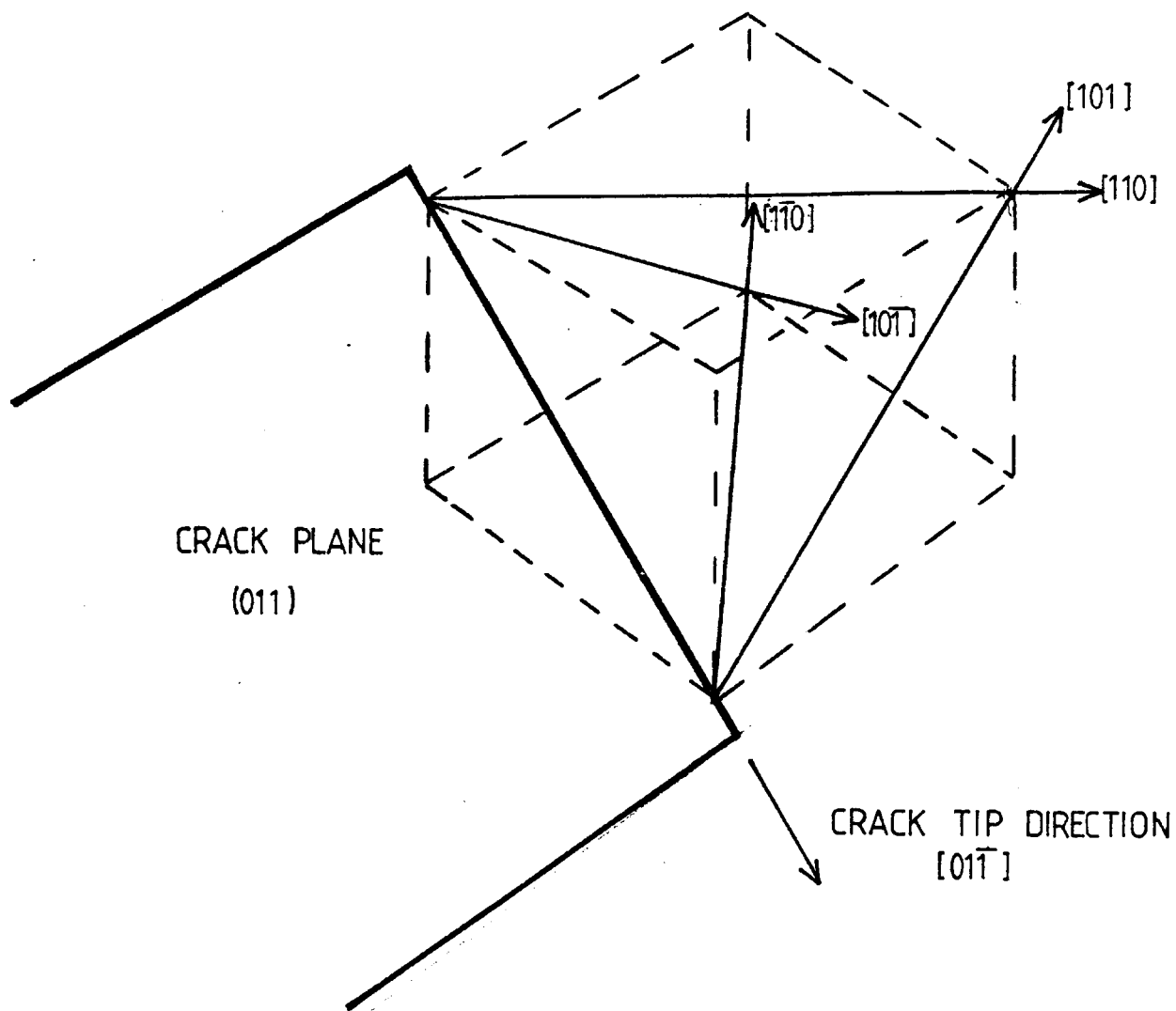
The 7010 plate was found to be heavily textured with {III} planes approximately parallel to the overall plane of fracture. This could have a profound effect on the occurrence of {OOI} and {OII} fracture planes: Assuming that the plane of fracture would tend to be as close to the overall plane of fracture as possible, i.e. at  $90^{\circ}$  to the tensile stress axis, {OII} planes generally would make a minimum angle of  $\approx 35^{\circ}$  to the overall plane, {OOI} planes however would make a minimum angle of  $\approx 55^{\circ}$ . Hence if both {OOI} and {OII} planes are potential fracture planes the {OII} planes would be expected to be most commonly observed. This observation of {OII} due to texture would be particularly marked in the case of electron diffraction observations, since, owing to the foil preparation technique (Fig. 2.10) only areas approximately parallel to the overall plane of fracture would be expected to be electron transparent.

The observation of a crystallographic fracture plane in fatigue

has been attributed to both cleavage fracture (70) and to a quasi-cleavage process involving the operation of slip systems symmetrically disposed about the crack tip (73). Both {001} and {011} fracture planes can be explained by the quasi-cleavage model of Pelloux, since they possess the appropriate symmetrical elements. However, the model implies that the fatigue crack tip must also follow a crystallographic direction of  $\langle 01\bar{1} \rangle$  in both cases. Pelloux used etch pit evidence to support his model but the more accurate electron diffraction techniques used in the present work were not in agreement with his results: The trace of the deformation band in the foil surface was clearly shown to be parallel to the striation front and this was not found to lie along any unique crystallographic direction. The most commonly observed direction was close to  $\langle 1\bar{1}1 \rangle$  (Figs. 5.28, 5.32, 5.33) although  $\langle 100 \rangle$ ,  $\langle 01\bar{1} \rangle$  and non crystallographic directions were also found (Figs. 5.37, 5.38). The etch pitting observations were also consistent with this, the  $\langle 1\bar{1}1 \rangle$  direction being most commonly close to the crack front direction (Fig. 5.49). Crack fronts were found to be curved in many cases (Fig. 5.22) (assuming that striations mark the crack front) and clearly the maintenance of a crystallographic crack front in such circumstances would not be possible without a curved, i.e. non-crystallographic, crack plane.

This evidence would appear to invalidate the simple model of Pelloux for the formation of a crystallographic fracture plane by the operation of two symmetrically disposed slip planes at the crack tip: According to this model the crack front direction must at any time be the line of intersection of the two active slip planes in the fracture plane (Fig. 5.55). If the crack front were to rotate from  $\langle 01\bar{1} \rangle$  then unequal slip would have to occur on the 4 systems at the crack tip in order to maintain an  $\langle 01\bar{1} \rangle$  fracture plane. Since the crack plane in this model would only follow  $\langle 01\bar{1} \rangle$  by virtue of slip system symmetry, however, it would seem more likely that the fracture plane would change in order to accommodate the new crack front direction. Since the TEM observations prove that this is not the case, a ductile shear mode of crystallographic failure would appear to be invalid.

Fig. 5.55



Crack tip slip system symmetry —  
[01 $\bar{1}$ ] crack tip direction

Further evidence against a shear mode of crystallographic fracture has been obtained by the observation of fractures produced in dry oxygen and argon environments. Here, fracture was not found to follow any crystallographic plane. Since this mode of crack propagation must be purely the result of shear, according to the Pelloux model, some kind of crystallographic dependence would be expected. Rewelding has been proposed to give rise to bifurcation of the crack front in vacuum but in an oxygen environment it is not thought that substantial rewelding could occur, a suggestion supported by Laird and Smith (83).

It is felt that the observation of {OII} fracture planes is more easily reconciled to a mode of failure involving cleavage, since here crack plane and crack front direction are not necessarily related. As discussed in I.4.I crystallographic failure has been observed under various conditions of environmental cracking in aluminium alloys and strong evidence has been presented to support transgranular cleavage (I05, I06). Transgranular cleavage has also been recently observed in Al-Zn-Mg alloy specimens pre-exposed to water vapour by Christodoulou (I3I). It would not seem unreasonable therefore, to expect a cleavage component in fatigue crack growth under moist conditions. The fracture planes observed in previous studies have included {OOI} (I05) and {OII} (I06). The occurrence of cleavage on planes other than those close packed (i.e. {III} ) has however been challenged by Laird (72) on surface energy grounds. However, theoretical calculations by Burton and Jura (I59) have shown that the surface energies of {OOI} and {OII} planes are not markedly higher than {III}. In fact  $\gamma\{III\}:\gamma\{OOI\}:\gamma\{OII\} = 1:1.6:2.5$ . The observations of crystallographic failure in aluminium alloys on {OII} and {OOI} planes which have been attributed to cleavage would not therefore seem unreasonable.

In summary therefore it is argued that the observation of a crystallographic plane of fracture in moist test conditions offers strong supportive evidence for a crack growth mechanism involving a cleavage component.

3.2.2 Crack Tip Deformation. It is proposed here to discuss

the formation of the deformation band structure and its possible significance. In the present work several important features of band formation have been noted:

- (a) The bands were only found under moist test conditions, laboratory air in this case.
- (b) They corresponded directly to fatigue striations in areas in which these features were observed, but were also found in areas of crystallographic fracture showing no striation topography.
- (c) The bands appeared to extend only to a very limited distance below the fracture surface ( $\sim 1\mu\text{m}$ ).
- (d) The trace of the band in the foil surface lay along a variety of crystallographic and non-crystallographic directions, approximately  $\langle \text{III} \rangle$  being most commonly observed.
- (e) The programme load tests demonstrated quite clearly that the deformation bands were formed on a cycle by cycle basis at some stage during each load cycle.

Using these observations as a basis it is possible to suggest processes occurring at the crack tip which might lead to band formation. Previous observations have been made of similar structures formed in 7075 T6 (84, I07) and two possible mechanisms of formation have been suggested: Firstly that the bands might form by spontaneous recovery at some critical amount of crack tip strain, possibly due to deformation occurring during crack closure (I07). The second proposed mechanism is that their formation is due to a brittle/ductile transition occurring during each increment of crack growth (84).

The idea that deformation bands are simply a closure effect is difficult to reconcile to conditions at the crack tip. Clearly the degree of strain involved in blunting the crack at maximum load (such blunting has been demonstrated by Bowles) must be equal to or greater than deformation during closure, since work hardening during opening must restrict deformation during closure. The premise could be made that since the crack may be advancing during opening and stationary during closure the plastic flow is more concentrated during closure. However, Bowles has proven that initial crack advance is accompanied by little or no plastic deformation and hence blunting

must be limited to the later stages of opening only. It would be expected therefore that evidence of this deformation in the form of dislocation debris would be observed in thin foil studies.

The suggestion of Bowles of a brittle/ductile transition occurring during each increment of growth is more easily reconciled to the experimental observations, in particular the extremely regular nature of the bands and the abrupt change in dislocation density; the regions between bands showing no evidence of recovered substructure. The absence of the bands under dry conditions would also appear to support this premise. Under these conditions regions of low dislocation density are not produced and hence these regions are clearly a result of the environmental influence.

The observation of both cross section and plane section thin foils demonstrated that the bands were very limited in their extent. At  $\Delta k \sim 15 \text{ MNm}^{-3/2}$  ( $R = 0.1$ ) the bands appeared to be around  $0.1 \mu\text{m}$  in width and extend to a distance of less than  $1 \mu\text{m}$  below the fracture surface. The bands can be related to the overall plastic zone size ( $r_p$ ) via one of the equations developed to describe this: Under plane strain conditions Lankford et al (1960) specify:

$$r_p(\theta=0) = \frac{(1-2\gamma)^2 K^2}{2\pi\sigma_y^2}$$

Where:

$\theta$  = angular direction across the plastic zone relative to the crack plane

$\sigma_y$  = yield stress

Various numerical solutions, discussed by Lankford et al, give a maximum for  $r_p$  at  $\theta \approx 70^\circ$  of:

$$r_p \approx 0.15 (K/\sigma_y)^2$$

$r_p \theta=0$  is often found to be the maximum. In the case of fatigue the situation is even further complicated by the presence of the reverse or cyclic plastic zone, concerned

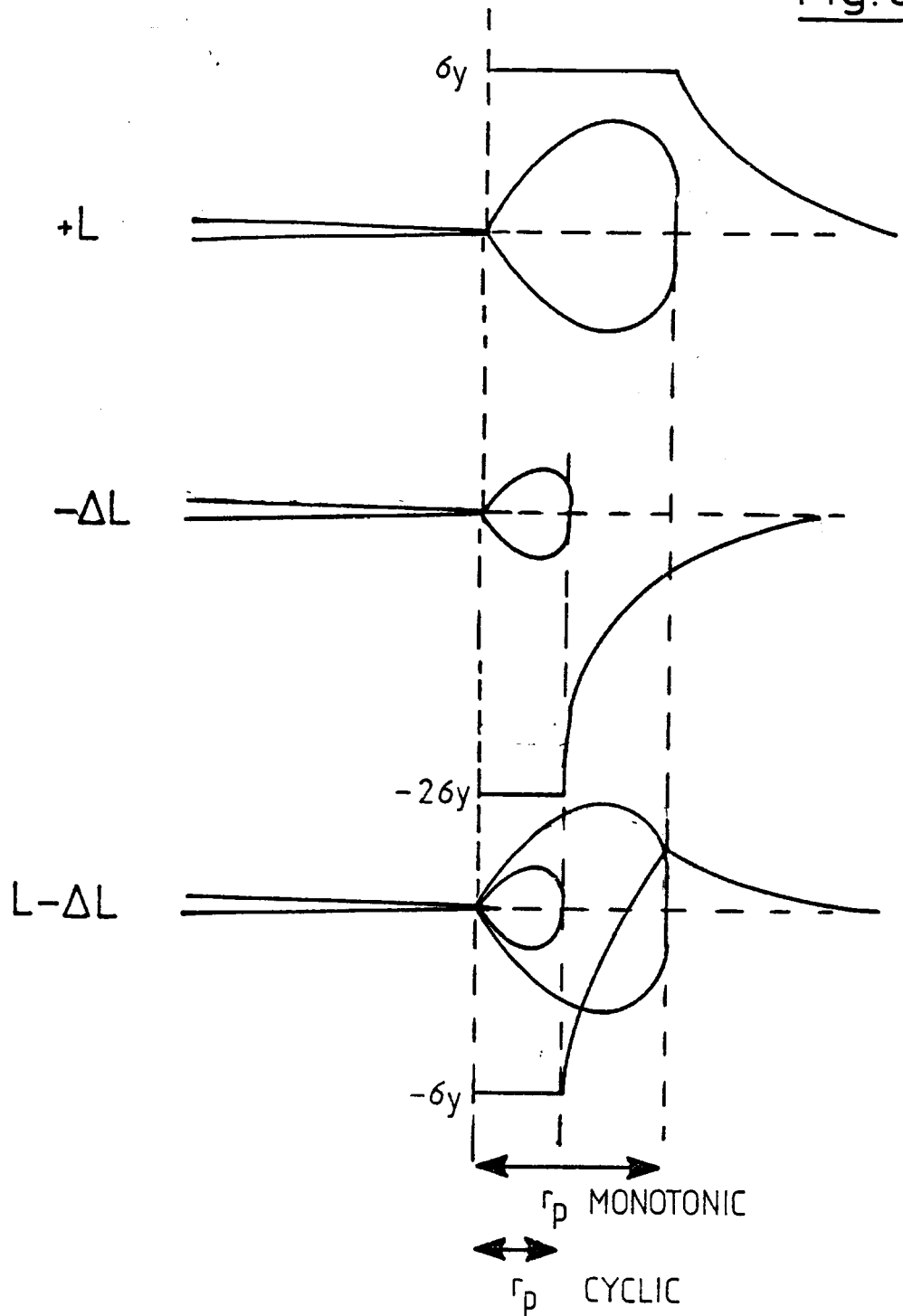
with deformation occurring during crack closure: Rice (I6I) used a superposition technique to calculate the reverse plastic zone size in which yield stress ( $\sigma_y$ ) was replaced by twice its original value to account for work hardening (Fig.5.56). Under fully reversed loading ( $R=0$ ) he calculated:

$$r_p \text{ cyclic} \approx \frac{1}{2} r_p \text{ monotonic}$$

To account for stress ratio  $K_{\max}$  has often been replaced by  $\Delta K$  giving for example the equation:

$$r_p \text{ cyclic} = \frac{1}{6\pi} \left( \frac{\Delta K}{\sigma_y} \right)^2$$

Using these equations the approximate monotonic and cyclic plastic zone sizes can be calculated as shown in Table 5.IV. Clearly the deformation bands cannot possibly account for the total amount of plastic deformation occurring ahead of the crack. It is well known however, that while the plastic zone size marks the overall extent of the region of plastic strain ahead of the crack tip, the degree of cyclic strain varies very greatly within the plastic zone. Hahn et al (I62), for example, studied plastic strains ahead of a propagating fatigue crack in Fe 3%Si and were able to represent the cyclic strain history within the plastic zone as shown in Fig.5.57. Three distinct regions were observed: A microstrain region ( $\epsilon_p < 10^{-3}$ ) which was related to the overall plastic zone size, a region equivalent to the cyclic plastic zone size,  $10^{-3} < \Delta \epsilon_p < 10^{-1}$  ( $\Delta \epsilon_p$  = plastic strain), and a region of extremely high strain  $10^{-1} < \Delta \epsilon_p < 1$  which could be related to the crack opening displacement. This region was found to extend to a distance ahead of the crack equivalent to about half the crack opening displacement, equal to around  $10 \times da/dn$ , in this material. This region, if present in aluminium alloys would be expected to be around 1 to  $2 \mu\text{m}$  in width ahead of the crack tip and hence would be somewhat more extensive than the deformation bands. In fact, the regions of recovered subgrains observed ahead of the crack in the modified, ion-beam thinned, cross section specimens may be a mark of this region.

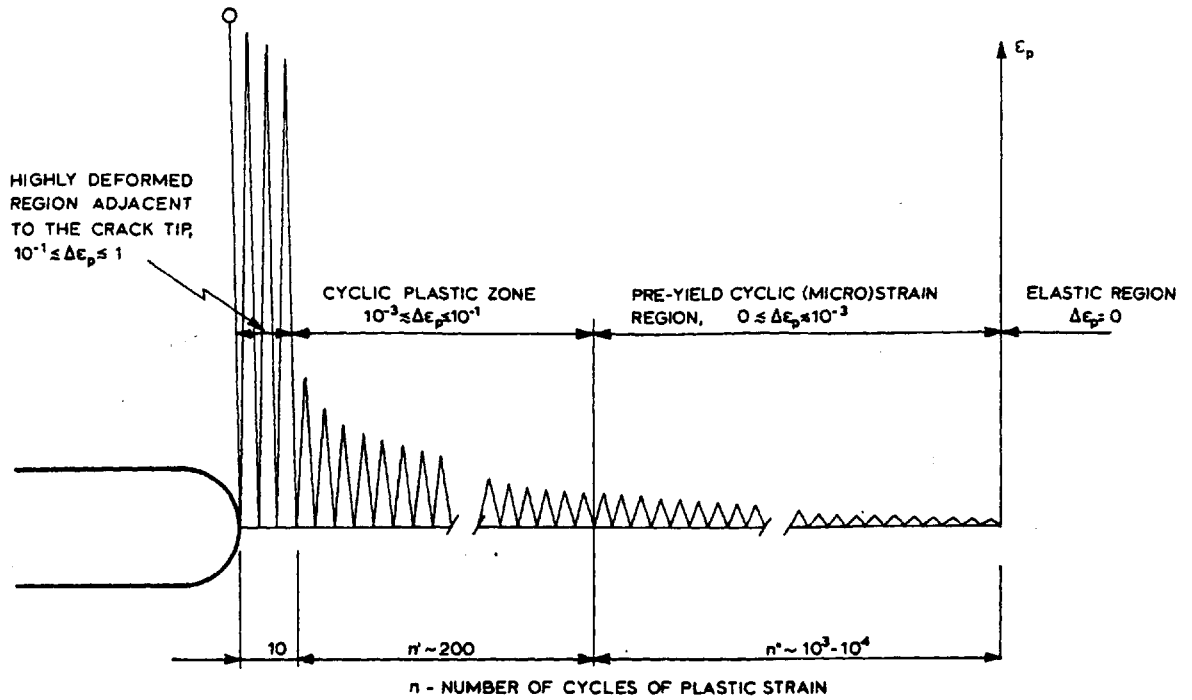


Superposition Process used by  
Rice [161] to Describe Reverse  
(or Cyclic) Plastic Zone

Table 5.IV. Plastic Zone Size Calculations.

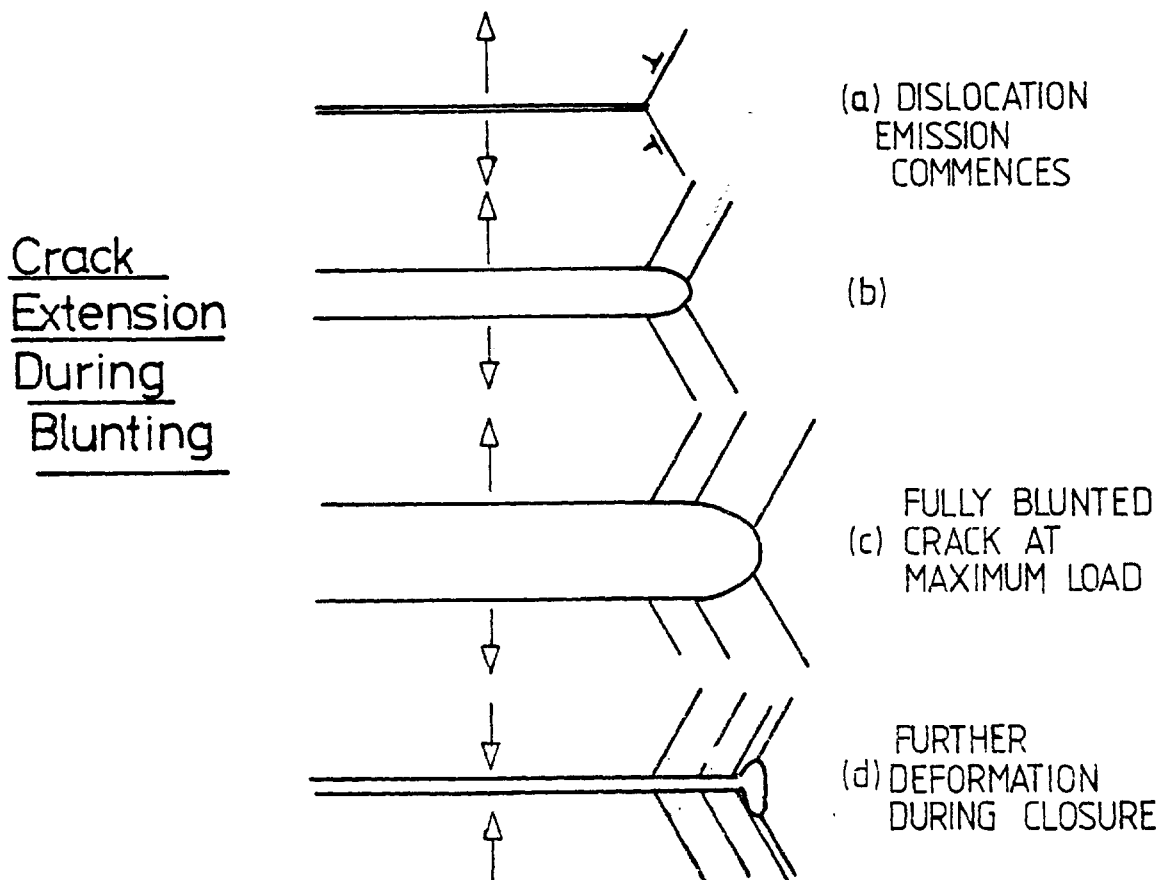
K <sub>max</sub>	ΔK(R=0.1)	rp monotonic (μm)		rp cyclic (μm)
		min	max	max
8	7.2	5	43	11
10	9.0	7	68	18
12	10.8	10	98	26
16	14.4	19	174	47
18	16.2	24	220	59
24	21.6	43	392	105
30	27.0	66	612	164

Fig 5.57



Cyclic Strain History ahead of a Fatigue Crack  
From Hahn et al [162]

Fig 5.58



It is felt that the deformation bands are produced by dislocation emission from the crack tip itself during the blunting phase, where, according to Hahn et al, plastic strains of the order of unity would be expected. The true width of the deformation band would in this case approximately mark the limit of crack extension during the blunting phase, as shown in Fig.5.58. The actual width if the deformation band could be considered to be equivalent to the extent of crack extension under dry conditions, the low dislocation density regions being equivalent to the environmentally influenced portions. The two component growth equation invoked by Selines and Pelloux (121) could be applied:

$$\frac{da}{dn} \text{ total} = \frac{da}{dn} \text{ corrosion} + \frac{da}{dn} \text{ mechanical}$$

This would imply a non-environmental growth rate equivalent to approximately one quarter of the total (i.e. the ratio of deformation band width to spacing). Selines and Pelloux presented evidence to support such a visualisation of corrosion fatigue crack growth in aluminium alloys and certainly if a two stage process as invoked in the present work is involved then such a visualisation is a useful one.

3.2.2(a) Crystallographic Considerations. Deformation bands and (where appropriate) fatigue striations were found to lie along a number of crystallographic directions, most commonly close to  $\langle 111 \rangle$ . However non-crystallographic directions were observed in some cases and since striations often appeared to be curved the crack tip direction cannot be exclusively crystallographic. However, rotations in crack front direction across grain boundaries did occur and hence some kind of crystallographic influence on crack front direction would appear to exist.

The most likely mechanism of control of crack tip direction is one involving slip system orientations during the blunting phase of the cycle, similar in concept to the Pelloux (73) model of crack growth although in this case it is felt, as discussed earlier, that the crack plane is controlled by the cleavage crack growth segment rather than by slip system

symmetry. The Pelloux mechanism specifies however that the crack tip direction must be a line of intersection of the crack plane and the active slip planes (Fig. 5.55) which implies an exclusively  $\langle OII \bar{\rangle}$  crack tip direction in the case of an  $\{OII\}$  crack plane. Such a mechanism would seem most unlikely from fractographic observation alone since, as only one such direction exists in any one  $\{OII\}$  plane, large rotations in crack front direction would be expected across grain boundaries of up to  $90^\circ$ . Angles of around  $30^\circ$  were the maximum observed in the present work. The Pelloux model is however based upon a single crystal analogue in which shear on two  $\{III\}$  planes throughout the crystal is proposed to lead to crack growth. In a polycrystalline aggregate this is clearly quite impossible and it is proposed therefore that the crack tip direction need not be a line of intersection of slip planes and crack plane. A more appropriate consideration would be one of the actual slip systems at the crack tip.

The slip system symmetry for a crack on an  $(OII)$  plane is shown in Fig. 5.55. Four slip systems can give displacements leading to crack extension and opening and these have an equal Schmid factor (assuming that the  $(OII)$  plane is perpendicular to the stress axis). Addition of all four Burgers vectors gives a total displacement perpendicular to the  $(OII)$  direction in the  $(OII)$  crack plane and hence, as predicted by the Pelloux model, equivalent amounts of slip on each of the four systems would give an  $\langle OII \bar{\rangle}$  crack tip direction.

In a real situation of a polycrystalline aggregate the position must however be considerably more complicated: On a macroscopic scale the overall crack plane tends to be perpendicular to the axis of maximum tensile stress and the crack front follows a certain direction, governed by fracture mechanics considerations and the tendency to minimise overall crack area. On a microscopic scale there also exist the further constraints of  $\{OII\}$  crack plane and crack front continuity from one grain to the next. Hence the symmetrical situation visualised by Pelloux would seem most unlikely. Unequal slip on a number of slip systems at the crack tip must therefore be expected. Consideration of cross-slip may also be of

importance: McEvily and Boettner (1963), for example, observed that crack propagation in Cu-Al alloys of low stacking fault energy (S.F.E.) was characterised by a linear crack front while in high S.F.E. materials such as aluminium alloys curved striations were found.

Within this complex situation of unequal slip there may exist certain crack front directions which are minimum energy situations. This may explain the apparent tendency towards a crystallographic crack front, most commonly of  $\langle 11\bar{1} \rangle$ . The  $\langle 11\bar{1} \rangle$  crack tip direction can for example be described by the activation of only two slip systems at the crack tip: The equal operation of only slip systems (1) and (3) in Fig. 5.55 would give a total displacement in the  $(21\bar{1})$  direction and hence a crack direction perpendicular to this of  $(\bar{1}1\bar{1})$ . This may explain the observed crystallographic crack front tendency although it must be emphasised that the overall situation regarding crack tip dislocation activity must be more complex.

3.2.3 Environmental Considerations. The evidence presented in the preceding two sections is strongly supportive of a crack growth mechanism, in a laboratory air environment and at test frequencies up to 100 Hz, involving initially cleavage mode crack extension followed by blunting. In dry oxygen and argon environments the mechanism appears to be completely different involving only dislocation motion. With reference to the studies of, for example, Bradshaw and Wheeler (88), discussed earlier, it is clear that the change in water vapour content from <10 ppm to ~50%RH involved in the present work would be expected to markedly effect the crack growth rate, little environmental influence being observed at 10 ppm H<sub>2</sub>O at a frequency of 100 Hz, with a full environment effect in laboratory air at all frequencies employed.

From the mechanistic viewpoint, the absence of both crystallographic fracture and deformation bands in dry atmospheres obviously demonstrates that cleavage is environmentally induced, a conclusion which is in agreement with the recent findings of Bowles (84). No differences were observed in growth mechanism between dry oxygen and argon environments, so clearly

surface oxidation per se cannot be the factor leading to the change in fracture mode and so the Stoltz and Pelloux (II5) type of mechanism can be discounted. The occurrence of the ductile/brittle transition is of great interest since the implication is that during each load cycle the mode of crack extension changes. Several mechanisms of environmentally induced embrittlement have been proposed, as discussed in I.4.2. Clearly the actual operative mechanism must be able to predict this transition: If an adsorption mechanism of embrittlement is applied, such as that of Bowles, the transition is not readily predicted, together with various effects involved with, for example, stress wave shape as detailed in the earlier discussion.

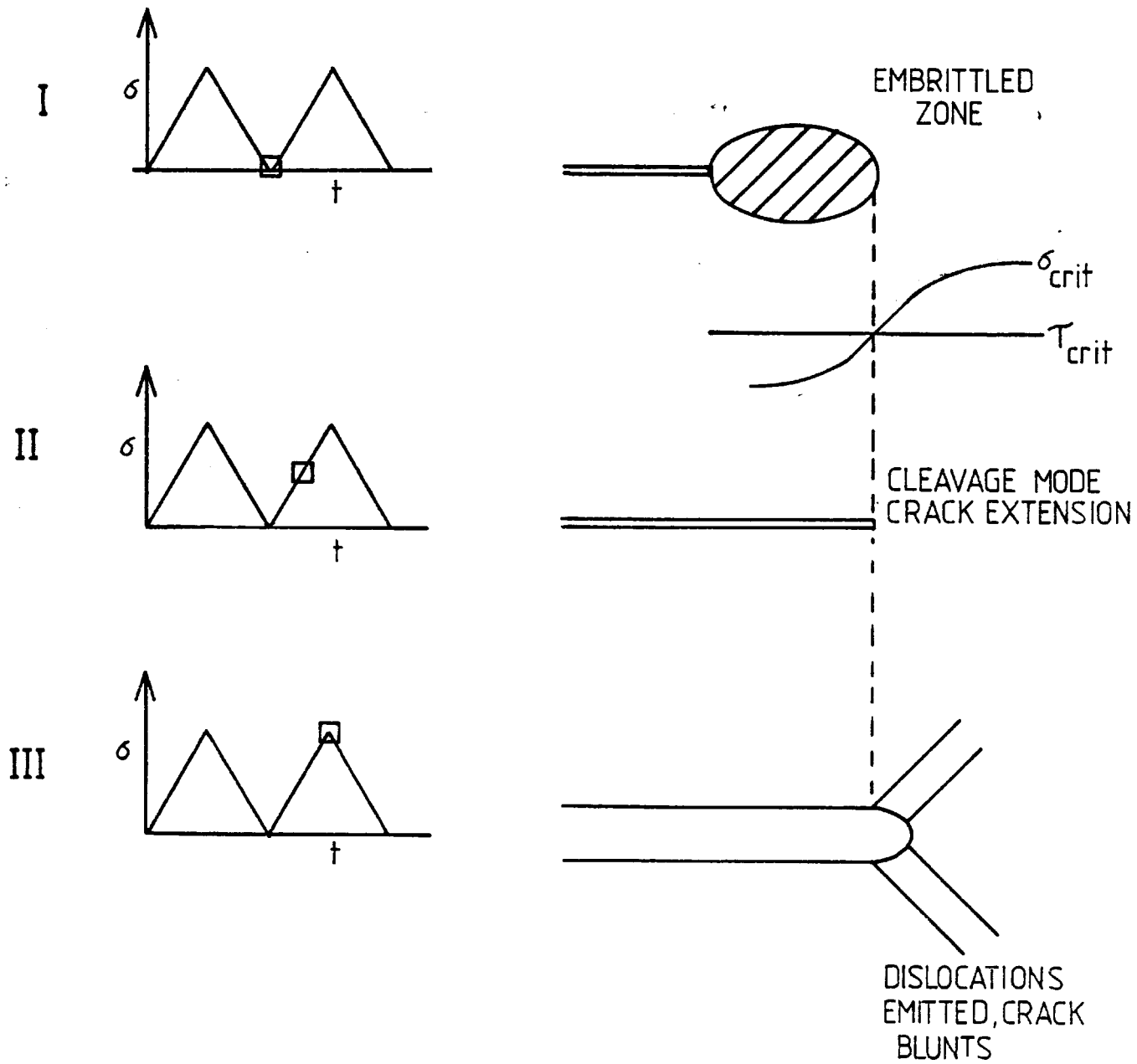
The formation of an embrittled zone ahead of the crack due to hydrogen penetration in to this region offers a more plausible explanation of the effect. Taking the simple approach that hydrogen reduces  $\sigma_{crit}$  while  $\tau_{crit}$  remains unchanged (assuming the Kelly et al (II0) model) then the mechanism can be visualised as shown in Fig.5.59.

An exactly similar mechanism has been proposed to explain transgranular S.C.C. in aluminium alloys by Bursle and Pugh (IO6) and has been supported by the recent acoustic emission studies of Beavers and Pugh (I64) in a Cu-Zn alloy. The presence of an embrittled zone due to hydrogen penetration has been postulated in both cases and Beavers and Pugh found that the crack velocity during cleavage extension was extremely high, possibly  $10^5$  cm/s.

The overall crack velocity observed in their studies was however found to be very low  $\sim 0.1 \mu\text{m/s}$  with crack jump distances of several  $\mu\text{m}$ . In the present work the embrittlement effect has been observed at test frequencies upto 100 Hz and as shown in Table 5.1, the depth of hydrogen penetration during one cycle (i.e. in 0.01s) by lattice hydrogen diffusion is a maximum of  $10 \text{ \AA}$ . Hence the embrittled zone width of up to  $0.5 \mu\text{m}$  cannot possibly be explained by lattice hydrogen diffusion.

The formation of an embrittled zone via lattice diffusion

Fig. 5.59



Proposed Crack Growth Mechanism

also implies that the embrittled zone width would be determined purely by diffusional considerations and would therefore be unaffected by stress intensity. This is quite clearly not the case since, with increasing crack growth rates, the width of the embrittled zone was found to increase.

It is argued that both the width of the embrittled zone and its dependence on stress intensity range may be explicable by a growth mechanism involving dislocation transport of hydrogen. As shown in Table 5.II Tien (I38) gave predictions for the enhancement of hydrogen penetration distance, due to dislocation transport, during various periods of cyclic strain. His calculations did not refer to hydrogen in aluminium but, according to the model,  $X_C/X_D$  (the enhancement of penetration) was proportional to  $D_H^{1/2}$ . Hence the model can simply be extended to cover the range of possible  $D_H$  for aluminium alloys at room temperature. As discussed in I.4.6 the likely range is  $10^{-19} < D_H < 10^{-8} \text{cm}^2 \text{s}^{-1}$ . Using Tien's approximation of equal binding energy and Burgers vector for different materials the model gives results as shown in Table 5.V. Clearly at  $D_H = 10^{-19} \text{cm}^2 \text{s}^{-1}$  no enhancement of diffusion distance is possible even at extremely low cyclic frequency and an embrittlement mechanism involving hydrogen penetration would be quite impossible. At a high diffusivity of  $10^{-8} \text{cm}^2 \text{s}^{-1}$ , however, considerable enhancement of penetration is predicted and the formation of a brittle zone of up to  $\sim 0.1 \mu\text{m}$  in width could be explained at test frequencies up to 1 KHz. Clearly the assumptions made in this model do not allow the dislocation transport mechanism to be quantitatively tested but it would appear that an embrittled zone of the width observed in the present work at frequencies up to 100 Hz would be possible provided  $D_H > 10^{-10} \text{cm}^2 \text{s}^{-1}$ . It is believed that the factor of major importance here is the maximum dislocation velocity for hydrogen transport ( $V_C$ ) which is related to the binding energy between dislocation and hydrogen atom. Provided this velocity is not exceeded dislocation transport distances can clearly be related to the distances which transporting dislocations move rather than to a time dependent factor. This view would appear to be supported by experimental observations in the present work, since according to the Tien model  $X_C \propto t$  (i.e.  $\propto I/f$ ) and hence a much narrower embrittled zone would be expected at high

Table 5.V. Possible Hydrogen Penetration Distances Due to Dislocation Transport.

Cyclic Frequency	$D=10^{-19} \text{ cm}^2 \text{ s}^{-1}$	$D=10^{-10} \text{ cm}^2 \text{ s}^{-1}$		$D=10^{-8} \text{ cm}^2 \text{ s}^{-1}$	
	$X_C/X_D$	$X_C/X_D$	$X_C$	$X_C/X_D$	$X_C$
ICPH	$1.32 \times 10^{-1}$	$4.4 \times 10^2$	1.06cm	$4.4 \times 10^3$	106cm
ICPM	$5.40 \times 10^{-2}$	$1.8 \times 10^2$	0.50cm	$1.8 \times 10^3$	5.5cm
IHz	$7.20 \times 10^{-3}$	$2.4 \times 10^1$	9.60 $\mu\text{m}$	$2.4 \times 10^2$	960 $\mu\text{m}$
60Hz	$9.00 \times 10^{-4}$	$3.0 \times 10^0$	0.15 $\mu\text{m}$	$3.0 \times 10^1$	15.0 $\mu\text{m}$
IKHz	$2.20 \times 10^{-4}$	$7.4 \times 10^{-1}$	9 $\text{\AA}$	$7.4 \times 10^0$	0.09 $\mu\text{m}$
IOKHz	$6.60 \times 10^{-5}$	$2.2 \times 10^{-1}$	----	$2.2 \times 10^0$	88 $\text{\AA}$

Based on the Model by Tien (I38)

$X_C$  = Dislocation transport distance

$X_D$  = Bulk diffusion distance

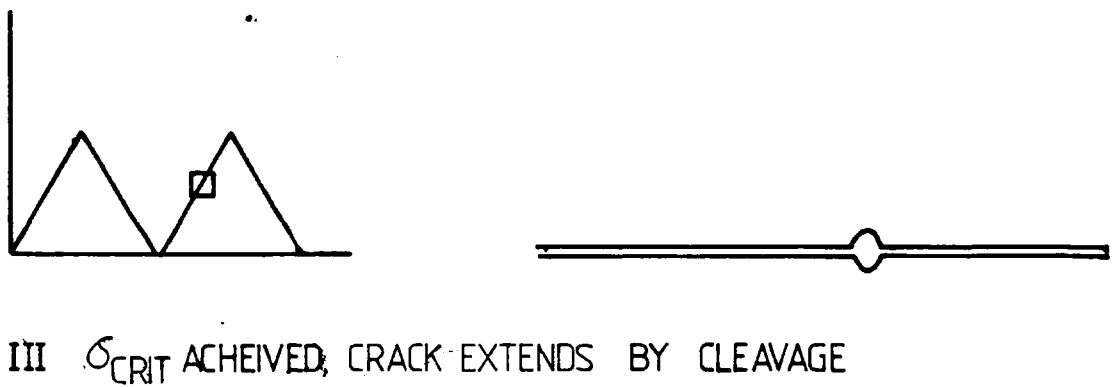
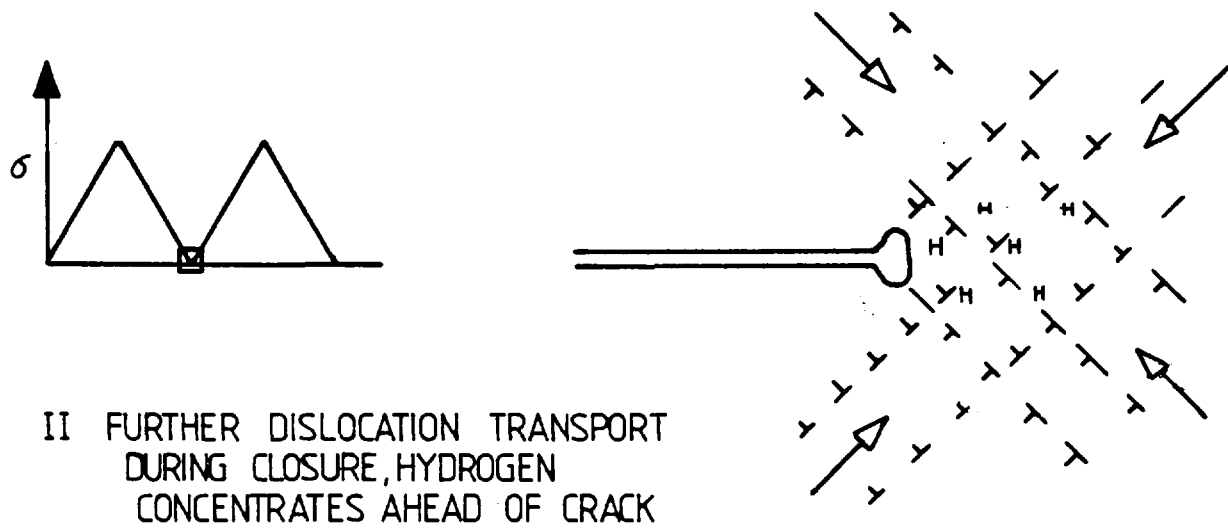
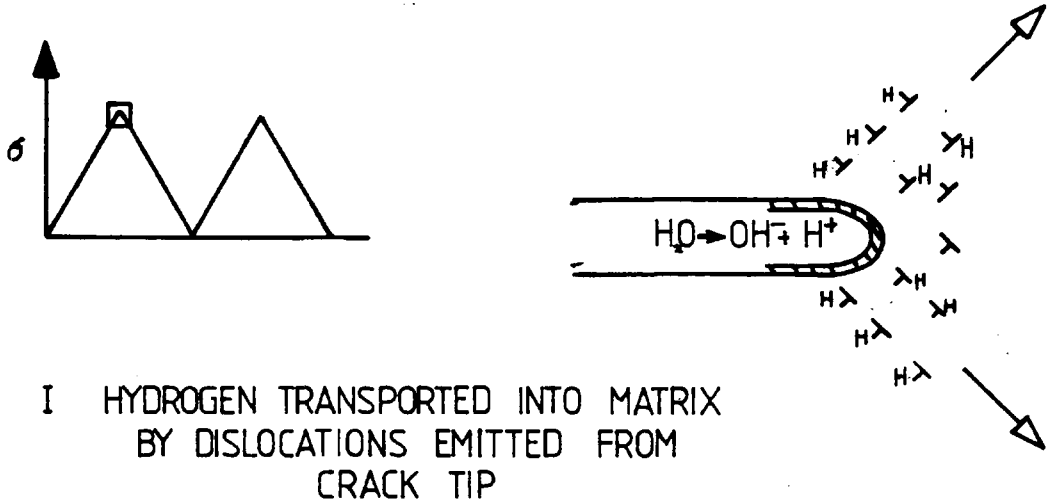
$X_D = 4\sqrt{D_H t}$ . (equation used by Tien)

frequency. This has not been qualitatively observed, the embrittled zones being of approximately the same width at equivalent  $\Delta K$  over the whole frequency range employed.

Since hydrogen must be produced by reaction of water vapour with the newly exposed surfaces at the crack tip, initial transport can only occur via dislocations escaping from this region. These dislocations would appear to be those involved in the formation of deformation bands. The extent of deformation bands may therefore be related to the depth of the embrittled zone. The deformation bands are however composed of trapped dislocations and further mobile dislocations must therefore be involved in the final transport of hydrogen into the region ahead of the crack leading to embrittled zone formation. This secondary transport must be of importance since, as demonstrated by the thin foil studies, the deformation bands lie on planes of high shear stress at an angle to the crack plane, and slip on these systems would tend to transport hydrogen away from the crack tip region. As discussed earlier the deformation bands do not define the limit of dislocation activity within the plastic zone and hence such secondary transport is possible. Reverse motion of dislocations during crack closure may also play an important role in increasing the hydrogen concentration in the crack tip region. The overall process may be as visualised in Fig. 5.60. The possible relationship between embrittled zone width and crack tip dislocation activity is an interesting one: Certainly the number of hydrogen atoms transported and the depth of penetration must be related to the number of mobile dislocations and hence to plastic strain. The experimental observation that the embrittled zone width depends on  $\Delta K$  is clearly in agreement with this.

Despite the possible limit to embrittled zone size due to crack tip dislocation activity, there must exist a frequency above which the dislocation velocity exceeds the critical value and dislocation transport does not occur. With reference to Table 5.V a frequency of the order of  $10^4$  Hz would be implied, using the Tien model. Clearly this frequency is well outside the range of present study and also those of Bradshaw

Fig. 5.60



Proposed Mechanism of Embrittlement

and Wheeler (88) and Wei et al (97) discussed in I.3. Crack growth rate measurements at very high frequencies have been carried out by Hockenhull and Monks (165). Here, tests were carried out on specimens of RR58 in laboratory air and water environments at frequencies of 100 Hz and 20KHz. The fatigue lives of specimens tested in both environments were found to increase at high frequency and crack growth rates were apparently reduced. This effect could be attributed to reductions in hydrogen transport distance, but, at frequencies of this magnitude, reaction rate and water vapour transport kinetics may be of importance, even in high water vapour pressure environments such as those studied by Hockenhull and Monks. The equation developed by Bradshaw and Wheeler (88) (at much lower test frequencies) to describe experimental observations of the influence of water vapour pressure may be applicable:

$$P_c = 4.0 \times 10^2 \frac{da}{dn} \cdot f$$

(See I.3 for details.)

At 100%RH at 20°C,  $P_{H_2O} \approx 17.5$  Torr and hence the critical growth rate for full environmental influence  $\approx 5.6 \times 10^{-6}$  cm (=0.05 $\mu$ m) at  $f=20$  KHz. Hence it is clear that at high test frequencies, even in pure water environments, limitation on reaction and water transport rates may be controlling the rate of crack growth as well as the removal of dislocation transport of hydrogen and the two effects may not therefore be experimentally separable.

In conclusion the factors influencing the hydrogen concentration in the crack tip region are complex and it is not possible to propose a quantitative mechanism of embrittlement. The experimental observations are however most readily explained by a process involving the dislocation transport of hydrogen.

### 3.3 Fractographic Features.

3.3.1 General Features. The formation of flat fracture facets, most clearly defined at low  $\Delta K$ , can be simply described as further supportive evidence for the occurrence of crystallographic fracture on {OII} planes. The facets are evidently not continuous across grain boundaries, and facet angles

differ between adjacent grains, the planar grain boundaries being particularly clearly defined on the fracture surface owing to this. However, in the case of the centre notched specimen types they were observed to be almost continuous, even across grain boundaries, with only small changes in facet angle. This would not be expected in a material of random grain orientation. As described in Part 2 section 2 however, the 2.54cm alloy plate was found to be heavily textured with {III} planes lying approximately in the overall plane of fracture, and {OII} planes lying therefore at an angle of around  $30^{\circ}$  to it (Fig.3.10). Crack growth on {OII} planes would therefore lead to facets at an angle of  $30^{\circ}$  to the overall fracture plane. In order to maintain the overall crack plane approximately perpendicular to the load axis cooperative growth on symmetrically disposed {OII} planes would be expected, leading to the formation of a 'roof top' structure, with facet intersections lying along the direction of crack growth. This could be visualised as shown in Fig. 5.6I. Such a structure is consistent with those experimentally observed (Fig.5.15) although small regions of ductile tearing have been found to link facets in some cases (Fig.5.62). Similar structures have previously been observed in aluminium alloys by, for example, Forsyth and Bowen (57) and Cina and Kaatz (148). Cina and Kaatz in fact attributed the formation of facets (described as 'ridges' in their study) to a low  $\Delta K$  growth mechanism not involving the formation of fatigue striations. This is clearly not the case, striations being readily observed on these facets in the present study (Fig. 5.2I).

The gradual disappearance of the faceting with increasing  $\Delta K$  is believed to be related to plastic zone size (Fig.5.63). As  $\Delta K$  increases large intermetallics become incorporated within the plastic zone and affect the stress distribution ahead of the crack. They may become cracked or debonded forming a micro-crack ahead of the crack front. This may lead to deviation of the crack path, resulting in incorporation of the micro-crack into the overall fracture plane. Such effects as this are likely to lead to transfer of crack growth to {OII} planes more steeply angled to the fracture surface leading to a break down of the faceted structure. The crack growth mechanism

Rooftop Fracture Morphology

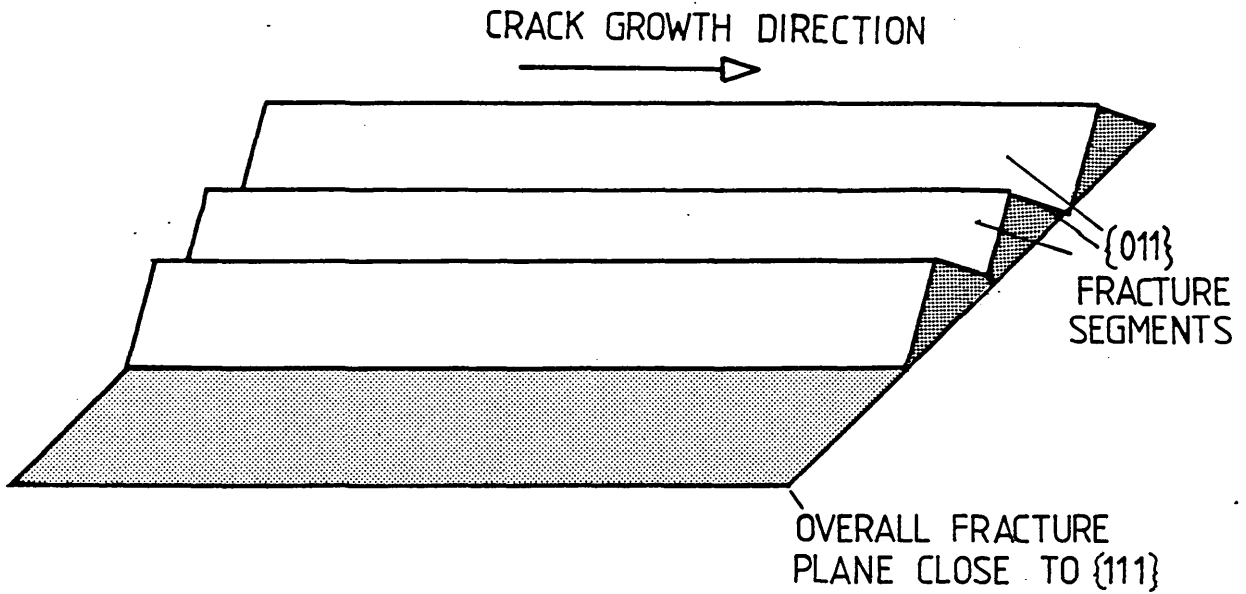
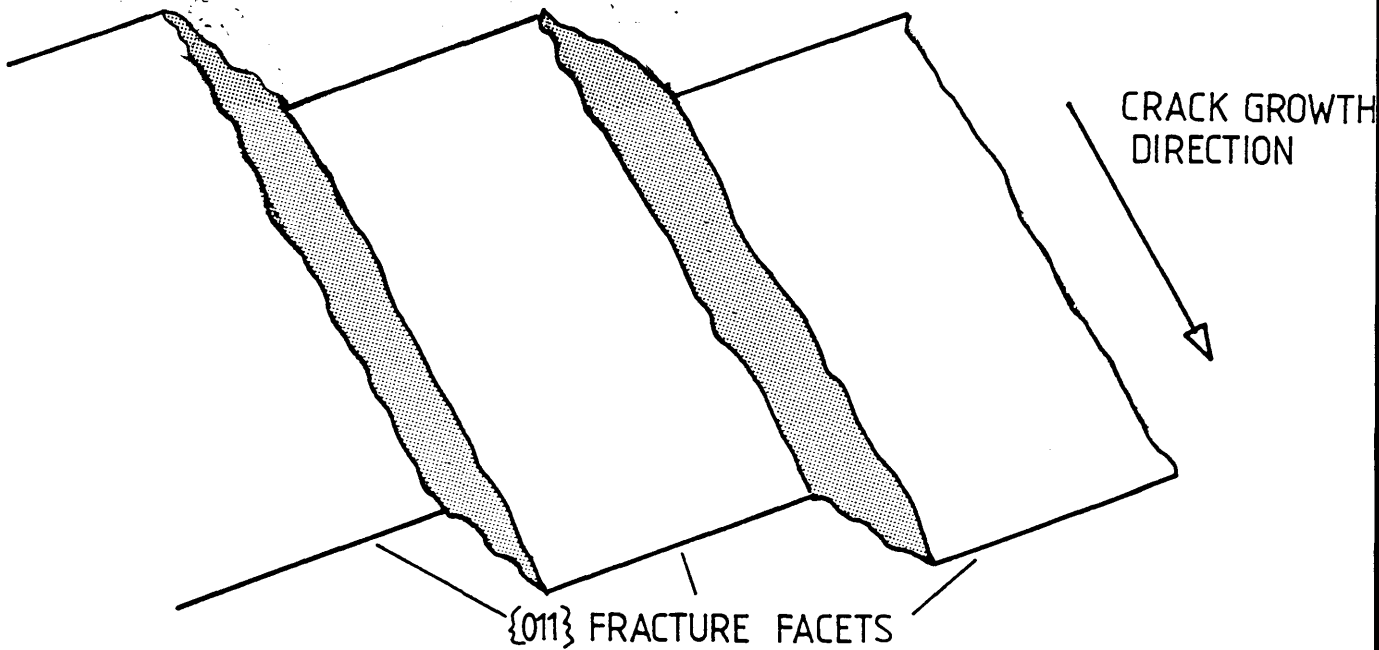
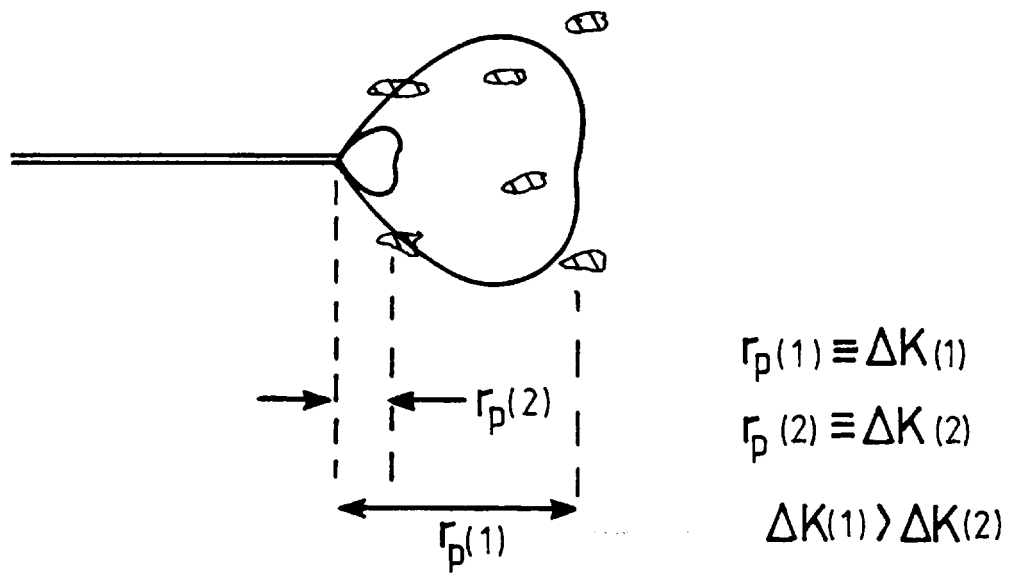


Fig 5.62

Crystallographic Fracture Facets  
Linked by Ductile Tearing





Involvement of Large Inclusions in Fracture:  
Effect of Plastic Zone Size

is still believed to be one of cyclic crack growth however, even in regions very close to intermetallics as demonstrated in Fig. 5.35.

At still higher  $\Delta K$ ,  $K_{\max}$  close to  $K_c$ , substantial areas of ductile tearing were found to be prevalent giving a typical ductile dimple failure appearance. Small regions of crystallographic fatigue crack growth were observed nevertheless, up to the point of final failure. The overall sequence of crack growth would therefore appear to include faceted fatigue crack growth, followed by irregular fatigue crack growth and finally dimple rupture.

In the C.T. design of test piece the faceted structure was found to be less well marked. Two possible explanations exist: Firstly the long transverse growth direction may mask the effect since the crack growth direction is along the planar grain boundaries in this case. Secondly, and it is believed, most probably, the effect is due to a reduction in texture strength in this type of specimen: The centre notched specimens were prepared from 2.5 cm 7010 plate while the C.T. design specimens were from 7.5 cm plate. The thick plate texture was not determined but since initial billet sizes were similar the amount of hot rolling involved in the 7.5 cm plate preparation would be correspondingly reduced.

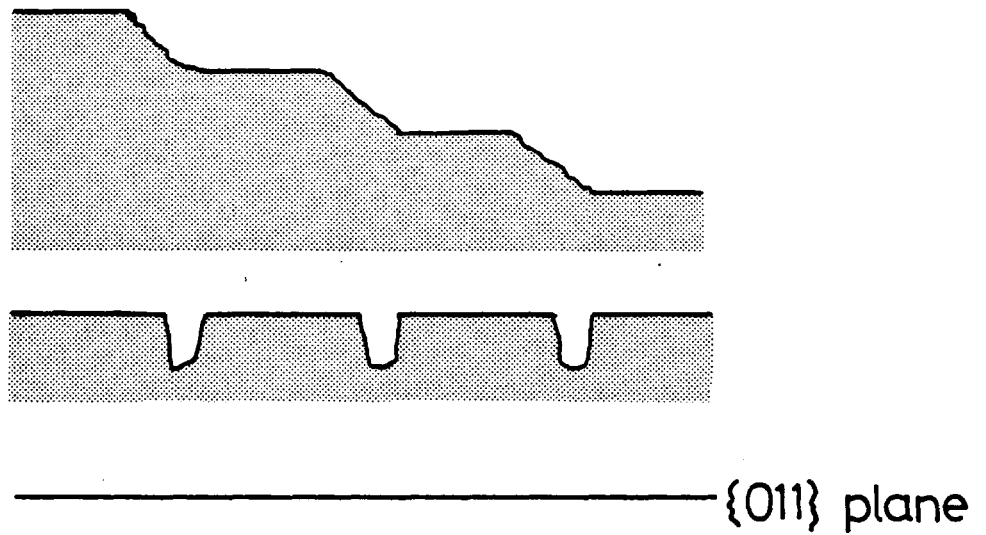
3.3.2 Fatigue Striations. In the present work two basic types of fatigue striation were observed, one of sawtooth profile (type A using the Stubbington (70) nomenclature), and another consisting of deep slots separated by parallel featureless regions of fracture (type B). The plane section foil TEM observations, in which striations were related to underlying substructure, demonstrated that the basic crack growth mechanism was the same in the two cases. This finding is not in general agreement with many earlier observations, for example, those of Stubbington (70), in which type A was believed to be associated with a ductile fracture mode and type B with a brittle failure.

In earlier studies, clear distinction between the two striation types was often not possible since facilities for high resolution

stereo imaging, as used in the present study, were not available. On the basis of these observations, a number of mechanisms for striation formation were proposed, as discussed in I.5.I, which cannot successfully predict the formation of both striation types. Clearly the mechanism of striation formation must be able to predict the formation of both types, be consistent with the observation of crystallographic fracture and the brittle /ductile transition, and must also allow for the non-occurrence of resolvable striations in some areas.

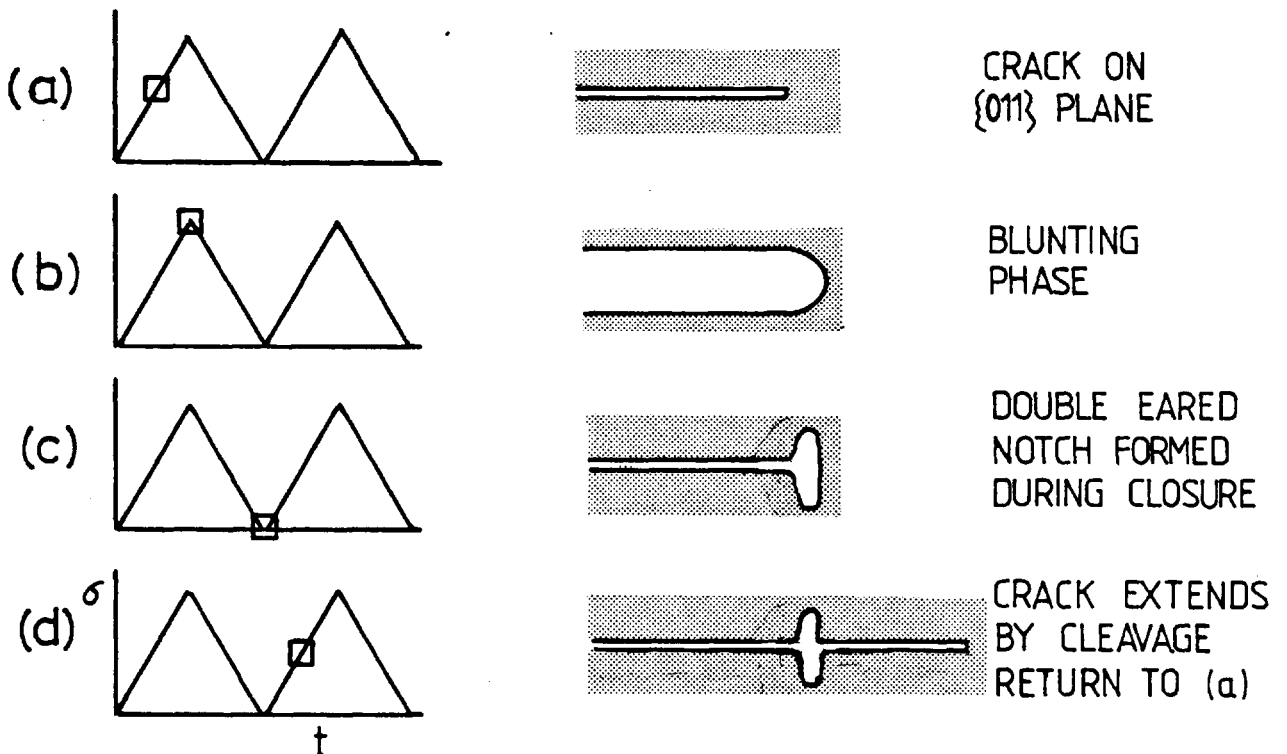
The crystallographic evidence, based on electron diffraction and etch-pit studies, demonstrated that in the case of both striation types segments of fracture were found on {011} planes, as summarised in Fig.5.64. In the case of type B striations the simplest mechanism to describe their formation is as shown in Fig.5.65. This mechanism is in fact basically similar to the plastic blunting process (PBP) of Laird (72), except that a brittle component is included in the regions between the striation slots. The Tomkins and Biggs (I45) type of model could be applied to explain features of this type but their mechanism implies plastic deformation in the early, rising load, part of the cycle which, previous evidence suggests, is not occurring in this case (84). The regions between the slots would, according to the model as shown here be expected to be crystallographic and this is supported by electron diffraction and etch pit data (Figs.5.33, 5.49).

Type A striations have been considered to be similarly produced during crack closure by a mechanism similar to that of Pelloux (73) or Bowles and Broek (I07) (see Figs.5.2 and 5.12 for details). These models cannot possibly be reconciled to a crack growth process involving cleavage since they imply a peak to peak relationship between opposing fracture faces (Fig. 5.66a). In the case of a cleavage mode of fracture the regions of brittle crack growth must be parallel to one another on opposing fractures. A mechanism involving cleavage must therefore involve the matching of fracture faces, perhaps as visualised by Stubbington (70) (Fig. 5.66b). Such a visualisation could be related to present crystallographic observations since using the etch pit technique both a crystallographic and non-crystallographic face were observed (Fig. 5.49). More detailed fractographic obser-

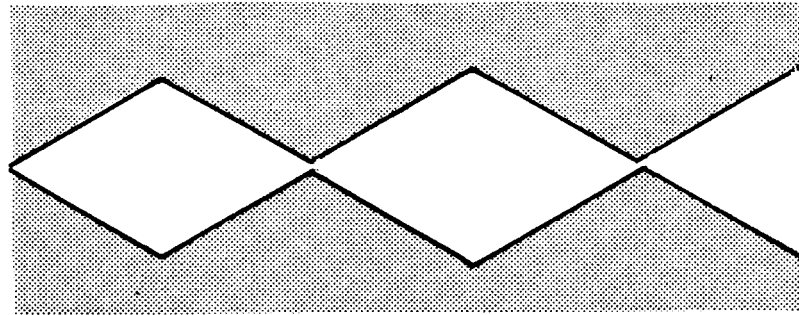


Striation Crystallography (schematic)

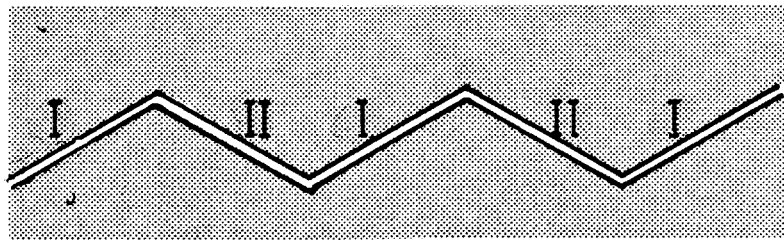
Fig. 5.65



Simple Mechanism to Predict the Formation of type B Striations



(a) Peak to Peak

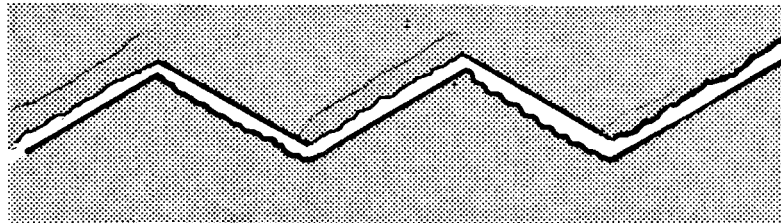


(b) Matching of Fracture Surfaces

I CRYSTALLOGRAPHIC FACE

II NON-CRYSTALLOGRAPHIC FACE

FROM STUBBINGTON (70)



(c) Taking into account Slip Step Observations

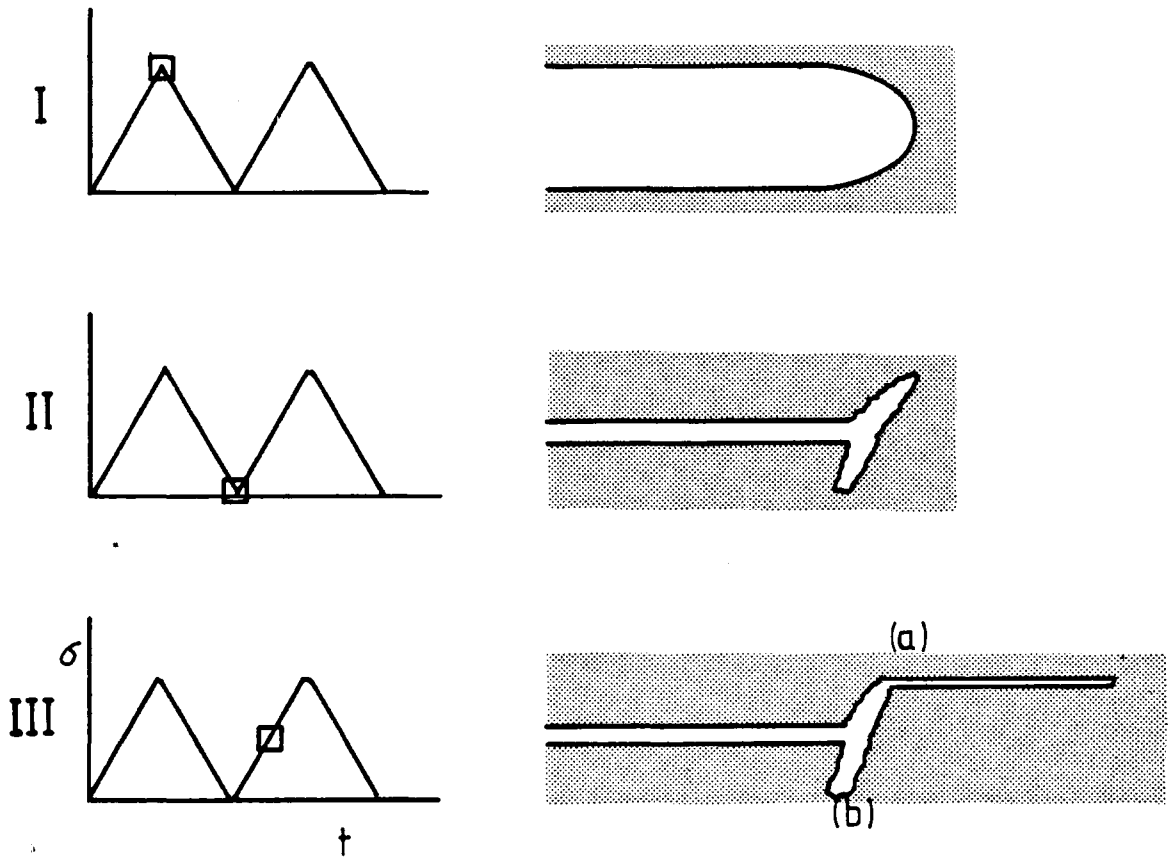
Possible Relationships Between type A Striations on Opposing Fracture Surfaces

vations, however, revealed evidence which invalidates this possible model: The type A striation profile, (Fig. 5.18) is of one featureless face (shown to be crystallographic by etch pitting) and one delineated by slip steps. The featureless face was in all cases found to be the trailing edge of the striation, i.e. the face angled towards the origin. If this information, which is supported by the earlier observations of Bowles and Broek, is applied to a visualisation involving matching fracture faces (Fig. 5.66(c)) a most unlikely situation is depicted of the featureless faces matching those delineated by slip markings.

The HRSEM observation of matching fracture surfaces (Fig. 5.25) has provided information which suggests that at least in some circumstances a mechanism may be operative which does not lead to the formation of type A striations on opposing fracture surfaces. In this case type A striations on one surface were found to correspond to type B striations on the other. It is suggested that a process of the type shown in Fig. 5.67 may operate in order to produce this striation topography. The mechanism remains basically similar to that shown in Fig. 5.65 except that brittle fracture occurs at the tip of one of the crack tip notches (a) rather than between the two. The non symmetrical crack tip would, when loaded, lead to fracture at point (a) since the stress intensity developed at this point would be higher than at (b) since notch (b) extends beneath the crack itself and stress relieving at the notch tip would be expected.

This mechanism can explain several of the observed fractographic features:

- (1) The mechanism can predict the simultaneous production of both striation profiles.
- (2) The regions of crystallographic fracture are parallel and hence the process is consistent with a cleavage involvement in fracture.
- (3) The face delineated by slip steps on the type A face is always the leading edge of the striation (i.e. the edge angled away from the origin).
- (4) The 'type B' fracture face shows a staircase structure with each of the parallel crystallographic regions



- I BLUNT CRACK AT MAXIMUM LOAD
- II NON SYMMETRICAL CRACK PROFILE PRODUCED DURING CLOSURE
- III BRITTLE EXTENSION AT TIP OF NOTCH (a) RESULTING IN BOTH STRIATION TYPES

Mechanism of formation of type A Striations

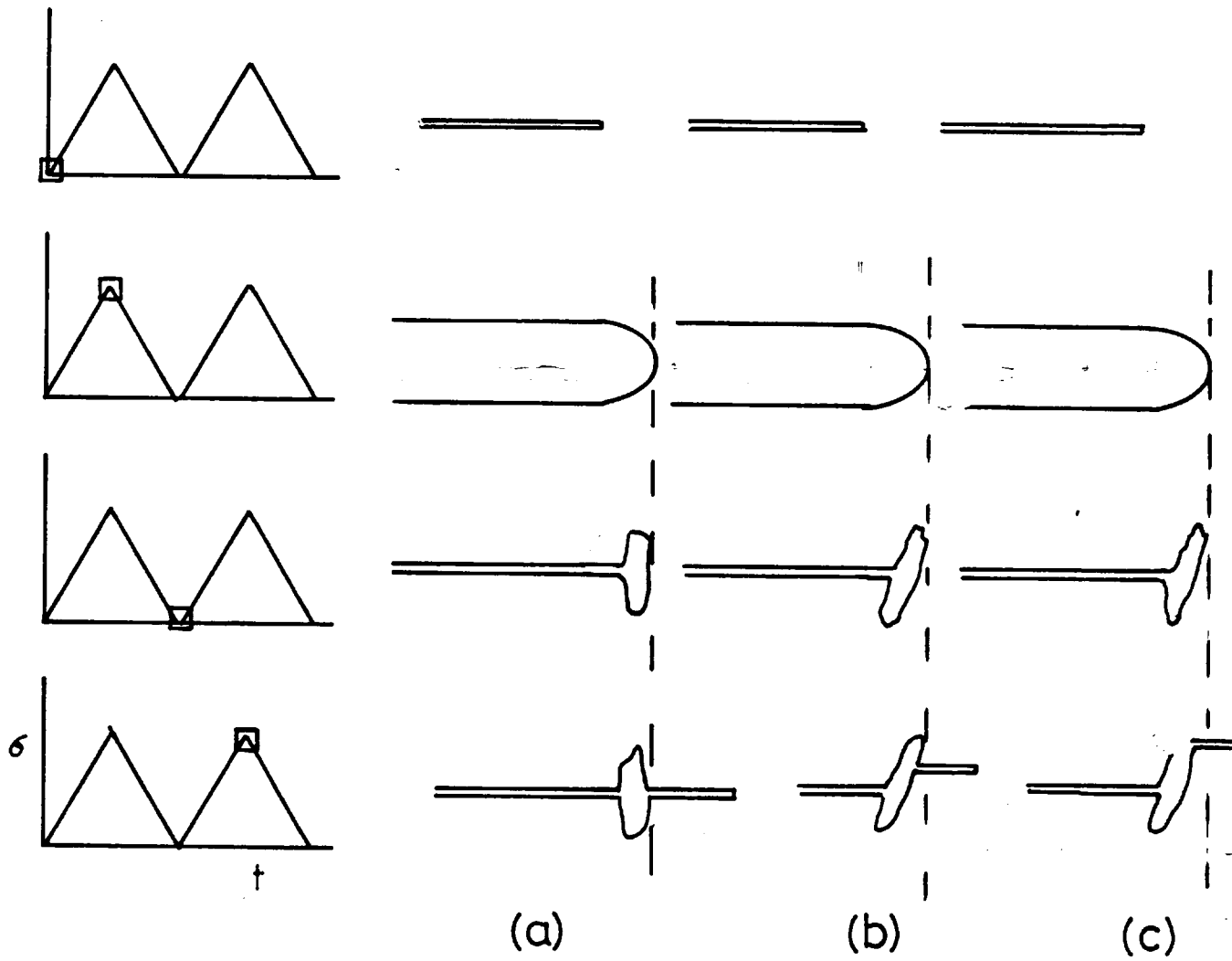
vertically displaced from its neighbour. Such regions were frequently observed (Figs. 5.21, 5.23).

The occurrence of the intermediate type of striation observed in Fig. 5.27 may be also explicable by such a process: A general striation formation mechanism could be visualised as shown in Fig. 5.68. Hence the intermediate striation type could be produced by a process similar to that shown in (b) .

It is felt that the operation of such a mechanism as detailed above could explain the circumstances in which the two types of striation are found: In the symmetrical case the overall crack plane must be close to an {OII}, while in the non symmetrical case it is possible for the crack to follow a plane other than {OII} while retaining cleavage segments on that plane. In a situation therefore where the {OII} plane most favourably orientated is not at  $90^{\circ}$  to the load axis, the type A or intermediate striation may be produced. Another possible situation occurs where the crack is tending to deviate onto a steeply inclined plane due to local inhomogeneity in the stress distribution, for example, in the proximity of an intermetallic particle. Hence type A striations would tend to be found more commonly on steeply inclined regions of fracture; fractographic observations support such a suggestion.

The occurrence of steeply sloping regions of fracture was found to be dependent on stress intensity, a fact which may be attributed to the increasing plastic zone size, as discussed in 3.3.I. Hence type A striations might be expected to be more common at high  $\Delta K$ ; it would however be quite impossible to prove this statistically. Their occurrence on steeply sloping facets may explain some earlier observations (7I) in which type A striations were rarely found on corrosion fatigue fractures in, for example, NaCl solutions. Here the plastic zone size would be much smaller than in laboratory air and steeply sloping regions of fracture would be rarely observed. This may explain the earlier delineation of the two striation types as 'brittle' and 'ductile'. It must be emphasised however that type A striations were not exclusively observed on steeply sloping regions.

Many areas of fracture delineated by deformation bands, i.e.



General Striation Formation Process

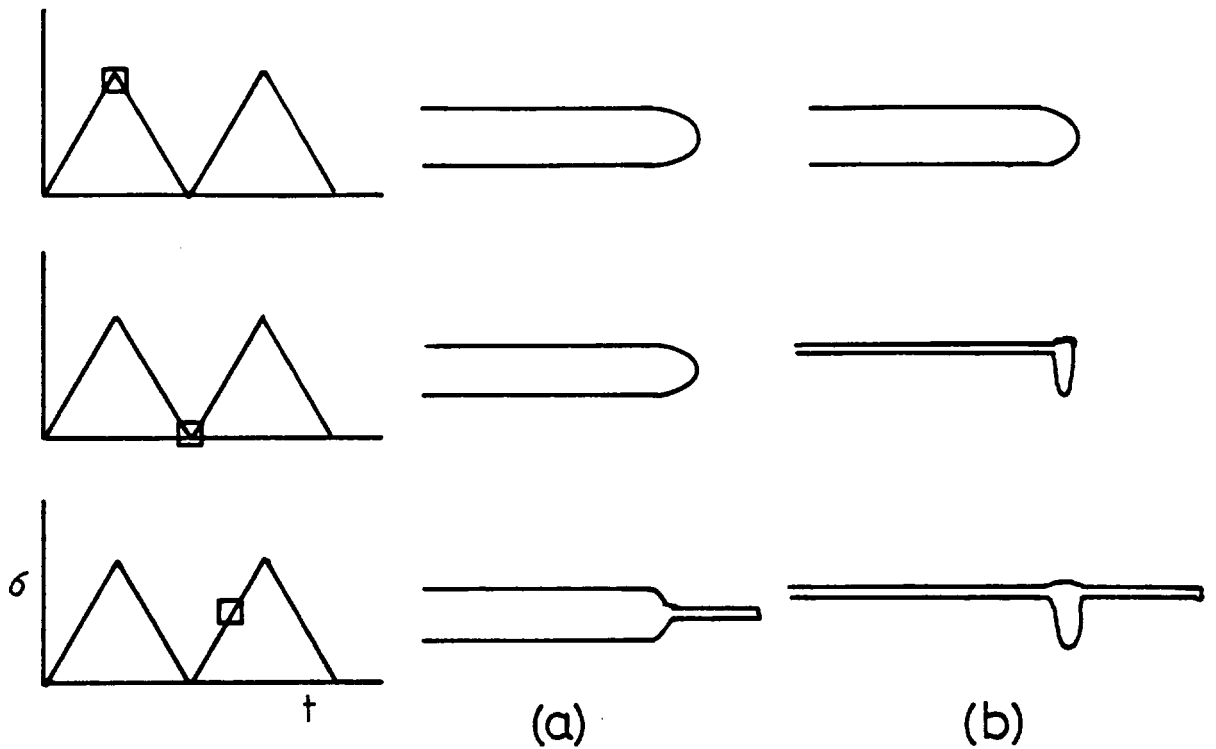
- (a) TYPE B STRIATION
- (b) INTERMEDIATE STRIATION TYPE
- (c) STRIATION TYPES A and B.

areas of cycle by cycle growth rather than tearing, were found to be striation free. Also in areas showing striations the vertical height of the striation topography varied greatly between adjacent areas (Fig.5.36 ). Hence some account must be taken of this in the mechanism of striation formation. Two possibilities exist: Firstly the crack may remain open during load reduction, no plastic deformation occurring, or secondly plastic deformation occurs almost exclusively on the opposite fracture face and hence little or no evidence remains. Diagrammatically the two possibilities can be represented as in Fig. 5.69 . The possibility that crack closure does not occur in certain areas is an unlikely one, since, even under tensile mean load conditions, there exist , at minimum load, considerable compressive residual stresses in the region around the crack tip (Fig. 5.70) (I66). Also as shown in Fig.5.69 some evidence of crack blunting would be expected on the surface and in fact a mechanism of striation formation during stress corrosion cracking has been proposed giving a similar fracture topography. (I67). It is believed that the second explanation of asymmetric blunting is the most likely. In fact, as demonstrated by the fracture matching experiments, while type B striations match one another in certain areas, areas showing equivalent topography are very rare. Clearly symmetrical blunting at the crack tip would only be possible if equal amounts of slip on slip systems on the two sides of the crack occurred. As discussed earlier such situations are considered rare and hence the mechanism involving asymmetric blunting would appear a likely one.

At high  $\Delta K$  in particular, many areas were found to show striation splitting (Fig. 5.36). Here a secondary crack was found to extend from the base of each type B slot. It is believed that this effect may be a result of considerable tensile stresses across the fracture surface built up at high  $\Delta K$ . Hence as tensile load is applied limited secondary crack growth occurs from the striation base (Fig. 5.71). This effect has been observed previously (II5) particularly on corrosion fatigue fracture surfaces and hence some environmental influence would be expected on this secondary growth,

The environmental influence on striation formation was clearly demonstrated by the observation of 'dry' fractures which showed

Fig.5.69



(a) NON OCCURRENCE OF CLOSURE

(b) NON SYMMETRICAL CLOSURE GIVING UNRESOLVABLE STRIATION ON UPPER FRACTURE FACE

Possible Mechanisms to explain the Non-Observation of Striations

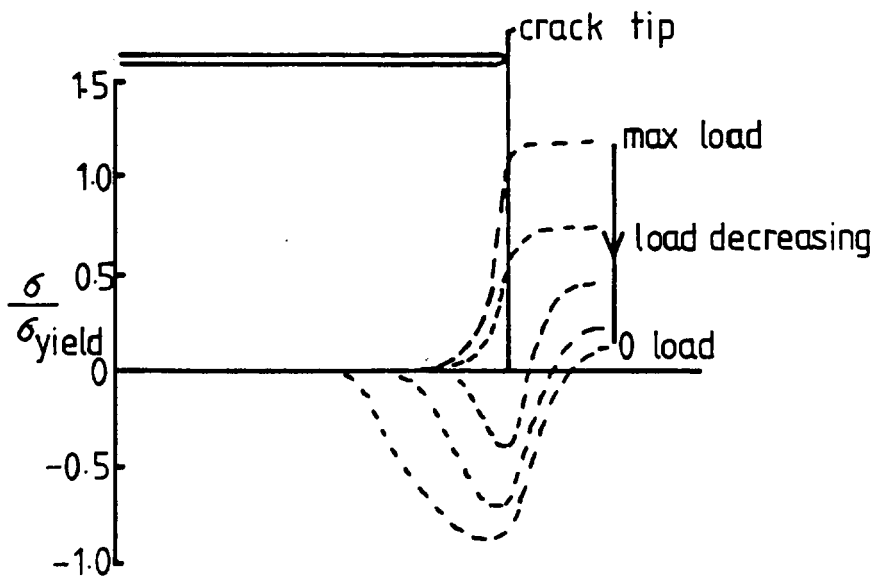
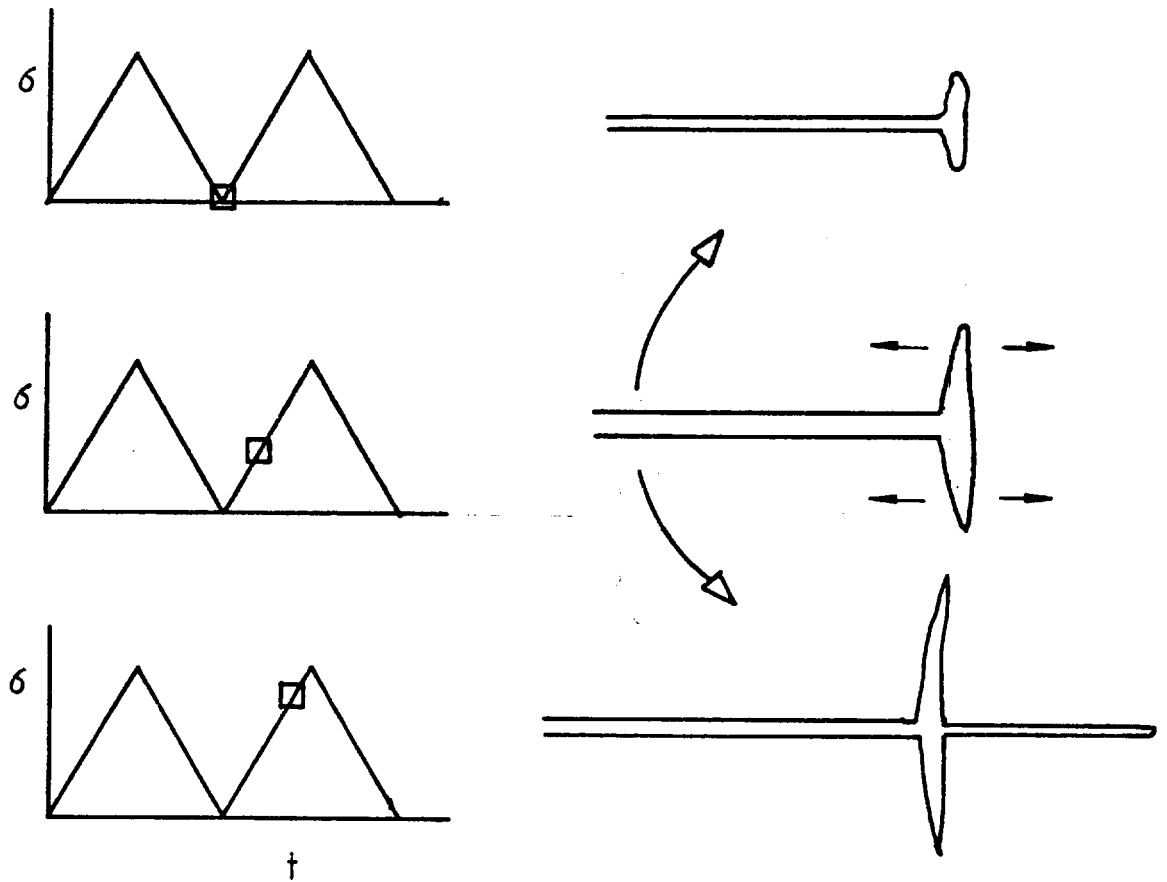


Fig.5.70

Stress Distribution Around Fatigue Crack Tip During Unloading

AFTER NEWMAN (166)

Fig. 5.71

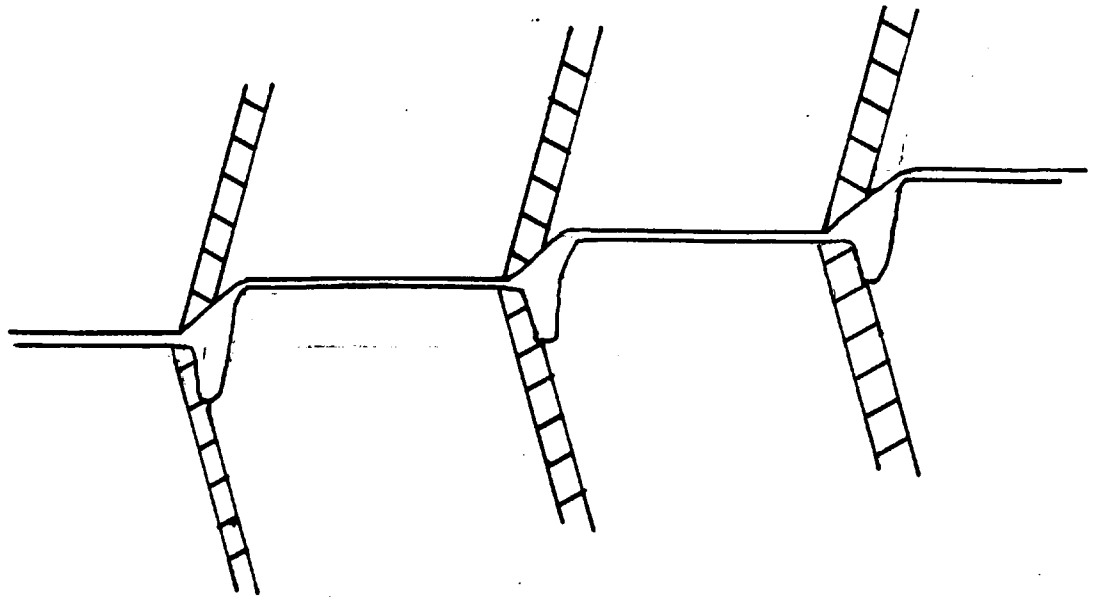


Schematic Diagram to Describe the Occurrence of Striation Splitting

no evidence of surface markings which could be considered to be striations of either profile detailed earlier. Some surface markings were found in a few isolated areas which were similar to type A but much less regular (Fig.5.52). These markings appear to be very similar to the features described by Wanhill (IO8) as 'complex ripple markings' produced on vacuum fatigue fractures of 7075 T6. Wanhill, together with other workers, for example, Pelloux (73) and Bowles and Broek (IO7) was of the opinion that the non occurrence of striations in vacuum was due to a surface oxidation effect. However the controlling factor would appear to be specifically water vapour, since surface oxidation would still be expected.(90), in the case of dry oxygen atmospheres. It is believed that the change in crack growth mechanism which leads to the non occurrence of striations is the removal of the cleavage component in crack growth. In other materials, striations have been observed under conditions, where a cleavage component in crack growth is quite impossible. An example would be the observations of striations in pure copper single crystals made by Neumann (74). In this material cleavage cannot be involved and a striation mechanism as described here could not be applied. It is argued however that the highly regular, extremely well marked, striations observed in aluminium alloys under moist conditions are concerned with the cleavage involvement in crack growth.

3.3.3 The Relationship Between Crack Tip Deformation Structure and Fatigue Striations. The prediction of the brittle/ductile transition during each increment of growth, discussed earlier, must imply that the deformation bands are formed in all cases at the same stage during each load cycle. Hence the deformation bands must show a constant relationship to fatigue striations and must correspond on opposing fracture surfaces.

Constant spatial relationships to both types of striation were observed and these relationships are consistent with the mechanism of striation formation proposed in the previous section. A simple visualisation of this is shown in Fig. 5.72. Bowles and Broek (IO7) made similar observations to those in the present work and were of the opinion that deformation bands were exclusively a result of the deformation, occurring during crack



Schematic Diagram Demonstrating that  
Deformation Band Positions are consistent  
with Proposed Striation Mechanism

closure, resulting in striation formation. Certainly this is a possibility and the positions of the deformation bands relative to striations could be considered consistent with such a suggestion.

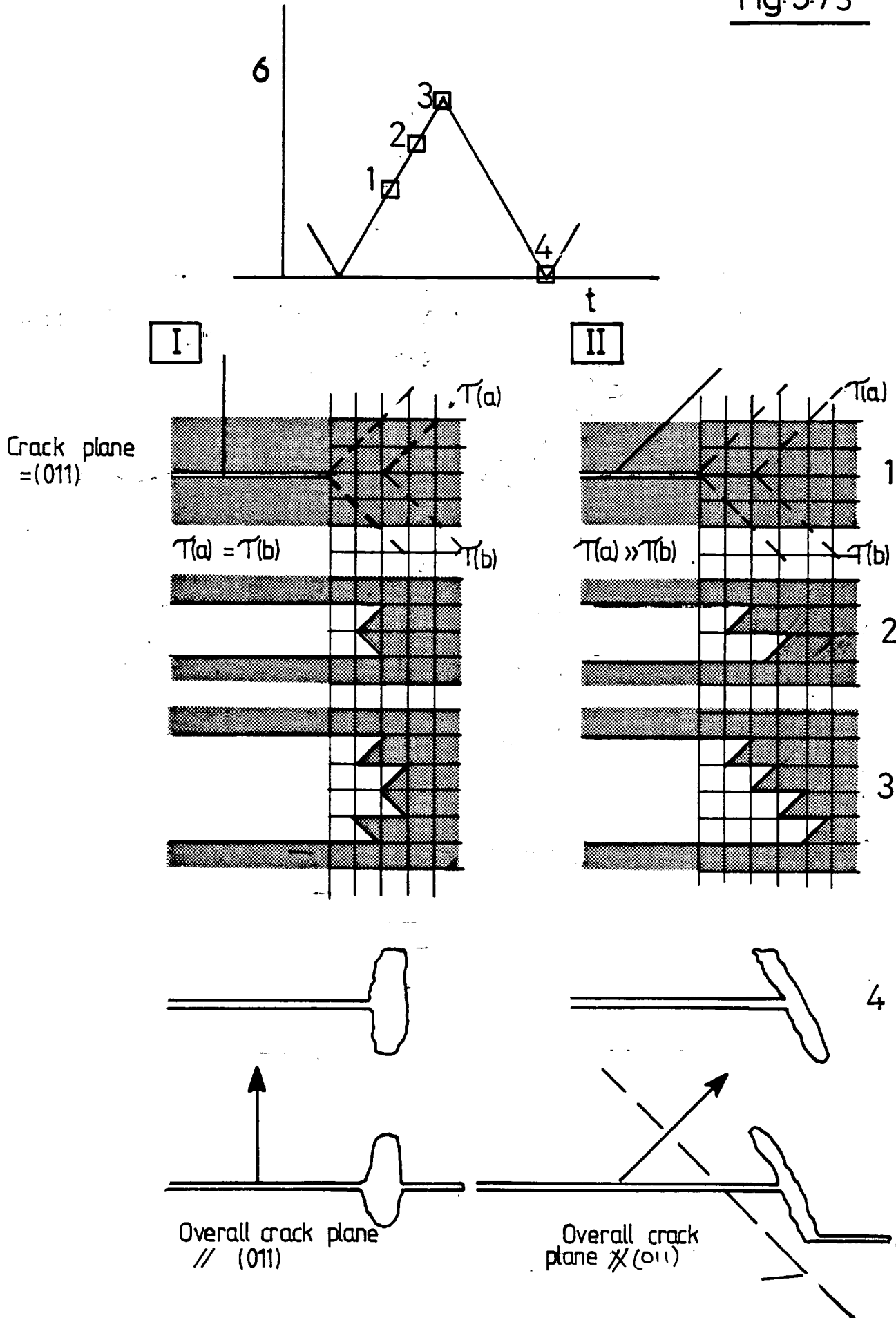
As discussed in detail earlier however, deformation bands were found in areas showing no evidence of striation topography and it is felt that the regular nature of the bands is a result of the brittle/ductile transition rather than simply a closure effect. There is however, almost certainly, a contribution made to deformation band formation by dislocation motion occurring during crack closure.

Striation formation clearly involves dislocation motion on slip systems at the crack tip and hence crystallographic considerations must also be taken into account in this case, in particular to explain the non symmetrical deformation postulated earlier for type A striation formation: A simple two dimensional representation of a crack can be considered as shown in Fig. 5.73, with two groups of slip systems, (a) and (b), symmetrically disposed about the crack tip. In case I the two groups of systems are subject to equal shear stress while in case II the shear stress on group (a) is much greater than on group (b). As shown in the simple model a non symmetrical profile is thus developed at the crack tip at maximum load. Clearly the model is a gross over simplification and cannot successfully predict the shape developed by plastic deformation occurring during closure which must involve the activation of other slip systems. However, the model can predict the development in case II, of an overall crack plane approximately perpendicular to the local plane of maximum shear stress while maintaining {011} fracture segments.

#### 3.4 The Influence of Loading Conditions on Crack Growth.

The crack growth and striation formation mechanisms discussed so far have been based upon the observations carried out at a stress ratio of 0.1 at constant load amplitude. However further observations were made of fractures produced at stress ratios (R) of +0.5 and -0.3 and also under a simple load programme. It is now proposed to discuss these results in order to further develop the crack growth mechanism.

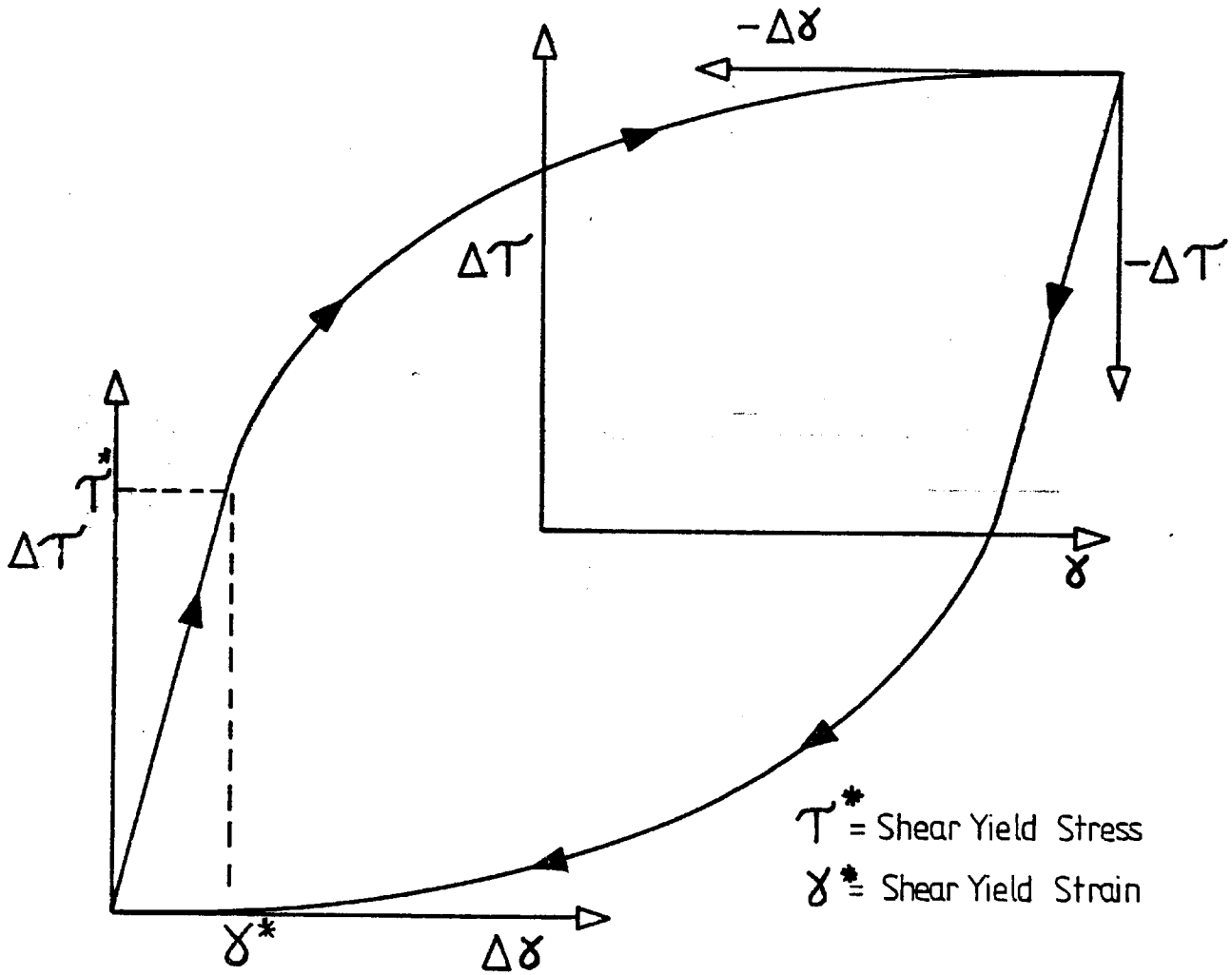
Fig. 5.73



3.4.I The Effect of Mean Stress. Perhaps the most significant result to be produced by observation of fractures at different stress ratios was that of the effect on the deformation band structure. The mean stress, and corresponding  $K_{\max}$ , was found to have virtually no effect upon the fracture appearance in terms of deformation band structure and band/striation spacing. These results indicate that the amount of deformation involved in, and size of, each crack growth increment is controlled by  $\Delta K$  rather than  $K_{\max}$ .

In order to explain these observations it is necessary to consider the factors controlling plastic strain at the crack tip. Rice (I6I) carried out an analysis of the situation and considered that a stable shear stress/plastic strain hysteresis loop was developed within the reversed plastic zone as shown on Fig. 5.74. According to this model the amount of strain following a load reversal,  $\Delta\tau$ , is independent of the maximum amplitude of the loop,  $\tau_{\max}$ . Rice therefore believed that the amount of plastic deformation within the crack tip plastic zone would be controlled by  $\Delta K$  rather than  $K_{\max}$ . The observations of deformation band structure would appear therefore to be consistent with such a visualisation, implying that the basic cyclic crack growth mechanism is itself controlled by  $\Delta K$  rather than  $K_{\max}$ .

A number of crack growth laws have been proposed which relate crack growth rate to  $\Delta K$  (see Rice (I6I) for details). Generally these laws give a relationship of the form:  $da/dn \propto \Delta K^n$ , where  $n=2$  in many cases. These laws have been based on analytical approaches, of the kind made by Rice (I6I) and also on experimental observations of crack opening displacement (C.O.D.) which is itself related to the amount of plastic deformation at the crack tip. The view that the deformation bands are a result of dislocation activity in this region immediately adjacent to the crack tip would therefore appear consistent with the (C.O.D.) concept. There does of course exist a stress ratio (R) effect on the overall crack growth rate in aluminium alloys as studied by Pearson (I68) and Rhodes et al (4): Pearson found that R had little effect in alloys of high fracture toughness but in low toughness alloys crack growth rates at high positive R increased rapidly at



Stable Shear Stress/Strain  
Hysteresis Loop at Crack Tip

after Rice[161]

high  $\Delta K$ . Pearson in fact developed an equation to predict the effect in aluminium alloys

$$\frac{da}{dn} = \frac{1.9 \times 10^{-11} K_C (\Delta K)^2}{((1-R)K_C - \Delta K)^{\frac{1}{2}}}$$

Where:

$K_C$  = critical stress intensity for stable crack growth

$K_C = K_{IC}$  in plane strain

Hence as  $\Delta K$  approaches  $(1-R)K_C$  crack growth rates would rapidly increase. Both Pearson and Rhodes et al related the stress ratio effect to a contribution of ductile tearing to fracture, dependent on the proximity of  $K_{max}$  to  $K_C$ . In terms of fractographic observations this approach is certainly consistent with the present observations: At high R large areas of tearing were observed with an extremely rough fracture surface even at comparatively low  $\Delta K$ . The fracture appearance is greatly influenced by the presence of large intermetallics, many of which were observed on the fracture surface: At high positive R, the increased size of the monotonic plastic zone leads to the incorporation of many more such particles into the fracture than at comparative  $\Delta K$  at  $R=0$ . In fact, well marked striations and heavy deformation band structures were impossible to observe at  $R=0.5$ , fracture at high  $\Delta K$  being dominated by tearing.

3.4.2. Programme Loading. The programme loading tests yielded some interesting results which can provide further information about the mechanism of crack growth. The first, and perhaps most significant result which has been considered in all the previous discussion, is that fatigue striations and deformation bands are produced on a cycle by cycle basis, one striation and one band per cycle. This was found to be the case at all stress intensities observed and no evidence could be found for the Tomkins and Biggs (I45) type of mechanism where subsidiary striations would be expected to follow each primary striation leading to more than one striation in each cycle.

The overall relationship between deformation bands, striations and striation spacing is represented schematically in Fig.

5.75 together with the applied load programme. The significant

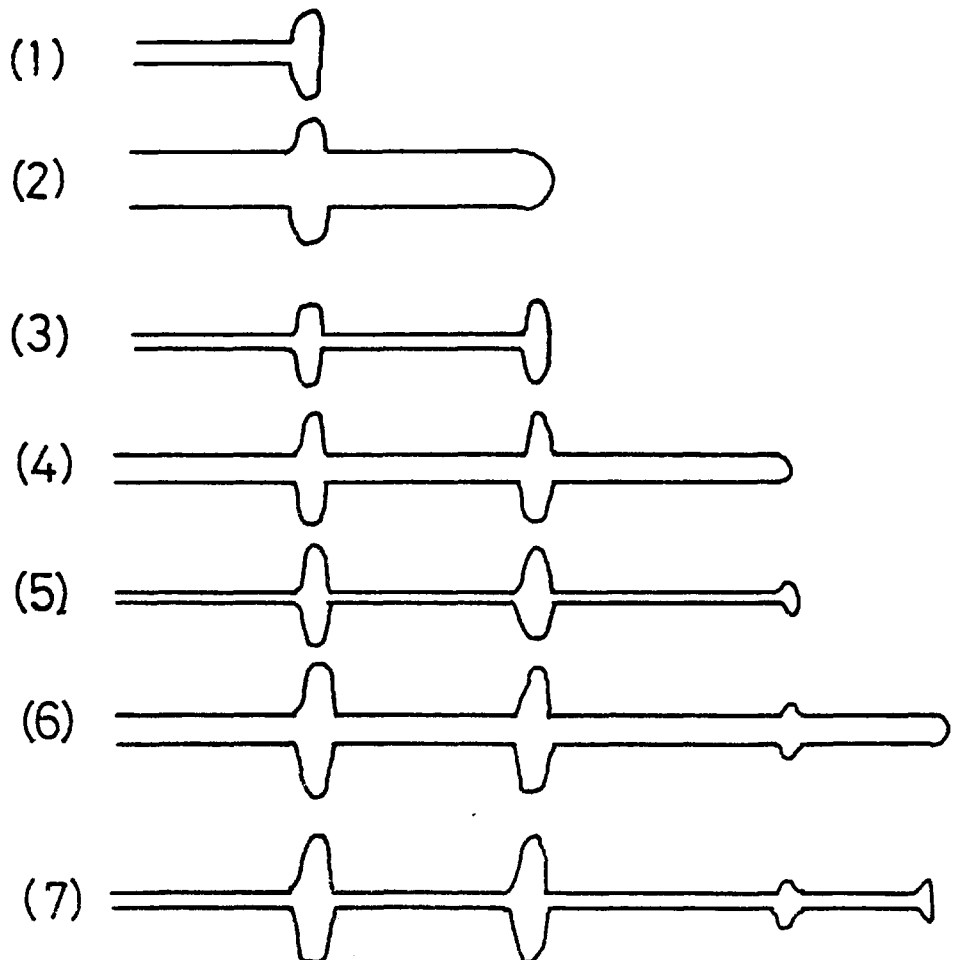
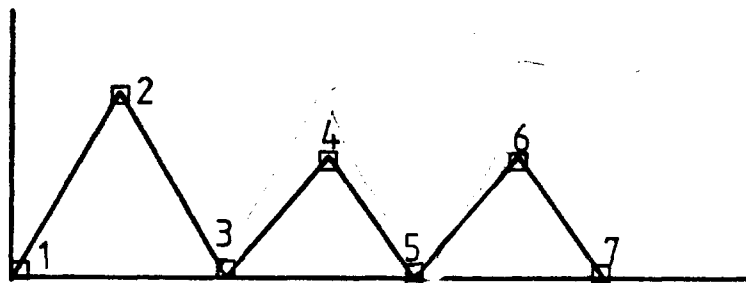
Fig.5.75



Programme Load Fracture :

Deformation Band/Striation  
Relationship

Fig.5.76



Programme Load Crack Growth Model

facts are that the well marked striations and heavy deformation bands correspond to one another and lead the broad crack growth increments. The relationship between bands and striations is in accord with the previously discussed mechanism since both are related to the amount of plastic deformation occurring during crack blunting and closure. However this has been assumed to occur at the end of each load cycle, brittle crack extension occurring during initial loading of the crack. A mechanism involving striation and deformation band formation at the beginning of each cycle would be very difficult to relate to the present observations and would be also contrary to the plastic casting results of Bowles (84) and the striation observations of Laird and De la Veaux (I46).

Striation splitting and secondary cracking, as discussed earlier, has been observed in local areas at high  $\Delta K$  and could perhaps explain the fractographic results. The width of each striation image would then depend on the subsequent load cycle which would determine the amount of secondary cracking. However, this process would imply that in this case a broad striation image would not correspond to a heavy deformation band; the deformation band being determined by  $\Delta K$  in one cycle and the striation image by that in the following.

The third possibility is that the amount of plastic deformation during blunting and closure, and hence the width of the striation slot image (type B) and the weight of the deformation band, is related to  $\Delta K$  during each cycle and that the striation spacing is not. This would imply the process shown in Fig.

5.76 (assuming the simple case of symmetrical type B striations). Hence the size of the first crack growth increment at lower  $\Delta K$  stage 4, is related to  $\Delta K$  for the previous load cycle. This interpretation has the advantage that it can be related to previous mechanisms of striation formation and deformation band formation. Such delays in crack growth rate modification with reduction in  $\Delta K$  have been previously observed, for example by Hertzberg (I43) who found a delay in the modification of striation spacing upon reduction of load levels. The first few striations at the lower load level being more widely spaced than those following. Delays in response to increases in  $\Delta K$  have not been generally noted but it must be emphasised

that in no earlier studies of crack growth in commercial aluminium alloys has it been possible to relate striation slot image width to slot spacing. Apart from Hertzberg's studies, most crack growth retardation and programme load investigations have involved very large changes in  $\Delta K$  leading to significant modification in macroscopic growth rate over a large number of cycles (see for example the studies of Hardrath (I69)). Observations of striation topography under programme loading have been made by Schijve and these have been interpreted by Wanhill (I08) as evidence for the Tomkins and Biggs mechanism. However, as discussed by Laird and De la Veaux (I46), these observations are subject to several different interpretations and no unambiguous conclusions can be made.

This delay effect would be expected to occur if a mechanism of the type proposed here is considered: The mechanism involves the formation of a brittle zone via dislocation motion at the end of one load cycle, through which the crack propagates during the following load cycle. Hence, the width of the embrittled zone would be expected to be controlled by the applied  $\Delta K$  in the first cycle. In order to be conclusive here it is felt that more tests using different load programmes would be necessary but the present results appear to be consistent with the embrittled zone formation process. Certainly any adsorption embrittlement mechanism would imply an immediate response to changes in  $\Delta K$ .

### 3.5 The Relationship Between the Cyclic Crack Growth Mechanism and Crack Growth Rate.

The results of the programme load tests have proven that fatigue striations, and similarly deformation bands, are produced on a cycle by cycle basis and hence their spacing gives a measure of the local crack growth rate. In the case of C.T. design specimens, macroscopic growth rates, as measured optically, had previously been measured by Rhodes (I70.) and hence it was possible to compare the growth rates as measured by the two routes (Fig. 5.50). Macroscopic and microscopic crack growth rates were found to correspond only over a narrow range of  $\Delta K$ , deviations being particularly marked at  $\Delta K > 20 \text{ MNm}^{-3/2}$ , at  $R = 0.1$ . Other considerations must therefore be of importance in assessment of the overall failure mode.

A large scatter of striation/deformation band spacings was observed at all values of  $\Delta K$ . It is felt that this effect must be attributable to local variations in  $\Delta K$  along the crack front. The striation/deformation band spacing was found to approximately follow a relationship :

$$\frac{da}{dn_{\text{local}}} \propto (\Delta K)^2$$

Analyses of fatigue crack growth have on many cases been related to the crack opening displacement (C.O.D.) (I71,I72). Such a relationship yields an equation for crack growth rate of the form:

$$\frac{da}{dn} = C \left( \frac{\Delta K}{E} \right)^2$$

Where:

C = constant

E = Youngs Modulus

The present results for microscopic crack growth rate would therefore appear to be consistent with this analysis.

The overall crack growth rate cannot however be attributed totally to such a process: Recently Rhodes et al ( 4 ) have developed a relationship to predict crack growth rates taking into account both the cyclic mechanism discussed above and contributions from ductile tearing mode of fracture as predicted by stable crack growth resistance or 'R' curves. A relationship of this type can predict the observed underestimate of overall crack growth rate provided by striation spacing at high  $\Delta K$ . The fractographic observations at high  $\Delta K$  (Fig. 5.I5(c)) would appear to be consistent with this since large regions of ductile tearing were observed on the fracture surface in the present work. The combined operation of two mechanisms, the tearing mechanism being prevalent at high  $\Delta K$  would appear to be an appropriate visualisation of the total crack growth process.

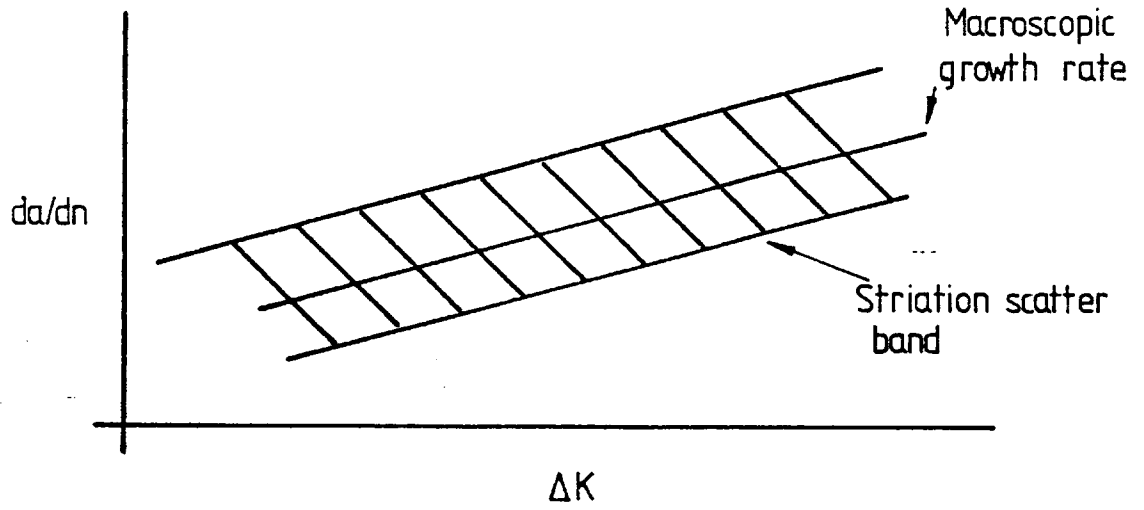
The close correspondence between average microscopic and macroscopic crack growth rates at intermediate  $\Delta K$  provides, it is felt,

further circumstantial evidence for a cyclic growth process involving one increment of crack growth, as defined by striation or deformation band spacing, per cycle. Tomkins (173) in a recent study of crack growth in 304 stainless steel was of the belief however that striations were somewhat more complex: He found that two types of striation were produced, a coarser striation pattern being superimposed over an array of fine striations. The fine striations were found to correspond to macroscopic crack growth rate at intermediate  $\Delta K$ . The coarse striations gave a general overestimate of growth rate. Tomkins related his observation to the Tomkins and Biggs model of striation formation (detailed earlier) to predict the formation of the two striation types. In this model one fine striation is not necessarily formed during each load cycle. While striation patterns of the type observed by Tomkins, of type B striations showing different slot widths, have been observed in the present study, these were by no means a commonly observed feature. All the evidence obtained in the present work would suggest the formation of one striation in each load cycle.

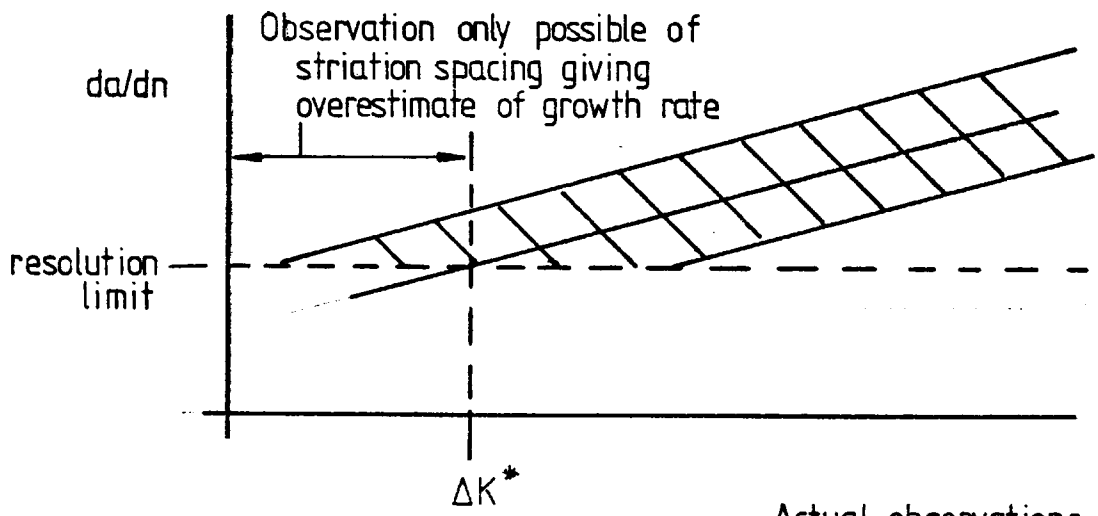
At low stress intensities  $< IOMNm^{-3/2}$  only a very limited number of striation observations were possible in the present work. Striation and deformation band spacings measured did however give a general overestimate of crack growth rate. This observation is consistent with the recent studies of Tomkins (173) and Kirby and Beevers (61), the latter in the aluminium alloy 7075. While this may be a real effect great care must be taken in the interpretation of microscopic observations of growth in this regime: Both in this part of the present study and in the observations of short crack growth in Part 4, it was not possible to resolve striations of less than  $0.04\mu m$  spacing. Despite the resolution of the HRSEM being of an order of magnitude higher than this it is felt that the non-observations of finer striations was due to their vertical separation falling below the resolution limit. Deformation band observations, although not limited by resolution, were also found to be difficult due to very low misorientation between bands and matrix.

If a hypothetical situation as shown in Fig.5.77 is now considered, a biased result would be obtained for average striation spacing: At all stress intensity ranges below  $\Delta K^*$  only

Fig. 5.77



Possible "real" situation



Actual observations

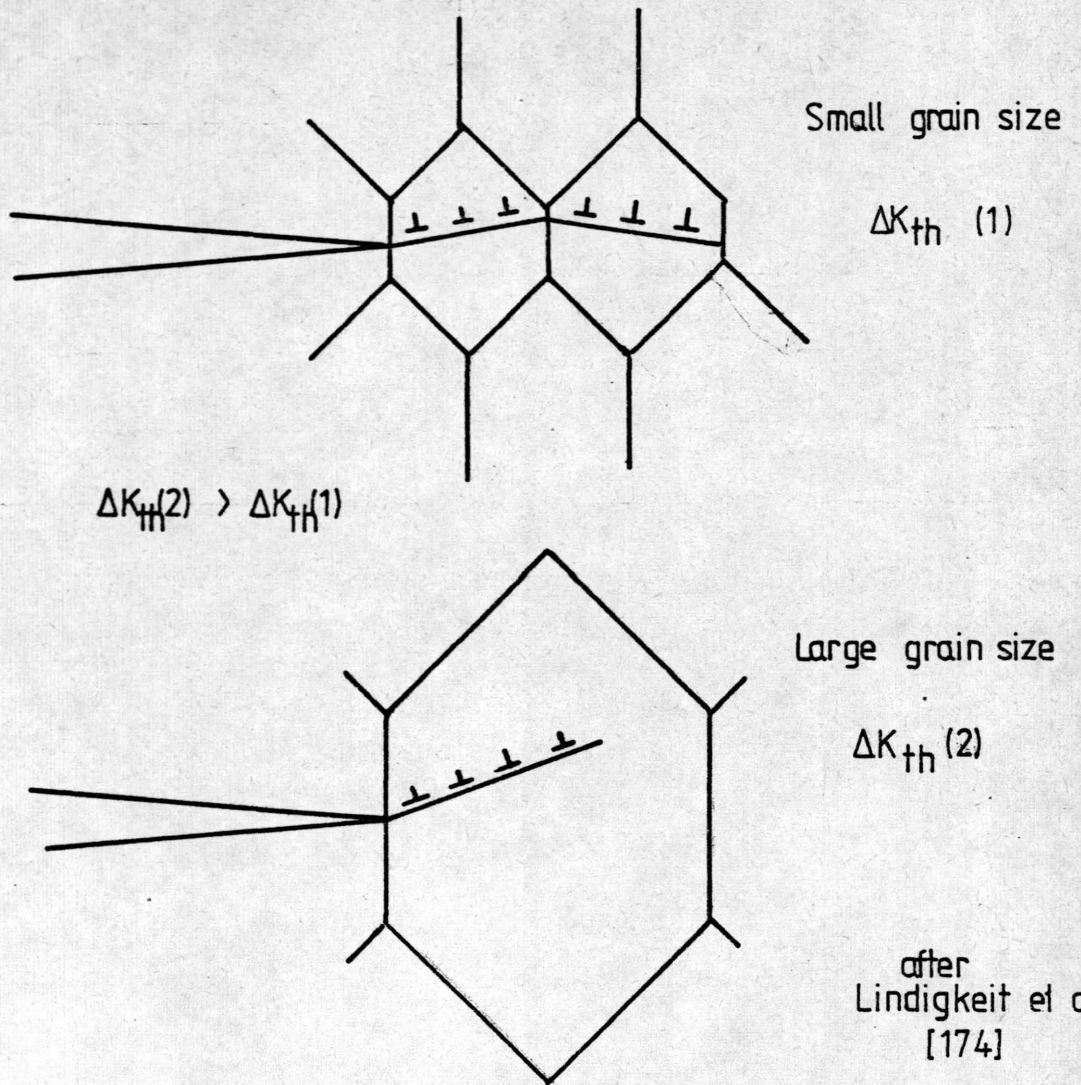
Illustration of the Possible Biased  
Average Striation Spacing at Low  $\Delta k$

observation of striation spacings giving an overestimate of macroscopic growth rate would be possible.

It is felt that this resolution limit has not been given sufficient consideration in earlier observations of crack growth at low  $\Delta K$ . For example, Cina and Kaatz (I48) quote the non-occurrence of striations at low  $\Delta K$ . Also Kirby and Beevers (6I) quote an average striation spacing of  $2.5\mu\text{m}$  in 7075 at a macroscopic growth rate of  $0.01\mu\text{m}/\text{cycle}$ . The present results would indicate that such a striation spacing is a vast overestimate of the real situation.

Despite these possible instrumental limitations there do appear to be some indications in the literature, as in the present work, of an overestimate of macroscopic growth rate at low  $\Delta K$  provided by striation spacing measurements. For example, Tomkins (I73) showed a pronounced deviation between striation spacing and growth rate in 304 stainless steel which could not obviously be covered by resolution limit problems. Tomkins believed that the deviation was due to the formation of one striation over a number of load cycles. Similar proposals have been made by Kirby and Beevers. There must also exist, however, the second possibility of crack growth in bursts over several hundred cycles followed by periods of arrest.

At low  $\Delta K$ , approaching  $\Delta K_{th}$ , crack growth rates have been found to be highly dependent on environment and stress ratio (i.e.  $K_{max}$ ). Kirby and Beevers (6I) observed a well defined threshold under vacuum test conditions but crack growth in laboratory air was found to occur at  $\Delta K < \Delta K_{th}$  (in vacuo) and growth rates were highly dependent on  $K_{max}$ . Lindigkeit et al (I74) investigated the occurrence of a vacuum threshold and concluded that in age-hardened aluminium alloys threshold occurred when the maximum plastic zone size fell below the grain size of the alloy (Fig. 5.78). At  $\Delta K > \Delta K_{th}$  these workers believed that activation of slip systems in secondary grains during opening prevented full reversal of slip during closure. At  $\Delta K < \Delta K_{th}$  reversed slip was proposed to occur repeatedly with cycling until the dislocation back stress equalled the friction stress leading presumably to inhibition of crack growth.



The Possible Relationship Between Grain Size and Threshold

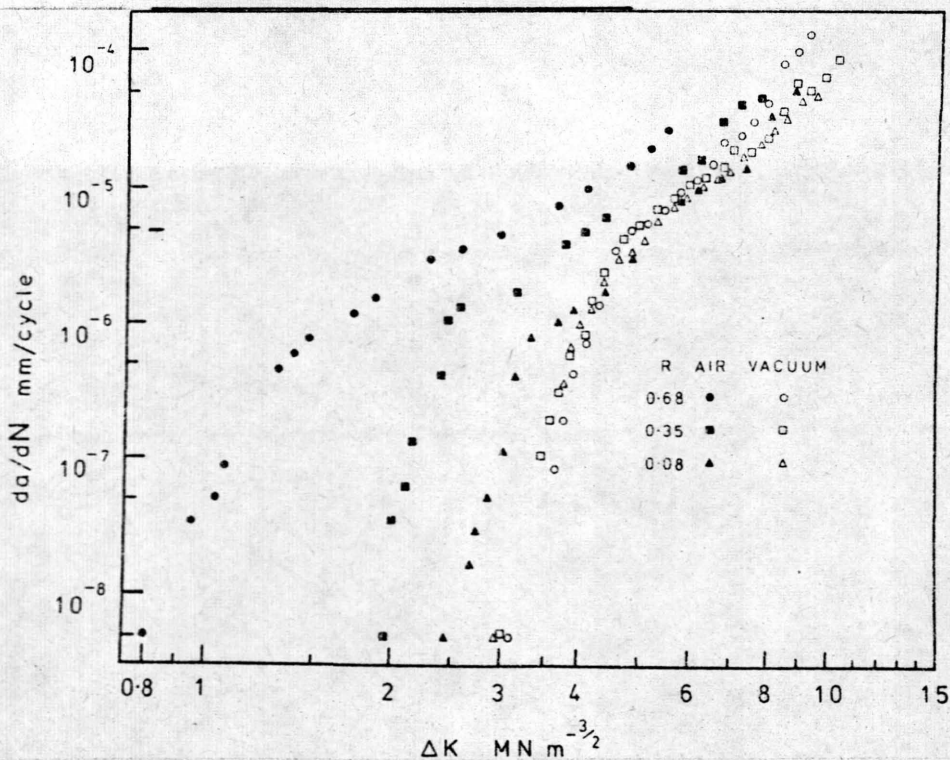


Fig.5.79

The Influence of Environment on  $\Delta k$  in 7075 T73

after Kirby and Beevers [61]

It is interesting to relate these observations of threshold behaviour to the present mechanism. In the mechanism proposed earlier crack growth under moist conditions involves shear and cleavage components, while in vacuum shear is exclusively involved. The amount of local crack tip dislocation emission has been found to be reduced with decreasing  $\Delta K$ , very weak deformation bands being observed at low  $\Delta K \approx 6 \text{ MNm}^{-3/2}$ ,  $R = 0.1$ . Perhaps unfortunately, this minimum  $\Delta K$  investigated lies approximately at the maximum of the threshold transition region investigated by Kirby and Beevers in 7075 (Fig. 5.79). These workers found that vacuum threshold occurred at approximately  $\Delta K = 4 \text{ MNm}^{-3/2}$ . According to the present mechanism and that of Lindigkeit et al at  $\Delta K < \Delta K_{th}$  (in vacuo) dislocation emission from the crack tip would be expected to cease thereby preventing crack growth in vacuum. In moist conditions the dislocation transport of hydrogen would also be prevented and hence the brittle/ductile process of crack growth would not be possible. However, the macroscopic crack growth rates involved here are very small ( $< 100 \text{ \AA/cycle}$ ) and hence lattice diffusion of hydrogen would be sufficiently fast (see I.4.6.) for a purely cleavage mechanism. Such a mechanism was proposed in fact by Kirby and Beevers to explain their results. Lindigkeit et al also put forward a purely stress corrosion type reaction to explain their observations of crack growth in NaCl solution at  $\Delta K < \Delta K_{th}$  (in vacuo). Intergranular crack growth was involved in their studies but the conclusion reached, that with increasing  $\Delta K$  ( $> \Delta K_{th}$  (in vacuo)) dislocation transport of hydrogen began to occur, displacing the S.C.C. mechanism, is in complete agreement with the present proposals.

As detailed earlier, the cyclic crack growth mechanism involving crack tip dislocation activity is largely independent of  $K_{max}$  and depends on  $\Delta K$ . The pure cleavage process, however, would be expected to depend on  $K_{max}$  and hence the  $K_{max}$  dependence observed by Kirby and Beevers in the threshold regime might well be exhibited by such a process.

In conclusion it is argued that in total there are three mechanisms of environmentally enhanced fatigue crack growth.

- (I) The cyclic crack growth mechanism discussed in the present work, contributing to crack growth

- at all  $\Delta K > \Delta K_{th}$  (in vacuo).
- (2) A purely brittle crack growth mechanism operative in the regime  $\Delta K < \Delta K_{th}$  (in vacuo).
  - (3) A ductile tearing process becoming increasingly important as  $K_{max}$  approaches  $K_C$ .

### 3.6 The Influence of Metallurgical Variables on Crack Growth.

The observations of fatigue crack growth in 7010 T76 have formed the basis of all the earlier discussion. It is now proposed to relate these observations to those made of growth in the alloy 2024 T3. The influences of such metallurgical variables as intermetallic particles and texture are also noted.

It is difficult to directly compare the results obtained in 2024 T3 and 7010 T76 since there exist great differences in alloy composition and heat treatment. As noted earlier however, the basic mode of cyclic crack growth appears unchanged.

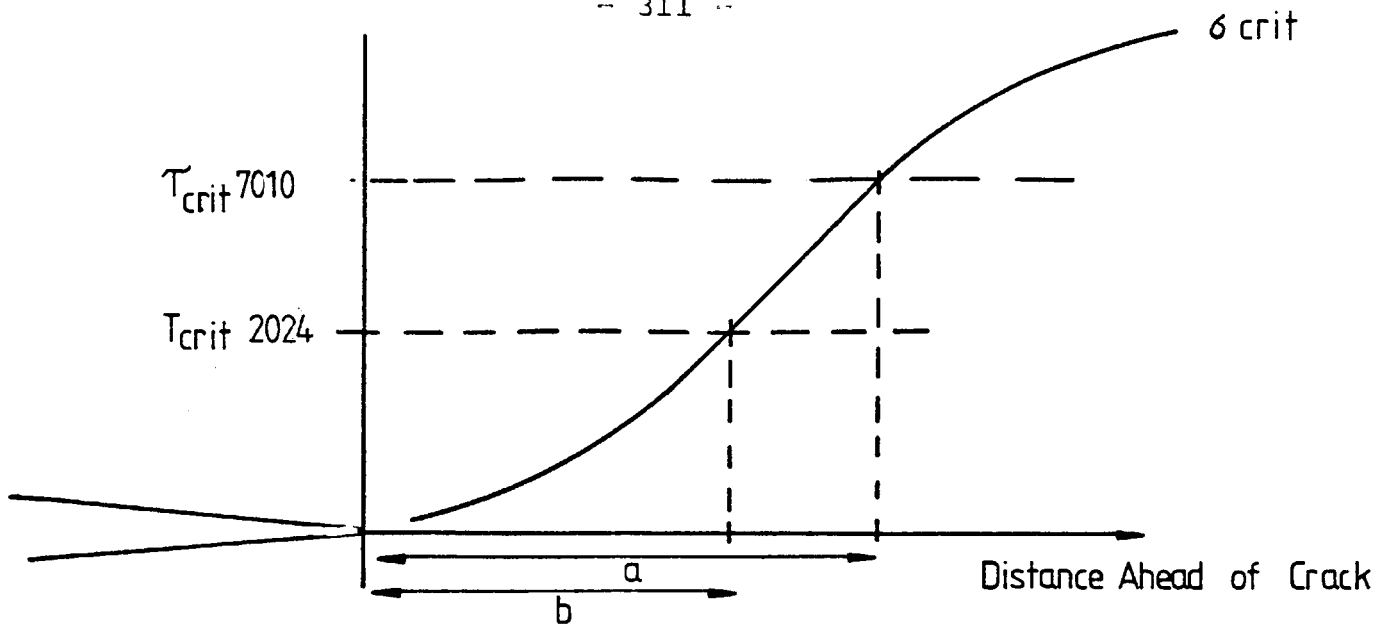
Fatigue crack growth rates in 2024 T3 in laboratory air conditions are well known to be lower than in 7000 series alloys in standard heat treated condition at equivalent  $\Delta K$ . In vacuo, or in atmospheres of low water vapour content, the crack growth rates are not appreciably different but water vapour appears to have a greater influence on crack growth in, for example, 7075 T6 than in 2024 T3 (I08). In 1.6.I a discussion is carried out of the effects of age-hardening on fatigue crack growth and the general conclusion is that the susceptibility of the microstructure to planar slip is of major importance. Lin and Starke (I54) in fact invoked dislocation transport of hydrogen, arguing that the formation of intense slip bands in alloys containing shearable particles promoted hydrogen transport. This argument is clearly appropriate if a mechanism such as that proposed in the present study is operative: The formation of deformation slip bands at the crack tip must be involved in the initial stages of hydrogen transport into the matrix. Any factor which promotes band formation is therefore likely to increase crack growth rates. Unfortunately the present results cannot provide any conclusive evidence here since the two alloys studied lie at opposite ends of the precipitation sequence, the T3 process involving natural ageing to produce very fine particles and T76 producing an overaged

structure of intermediate and final precipitates. Hence neither alloy would be expected to show a great planar slip tendency and no evidence was obtained to suggest particle dissolution or shearing within deformation bands.

The deformation band structures observed in the two alloys were however different in some respects: The structure in the alloy 2024 T3 was less regular showing evidence of more plastic deformation accompanying crack growth at equivalent growth with an apparent involvement of small (<1 $\mu$ m diameter) inter-metallic particles in breaking up the bands. Dowling and Martin (175), for example, have studied the influence of small dispersoids of this size on slip band formation during straining. Their findings were that particles suppressed band formation and homogenised slip. The present observations of crack tip deformation bands would appear to be in agreement with these findings. It is felt that this disturbance of the deformation band structure may be contributory in reducing crack growth rates in 2024 T3. As shown in Part 3.2.I these particles are present to a relatively high volume fraction and the effect may therefore be significant.

The reduced strength level in 2024 T3 may also have an influence on the crack growth mechanism since  $\tau_{crit}$  is lower in 2024 T3 than in 7010 T76: This factor may lead to a reduction in the width of the embrittled zone as shown in Fig. 5.80. In the alloy of lower strength the width of the embrittled zone would be reduced, even assuming an identical effect of hydrogen on  $\sigma_{crit}$  in the two alloys. Hence the brittle component in crack growth would be of less significance in 2024 T3 and overall growth rates would be reduced. (This assumes an equal contribution from growth during blunting which would appear correct since growth rates in vacuo are approximately equal (108)).

Larger intermetallics, present in both alloys, were found to have an increasing role in fracture at high  $\Delta K$  and at high positive R, giving rise to increases in crack growth rate via the ductile tearing contribution to fracture. This supports the evidence of Sanders and Starke (155) who found in the alloy 7050 that large S phase particles had a deleterious effect on crack growth resistance at high  $\Delta K$ . The large inter-



- (a) Embrittled zone 7010 T76
- (b) " " 2024 T3

Fig. 5.80. Possible Effect of Strength Level on width of Brittle Zone

metallics in the case of 7010 were, however, found to be principally  $\text{CuFeAl}_7$  and  $\text{Mg}_2\text{Si}$  (see Part 3.2 for details). At lower stress intensities large intermetallic particles have generally been considered to have little effect on overall crack growth rate (I57,I58). Observations of thin foil specimens in the present work were supportive of this view: In Fig.5.35 the deformation band structure is only modified over a very limited distance as the crack approaches the particle and to the sides of the particle no effect is apparent. Hence the crack growth rate even in the locality of the particle was only modified very slightly. The contribution of the particles alone from static fracture would not be expected to have any effect in this case since the overall volume fraction of particles is low. Some small effect was observed by Sanders and Starke however, in 7050 containing >1 vol% S phase.

The influence of alloy texture on crack growth has not been generally considered of any importance in aluminium alloys. In h.c.p. titanium alloys the growth of fatigue cracks, found to occur on basal planes, has been found to be greatly influenced by texture as recently discussed by Beevers (I76). The observation of growth on {OII} planes in the present work might be expected to induce some textural influence: {OII} planes are separated, unlike basal planes in h.c.p. materials, by a minimum angle of only  $45^\circ$  and hence in all orientations an {OII} plane would always lie at a maximum angle of  $22.5^\circ$  to the overall fracture plane. Hence absolute grain orientation would have only a negligible effect. It is argued however, that the degree of texture may be of some importance: As noted in the discussion of fractographic features the heavily textured 2.5 cm plate was found, particularly at low  $\Delta K$ , to show a smooth 'rooftop' fracture morphology. In the case of 7.5 cm plate the texture was believed to be somewhat reduced and less regular fracture surfaces were observed on specimens prepared from this material. As discussed by Forsyth and Bowen (57), any factor which increases the overall crack front length at a certain crack depth must reduce crack growth rates. Hence in this heavily textured material the shorter crack front length, produced by the much flatter fracture, might be expected to increase crack growth rates to some extent.

PART 6. PROPOSALS FOR FUTURE RESEARCH.

## 6. PROPOSALS FOR FUTURE RESEARCH

The crack initiation studies have proven that hole preparation techniques can have a significant effect on fatigue properties. These results are clearly of technological importance but in order to fully assess their significance further fatigue tests are necessary. For example, the possible effects of compressive loading have been discussed and tests in this area would be informative. It would also be most interesting to vary the machining conditions used, such as drill speed, feed rate etc., since these factors must all influence surface microstructure and topography and consequently have an effect on crack initiation. Such factors are not at present closely controlled in industrial practice, but if machining parameters were shown to influence fatigue life, further improvements in the fatigue performance of bored components might be possible by such controls.

Residual stresses are another important area requiring further study: The present results indicate that residual stresses may have an influence on initiation, it has not however been possible to measure the residual stress distribution adjacent to the various hole types. The use of X-ray techniques to measure lattice distortion would probably be the only experimental route available. It is believed, however, that experimental difficulties might be encountered owing to the curved hole surface: Elastic strains in the hoop direction would not therefore lie in a plane. This, together with the small specimen size (assuming much larger holes were not employed) might preclude the use of X-ray techniques. If such studies were possible it would be most interesting to also investigate the possible 'shake down' of residual stresses during cycling.

The observations of short crack growth have provided some results which are not in agreement with earlier studies and cannot be simply explained. Since the great proportion of the fatigue life of a component is taken up by crack nucleation and short crack growth further information in this area is clearly of vital importance. Measurements of short crack growth rate during testing are clearly very

difficult, except along the specimen surface, since commonly used methods such as compliance or potential difference measurement may not be sufficiently sensitive. The observation of fatigue striations in the HRSEM, within the limitations of the effective resolution limit of  $\approx 400 \text{ \AA}$  might therefore prove of great value.

Very few workers have conducted studies of crack growth using metallographic techniques of the type used here and there therefore remains a great deal of scope for future research:- The present studies have been confined to two particular alloys, each in a single heat treated condition. It would be most informative to carry out similar studies in a series of aluminium alloys in different heat treated conditions: Many workers have reported that precipitate distribution has an influence on fatigue crack growth and thin foil observations of this might allow its effect on the crack growth mechanism to be identified. Precipitate dissolution due to dislocation interaction has been postulated. In suitably aged specimens such effects could be investigated with relation to deformation band formation. This, so called 'coplanar slip' effect has often been invoked in environmental cracking and the present results indicate that it may have an important role, via the dislocation transport of hydrogen. Environmental factors could also be varied, for example, the techniques used here could be applied to more corrosive environments, such as NaCl solution in order to compare and contrast the crack growth mechanism under these conditions with that in laboratory air.

To the authors knowledge no studies using TEM techniques of this type have been carried out in materials other than commercial 7000 and 2000 series aluminium alloys. The observation of other alloy systems would be most valuable: For example, Titanium alloys are well known to show crystallographic fatigue crack growth under certain circumstances, observations of the dislocation structures would allow comparison to be made between the crack growth mechanism in the two cases. Observations in other engineering materials subject to fatigue problems such as high strength steels, would also be interesting.

The high resolution fractography and TEM observations under simple programme load conditions yielded some interesting results concerning the possibility of a delay in response of crack growth rate to change in  $\Delta K$ . It was not, however, possible to be conclusive on the basis of the one programme used. Tests carried out with differing changes in load amplitude with varying numbers of cycles at each might allow some ambiguities to be removed. Tests at constant maximum load with varying minimum load might also prove valuable in the identification of the precise crack growth mechanism.

A mechanism of crack growth involving dislocation transport of hydrogen must imply a change in crack growth mechanism at high test frequencies, since dislocation transport cannot occur if the dislocation velocity exceeds some critical value, related to strain rate. This frequency would appear, from available information, to exceed  $10^4$  Hz. Tests carried out in this frequency regime, combined with metallographic studies, might detect the presence of a transition frequency allowing the validity of dislocation transport to be proven. Water vapour partial pressures in the environment would also have to be carefully monitored since, as detailed earlier, this factor also influences crack growth mechanism.

A very important area of fatigue crack growth is that at low stress intensity close to threshold. Some interesting results have been provided by other workers which suggest a change in, or at least a modification of, the crack growth mechanism. These changes have been found to be environmentally influenced. Metallographic studies using, in particular, TEM techniques might permit any change in mechanism to be identified thereby allowing a greater understanding to be developed in the  $\Delta K$  regime close to threshold.

An area of the present study which, while providing valuable information, was not fully exploited, is that of crack tip cross section thin foil observations. Great problems were experienced in specimen preparation: The electropolishing techniques could, it is believed, prove successful if a sufficiently large number of specimens were available. Ion beam thinning was found to destroy the original microstructure

as a result of beam heating. It might be possible however, to avoid this by the use of a cold stage in the ion-beam thinner combined with an extremely low thinning rate.

CONCLUSIONS.

Crack Initiation Studies.

- (1) The fatigue lives of test pieces containing bored holes are shown to be significantly influenced by the method of hole manufacture.
- (2) Corner burrs are found to be closely associated with crack initiation and their removal results in the greatest improvement in fatigue life.
- (3) The methods of hole bore preparation, drilling and deburring, are observed to result in differences in both hole surface topography and underlying microstructure: The drilling process gives rise to a hole surface of greater roughness, with evidence of smearing and folding, absent on reamed surfaces. Marked surface hardening is also found adjacent to drilled holes to a depth  $\approx 40\mu\text{m}$ , and this is accompanied by a surface microstructure of ultrafine grain size. No such severely deformed layer is observed adjacent to reamed surfaces.
- (4) Despite the differences in bore surface topography and microstructure the methods of bore preparation are not found to exert a great influence on fatigue life in deburred specimens.
- (5) Crack initiation behaviour is quite different in the two cases, intermetallic particles being involved at reamed surfaces and machining defects at drilled.
- (6) The similar fatigue performance of the two specimen types is believed to be a result of the inhibition of microcrack growth in the region adjacent to the hole bore, due to the highly deformed layer.
- (7) The growth rate of short cracks ( $< 1\text{mm}$  in length) as measured by striation spacing, cannot be successfully predicted by L.E.F.M. analysis. Cracks are observed

to grow more slowly than predicted in the direction perpendicular to the hole bore.

Crack Propagation Studies.

- (1) Fatigue crack growth in laboratory air environments is crystallographically influenced with segments of fracture on {OII} planes. This crystallographic growth becomes interspersed with progressively larger areas of ductile tearing with increasing  $\Delta K$ .
- (2) A structure of regularly spaced deformation bands, separated by regions of much lower dislocation density, is observed below the fracture surface. The bands are produced during each load cycle, one per cycle, and exhibit a constant relationship to fatigue striations in regions in which these features are apparent. It is proposed that the deformation band structure is a result of a crack growth mechanism involving initially cleavage mode crack extension followed by blunting. The bands are believed to be a result of dislocation emission from the crack tip during blunting and do not therefore represent the limit of plastic deformation in the crack tip region.
- (3) The deformation structure is quite different in dry (<10ppm H<sub>2</sub>O) argon and oxygen environments. A uniformly high dislocation density is observed, and the cleavage component of growth is therefore related to the presence of water vapour.
- (4) The crack growth process is best described by a mechanism involving the formation of a brittle zone ahead of the crack during each load cycle, through which the crack propagates during the following cycle. A hydrogen embrittlement mechanism is invoked, with dislocation transport of hydrogen involved in the transport of hydrogen ahead of the crack.
- (5) Two types of fatigue striation are observed under lab-

oratory air conditions, both of which are absent in dry atmospheres. The first is basically of a sawtooth profile and shows one face delineated by slipmarkings and one featureless face which is a segment of an {OII} plane. The second type consists of essentially parallel regions of fracture separated by deep slots. The inter-slot regions are also featureless and are segments of {OII} planes. Striations are clearly proven to be formed on a cycle by cycle basis, one striation per cycle.

- (6) Both types of fatigue striation occur in adjacent areas and can be produced simultaneously on opposing fracture faces. A mechanism is proposed to describe the formation of both types and to relate their formation to the basic crack growth mechanism. The occurrence of the two types is believed to be related to the relationship between {OII} planes and the overall local plane of crack growth, the sawtooth type of striation therefore allows the crack to follow an overall growth plane at an angle to {OII} while maintaining segments of fracture on that plane.
  
- (7) The spacing of fatigue striations is related to the overall rate of crack growth over a wide range of  $\Delta K$  (at  $R=0.1$ ), from  $\approx 6$  to  $30 \text{ MNm}^{-3/2}$ . Striation spacing is found to give a large underestimate of crack growth rate, due, it is believed, to static crack jumps. At low  $\Delta K$  striation spacing appears to give an overestimate of crack growth. Here crack arrests are invoked to explain the effect. Assuming a linear relationship between  $\log_{10}$  striation spacing and  $\log_{10} \Delta K$ , striation spacing is proportional approximately to  $\Delta K^2$ .

ACKNOWLEDGEMENTS.

I wish to thank the S.R.C. together with the Royal Aircraft Establishment for the provision of financial support under the S.R.C. C.A.S.E. award scheme and also Professor J.G.Ball and Professor D.W.Pashley for the provision of research facilities.

I would particularly like to express my gratitude for the guidance and encouragement given throughout my studies by Dr H.M.Flower, under whose supervision this work was conducted. I am also indebted to Dr C.J.Peel of the Materials Department, Royal Aircraft Establishment for his invaluable assistance and to Dr P.J.E.Forsyth for many useful discussions.

I would like to thank the staff and students of the Electron Microscopy group in the Metallurgy Department for their help and friendship, in particular Mr G.W.Briers. The members of the photographic section also deserve much praise for their excellent reproduction of photographs.

I would also like to thank Mr D.Rhodes of the Mechanical Engineering Department for the provision of specimens and for much useful advice.

Thanks are also due to many members of staff at IC and at the RAE, too numerous to mention.

Finally I must also thank my wife and my parents for their untiring support. My wife must also be praised for her excellent typing of my almost unintelligible script and for collating the thesis from the confused mass of pages.

REFERENCES.

- (I) M.E.Reynolds and T.E.Fitzsimmons, Aluminium Alloys in the Aircraft industry: Proc. Turin Symp. Technicopy Ltd. (I978) pII5
- (2) P.J.E.Forsyth, Met. Sci. II (I977) p293
- (3) Proc. A.G.A.R.D. Symp. Critically Loaded Hole Technology (I977).
- (4) D.Rhodes, J.C.Radon and L.E.Culver, Int. J. Fatigue (I980) p6I.
- (5) D.Rhodes, L.E.Culver and J.C.Radon, Fatigue '8I: Proc Int. Conf. Pergamon Press. In Press.
- (6) British Aerospace, Aircraft Group. Report No. GEN/B20 O3/FA/MISC/29. (I979).
- (7) P.N.Unwin and M.A.Wilkins, J. Sci. Inst. 2, 2 (I969) p739
- (8) L.F.Mondolfo, Met. Rev. I53 (I97I).
- (9) L.F.Mondolfo, Aluminium Alloys - Structure and Properties. Butterworth (I976).
- (IO) E. Di Russo, Aluminium Alloys in the Aircraft Industry: Proc. Turin Symp. Technicopy Ltd. (I978) p7I.
- (II) G.T.Hahn and A.R.Rosenfield, Met. Trans. 6A (I975) p653.
- (I2) C.J.Peel and P.J.E.Forsyth, Met. Sci. J. 7 (I973) pI2I.
- (I3) E. Di Russo and M.Buratti, Aluminium Alloys in the Aircraft Industry: Proc. Turin Symp. Technicopy Ltd. (I978) pI25.
- (I4) N.Ryum, Acta Met. I7 (I969) p269.
- (I5) C.J.Peel, PhD. Thesis Southampton University (I977).
- (I6) S.N.Singh and M.C.Fleming, Trans. Met. Soc. AIME 245 (I969) pI803.
- (I7) A.Kelly and R.B.Nicholson, Prog. Mat. Sci. IO,3 (I963)
- (I8) G.W.Lorimer and R.B.Nicholson, Acta Met. I4 (I966) pI009.
- (I9) G.Thomas and J.Nutting, JIM 88 (I959) p8I.
- (20) P.A.Thackery, JIM 96 (I968) p228.
- (2I) R.Graf, Comp. Rend. 244 (I957) p337.
- (22) J.H.Auld and S.Mck.Cousland, J. Aust. Inst. Met. I9 (I974) pI94.
- (23) J.Gønnes and Chr.J.Simensen, Acta Met. I9 (I970) p88I.
- (24) A.Saulnier, Comp. Rend. 226 (I948) pI8I.
- (25) G.C.Weatherly, PhD. Thesis Cambridge University (I966).
- (26) N.Sen and D.R.F.West, Proc. Conf. Phase Transf. Inst. Met. Monograph 33 (I969) p49.

- (27) A.Preston, Proc. Roy. Soc. A I67 (I938) p526.
- (28) G.E.Lyman and J.B.Van der Sande, Met. Trans. 7A (I976) pI2II.
- (29) J.H.Auld and S.Mck.Cousland, Met. Sci. IO (i976) p445.
- (30) A.C.Chou, Scripta Met. I2 (I978) p42I.
- (3I) T.H.Sanders and E.A.Starke, Met. Trans. 7A (I976) pI407.
- (32) P.J.E.Forsyth, Aircraft Eng. Nov. (I972) p20.
- (33) D.J.Abson and J.J.Jonas, Met. Sci. J. 4 (I970) p24.
- (34) P.L.B.Oxley and W.F.Hastings, Proc. Roy. Soc. A 356 (I977) p395.
- (35) P.Wright and E.M.Trent, Met. Tech. I (I974) pI3.
- (36) J.J.Jonas, C.M.Sellars and W.J.McG.Tegart, Met. Rev. I30 (I969).
- (37) H.Dölle and J.B.Cohen, Met. Trans. IIA (I980) pI59.
- (38) K.Tsuchida, Y.Kawada and S.Kodama, Bull. Jpn. Soc. Mech. Eng. I8 (II6) (I975) pI23.
- (39) D.L.Rich and I.F.Impellizzeri, ASTM. STP. 637, ASTM Philadelphia.Pa. (I977) p5I3.
- (40) J.Schijve, ASTM. STP. 4I5, ASTM Philadelphia.Pa. (I967) p4I5.
- (4I) H.Mughrabi, ICSMA 5,3. Permagon Press (I980) pI6I5.
- (42) C.A.Stubbington and P.J.E.Forsyth, Acta Met. I4 (I966) p5.
- (43) C.A.Stubbington, Acta Met. I2 (I964) p93I.
- (44) J.C.Grosskreutz and G.G.Shaw, 'Fracture'. Permagon Press (I969) p20.
- (45) P.J.E.Forsyth and A.G.Smale, RAE. Tech. Report No. 68205. (I969). Royal Aircraft Establishment, Farnborough Hampshire.
- (46) C.Q.Bolwes and J.Schijve, Int. J. Fract. Mech. 9,2 (I973) pI7I.
- (47) W.L.Morris, Met. Trans. 9A (I978) pI345.
- (48) C.Y.Kung and M.E.Fine, Met. Trans. IOA (I979) p603.
- (49) R.Chang, W.L.Morris and O.Buck, Scripta Met. (I979) pI9I.
- (50) W.L.Morris and M.R.James, Met. Trans. IIA (I980) p850.
- (5I) D.K.Benson, ASTM. STP. 467 ASTM. Philadelphia.Pa. (I970) pI88.
- (52) E.R.Speakman, *ibid.* p209.
- (53) G.S.Leverant, B.S.Langer, A.Yuen and S.W.Hopkins, Met. Trans. IOA (I979) p25I.
- (54) J.H.Underwood, L.P.Pook and J.K.Sharples, ASTM. STP.

- 63I, ASTM Philadelphia.Pa. (I977) p402.
- (55) C.Laird, Met. Trans. 8A (I977) p85I.
- (56) S.Pearson, RAE Tech.Report No. 7II09. (I97I). Royal Aircraft Establishment, Farnborough Hampshire.
- (57) P.J.E.Forsyth and A.W.Bowen, RAE Tech. Report No.78006. (I978). Royal Aircraft Establishment, Farnborough Hampshire.
- (58) G.H.Haslam, J Mech. Eng. Sci. I3 (I97I) pI30.
- (59) A.Talug and K.Reifsnider, ASTM. STP. 637, ASTM Philadelphia.Pa. (I977) p8I.
- (60) S.Pearson RAE Tech. Report No. 72236. (I973). Royal Aircraft Establishment, Farnborough Hampshire.
- (6I) B.R.Kirby and C.J.Beevers, Fat. Eng. Mat. Struct. I (I979)p20
- (62) D.P.Rooke and D.J.Cartwright, Compendium of Stress Intensity Factors (I976). H.M.S.O., London.
- (63) G.R.Sippel, Metals Progress 92 (I967) pII02.
- (64) R.C.Shah, ASTM STP 590, ASTM Philadelphia. Pa. (I976) p429.
- (65) I.S.Raju and J.C.Newman, NASA Tech. Mem. No.78728 (I978).
- (66) C.A.Zappfe and C.O.Worden, Trans. A.S.M. 43 (I95I) p958.
- (67) P.J.E.Forsyth and D.A.Ryder, Aircraft Eng. 32 (I960) p96.
- (68) P.J.E.Forsyth and D.A.Ryder, Metallurgia 63 (I96I) pII7.
- (69) C.A.Stubbington, RAE Tech Report No.CPM4. (I963). Royal Aircraft Establishment, Farnborough Hampshire.
- (70) C.A.Stubbington, Metallurgia 68 (I963) pIO9.
- (7I) P.J.E.Forsyth, Acta Met. II (I963) p703.
- (72) C.Laird, ASTM. STP. 4I5, ASTM Philadelphia.Pa. (I967) pI3I.
- (73) R.M.N.Pelloux, Trans A.S.M. 62 (I969) p28I.
- (74) P.Neumann, Acta Met. 22 (I974) pII55.
- (75) H.Vehoff and P.Neumann, Acta Met. 27 (I979) p9I5.
- (76) J.C.Grosskreutz, Surface Science 8 (I967) pI73.
- (77) J.C.Grosskreutz, J. Electrochem Soc. II6 (I969) pI232.
- (78) A.Hartman, Int. J. Fract. Mech. I (I965) pI67.
- (79) R.P.Wei, Eng. Fract. Mech. I (I970) p683.
- (80) M.R.Achter, ASTM. STP. 4I5 (I8I), ASTM Philadelphia.Pa. (I967) pI8I.
- (8I) W.J.Wadsworth and H.Hutchings, Phil. Mag. 3 (I958) pII54.
- (82) H.Fuhrrott and P.Neumann, Mech Env. Sens. Fail. Mat: Proc.Int.Conf. Guildford Metals Society (I977) p375.
- (83) C.Laird and G.C.Smith, Phil. Mag. 7 (I962) p847.

- (84) C.Q.Bowles, Report No. 270. Delft University. Department of Aerospace Technology. The Netherlands. (1978).
- (85) H.Shen, S.E.Podlasek and I.R.Krammer, Acta Met. I4 (1966) p34I.
- (86) W.A.Wood, S.Mck.Cousland and K.R.Sargent, Acta Met. II (1963) p643.
- (87) T.Ogura and S.Karashima, Trans. J.I.M. I5 (1974) p324.
- (88) F.J.Bradshaw and C.Wheeler, Int. J. Fract. Mech. 5,4 (1969) p255.
- (89) C.J.L.Booker, Corrosion I Metal/Environment Reactions. Newnes-Butterworths. London (1976) pI.
- (90) F.Jona, J. Phys. Chem. Solids 28 (1967) p2I55.
- (9I) A.Hartman and F.A.Jacobs, Report No. NLR-TN-M-2I33. NLR Amsterdam, The Netherlands (1964).
- (92) T.Broom and A.Nicholson, J.I.M. 89 (196I) p599.
- (93) F.J.Bradshaw, Scripta Met. I (1967) p4I.
- (94) K.U.Snowden, Acta Met. I2 (1964) p295.
- (95) M.R.Achter, Scripta Met. 2 (1968) p525.
- (96) M.J.Horden, Acta Met. I4 (1966) pII73.
- (97) R.P.Wei, P.S.Rao, R.G.Hard, T.W.West and G.W.Simmons, Met. Trans. IIA (1980) pI5I.
- (98) N.F.Mott, Trans. Faraday Soc. 36 (1940) p427.
- (99) L.Montgrain, G.M.Scammans and P.R.Swann, Proc 3rd Tewksbury Symp. Melbourne, Australia (1974) pI94.
- (IO0) J.E.Draley and W.E.Ruther, J. Electrochem. Soc. IO4 (1957) p329.
- (IOI) M.O.Speidel, Int. Conf. 'H' in Metals. ASM. Metals Park Ohio. (1974) p
- (IO2) I.M.Bernstein and A.W.Thompson, Advances in Corrosion Science and Technology. Plenum Press 7 (1972) p235.
- (IO3) B.G.Ateya and H.W.Pickering, J. Electrochem. Soc. I22 (1975) PIOI8.
- (IO4) D.Harris and H.W.Pickering, Mech Env. Sens. Fail. Met: Proc. Int. Conf. Guildford, Metals Soc. (1977) p229.
- (IO5) A.R.C.Westwood, C.M.Reece and M.H.Kamdar, Trans. A.S.M. 60 (1967) p723.
- (IO6) A.J.Bursle and E.N.Pugh, Mech. Env. Sens. Fail. Mat: Proc. Int. Conf. Guildford, Metals Soc. (1977) p229.
- (IO7) C.Q.Bowles and D.Broek, Int. J. Fract. Mech. 8,I (1972) p75.
- (IO8) R.J.Wanhill, Met. Trans. 6A (1975) pI587.
- (IO9) J.Petit, B.Bouchet, C.Goss and J. de Fouquet, Fracture

- Proc. Int. Cong. Waterloo, Canada, University of Waterloo Press 2 (I977) p867.
- (II0) A.Kelly, W.R.Tyson and A.H.Cottrell, Phil. Mag. I5 (I97I) p567.
- (III) J.R.Rice and R.Thomson, Phil. Mag. 29 (I974) p73.
- (II2) G.R.Irwin, J. Appl. Mech. 24 (I977) p36I.
- (II3) E.Orowan, 'Fracture' M.I.T. and Wiley. Reading and New York (I959) pI47.
- (II4) C.J.Macmahon and V.Vitek, Acta Met. 27 (I979) p507.
- (II5) R.E.Stoltz and R.M.Pelloux, Met. Trans. 3A (I972) p243.
- (II6) I.M.Bernstein and A.W.Thompson, Mech. Eng. Sens. Fail. Mat: Proc. Int. Conf. Guilford Metals Society (I977) p4I2.
- (II7) D.J.Duquette, *ibid.* p305.
- (II8) N.J.Petch and D.Stables, Nature (London) I69 (I952) p842.
- (II9) G.M.Scamans, Scripta Met. I3 (I979) p245.
- (I20) J.M.Barsom, Corrosion Fatigue: Chemistry, Mechanics, and Microstructure. NACE-2 (I97I) p424.
- (I2I) R.J.Selines and R.M.Pelloux, Met. Trans. 3A (I972) p2524.
- (I22) A.R.Troiano, Trans. A.S.M. 52 (I960) p54.
- (I23) R.A.Oriani, Fundamental Aspects of Stress Corrosion Cracking. NACE (I969) p32.
- (I24) J.Guest and A.R.Troiano, Corrosion, NACE 30 (I974) p274.
- (I25) L.Christodoulou and H.M.Flower, Acta Met. 28 (I980) p48I.
- (I26) E.F.Smith, R.Jacko and D.J.Duquette, Effect of Hydrogen on the Behaviour of Materials: Proc. Int. Conf. AIME (I975) p2I8.
- (I27) H.P.Van Leeuwen, PhD. Thesis, Delft University, Delft. The Netherlands (I976).
- (I28) E.Eichenauer and A.Pebler, Z. Metallkd. 48 (I957) p378.
- (I29) C.E.Ransley and A.J.Talbot, Z. Metallkd. 46 (I955) p328.
- (I30) R.Eborall and C.E.Ransley, JIM 7I (I945) p525.
- (I3I) L.Christodoulou, PhD. Thesis Imperial College, London, (I980).
- (I32) C.E.Ells and W.Evans, Trans, Met. Soc. AIME. 227 (I963) p435.
- (I33) R.G.Shewmon, Diffusion in Solids, Magraw Hill, New York, (I963).
- (I34) P.Bastien and P.Azou, Proc. Ist World Met. Congress, ASM, Cleveland, (I95I) p535.

- (I35) P.Bastien, Phys. Met. of Stress Corrosion Fracture Interscience, New York, (I959) p3II.
- (I36) L.M.Foster, T.H.Jack and W.W.Hill, Met. Trans. IA (I970) p3II7.
- (I37) J.A.Donovan, Met. Trans. 7A (I976) p82I.
- (I38) J.K.Tien, R.J.Richards, O.Buck and H.L.Marcus, Scripta Met. 9 (I975) pI097.
- (I39) J.K.Tien, Effect of Hydrogen on the Behaviour of Materials Proc. Int. Conf. AIME (I975) p309.
- (I40) J.K.Tien, A.W.Thompson, I.M.Bernstein and R.J.Richards, Met. Trans. 7A (I976) p82I.
- (I4I) D.A.Meyn, Trans. ASM 6I (I968) p52.
- (I42) D.Ritter and R.P.Wei, Met.Trans. 2A (I97I) p3229.
- (I43) R.W.Hertzberg, ASTM. STP. 4I5, ASTM Philadelphia.Pa (I967) p205.
- (I44) B.Tomkins, Phil. Mag. I8 (I968) pI04I.
- (I45) B.Tomkins and W.D.Biggs, J. Mat. Sci. 4 (I969) p544.
- (I46) C.Laird and R.De la Veaux, Met. Trans. 8A (I977) p657.
- (I47) A.J.McEvily, (see C.Laird and R.De la Veaux ibid). Unpublished.
- (I48) B.Cina and T.Kaatz, Fatigue Eng. Mat. Struct. 2 (I979) p85.
- (I49) M.E.Fine, Met. Trans. 6A (I975) p625.
- (I50) S.P.Lynch and D.A.Ryder, Aluminium 49 (I973) p748.
- (I5I) J.M.Papazian, R.J.Delasi and P.N.Adler, Met. Trans. IIA (I980) pI35.
- (I52) S.P.Lynch, Met. Sci. J. 9 (I975) p40I.
- (I53) M.O.Speidel, Phys. Status Solidi. 20 (I967) p.K7I.
- (I54) F.S.Lin and E.A.Starke, Mat. Sci. Eng. 43 (I980) p65.
- (I55) R.E.Sanders and E.A.Starke, Met. Trans. 9A (I978) pI087.
- (I56) J.Albrecht, J.W.R.Martin, G.Lütjering and J.W.Martin, Strength of Metals and Alloys. Proc. 4th Int. Conf. Nancy, France 2 (I976) p754.
- (I57) D.Broek, Fracture. Chapman and Hall. (I969) p754.
- (I58) S.M.El Soudani and R.M.Pelloux, Met. Trans. 4A (I973) p5I9.
- (I59) J.J.Burton and G.Jura, J.Phys. Chem. 7I (I68) pI937.
- (I60) J.Lankford, D.L.Davidson and T.S.Cook, ASTM. STP. 590 ASTM. Philadelphia Pa. (I977) p36.

- (I61) J.R.Rice, ASTM. STP. 415 ASTM Philadelphia Pa. (I967)  
p247.
- (I62) G.T.Hahn, R.G.Hogland and A.R.Rosenfield, Met. Trans.  
3A (I972) pII89.
- (I63) A.J.McEvily and R.C.Boettner, Acta Met. II (I963)  
p703.
- (I64) J.A.Beavers and E.N.Pugh, Met. Trans. IIA (I980) p809.
- (I65) B.S.Hockenull and H.A.Monks, Met. Sci. J. 5 (I97I)  
pI25.
- (I66) J.C.Newman, ASTM. STP. 590 ASTM Philadelphia Pa. (I977)  
p290.
- (I67) A.J.McEvily, J.B.Clark and A.P.Bond, Trans. A.S.M.  
60 (I967) p66I.
- (I68) S.Pearson, Eng. Fract. Mech. 4 (I972) p9.
- (I69) H.F.Hardrath, Fatigue:Interdisciplinary Approach.  
Syracuse University Press, Syracuse New York (I964).
- (I70) D.Rhodes, private communication. (I980).
- (I7I) F.A.Mclintock, ASTM.STP. 4I5 ASTM Philadelphia Pa. (I967)  
pI70.
- (I72) G.T.Hahn, H.Sarrat and A.R.Rosenfield, AFFDL TR-70  
I44 (I970) p425.
- (I73) B.Tomkins, Met. Sci. I4 (I980) p408.
- (I74) J.Lindigkeit, G.Terlinde, A.Gysler and G.Lütjering,  
Acta Met. 27 (I979) pI7I7.
- (I75) J.M.Dowling and J.W.Martin, Acta Met, 24 (I976) pII47.
- (I76) J.Beevers, Met. Sci. I4 (I980) p4I8.

APPENDIX I.

APPENDIX I.

Stress Intensity Calibration.

In this section it is proposed to develop approximate stress intensity calibrations for the crack configurations observed, principally in the initiation type specimens, but also in the specimen type used in 'dry' tests.

In the initiation studies, fatigue cracks were found to initiate along the hole or at the hole corner and to grow in the early stages as approximately semi-circular or quarter circular cracks respectively. It is therefore necessary to obtain stress intensity calibrations for the two crack geometries in the actual specimen types used in the present study. There are two routes open in these calculations as discussed in Part 4.

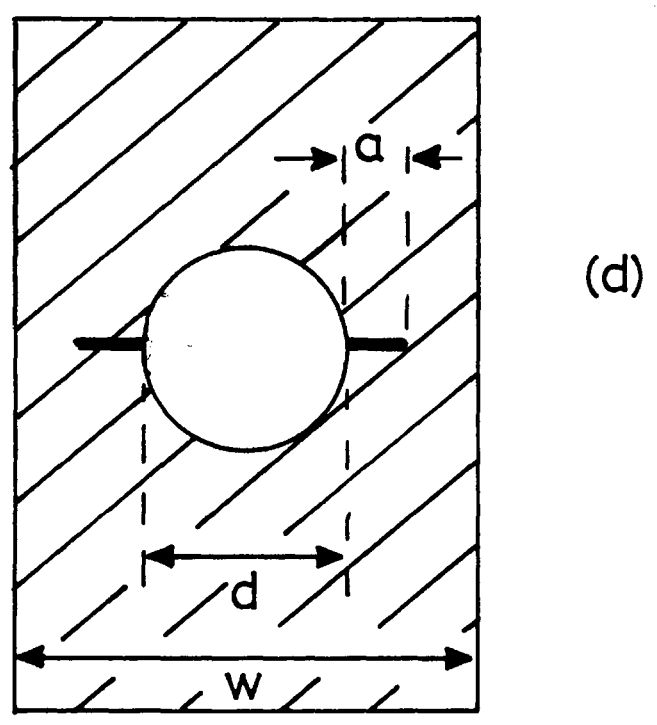
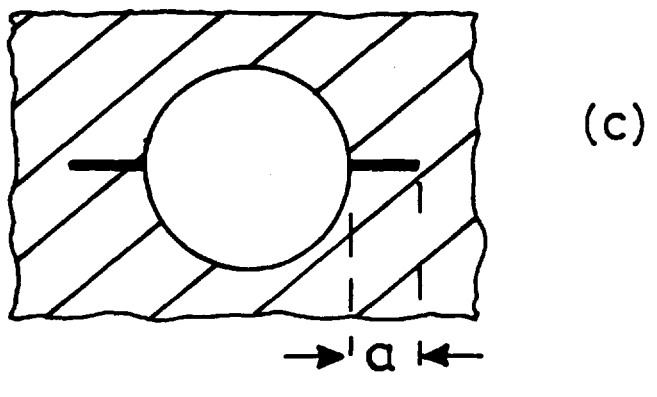
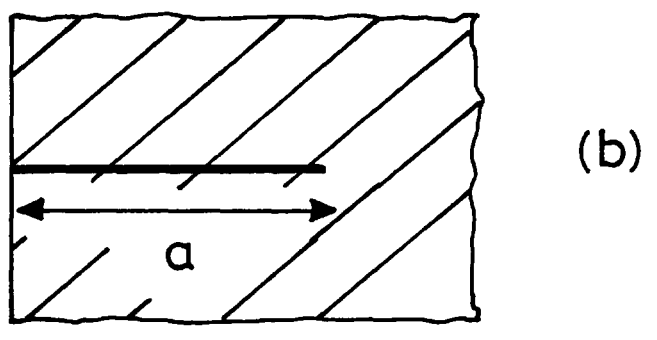
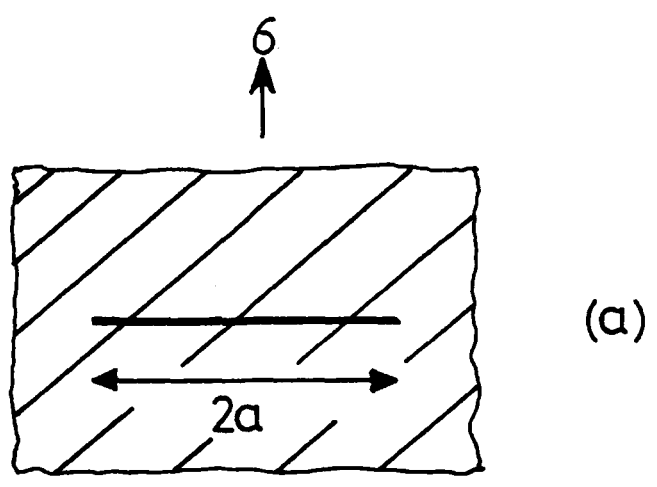
The first is to use two dimensional solutions which are readily available (see for example Rooke and Cartwright (62)). These solutions apply for straight fronted 'through' cracks and it is then possible to adjust the calibration for crack front shape using correction factors, which are also available in the literature (see for example Sippel (63)).

The second route is to use direct three dimensional calculations. Such solutions are available for semi and quarter circular cracks emanating from open circular holes. These solutions are developed by complex analytical and finite element calculations, see for example Raju and Newman (65) and Shah (64). Unfortunately no solutions of this type are available for the specimen geometry used in the initiation studies, which has a rather high ratio of hole diameter to specimen width,  $d/w$ , of  $\sim 0.5$ . The solutions can however be used to check the accuracy of the approximate, corrected two dimensional calculations.

I. Corrected Two Dimensional Solutions. The two dimensional crack tip stress intensity solution for a crack in an infinite plate subject to a remotely applied stress  $\sigma$  is given by: (Fig. A.I(a))

$$K_0 = \sigma \sqrt{\pi a} \quad (I)$$

Fig.A.1



Where:

$K_0$  = stress intensity factor

$2a$  = total crack length

Using this as a basis the stress intensity of a crack in any other circumstances ( $K_1$ ) can be described by:

$$K_1 = \frac{K_1}{K_0} \sigma \sqrt{\pi a} \quad (2)$$

Where  $K_1/K_0$  is known as the stress intensity correction factor or normalised stress intensity factor. The factors are not in all cases normalised to  $K_0$  as given by equation (I), often a more appropriate equation is used. Such correction factors are tabulated by Rooke and Cartwright (62) for many different crack configurations.

In the case of surface flaw two simple equations are possible, in the simple case of a plane section crack in a semi-infinite plate (Fig. A.I(b)):

$$K_1 = I. I2 \sigma \sqrt{\pi a} \quad (3)$$

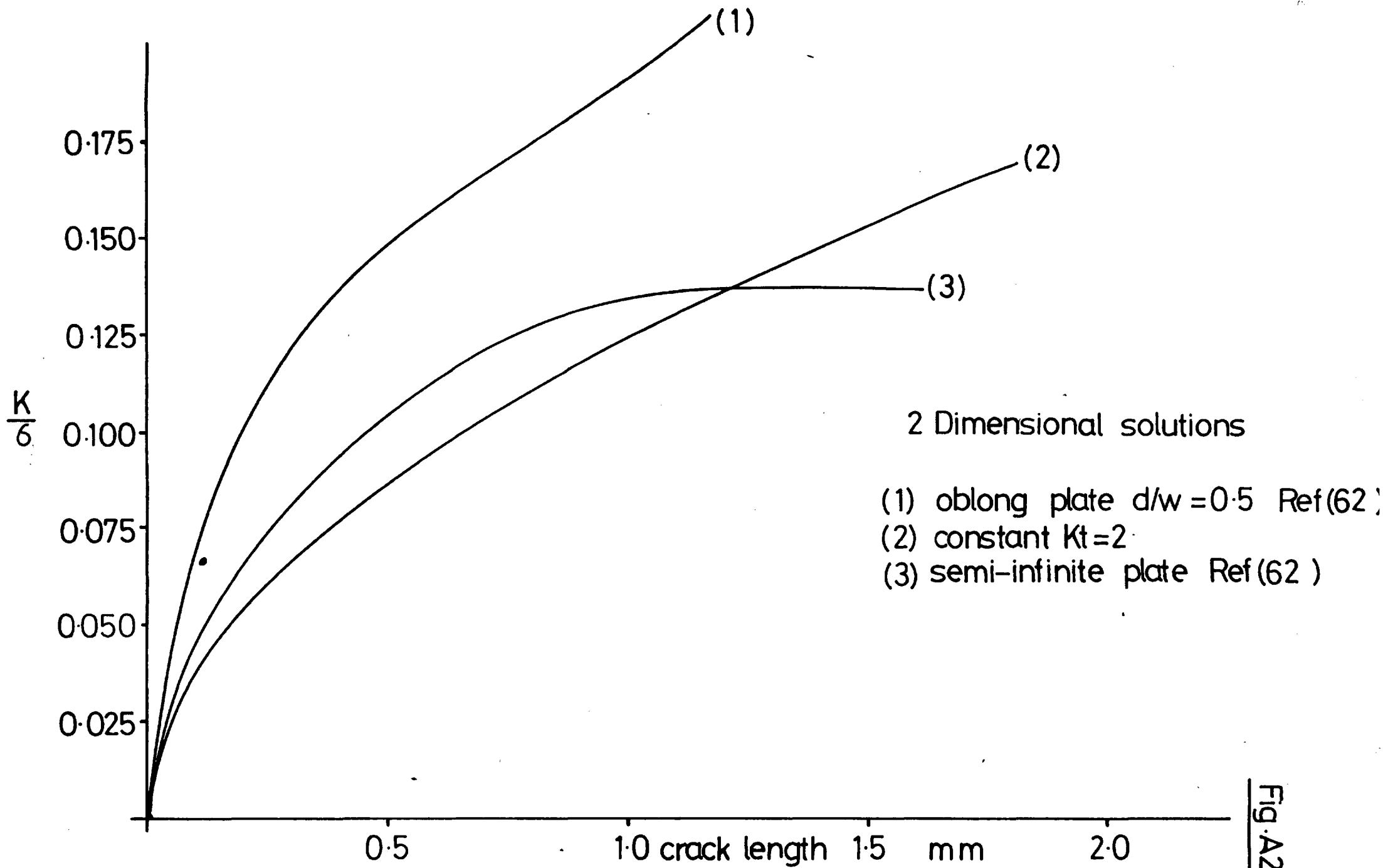
Directly adjacent to a stress concentration, for example a circular hole, the stress intensity can be approximated to:

$$K = K_t \times I. I2 \sigma \sqrt{\pi a} \quad (4)$$

Where:

$K_t$  = the elastic stress concentration factor

The effect of  $K_t$  diminishes however with distance from the hole surface and hence a calibration based on this equation would give a large overestimate of  $K$  at all but the shortest crack lengths. The actual solution for the situation in Fig. A.I(c) given by Rooke and Cartwright for a circular hole 6.5mm in diameter in an infinite plate. All solutions are given as  $K/\sigma$  rather than  $K_1/K_0$  as they refer to a specific situation of crack length and hole diameter. In this case however the restrictions of specimen size are not taken into account. Solution (I) in Fig. A.2 demonstrates the effect of the specimen back



surface, here a solution is given for a crack in a plate containing a circular hole of diameter equal to half the plate width. Another simple solution is also given where  $K_t$  is considered to equal 2, i.e. the hole is simply considered to reduce the cross sectional area. (In fact  $K_t=4.32$  in this situation Fig. 4.I4)

$$K/\sigma = 1.12 \times 2 \sqrt{\pi a} \quad (5)$$

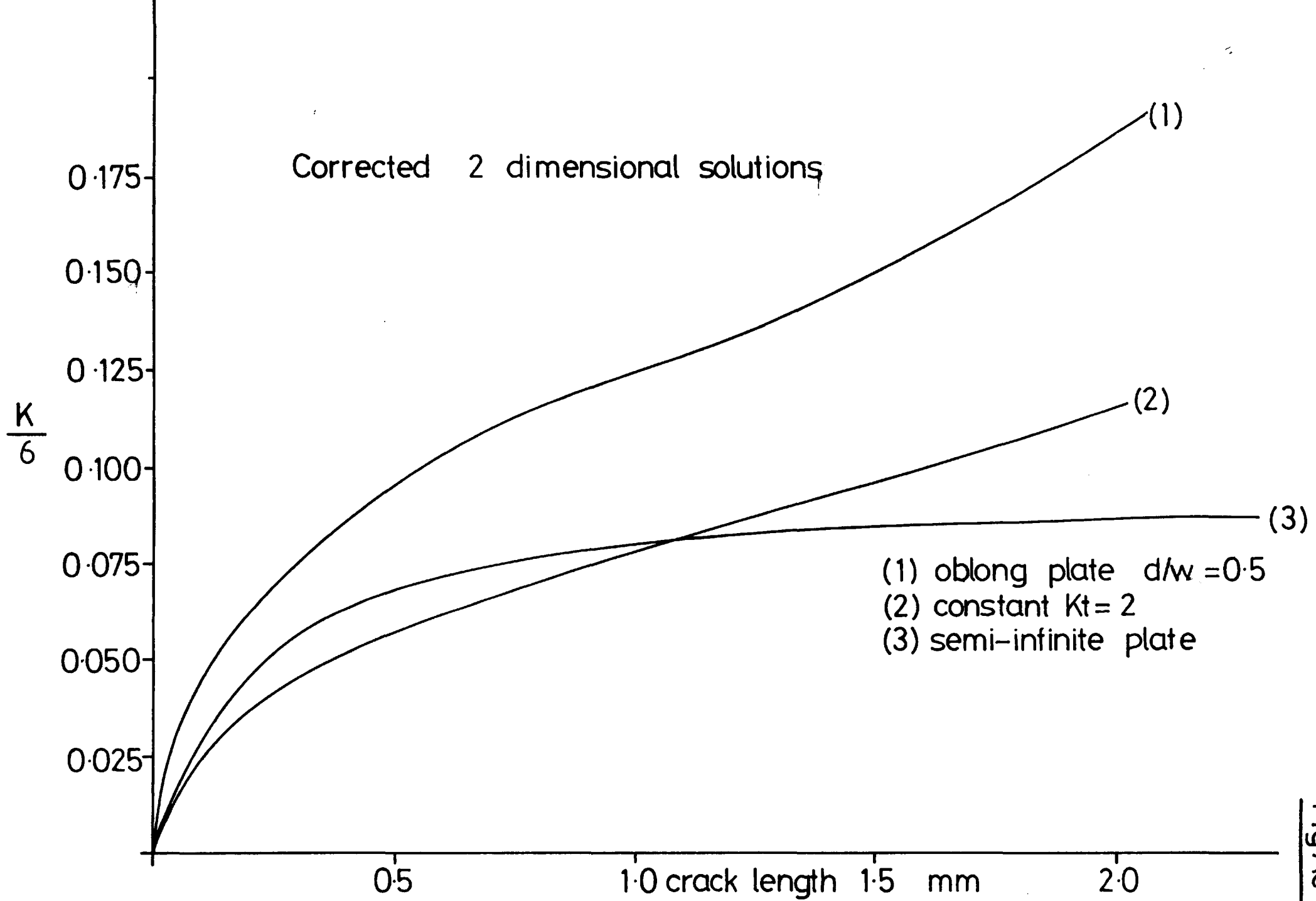
Hence this solution gives a minimum possible value for stress intensity at any particular crack length.

All these solutions can be approximately corrected for the three dimensional situation of semi-circular crack front by using the shape factor  $\phi$ , given as 1.57 for such a shape by Sippel (63).

$$K_1 = \frac{K_1}{K_0 \phi} \sigma \sqrt{\pi a}$$

Hence by dividing through the previous solutions which describe the situation in Fig.A.I by  $\phi$  approximate solutions for 2 semi-circular cracks can be obtained Fig.A.3. The actual solution for two semi-circular cracks is likely to be in this case between curves (1) and (2): Curve (1), based on the 2d through crack solution, is dominated, particularly at higher crack lengths, by the reduction in cross sectional area. This factor is of less importance in the case of a semi-circular or semi-elliptical crack since at equal crack lengths the area of a semi-circular crack is lower than the equivalent depth through crack. Similarly the  $K_t = 2$  solution, curve (2), gives an underestimate of stress intensity since no account is taken here of the effect of reduction of cross sectional area at long crack lengths or  $K_t$  at short crack lengths.

2. Three Dimensional Solutions. It is proposed here to compare the 3d solutions computed by Shah (64) with the corrected 2d solutions, to establish the validity of the use of the shape correction factor. The solution obtained by Shah shown in Fig 4.I7 implies that stress intensity depends on the position along the crack front, being a maximum at the hole bore and a minimum at



FigA3

90° to it. For  $\phi=0^\circ$  45° and 90° solutions for  $K/\sigma$  in a semi-infinite plate are given in Fig.A.4 . The solutions clearly approximate quite closely to the corrected two dimensional solution so the use of the crack front shape correction factor would appear to be valid at least at short crack lengths. At long crack lengths in finite plates the reduction in area effect is likely to lead to some discrepancy however.

3. Single and Quarter Circular Crack Solutions. All solutions developed so far have applied to two semi-circular cracks at the hole bore. It is however possible to use these solutions to calculate the stress intensity at the tip of quarter circular corner cracks, the situation in Fig.4 I6(c) and also single cracks. The techniques used are detailed by Shah.

The development of the solution from a semi-circular to a quarter circular crack is achieved using a front face correction factor  $M_F$ . This accounts for the influence of the front surface of the specimen on the stress intensity at a corner crack.

$$M_F = 1.0 + 0.12 \left( 1 - \frac{a}{2c} \right)^2$$

This solution applies for an elliptical crack of dimensions  $a$  and  $c$ , and is therefore equal to  $1 + 0.12(1 - \frac{1}{2})^2$  for a quarter circular crack = 1.0075. Hence the effect is likely to be negligible and  $M_F$  cannot exceed 1.12 under any circumstances.

To convert the stress intensity calibration for two cracks to that for a single crack an equal area criterion has been used by Shah (64)

$$K_{\text{one crack}} = \sqrt{\frac{2R+L}{2R+2L}} \cdot K_{\text{two cracks}}$$

This applies for two dimensional solutions where  $R$  = hole radius and  $L$  crack length. In the case of elliptical or circular crack fronts a similar equation is used: For example a semi-circular crack of length  $a$  has an area equal to a through crack of length  $\pi a^2/2t$  ( $t$  = specimen thickness) hence:

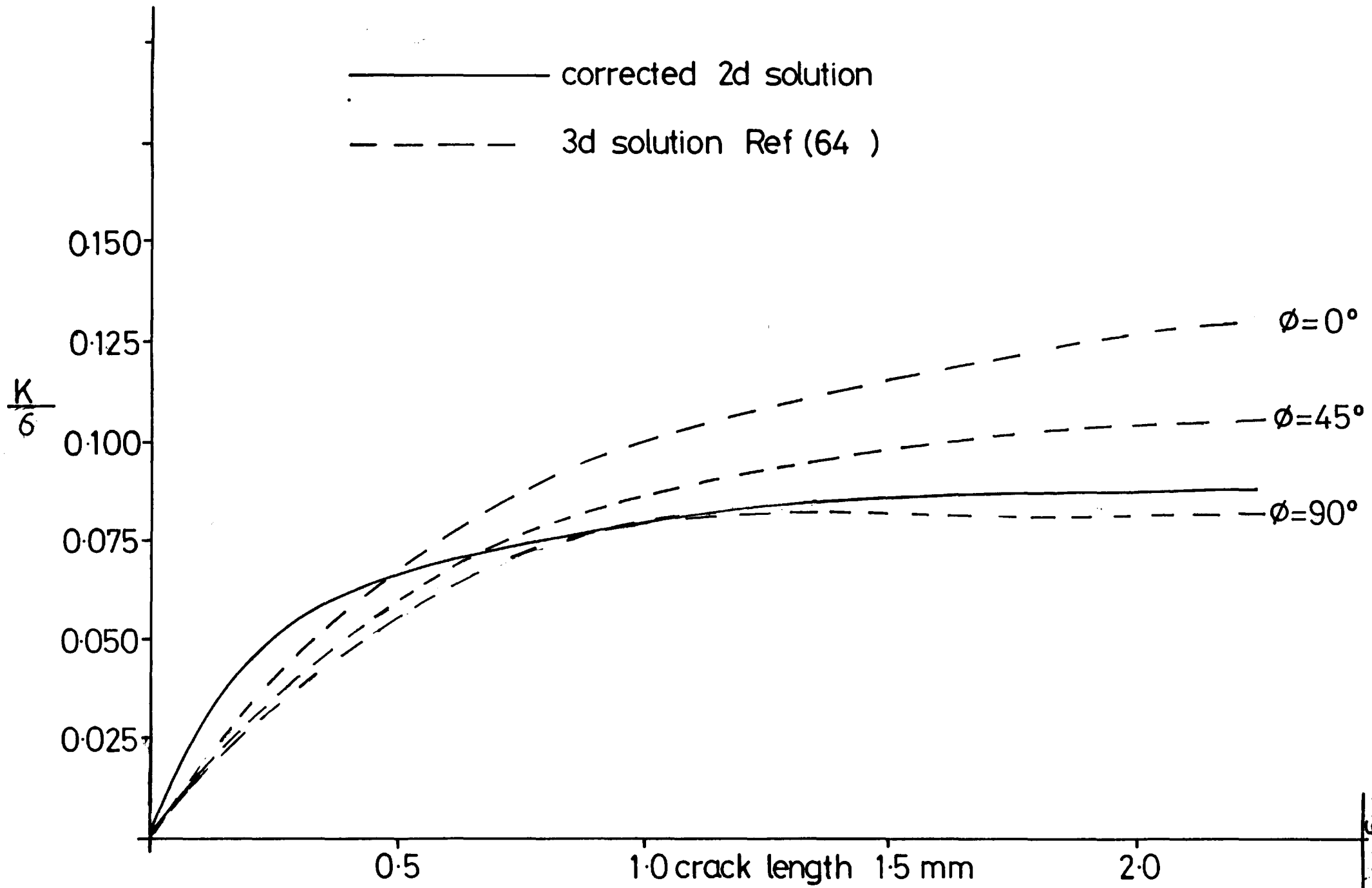


Fig A.4

$$K_{\text{one crack}} = \sqrt{\frac{2R + \pi a^2 / 2t}{2R + 2\pi a^2 / 2t}} \cdot K_{\text{two cracks}}$$

Similar solutions apply for quarter circular cracks. Examples of the use of these factors are shown for the specimen geometry used in the initiation studies in Fig.A.5 .

4. Calibration of Stress Intensity for Specimen Type Used in Environmental Tests. The specimen type used here was basically similar to that in the initiation studies being of the centre notched type. In this case however the ratio of hole diameter to specimen width,  $d/w$ , was considerably lower,  $\sim 0.1$  and hence 'break through' of the crack to form a through crack occurred at a crack depth of around 2mm and at depths greater than this a simple  $2d$  solution could be used. In fact at crack lengths greater than the hole diameter a simple solution for a centre cracked panel as shown in Fig.4.I5 gives a close approximation to the actual situation.

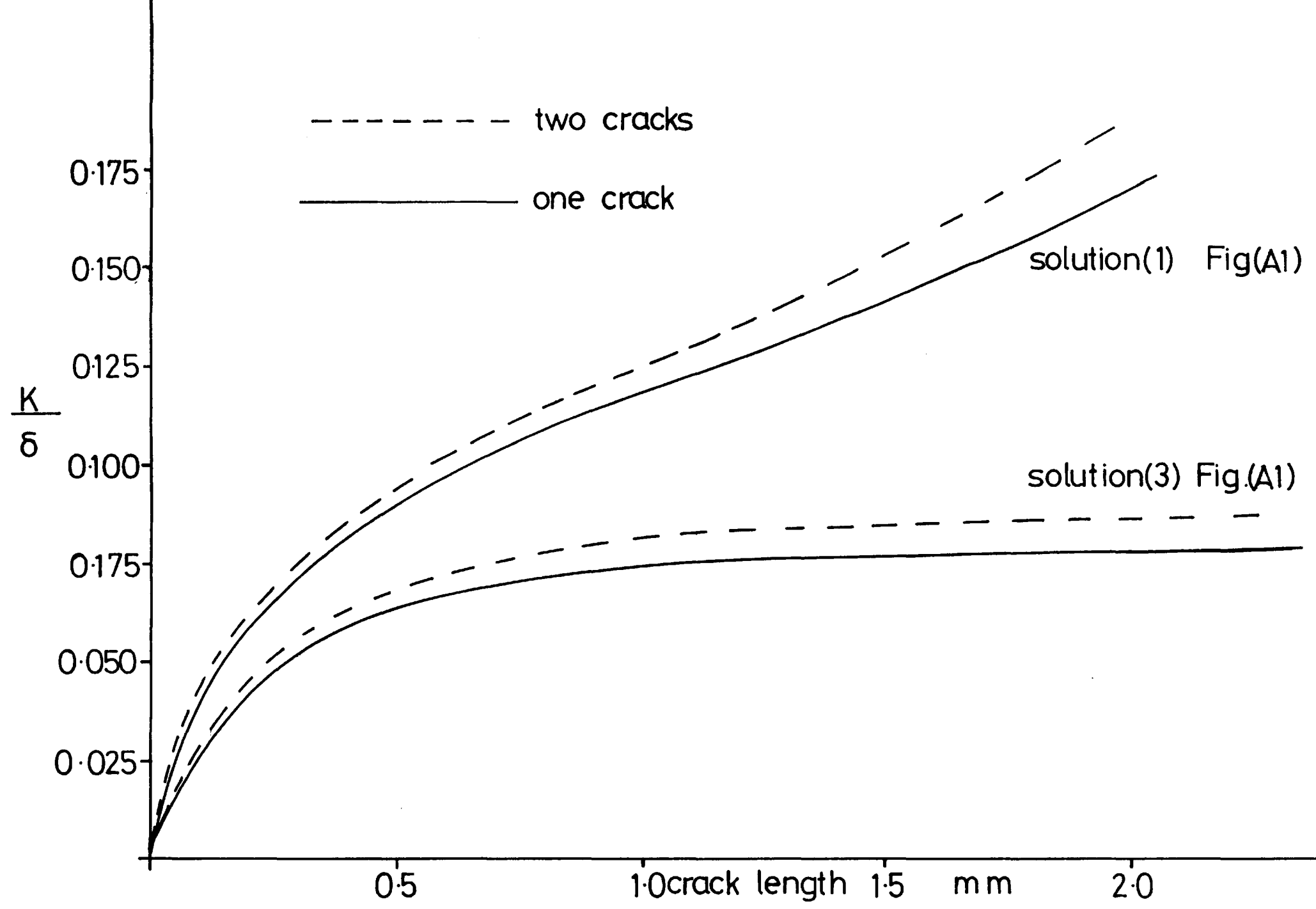


Fig A5

10

APPENDIX II.

APPENDIX II.

• Table I. Chemical Composition and Mechanical Properties of 7010 T76 and 2024 T3.

Chemical Composition.

Element	Zn	Mg	Cu	Zr	Mn	Cr	Fe	Si
7010 wt%	6.20	2.50	1.70	0.14	<0.03	<0.05	<0.15	<0.10
2024 wt%	0.25	1.50	4.40	--	0.60	--	<0.50	<0.50

Mechanical Properties. (L-T direction)

	7010 T76	2024 T3
0.2% Proof Stress $\text{MNm}^{-2}$	484	310
Ultimate Tensile Stress $\text{MNm}^{-2}$	544	430
Elongation %	12.1	7.8
(E) Tensile Modulus $\text{GNm}^{-2}$	74.3	72.0
( $K_{IC}$ ) Plane Strain Fracture	$\approx 36$	$\approx 49$
Toughness $\text{MNm}^{-3/2}$		

Table II. Chemical Composition of Other Commercial Alloys Mentioned in the Text.

Series	Zn	Mg	Cu	Cr	Zr	Ni	Si	Mn
7000								
7075	5.6	2.5	1.6	0.30	--	--	--	--
7175	6.1	2.9	2.0	0.18	--	--	--	0.1
	6.8	2.7	2.0	0.30	--	--	--	--
	6.2	2.25	2.3	--	0.12	--	--	--
2000								
2219	--	1.6	6.3	--	0.18	1.0	--	--
2618	--	1.6	2.3	--	--	1.0	0.18	--
5000								
5083	--	4.45	--	0.15	--	--	--	0.7
5086	--	4.0	--	--	--	--	--	0.45

Table III. Commercial Thermomechanical Treatments.

The nature of commercial thermomechanical treatments are delineated by the prefix and first numbers as follows:

- T Tempers - thermally treated material.
- T3 Solution heat-treated and then cold worked, - naturally aged.
- T6 Solution heat-treated and then artificially aged, - normally to peak strength.
- T7 Solution heat-treated and then artificially aged to a point beyond that of maximum strength.
- T8 Solution heat-treated, cold worked and then artificially aged.

The second and possibly third and fourth number in the temper refer to the specific heat treatment. For example, the T73 treatment, applicable to 7075, normally involves solution treatment followed by a two stage ageing process at 120°C and 170°C.

The T76 heat treatment applied to 7010 involves solution treatment followed by heating to 170°C at a rate not exceeding 20°C per hour, followed by 6-15 hours at that temperature.

- H Tempers - mechanical working.
- H4 35% cold reduction after full anneal.
- H6 55% cold reduction after full anneal.
- H8 75% cold reduction after full anneal.

Further digits may be included to specify the nature of the working process.